DATE DUE	DATE DUE	DATE DUE

Stochastic Estimation of the Flow Structure Downstream of a Separating/Reattaching Flow Region Using Wall-Pressure Array Measurements

By

Mohamed Ibrahim Daoud

A DISSERTATION

Submitted to
Michigan State University
in partial fulfillment of the requirements
for the degree of

DOCTOR OF PHILOSOPHY

Department of Mechanical Engineering

2004

ABSTRACT

Stochastic Estimation of the Flow Structure Downstream of a Separating/ Reattaching Flow Region Using Wall-Pressure Array Measurements

By

Mohamed Ibrahim Daoud

This study examines the *spatio-temporal* characteristics of the surface-pressure fluctuations and associated flow structures in the developing flow downstream of the reattachment point of a fence-with-splitter-plate flow. The investigation focuses on understanding the wall-pressure field characteristics, and the flow sources responsible for its generation in the non-equilibrium boundary layer originating from the separating/reattaching shear layer associated with the flow over the fence, using a wall-pressure database that was simultaneously acquired with X-hotwire time series. This is motivated by guiding efforts to predict and/or control flow-induced noise and vibration in applications involving flows downstream of appendages and surface protrusions.

Characterization of the wall-pressure data alone showed that the wall-pressure fluctuations were dominated by large-scale downstream-traveling disturbances that were generated upstream in the separated shear layer. Notwithstanding this dominance, the p' signature of these structures decayed with increasing downstream distance as the vortices underwent a relaxation process while the contribution of eddies, associated with the development of a "sub-boundary layer", became more significant with increasing downstream distance. In addition, wavenumber-frequency-spectrum results showed that pressure signatures of all wavenumbers and frequencies were associated with flow disturbances that travel downstream with the same convection velocity.

Finally, multi-point Linear Stochastic Estimation of the flow field based on instantaneous wall-pressure information confirmed the dominance of wall-pressure generation by the passage of the outer-shear layer vortical structures and their mutual interaction. Examination of the linear source term in Poisson's equation of the pressure in conjunction with the stochastically-estimated velocity field revealed two mechanisms for p' generation associated with the quasi-periodic vortex passage. One mechanism was related to sources localized at the height of the vortex centers in the outer-shear layer, which represented *direct* generation of p' caused by the strong vortex-induced disturbances in the outer part of the flow. The other was located near the wall ($y/\delta < 0.2$, where δ is the boundary layer thickness) and resulted from interaction of the weak near-wall disturbances generated by the vortex passage with the strong mean wall shear. It is important to realize that while it is likely that the former mechanism could be modeled by the wall-pressure field associated with quasi-periodic passing of vortices embedded in uniform inviscid flow, the latter mechanism requires proper account of viscous effects near the wall and associated mean shear.

DEDICATED TO MY MOTHER AND THE MEMORY OF MY FATHER

ACKNOWLEDGMENT

I would like to deeply acknowledge my family, advisor, committee members and colleagues, because this thesis work could not have been done without their support and/or contribution.

I owe a great debt of gratitude and appreciation to my little family, Nermeen, Mariam and Omar, who have had selflessly sacrificed to stand by and assist me by any means to overcome the toughest moments when I became stuck between a rock and a hard place. My lovely family, whose age is the same as that of this thesis work, has made my whole life much easier due to their understanding and support. Also, I would like to express my love and respect to my mom who also has greatly suffered because of my stay away from her. I would like also to thank my sisters and brother, my brothers in law, and my nieces and nephews for their love and support.

I would like to express my special appreciation to my advisor, Dr. Ahmed Naguib, whose guidance and directions have been greatly supportive of my work. I wish also to emphasize that his warm friendship and brotherhood-like relationship with his students and me myself has been the thrust of my Ph.D. rocket.

I would like also to thank my committee members Dr. Giles Brereton, Dr. Dennis Gilliland and Dr. Manooch Koochesfahani whose advice and recommendations were greatly helpful throughout my thesis work.

Finally, I wish to thank my colleagues whom I have worked with at the Flow Physics and Control Lab. This includes Laura Hudy, Yongxiang Li, Antonious Aditjandra, and Chad Stimson.

This work has been partially supported by NSF grant CTS-0116907.

TABLE OF CONTENTS

LIST OF FIGURES viii

LIST OF TABLES xv

NOMENCALTURE xvi

1. INTRODUCTION 1
    1.1. Literature Review 3
        1.1.1. Separating, Reattaching and Developing Flows 3
        1.1.2. Characteristics of the Turbulent Wall Pressure 13
        1.1.3. Stochastic Estimation 18
    1.2. Motivation 22
    1.3. Objectives 23

2. EXPERIMENTAL SET-UP AND METHODOLOGY 25
    2.1. Experimental Set-up 25
        2.1.1. Wind Tunnel Facility 25
        2.1.2. Test Model 28
        2.1.3. Instrumentation 31
    2.2. Experimental Methodology 40
        2.2.1. Static Pressure System 40
        2.2.2. Microphones 42
        2.2.3. Tufts 50
        2.2.4. Hotwire Sensors 55

3. WALL-PRESSURE RESULTS 76
    3.1. Mean-pressure Distribution and the Reattachment Length 77
    3.2. Fluctuating Pressure Distribution 79
    3.3. Autocorrelation 82
    3.4. Power Spectra 87
    3.5. Cross Correlation 96
    3.6. Wavenumber-Frequency Spectrum 103

4. VELOCITY-PRESSURE ANALYSIS AND STOCHASTIC ESTIMATION 107
    4.1. Velocity Characteristics 107
        4.1.1. Characteristics of the Boundary-Layer Mean and Turbulent Velocity Profiles 107
        4.1.2. Velocity Spectra 123
    4.2. Velocity-Pressure Characteristics 134
        4.2.1. Velocity/Wall-Pressure Cross-Spectra 134
        4.2.2. Velocity/Wall-Pressure Cross-Correlations 145
        4.2.3. Conditionally-Averaged-Data Analysis 156
    4.3. Stochastic Estimation 165

4.3.1. Principle and Equations 167
4.3.2. Comparison between ML, SL and SQ 174
4.3.3. Stochastic Estimation Results and Wall-Pressure Sources 184

5. CONCLUSIONS AND RECOMMENDATION FOR FUTURE WORK 207
5.1. Conclusions 207
5.2. Future Work 211

A. Derivation of Equation (2.6) 213

B. Data Acquisition Settings 214

REFERENCES 216

Figure 1.1
Figure 2.1
Figure 2.2
Figure 2.3
Figure 2.4
Figure 2.5
Figure 2.6
Figure 2.7
Figure 2.8
Figure 2.9
Figure 2.1
Figure 2.1
Figure 2.1
Figure 2.1
Figure 2.1
Figure 2.1
Figure 2.1
Figure 2.1
Figure 2.1
Figure 2.1
Figure 2.2
Figure 2.2

LIST OF FIGURES

Figure 1.1. A schematic of an ideal two-dimensional flow over a splitter-plate-with-fence 2

Figure 2.1. Schematic of the wind facility (dimensions in meters) 26

Figure 2.2. A schematic of the test model 28

Figure 2.3. A frontal picture of the model showing the blockage effect of the fence 30

Figure 2.4. A schematic of the instrument and middle plates depicting the locations of the pressure taps and microphones 30

Figure 2.5. A picture of the fence-with-splitter-plate model inside the wind tunnel 31

Figure 2.6. An image of a tuft attached to the I-plate 33

Figure 2.7. An image of one of the microphones used in the array 35

Figure 2.8. A schematic of the microphone driving circuit 35

Figure 2.9. A schematic of the X-probe 36

Figure 2.10. Images showing top and side views of the X-probe 37

Figure 2.11. Images of the traversing mechanism and the LVDT: overall (left) and close-up (right) views 39

Figure 2.12. LVDT calibration 39

Figure 2.13. Mean-pressure-coefficient distribution for the top and bottom sides of the splitter plate 42

Figure 2.14. Microphone installation in the Instrument and Middle plates 43

Figure 2.15. A picture of the microphone-calibration setup 45

Figure 2.16. PWT calibration results: pressure ratio (top) and phase shift (bottom) 47

Figure 2.17. Frequency response of a microphone/hole assembly 48

Figure 2.18. Mean sensitivity (Km) of themicrophones (top) and Corresponding time-delay (bottom). Microphone #1 is the most upstream microphone 51

Figure 2.19. Cross-talk check of Microphone # 13 (Mic. #1 is the most upstream one) 52

Figure 2.20. A sample wide-aperture tuft image 54

Figure 2.21. FFP of the reattaching flow versus the x-location of the tuft 55

Figure 2.2
Figure 2.2
Figure 2.2
Figure 2.2
Figure 2.2
Figure 2.2
Figure 2.2
Figure 2.2
Figure 2.3
Figure 2.3
Figure 2.3
Figure 2.3
Figure 2.3
Figure 2.3
Figure 2.
Figure 3.
Figure 3.
Figure 3.
Figure 3
Figure 3
Figure 3

Figure 2.22. A schematic of the X-wire probe and angles definition 57
Figure 2.23. An image of the yaw calibration setup 59
Figure 2.24. Schematic of the yaw calibration setup 62
Figure 2.25. Yaw calibration: voltage results 62
Figure 2.26. Sample calibration data for the X-probe hotwires 63
Figure 2.27. Yaw calibration data after conversion of voltage to velocity 63
Figure 2.28. Yaw-calibration data and corresponding curve fits for hotwire #1 (top plot) and hotwire #2 (bottom plot) 64
Figure 2.29. A photograph of the X-wire probe and its reflection in the splitter plate 66
Figure 2.30. A close-up image of the X sensor 67
Figure 2.31. Leading edge for X- and single-wire in-situ calibration 69
Figure 2.32. Boundary-layer streamwise mean-velocity profiles from single- and X-wire measurements at $x/X_r = 3.05$ 71
Figure 2.33. Boundary-layer RMS streamwise-velocity profiles from single- and X-wire measurements at $x/X_r = 3.05$ 72
Figure 2.34. Pressure spectra of the microphone immediately upstream ($x/X_r = 3.0$) of the X-wire for three y locations of the wire 74
Figure 2.35. Pressure spectra of the microphone immediately downstream ($x/X_r = 3.11$) of the X-wire for three y locations of the wire 75
Figure 3.1. Streamwise distribution of the mean pressure coefficient from the present study compared to Hudy *et al.* (2003) 78
Figure 3.2. Streamwise distribution of the coefficient of the RMS pressure fluctuation 80
Figure 3.3. A comparison between the $C_{p'}$ streamwise distribution of Hudy *et al.* (2003) and the present work with that of Farabee and Casarella (1986) 81
Figure 3.4. Autocorrelation coefficient at five different streamwise locations downstream of the reattachment region for Re = 7600 and 15700 84
Figure 3.5. Contour maps of the autocorrelation coefficient for all 16 Microphones and the two Reynolds numbers; Re = 7600 and 15700 85
Figure 3.6. A comparison of the auto-correlation results at zero time delay and five different streamwise locations downstream of the reattachment region for Re = 7600 86

Figure 3.7
Figure 3.8
Figure 3.9
Figure 3.1
Figure 3.1
Figure 3.1
Figure 3.1
Figure 3.1
Figure 3.1
Figure 3.1
Figure 3.1
Figure 3.1
Figure 4.1
Figure 4.2
Figure 4.
Figure 4.
Figure 4.
Figure 4.
Figure 4.
Figure 4.

Figure 3.7. A full contour map of the p′ autocorrelation coefficient for the separating/reattaching (Hudy *et al.* 2003) and the present recovering flows 87

Figure 3.8. Spectra of the wall-pressure fluctuation for Re = 7600: logarithmic (top) and semi-logarithmic (bottom) plots 89

Figure 3.9. Spectra of the wall-pressure fluctuation for Re = 15700: logarithmic (top) and semi-logarithmic (bottom) plots 90

Figure 3.10. Definition of the frequency used in the splitting procedure Of p′ spectrum 94

Figure 3.11. The ratio between high- and low-frequency pressure fluctuations energy 95

Figure 3.12. Cross-correlation results at five different locations for Re = 7600 and 15700 98

Figure 3.13. Cross-correlation results for all 16 microphones and Re = 7600 (top); and 15700 (bottom) 99

Figure 3.14. Plot for extraction of the convection velocity for the two Reynolds numbers of 7600 and 15700 100

Figure 3.15. Contour map of the cross-correlation coefficient for all 16 microphones and Re = 7600 102

Figure 3.16. Contour map of the cross-correlation coefficient for all 16 microphones and Re = 15700 102

Figure 3.17. Wavenumber-frequency spectrum for Re = 7600 104

Figure 3.18. Wavenumber-frequency spectrum from the separating/ reattaching flow of Hudy *et al.* (2003) 106

Figure 4.1. Wall scaling of boundary-layer mean-velocity profile 110

Figure 4.2. Shear-layer scaling of the boundary-layer mean-velocity profile 114

Figure 4.3. Wall scaling of the boundary-layer u_{rms} profile 115

Figure 4.4. Shear-layer scaling of the boundary-layer u_{rms} profile 117

Figure 4.5. Wall scaling of the boundary-layer v_{rms} profile 119

Figure 4.6 Shear-layer scaling of the boundary-layer v_{rms} profile 120

Figure 4.7. Wall scaling of the boundary-layer Reynolds stress profile 121

Figure 4.8. Shear-layer scaling of the boundary-layer Reynolds stress profile 123

Figure 4.9. Streamwise-velocity spectra at $y/\delta = 0.05$, 0.125, 0.25, 0.375, 0.5 and 0.625 and $\xi = 2.05$ 125

Figure 4.1
Figure 4.1
Figure 4.1
Figure 4.1
Figure 4.1
Figure 4.1
Figure 4.1
Figure 4.1
Figure 4.1
Figure 4.1
Figure 4.2
Figure 4.2
Figure 4.2
Figure 4.2

Figure 4.10. Semi-log plots of the streamwise-velocity spectra at $y/\delta = 0.05$, 0.125, 0.25, 0.375, 0.5 and 0.625 and $\xi = 2.05$ 128

Figure 4.11. Normal-velocity spectra at $y/\delta = 0.05$, 0.125, 0.25, 0.375, 0.5 and 0.625 and $\xi = 2.05$ 128

Figure 4.12. Semi-log normal-velocity spectra at $y/\delta = 0.05$, 0.125, 0.25, 0.375, 0.5 and 0.625 at $\xi = 2.05$ 129

Figure 4.13. Boundary-layer velocity cross spectra at $y/\delta = 0.05$, 0.125, 0.25, 0.375, 0.5 and 0.625 and $\xi = 2.05$ 131

Figure 4.14. Semi-log plot of the boundary layer velocity cross spectra at $y/\delta = 0.05$, 0.125, 0.25, 0.375, 0.5 and 0.625 and $\xi = 2.05$ 132

Figure 4.15. Cross-spectra between the streamwise velocity (at $\xi = 2.05$) and wall-pressure (at $\xi = 1.33$) for $y/\delta = 0.05$, 0.125, 0.25, 0.375, 0.5 and 0.625 137

Figure 4.16. Semi-log plot of the cross-spectra between the streamwise velocity (at $\xi = 2.05$) and wall-pressure (at $\xi = 1.33$) for $y/\delta = 0.05$, 0.125, 0.25, 0.375, 0.5 and 0.625 137

Figure 4.17. Cross-spectra between the streamwise velocity (at $\xi = 2.05$) and wall-pressure (at $\xi = 2.0$) for $y/\delta = 0.05$, 0.125, 0.25, 0.375, 0.5 and 0.625 138

Figure 4.18. Semi-log plot of the cross-spectra between the streamwise velocity (at $\xi = 2.05$) and wall-pressure (at $\xi = 2.0$) for $y/\delta = 0.05$, 0.125, 0.25, 0.375, 0.5 and 0.625 138

Figure 4.19. Cross-spectra between the streamwise velocity (at $\xi = 2.05$) and wall-pressure (at $\xi = 2.33$) for $y/\delta = 0.05$, 0.125, 0.25, 0.375, 0.5 and 0.625 139

Figure 4.20. Semi-log plot of the cross-spectra between the streamwise velocity (at $\xi = 2.05$) and wall-pressure (at $\xi = 2.33$) for $y/\delta = 0.05$, 0.125, 0.25, 0.375, 0.5 and 0.625 139

Figure 4.21. Cross-spectra between the normal velocity (at $\xi = 2.05$) and wall-pressure (at $\xi = 1.33$) for $y/\delta = 0.05$, 0.125, 0.25, 0.375, 0.5 and 0.625 141

Figure 4.22. Semi-log plot of the cross-spectra between the normal velocity (at $\xi = 2.05$) and wall-pressure (at $\xi = 1.33$) at for $y/\delta = 0.05$, 0.125, 0.25, 0.375, 0.5 and 0.625 141

Figure 4.23. Cross-spectra between the normal velocity (at $\xi = 2.05$) and wall-pressure (at $\xi = 2.0$) for $y/\delta = 0.05$, 0.125, 0.25, 0.375, 0.5 and 0.625 143

Figure 4.2
Figure 4.2
Figure 4.2
Figure 4.2
Figure 4.2
Figure 4.2
Figure 4.3
Figure 4.3
Figure 4.3
Figure 4.3
Figure 4.3
Figure 4.3

Figure 4.24. Semi-log plot of the cross-spectra between the normal velocity (at ξ= 2.05) and wall-pressure (at ξ= 2.0) for y/δ= 0.05, 0.125, 0.25, 0.375, 0.5 and 0.625 143

Figure 4.25. Cross-spectra between the normal velocity (at ξ= 2.05) and wall-pressure (at ξ= 2.33) for y/δ= 0.05, 0.125, 0.25, 0.375, 0.5 and 0.625 144

Figure 4.26. Semi-log plot of the cross-spectra between the normal velocity (at ξ= 2.05) and wall-pressure (at ξ= 2.33) at for y/δ= 0.05, 0.125, 0.25, 0.375, 0.5 and 0.625 144

Figure 4.27. Contour plots of the cross-correlation coefficient at zero time shift between the streamwise (top plot) and normal (bottom plot) velocity and the wall-pressure at the location of the ten downstream most microphones (from ξ = 1.33 to 2.33) 147

Figure 4.28. Maps of the cross-correlation coefficient between the streamwise velocity at ξ = 2.05 and wall-pressure at ξ= 1.33 (top plot), ξ= 2.0 (middle plot) and ξ= 2.33 (bottom plot) 151

Figure 4.29. Maps of the cross-correlation coefficient between the normal velocity at ξ = 2.05 and wall-pressure at ξ= 1.33 (top plot), ξ= 2.0 (middle plot) and ξ= 2.33 (bottom plot) 152

Figure 4.30. The averaged cross-correlation between the normal-velocity and wall-pressure in the range of y/δ = 0.375 to 0.625 for ξ = 1.67, 1.89 and 2.11 155

Figure 4.31. Plot for extraction of the convection velocity from R_{vp} results 155

Figure 4.32. Contour plots of the cross-correlation coefficient at zero-time shift between the low-pass filtered streamwise (top plot) and normal (bottom plot) velocity and the wall-pressure at the ten downstream most microphones (from ξ= 1.33 to 2.33) 158

Figure 4.33. Maps of the cross-correlation coefficient between the low-pass filtered streamwise velocity at ξ = 2.05 and wall-pressure at ξ = 1.33 (top plot), ξ= 2.0 (middle plot) and ξ= 2.33 (bottom plot) 159

Figure 4.34. Maps of the cross-correlation coefficient between the low-pass filtered normal velocity at ξ = 2.05 and wall-pressure at ξ= 1.33 (top plot), ξ= 2.0 (middle plot) and ξ = 2.33 (bottom plot) 160

Figure 4.35. Wall-pressure, <p>, and conditionally-averaged mean-removed velocity-vector field associated with positive (top plot) and negative (bottom plot) wall-pressure peaks at ξ = 2.05 161

Figure 4.3

Figure 4.3

Figure 4.3

Figure 4.3

Figure 4.4

Figure 4.4

Figure 4.4

Figure 4.4

Figure 4.4

Figure 4.4

Figure 4.36. Comparison between the mean streamwise-velocity profile and the conditionally-averaged streamwise-velocity profiles associated with positive and negative wall-pressure peaks 164

Figure 4.37. Wall-pressure, <p>, and conditionally-averaged velocity-vector Field associated with positive (top plot) and negative (bottom plot) wall-pressure peaks, viewed in a frame of reference moving with $0.81U_\infty$ 166

Figure 4.38. Correlation coefficient between the measured and stochastically-estimated streamwise- (top plot) and normal- (bottom plot) velocity using ML, SL_1, SL_2 and SQ_2 176

Figure 4.39. Comparison between the measured and stochastically-estimated streamwise-velocity spectra using ML, SL_1, SL_2 and SQ_2 for $y/\delta = 0.05, 0.125, 0.25, 0.375, 0.5$ and 0.625..... 179

Figure 4.40. Comparison between the measured and stochastically-estimated normal-velocity spectra using ML, SL_1, SL_2 and SQ_2 for $y/\delta = 0.05, 0.125, 0.25, 0.375, 0.5$ and 0.625 180

Figure 4.41. Comparison of the conditionally-averaged and stochastically-estimated streamwise-velocity using SL_2 and SQ_2 for $y/\delta =$ $0.05, 0.125, 0.25, 0.375, 0.5$ and 0.625 182

Figure 4.42. Comparison of the conditionally-averaged and stochastically-estimated normal-velocity using SL_2 and SQ_2 for $y/\delta =$ $0.05, 0.125, 0.25, 0.375, 0.5$ and 0.625 183

Figure 4.43 Wall-pressure time series at $\xi = 2.0$ (bottom of each plot) and the associated stochastically-estimated velocity vector field (top of each plot) using ML for three consecutive time windows, viewed in a frame of reference translating with velocity of $0.81U_\infty$ (largest vector = $0.25U_\infty$) 187

Figure 4.44. The stochastically-estimated velocity vector field using ML viewed in frames of reference translating with three different velocities of $0.76U_\infty$ (top plot), $0.81U_\infty$ (middle plot) and $0.86U_\infty$ (bottom plot); largest vector = $0.25U_\infty$ (note that the "x" and "o" locations are fixed for all three plots to help identify the variability in the vortex and saddle-point locations, respectively) 189

Figure 4.45. Vorticity and associated stochastically-estimated velocity vector field at three consecutive time windows, viewed in a frame of reference translating with $0.81U_\infty$ 193

Figure 4.46. Pseudo-instantaneous *linear* pressure source (q_L) flooded contour maps and associated wall-pressure for three consecutive time windows 198

Figure 4.

Figure 4.

Figure 4.

Figure 4.

Figure 4.47. The conditionally-averaged normal velocity and its streamwise gradient associated with negative wall-pressure peak for y/δ= 0.05, 0.125, 0.25, 0.375, 0.5 and 0.625 201

Figure 4.48. Pseudo-instantaneous *linear* pressure source (q_L/r) flooded contour maps and associated wall-pressure for three consecutive time windows 203

Figure 4.49. RMS profile of the linear pressure source calculated from stochastically-estimated and measured velocity time series 205

Figure 4.50. RMS profile of the linear weighted pressure source calculated from stochastically-estimated and measured velocity time series 206

Table B.

LIST OF TABLES

Table B.1. Data acquisition settings 215

Abbrevi:

AD

AC

CCD

DC

FFP

FFT

FPaCL

HPF

HW

I-Plate

k_y-f

ld

LSE

LVDT

ML

M-Plate

MS

PDF

PIV

PWT

QSE

NOMENCLATURE

Abbreviation

A/D	Analog to Digital
AC	Alternating Current
CCD	Charge Coupled Device
DC	Direct Current
FFP	Forward Flow Probability
FFT	Fast Fourier Transform
FPaCL	Flow Physics and Control Laboratory
HPF	High Pass Filter
HW	Hotwire
I-Plate	Instrument Plate
k_x-f	Wavenumber-Frequency
l/d	length-to-diameter ratio of hotwire
LSE	Linear Stochastic Estimation
LVDT	Linear Variable Differential Transformer
ML	Multi-point Linear Stochastic Estimation
M-Plate	Middle Plate
MS	Mean-shear pressure-source term
PDF	Probability Density Function
PIV	Particle Image Velocimetry
PWT	Plane Wave Tube
QSE	Quadratic Stochastic Estimation

RMS

SAR

SL

SPL

SQ

TM

TT

TTL

Symbol

a

A_i

$A_{...im}$ &

$A_{...ad}$ &

B_i

B_c & B_v

C

c

C_p

$C_{p...max}$ &

RMS	Root Mean Square
SAR	Signal Attenuation Ratio
SL	Single-point Linear Stochastic Estimation
SPL	Sound Pressure Level
SQ	Single-point Quadratic Stochastic Estimation
TM	Turbulence-Manipulation section of wind tunnel
TT	Turbulence-Turbulence pressure-source term
TTL	Transistor-Transistor Logic

Symbol

a	Half of the plane-wave-tube width
A_i	Stochastic Estimation coefficient of the linear term
$A_{u,\,lin}$ & $A_{v,\,lin}$	LSE coefficients of the streamwise and normal velocities, respectively
$A_{u,\,quad}$ & $A_{v,\,quad}$	QSE coefficients of the linear term in the estimation of the streamwise and normal velocities, respectively
B_i	Stochastic Estimation coefficient of the quadratic term
B_u & B_v	QSE coefficient of the quadratic terms in the estimation of the streamwise and normal velocities, respectively
C	High-pass-filter capacitance
c	Speed of sound
C_p	Mean-pressure coefficient
$C_{p,\,max}$ & $C_{p,\,min}$	Maximum and minimum mean-wall-pressure coefficient values, respectively

C_p

C_{pp}

C_L & C_v

D_r

E

e_o

f

F_1 & F_2

H

h

K & K_m

k_1 & k_2

k_s

m

N

p'

p'_{rms}

p_{atm}

$C_{p'}$	Fluctuating wall-pressure coefficient
$C_{p'p'}$	Cross-correlation coefficient of the wall-pressure
C_u & C_v	Cross-correlation coefficient between the measured and stochastically-estimated streamwise and normal velocities, respectively
D_t	Half of the wind tunnel test-section height
E	Voltage output of hotwires
e_o	Voltage output of Linear Variable Differential Transformer
f	frequency
F_1^2 & F_2^2	Yaw-response functions of hotwire #1 and #2, respectively, of the X-wire sensor
H	Half of the total fence height
h	Fence height above the splitter plate
K & K_m	Frequency-dependent and mean microphone sensitivity, respectively
k_1 & k_2	Yaw-response constants of hotwire #1 and #2, respectively, of the X-wire sensor
k_x	Streamwise wavenumber
m	Correlation time delay expressed in number of data points
N	Total number of data points in a time series
p'	Fluctuating wall pressure
p'_{rms}	Root mean square of the wall-pressure fluctuations
p_{atm}	Atmospheric pressure

p_c & p_s

p_r

p_s

R_c

Re

Re_p

R_p

R_{pp}

$\bar{r}$ & r

R_{sc} & R

R_{sp} & R

t

t_0

U

u

$\langle u' \rangle$ &

$\hat{u}$

u'_s

p_o & p_i	Reference and variable microphone locations, respectively
p_r	Reference mean static-pressure upstream of the model
p_s	mean static-pressure at the pressure taps
R_2	High-pass-filter resistance
Re	Reynolds number based on the step height
Re_θ	Reynolds number based on local momentum thickness
R_p	Acoustic RMS pressure ratio
$R_{p'p'}$	Auto-correlation coefficient of the wall-pressure
$\bar{r}_o$ & r	Position vector and its magnitude, respectively, of the pressure-observation point
R_{up} & R_{vp}	Temporal cross-correlation coefficient between the streamwise- and normal-velocity, respectively, and wall-pressure
R_{up_o} & R_{vp_o}	Spatial cross-correlation coefficient at zero time shift between the streamwise- and normal-velocity, respectively, and wall-pressure
t	Time
t_o	Time reference of the stochastically-estimated velocity vector field
U	Total flow velocity for X-wire calibration
u	Mean streamwise velocity
<u'> & <v'>	Conditionally-averaged mean-removed streamwise and normal velocity, respectively
u^+	Wall-scaled mean streamwise velocity, u/ u_τ
$u'_{i,s}$	Stochastically-estimated velocity

u'_s, v'_s

U_x

U_z

U_e

U_{el} & U_e

u_{ref}

u_{rms}

V_0

v_{rms}

x, y

x_0, y_0 ar

X_f

x_s, y_s & z

$\bar{y}$

y_{ref}

α

α_0

β

δ

δ^*

u'_s, v'_s	Stochastically-estimated streamwise and normal velocity, respectively
U_∞	Freestream velocity
U_c	Convection velocity
U_e	Effective velocity of hotwire
U_{e1} & U_{e2}	Effective velocities of hotwire #1 and #2, respectively, of the X-wire sensor
u_{ref}	Mean streamwise velocity at the location of the Reynolds stress peak
u_{rms}	Root mean square of streamwise-velocity fluctuations
V_o	Voltage output of microphones
v_{rms}	Root mean square of normal-velocity fluctuations
x, y	Streamwise and wall-normal coordinates, respectively
x_o, y_o and z_o	Coordinates of the pressure-observation point
X_r	Mean reattachment length
x_s, y_s & z_s	Coordinates of the pressure source
y^+	Wall-scaled y location, yu_τ/ν
y_{ref}	y location of the Reynolds stress peak
α	$\beta(fX_r/U_\infty)$
α_o	Yaw-angle offset of hotwire
β	Dimensionless wall-pressure spectrum, $\Phi_{p'p'}/(1/2\ \rho\ U_\infty^2)^2$
δ	Boundary-layer thickness
δ^+	Ratio between outer- and inner-boundary-layer scaling, $\delta u_\tau/\nu$

$\Phi_{r,p}$

Φ_{ω} & Φ

Φ_{φ_1}, Φ

Φ_{ω}, $\Phi_{\cdot\cdot}$

$\Phi_{\cdot\varphi_1}$, Φ

l

i_a

$i_{\cdot}$ & $i_{\cdot}$

ν

θ

ρ

τ

τ_2

τ_b

ω

$\langle\omega_{\cdot\cdot}\rangle$

$\Phi_{p'p'}$	Wall-pressure spectrum
Φ_{up} & Φ_{vp}	Cross-spectrum of the wall-pressure with the streamwise and normal velocity, respectively
$\Phi_{up_1}, \Phi_{up_2}, \ldots \Phi_{up_{10}}$	Cross-spectra between the streamwise velocity and wall-pressure at the ten downstream-most microphone locations
Φ_{uu}, Φ_{vv} & Φ_{uv}	Streamwise- and normal-velocity auto- and cross-spectra, respectively
$\Phi_{vp_1}, \Phi_{vp_2}, \ldots \Phi_{vp_{10}}$	Cross-spectra between normal velocity and wall-pressure at the ten downstream-most microphone locations
ℓ	Characteristic length of the dominant eddies
λ_a	Acoustic wavelength
λ_o & λ_i	The characteristics size of the pressure signature associated with the dominant flow structures in the outer-shear and sub-boundary layers, respectively
ν	Kinematic viscosity of air
θ	Rotational-traverse yaw angle
ρ	Density of air
τ	Time delay
τ_d	Time-delay of microphones
τ_p	Time-shift of cross-correlation peaks
ω	Angular frequency, $2\pi f$
$<\omega_{z,s}>$	Spanwise vorticity of the conditionally averaged velocity field

ξ	Downstream distance from reattachment point, normalized by X_r, $(x-X_r)/X_r$

1. INT

S

large wa

excitatio

excitatio

surface's

and unde

domains

pressure

turbulen

generatio

understa

T

means

reattach

simultan

purpose

to exam

signatur

single-p

T

characte

overlapp

1. INTRODUCTION

Separating/reattaching flows contain very energetic structures, which generate large wall-pressure fluctuations. These fluctuations are a direct representation of the excitation forces produced by the turbulent flow on the underlying surface. If such excitation takes place at frequencies and wavenumbers of one or more of the underlying surface's resonant modes, unwanted vibrations and noise will be generated. Investigating and understanding the wall-pressure-field characteristics in both the spatial and temporal domains is important to predict and/or control such undesired effects. Moreover, wall-pressure measurements can be used as a non-intrusive technique for capturing the turbulent flow activities above the surface that are responsible for the wall-pressure generation. In this context, the wall-pressure signature can also be used to gain better understanding of the turbulence processes that occur in wall-bounded flows.

The present investigation examines the surface pressure spatiotemporally by means of a wall-microphone array in the developing flow downstream of the reattachment zone of the flow over a fence-with-splitter-plate. Furthermore, simultaneous measurements of the velocity field and wall pressure are conducted for the purpose of investigating their relationship. The simultaneous data are also used as a tool to examine the flow structures associated with the generation of various wall-pressure signatures using Linear and Quadratic Stochastic Estimation methods based on multi- and single-point wall-pressure information.

The flow geometry of a fence-with-splitter-plate is illustrated in Figure 1.1. The characteristic features of such a complex flow field may be described in terms of five overlapping flow zones. In zone I, a freestream flow approaches the fence. At the tip of

Figure 1

the fence
zone II.
reattache
(zone II)
recircula
impinge
have be
structure
shear an
IV. In
small-sc
The "bo
the cont
separate

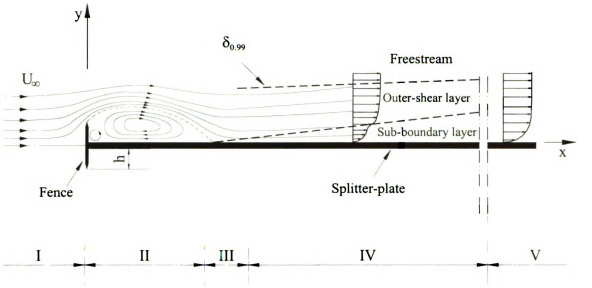

Figure 1.1. A schematic of an ideal two-dimensional flow over a splitter-plate-with-fence

the fence, the flow is forced to separate forming a free shear layer and recirculating flows, zone II. Due to entrainment, the shear layer grows in the downstream direction till it reattaches on the surface of the splitter-plate forming an energized reattachment zone (zone III). At the reattachment point, a portion of the flow goes upstream into the recirculation region, while the other goes with the downstream flow. As a result of the impingement of the shear layer on the splitter-plate's surface, the vortical structures that have been energized in the free shear layer create high-pressure fluctuations. As these structures travel downstream, they are exposed to a continually weakening mean-flow shear and, hence, undergo a relaxation process, progressively loosing their energy in zone IV. In parallel, the newly created strong mean shear near the wall produces energetic small-scale turbulence similar to that found near the wall of turbulent boundary layers. The "border" between this small-scale near-wall sustained turbulence, on one hand, and the continually-decaying, yet still energetic, large-scale vortices that were "born" in the separated shear layer upstream splits the flow in zone IV into two main regions: sub-

boundar

through

directio

sufficie

develop

zone IV

1.1. Lit

reattach

understa

boundar

the liter

prohibit

provided

the velo

studies

consider

1.1.1. Se

characte

layer zo

measure

of a blu

boundary layer and outer-shear layer, respectively. This terminology will be used throughout this document to designate these two different regions that "stack" in the y direction to form a non-equilibrium, or developing, boundary layer region. Given sufficient streamwise length, this boundary layer develops into an equilibrium, or fully-developed, turbulent boundary layer in zone V. The focus of the present measurements is zone IV.

1.1. Literature Review

Because the present study investigates a flow field that is transitioning from a reattaching free-shear-layer state to an equilibrium-boundary-layer one, reviewing and understanding the main physics of typical separating/reattaching as well as equilibrium-boundary-layer flows are important. These flows have been extensively investigated in the literature, and in order to review them comprehensively the discussion will be prohibitively lengthy. Therefore, given the specific scope of the present work, the review provided herein focuses *mainly* on investigations that address the relationship between the velocity-field and associated wall-pressure signature. In addition, a few selected studies dealing with fundamental flow physics pertaining to both flows are also considered.

1.1.1. Separating, Reattaching and Developing Flows

Many researchers have investigated separating/reattaching flows, in order to characterize the main flow features in the recirculating-flow and reattaching-free-shear-layer zones. Cherry *et al.* (1984) conducted simultaneous wall-pressure and velocity measurements in addition to smoke flow visualization in the separating/reattaching flow of a blunt-face splitter plate. Pressure was measured using two pressure transducers,

while v

dominar

attribute

zone be

simultar

reattach

with the

associat

between

shear-la

dimensi

structur

been rep

(1987) s

backwar

flapping

location

employi

the step.

shear lay

detachm

separatio

while velocity was measured using a conventional hotwire. Their data showed a dominant low frequency in the wall-pressure fluctuations near separation, which they attributed to the successive processes of expansion and contraction of the recirculation zone beneath the free shear layer, or the so called *flapping motion*. Furthermore, their simultaneous smoke flow visualization and pressure measurements downstream of the reattachment point revealed that negative wall-pressure-peak events were synchronized with the passage of what appeared to be the cores of vortical structures while those associated with positive pressure peaks occurred in the vicinity of inward-flow regions between the vortices. In addition, their spanwise measurements showed that the free-shear-layer structures became three dimensional soon after separation, but this three dimensionality did not seem to be influenced by the reattachment process as the structures "impinged"/interacted with the wall.

The flapping motion of the free shear layer in separating/reattaching flows has been reported by several researchers in addition to Cherry *et al.* (1984). Driver *et al.* (1987) studied the flapping motion observed in a reattaching free shear layer of a backward-facing step in order to determine the frequency and spatial extent of the flapping motion. To this end, they used thermal-tuft measurements at different x locations downstream of the step, in addition to velocity and wall-pressure measurements employing a wall-flush pressure transducer mounted at 5.5 step heights downstream of the step. Driver *et al.* explained the reasoning for the flapping motion as a disorder of the shear layer that arose when a vortical structure escaped the reattachment zone. Such a detachment process of a vortical structure reduced the engulfed reverse-flow by the separation bubble causing it to collapse momentarily, which increased the angle of

impingement and, consequently, the curvature of the shear layer. Therefore, they stated that a larger streamwise pressure gradient was created at reattachment, forcing the bubble to expand back again. Driver *et al.* also estimated the amplitude of the flapping motion to be less than 20% of the shear layer thickness. However, they stated that the motion was of relatively low energy and might be ignored. Lee and Sung (2002) suggested a similar explanation of the free-shear-layer flapping motion. They stated that the recirculation zone increased linearly in size as the shear-layer vortical structures grew in size and moved closer to wall. The expansion of the recirculation zone continued till a vortical structure left the free shear layer, after which the recirculation zone abruptly shrank in size causing a sawtooth-like behavior of the instantaneous location of the reattachment point.

Eaton and Johnston (1982), and later Kiya and Sasaki (1985), suggested the imbalance between rates of flow entrainment by the shear layer and reinjection at the reattachment point was the main source of the enlargement and shrinkage of the recirculation bubble. Furthermore, Kiya and Sasaki stated that such an imbalance was caused by the breakdown of the spanwise vortices in the shear layer. Spazzini *et al.* (2001) studied the unsteady behavior of a backward facing step flow using skin friction measurements and flow visualization. Their results exhibited a strong correlation between the growth and successive breakdown of the secondary re-circulation bubble (at the corner of the step) and the flapping motion of the free shear layer. This led them to hypothesize that the flapping motion was linked to the behavior of the secondary bubble. On the other hand, Heenan and Morrison (1998) conducted experiments to passively control the low-frequency, buffeting, wall-pressure fluctuation downstream of a

backwa

found t

with le

employ

associat

in the s

spatiote

microph

wavenu

structur

downstr

recent w

they refe

"isolate"

zeroth a

correspo

vortical

between

streamw

T

studied b

Castro

backward-facing step using a reattachment surface with different permeability. They found that the flapping motion totally vanished when a permeable reattachment surface with length extending from the step to 0.56 of the mean reattachment length, X_r, was employed. The permeable surface apparently inhibited the recirculating flow and associated upstream convection of disturbances produced at reattachment.

Lee and Sung (2001) made laboratory measurements of wall-pressure fluctuations in the separating/reattaching flow over a backward-facing step. They investigated the spatiotemporal statistical properties of the wall-pressure fluctuations using a 32 electret-microphone array in both the streamwise and spanwise directions. Based on the wavenumber-frequency spectra of their data, they suggested that the shear-layer vortical structures were modulated by the flapping motion of the free shear layer and moved downstream with a convection velocity of 60% of the freestream velocity. In a more recent work, Lee and Sung (2002) introduced a new spatial filtering technique, which they referred to as Spatial Box Filtering (SBF). This approach was basically utilized to "isolate" the wall-pressure signature of certain streamwise wavenumbers. Using the zeroth and second modes of the SBF, they could adequately isolate the fluctuations corresponding to the flapping motion from those corresponding to the passage of the vortical structures generated in the free shear layer. The data showed good agreement between the wavelength of the second mode of the SBF and the vortical structures streamwise spacing, which was approximately half of the mean reattachment length.

The separating/reattaching flow over a fence-with-splitter-plate model was first studied by Arie and Rouse (1956) and further investigated by many authors. For example, Castro and Haque (1987) reported detailed measurements within the

separa

motiv

lamina

the str

the sta

layer t

would

splitter

investig

X.). Ca

separate

the shea

being in

was als

reattach

F

state (la

axisymm

of Reyn

turbulen

initially

spread ra

separating/reattaching flow of a fence-with-splitter-plate model. They stated that their motivation for selecting this flow geometry was the attractiveness of having a thin laminar boundary layer at the separation point. The thin boundary layer is created due to the strong favorable pressure gradient towards the edge of the fence that is produced by the stagnation flow on the upstream face of the fence. Thus, the effect of the boundary-layer thickness at separation on the flow was negligible and the reattachment length would be only affected by the blockage ratio, h/D_t (h being the fence height above the splitter plate and D_t is the wind tunnel test-section's half width. Smits (1982) extensively investigated the relation between the blockage ratio and the mean reattachment length, X_r). Castro and Haque's measurements demonstrated that the turbulent structures of the separated shear layer and the plane-mixing layer were quite different. They reported that the shear-layer growth rate was neither linear nor equal to that of the plane-mixing-layer, being initially rather higher but reducing gradually as reattachment was approached. This was also associated with a continuous increase in turbulence energy all the way to reattachment, followed by a relatively rapid fall thereafter.

Hussain and Zedan (1978) also investigated the effect of the initial boundary layer state (laminar or turbulent) and Reynolds number on the flow characteristics of an axisymmetric free shear layer. They could show that the flow features were independent of Reynolds number, but dependent on whether the initial boundary layer is laminar or turbulent. In particular, they observed that while the separating boundary-layer was initially either laminar or turbulent, its momentum thickness showed independence of the spread rates, similarity parameters, and evolution of the shear layer. In contrast, those

values

turbule

pressur

pressur

They c

length

scale d

which

upstrea

second

found t

structur

downstr

the free

middle

oscillat

contrac

boundar

they tra

understa

one far

values showed significant dependency on whether the initial boundary layer was turbulent or laminar.

Recently, Hudy (2001) and Hudy *et al.* (2003) compiled a database of wall-pressure-array measurements for studying the spatiotemporal character of the surface pressure within the separating/reattaching flow region in a fence-with-splitter-plate flow. They could distinguish two regions, which are defined based on the mean reattachment length of the separated shear layer. In the first region, from the fence to $0.25X_r$, large-scale disturbances dominated the signature of the wall-pressure. These disturbances, which were associated with the shear layer flapping, were found to convect in both the upstream and the downstream directions with a convection velocity of $0.21U_\infty$. In the second region, which was located beyond $0.25X_r$, smaller time-scale structures were found to be responsible for the generation of the wall-pressure fluctuations. These structures corresponded to the free-shear-layer vortices and traveled with an average downstream convection velocity of $0.57U_\infty$. Hudy *et al.* could also relate the flapping of the free shear layer to an absolute instability zone, or self-sustained oscillator, near the middle of the recirculation region. They suggested that due to such a self-sustained oscillator, the separation bubble continuously underwent processes of expansion and contraction leading to the free-shear-layer flapping motion.

As mentioned above, the flow downstream of reattachment is a non-equilibrium boundary-layer flow, in which the shear-layer vortices undergo a relaxation process as they travel downstream. Several authors have investigated this flow seeking better understanding of how the flow relaxes from its shear-layer-like state to a boundary-layer one far downstream. For example, Bradshaw and Wong (1972) used existing

experin

their ov

nature

three d

categor

by a m

which c

the stro

cavity

overwh

to anot

classifi

two ov

free she

the latt

such as

shear la

height-t

the mea

an equi

the wall

law. B

experimental results on the low-speed flow downstream of steps and fences in addition to their own measurements downstream of a backward-facing step to demonstrate the flow nature in the separation/reattachment and relaxation (developing) zones. They defined three degrees of perturbations; i.e., weak, strong and overwhelming perturbation to categorize different separating/reattaching flows. The weak perturbation is that caused by a minor disturbance such as a mild change in pressure gradient or wall roughness, which does not significantly change the flow velocity or length scale. On the other hand, the strong perturbation resembles the flow of a boundary layer over a very small notch or cavity that significantly alters the turbulent structures in the flow, while the overwhelming perturbation is one that changes, all together, the flow from one "species" to another; e.g., a shear layer changing to a boundary layer. According to the classification of Bradshaw and Wong, the typical backward-facing-step flow involves two overwhelming perturbations: one when the flow changes from a boundary layer to a free shear layer at separation, and the other, at reattachment, when the flow switches from the latter to the former state back again. However in the case of a thin boundary layer, such as in the fence flow, the first perturbation may be ignored assuming that the free shear layer starts developing at the separation point.

Bradshaw and Wong (1972) conducted their experiments employing a 0.13 step-height-thin laminar boundary layer at separation. They observed a marked deviation in the mean-velocity profile of the boundary layer downstream of reattachment from that of an equilibrium boundary layer. This deviation manifested itself as an overshoot, closer to the wall, and undershoot, away from the wall, of the profile relative to the universal log-law. Bradshaw and Wong suggested that the main reason for the deviation was the

displ

wall

the lo

the st

inner

obser

up to

produc

measu

thin in

Haque

greatly

they ob

which

wall eff

the tran

wall-pre

forward

reattach

In the b

forward-

disproportionality between the heights of the dominant turbulent structures above the wall and their length scales. This disproportionality (i.e., length scale ~ y), upon which the log-law is based, was attributed to the practically constant length scale (of the order of the step height) of the free shear layer vortical structures at reattachment, except in the inner layer very near the wall. Such a deviation from the equilibrium boundary layer was observed as far as 52 step heights (approximately $8.6X_r$) downstream of the step.

Chandrsuda and Bradshaw (1981) made hotwire measurements, which extended up to two reattachment lengths downstream of the step, of the second- and third-order products of the turbulent velocity components behind a backward-facing step. Their measurements showed that the free shear layer in the separation/reattachment zone with a thin initial laminar layer was not sensitive to its initial conditions. Unlike Castro and Haque (1987), Chandrsuda and Bradshaw reported that the free shear layer was not greatly different from a plane mixing layer with a uniform external stream. Moreover, they observed that the shear layer underwent a rapid change near the reattachment zone, which was related to the confinement effect of the wall on the vortical structures. This wall effect also led to an attenuation of the normal component of the flow velocity and the transport of turbulence energy towards the wall.

Farabee (1986) and Farabee and Casarella (1986) conducted measurements of the wall-pressure field underneath two separated/reattached boundary-layer flows: over a forward- and backward-facing step. They found that the process of separation and reattachment of a turbulent boundary layer produces very large wall-pressure fluctuations. In the backward-facing step, the wall-pressure fluctuations were higher than those of the forward-facing step and equilibrium boundary layer by factors of five and ten,

respec

wall-p

still ic

height

the ob

bounda

layer o

layer d

blunt fl

that the

also ob

than the

that, no

develop

the *who*

recovery

similar

vortices

Farther

relaxatio

Reynold

respectively. Although the energetic flow structures responsible for the generation of the wall-pressure decayed as they were convected downstream by the mean flow, they were still identifiable in Farabee and Casarella's measurements at locations up to 72 step heights downstream of the backward-facing step. The latter observation, which sustains the observations of Bradshaw and Wong (1972), indicates that the upstream history of a boundary layer could be significant on the aero/hydro-acoustic features of the boundary layer over substantial streamwise distances.

Castro and Epik (1998) also conducted measurements in a developing boundary layer downstream of a separating/reattaching flow downstream of the leading edge of a blunt flat plate (the same model used in Cherry *et al.* 1984). Castro and Epik reported that the log-law did not exist immediately beyond the mean reattachment point. They also observed a slow development process in the inner sublayer; although it was faster than the development of the outer part of the flow. Nevertheless, Castro and Epik argued that, notwithstanding the faster rate of development of the inner region, the rate of development of the outer part of the flow determined the overall rate of development of the *whole* flow.

Recently, Song and Eaton (2002) investigated the separation, reattachment and recovery regions of a boundary layer flow over a curved ramp. Their flow exhibited similar structural features to those of the backward-facing step, including the roll-up of vortices downstream of separation followed by their partial distortion at reattachment. Farther downstream, a non-equilibrium boundary layer existed and underwent a similar relaxation process to that discussed above. Song and Eaton (2002) also investigated Reynolds number effects, varying the Reynolds number by changing the air density and

freestream velocity. They found evidence of the flapping motion of the free shear layer. They also reported that the remnants of the separated flow vortical structures dominated the outer layer in the recovery region. Moreover, this outer portion of the flow seemed to recover to the equilibrium state at much slower rate than that of the near-wall flow.

On the other hand, a few investigations studied the developing boundary layer flow downstream of the separating/reattaching flow over a fence-with-splitter-plate. Ruderich and Fernholz (1986) investigated the flow over a fence-with-splitter-plate model, and carried out mean and fluctuating velocity measurements using hotwire and pulsed-wire anemometry. Similar to Castro and Haque (1987), they selected this flow geometry because of the negligible effect of the upstream boundary layer on the flow downstream of separation. Another attractive feature of this flow field was the elongation of the recirculation region due to the steep angle of the velocity vector at separation, which improved the measurement resolution. Ruderich and Fernholz measurements were used to estimate the mean-velocity, Reynolds shear stress and Reynolds normal stress distributions in the wall-normal direction. The mean-velocity distribution of their flow downstream of reattachment exhibited a deviation from the equilibrium boundary layer similar to that reported by Bradshaw and Wong (1972) and Farabee (1986) in the back-step flow. Also, consistent with Farabee and Casarella (1986) and Bradshaw and Wong (1972), Ruderich and Fernholz (1986) could not observe any evidence of the equilibrium boundary layer even at the end of the splitter plate (68 step heights). Interestingly, Ruderich and Fernholz's study is one of the very few studies that found no evidence of the free-shear-layer flapping motion.

1.1.2.

surface
problen
physics
betwee
forces
problen
related
by taki
(e.g., s

where
applyin
import
pressur

where
turbule
respecti
the flow
(MS), o

1.1.2. Characteristics of the Turbulent Wall Pressure

In the past few decades, there have been many investigations of the fluctuating surface-pressure field in turbulent flows. Although the solution of the mathematical problem of turbulence (the closure problem) depends on the ability to understand the physics of, and successfully model, the Reynolds stress terms, understanding the relation between the pressure and velocity fields is important for predicting the unsteady flow forces acting on a surface for devising solutions for flow-induced noise and vibration problems and controlling the flow field. Basically, turbulent pressure fluctuations are related to the velocity field of incompressible flows through Poisson's equation, obtained by taking the divergence of the Navier-Stokes equations. Poisson's equation is given by (e.g., see Willmarth 1975 and Kim 1989):

$$\frac{1}{\rho}\nabla^2 p = -u_{i,j}\,u_{j,i}, \tag{1.1}$$

where p is the pressure, ρ is the fluid density and u_i is the total velocity vector. By applying the Reynolds decomposition for a two-dimensional mean flow with only one important mean-shear component, and considering only the turbulent component of the pressure, equation (1.1) simplifies to:

$$\frac{1}{\rho}\nabla^2 p' = -2\frac{du}{dy}\frac{dv'}{dx} - u'_{i,j}\,u'_{j,i}, \tag{1.2}$$

where u is the mean streamwise velocity, the prime denotes the mean-removed, or turbulent, quantities, and x and y are the streamwise and wall-normal coordinates, respectively. Equation (1.2) shows how the wall-pressure fluctuations are a function of the flow "sources" in the turbulent flow field. The source terms consist of the mean shear (MS), or linear term, and turbulence-turbulence (TT), or nonlinear terms (e.g., Chang *et*

al. 1999). Because the MS term represents the interaction between the mean shear and the fluctuating-velocity gradients (first term on the right hand side of equation 1.2), it changes instantaneously in response to changes in mean-flow conditions and is called the *rapid* term. On the other hand, because the TT term represents the interactions between the fluctuating-velocity gradients, it is affected only once the turbulence has had a chance to adjust to the new mean-flow conditions, and therefore this it is called the *slow* term (Kim 1989).

Ideally, it is desired to measure the pressure fluctuations inside a turbulent flow using a non-intrusive technique to avoid introducing any error into the measurements. However, measuring the pressure fluctuations in a turbulent flow without interfering with the flow field is not possible to date. Therefore, pressure fluctuations measurements have been limited to the wall in the case of wall-bounded flows. Such a measurement technique is non-intrusive, which made wall-pressure measurements attractive to many researchers who aim to gain better understanding of both the turbulent structures and their relationship to the wall-pressure signature.

Typically turbulent wall-pressure fluctuations are characterized using statistical methods, either conditional or long-time averaged. The former are used to study the spatiotemporal features of the wall-pressure using its ensemble-averaged data relative to the occurrence of strong positive or negative pressure peaks, while the latter include RMS values, spectra, probability density function (PDF), and higher-order moments of the wall-pressure. Below, an account is given of the wall-pressure characteristics in separating/reattaching, developing-boundary-layer and equilibrium-boundary-layer flows based on existing literature.

I. Sep

pressu

1987.

(Farab

have r

shear-

structu

on the

shear-

downs

by Ch

reporte

structu

flow e

slow re

layer a

pressur

and Su

shown

large-s

the dow

I. Separating/Reattaching Flows

As mentioned earlier in 1.1.1, several investigations have studied the wall-pressure characteristics in separating/reattaching (e.g., Cherry *et al.* 1984, Driver *et al.* 1987, Lee and Sung 2001 & 2002, and Hudy *et al.* 2003) and developing-boundary-layer (Farabee 1986, and Farabee and Casarella 1986) flows. The former set of investigations have reported that the wall-pressure beneath the recirculation bubble is dominated by the shear-layer flapping motion very close to separation. Farther downstream, the vortical structures in the free shear layer grow in size and approach the surface till they impinge on the wall at reattachment. As a result, the wall-pressure signature is dominated by the shear-layer vortices, and the wall-pressure fluctuation level increases with increasing downstream distance till it reaches a peak slightly upstream of reattachment, as discussed by Cherry *et al.* (1984) and Hudy *et al.* (2003). Similarly, Farabee and Casarella (1986) reported that the wall-pressure signature was dominated by the free-shear-layer vortical structures and their level remained higher than those of the equilibrium boundary layer flow even at 72 step heights ($\approx 12X_r$) downstream of the back step. They attributed that to slow relaxation of the vortical structures.

The physical relation between the large-scale vortices in the reattaching free shear layer and farther downstream in the non-equilibrium boundary layer and the wall-pressure signature has been an interest for many researchers (e.g. Cherry *et al.* 1984, Lee and Sung 2001, Lee and Sung 2002, Kiya and Sasaki 1985). Their investigations have shown that negative peaks in wall-pressure fluctuations are associated with the passage of large-scale vortex cores. On the other hand, positive peaks were found to occur beneath the downward inrush of freestream fluid inbetween the vortical structures.

separa

pressu

(e.g.,

Additi

pressu

reattac

–7 3 s

of Poi

downs

enhanc

fluctua

downst

II. Ful

bounda

at the w

Bull 19

of slow

high-sp

that the

even in

which

A few studies have investigated the spectral characteristics of wall-pressure in separating/reattaching flows, revealing that as the flow approaches reattachment its wall-pressure signature becomes more dominated by the free-shear-layer vortical structures (e.g., Lee and Sung 2001, Hudy *et al.* 2003, and Farabee and Casarella 1986). Additionally, Lee and Sung (2001) observed a build up of a frequency range in the wall-pressure spectra with a slope of –7/3 as the flow progressed towards and downstream of reattachment. This agrees with the study of George *et al.* (1984), who reported –11/3 and –7/3 spectral slopes associated with the MS and TT terms, respectively, in their solution of Poisson's equation in a free shear flow. Lee and Sung (2001) suggested that farther downstream of reattachment, the TT interaction term became more prominent due to the enhanced small-scale activity. Moreover, they concluded that the wall-pressure fluctuations are largely attributable to the free-shear-layer vortical structures even downstream of reattachment.

II. Fully-Developed Turbulent Boundary Layers

Most conceptual models of near-wall coherent structures in turbulent wall-bounded flows are based on the theme of a horseshoe (hairpin) vortex that forms locally at the wall, with the legs of the horseshoe trailing upstream of the arch (e.g., Thomas and Bull 1983 and Lueptow 1997). The horseshoe vortex structure is associated with ejection of slow speed fluid away from the wall (typically referred to as Q2 event) and inrush of high-speed fluid towards the wall (or Q4 event). Thomas and Bull (1983) found evidence that the wall-pressure positive peak was associated with a sudden step-like rise pattern, even in the outer part of the boundary layer, in the streamwise velocity fluctuations, which reflected a large-scale strong sweep event. On the other hand, Farabee and

Casar

regio

"wav

sourc

that

bound

layers

positi

turbul

peak

indica

How

slow a

the wa

type b

spectru

Gravar

spectru

range

of this

Casarella (1991) established the scaling law for the low-, mid-, and high-frequency regions of the wall-pressure spectra. Their results showed the existence of two "wavenumber" groups: a high wavenumber group that was associated with turbulent sources in the logarithmic region of the boundary layer, and a low wavenumber group that represented the large-scale turbulence contribution from the outer region of the boundary layer.

Johansson *et al.* (1987) used conditional-average data in turbulent boundary layers to show that the buffer region structures are responsible for the generation of large positive wall-pressure peaks, which indicated a link between wall-pressure peaks and the turbulence-producing mechanisms. Johansson *et al.*'s data indicated that the pressure-peak amplitude was found to scale linearly with the conditional-velocity amplitude indicating the dominance of the MS source term in generating the wall pressure. However, Kim (1989) and Chang *et al.* (1999) found that in turbulent channel flow the slow and the rapid pressure fluctuations are of equal importance very near the wall.

Over several decades, many researchers have used scaling arguments to show that the wall-pressure spectrum ($\Phi_{p'p'}$) for a certain frequency range should obey a power-law type behavior; i.e., $\Phi_{p'p'} \sim \omega^n$, where n is a function of the frequency range of the power spectrum. Bradshaw (1967), Panton and Linbarger (1974), Farabee and Casarella (1991), Gravante *et al.* (1998), and Chang *et al.* (1999) have shown that the wall-pressure power spectrum of a turbulent boundary layer should exhibit a fall-off rate of ω^{-1} in the middle range of frequencies. However, Gravante *et al.* (1998) showed that the frequency extent of this region decreased or even disappeared with decreasing Reynolds number, which

agree

Reyn

ω^{-3}

press

could

also n

this t

freque

behav

variab

literat

(1999

1.1.3.

here a

Stocha

condit

flow s

t); i.e.,

Adrian

and th

agreed with Kim (1989), who reported the nonexistence of the –1 region in their low Reynolds number channel flow.

On the other hand, Monin and Yaglom (1975) theorized a spectral fall-off rate of $\omega^{-7/3}$ in the inertial subrange of the wall-pressure power spectrum, corresponding to the pressure signature of locally isotropic turbulence. The results of Gravante *et al.* (1998) could not reveal a substantial –7/3 spectral range. Earlier, Farabee and Casarella (1991) also noted the absence of the -7/3 range from their spectral measurements and attributed this to the spatial-resolution limitation of their pressure sensors. Finally, in the high-frequency region of the turbulent wall-pressure spectrum, Blake (1986) theorized an ω^{-5} behavior that was independent of Reynolds number when scaled using wall, or viscous, variables. The decay rate of ω^{-5} has been also reported in several investigations in the literature of the turbulent boundary layer; e.g., Gravante *et al.* (1998) and Chang *et al.* (1999).

1.1.3. Stochastic Estimation

As will be outlined in the objectives of this work, stochastic estimation is used here as a tool to estimate the flow velocity field from its wall-pressure signature. Stochastic estimation was first used by Adrian (1977 & 1979) to characterize the conditional eddies of isotropic turbulence. He examined the existence of the conditional flow structures by computing the estimated velocity $u_s(x+r, t)$ from a known velocity $u(x, t)$; i.e., $\langle u_s(x+r, t) \,|\, u(x, t) \rangle$, which was referred to as "conditional eddies". Basically, Adrian proposed that the estimated velocity (u_s) could be expanded in a Taylor series of u, and then truncated at a certain order. When only the first term is included in the series,

the estimation is referred to as *Linear Stochastic Estimation* (LSE) while if the first two terms are contained in the expansion, *Quadratic Stochastic Estimation* (QSE) is obtained.

In the 1980s and 1990s many researchers employed stochastic estimation as a tool to estimate the turbulent velocity field from known velocity and/or wall-shear stress at a particular point in space. Tung and Adrian (1980) examined the conditional eddies in isotropic turbulence by estimating the velocity field around a point where the velocity was specified. They concluded that LSE was a satisfactory method for studying the qualitative large-scale features of the conditional eddy field. On the other hand, Adrian and Moin (1988) could characterize quantitatively the large-scale organized structures of a homogenous turbulent shear flow using LSE based on the velocity and the deformation tensor at an arbitrary point. They applied the linear estimate to the turbulent field data generated from direct numerical simulation, DNS. They found that using the Reynolds shear stress as the event in the estimation, the largest contribution to the Reynolds stress were associated with second- and fourth-quadrant events.

Guezennec (1989) applied the stochastic estimation technique to a fully-developed turbulent boundary layer. His study depicted the advantage of the technique in obtaining conditional averages from the unconditional statistics to estimate the spatiotemporal characteristics of the second- and fourth-quadrant events in the boundary layer. He also extended the usage of the stochastic estimation technique, based on a wall-shear-stress condition, to single- and two-point conditional averages. Although, the results showed that the difference between the linear and quadratic estimation was minimal, it appeared that the quadratic estimation included additional information.

in th

comp

as in

prese

time-

that t

provi

appro

terms.

recon

bound

the o

(LSE)

identi

Glaus

large-s

also s

unders

pressu

to cap

Guezennec also found that using higher estimation orders resulted in higher noise in the estimation, which indicated that the quadratic estimation represented a "good compromise" between the convergence of the series expansion and practical limitations, as indicated earlier by Tung and Adrian (1980). On the other hand, Brereton (1992) presented a procedure to assess the accuracy in the stochastic estimation model of the time-delayed conditional-averaged velocity in a turbulent boundary layer. He showed that the inclusion of higher-order terms in the estimation biases the stochastic model to provide better representation of rarer events. Therefore, Brereton introduced a new approach, which was based on tailoring the estimation model to include negative-order terms, seeking better accuracy in estimating more-frequent events.

In addition, Choi and Guezennec (1990) used stochastic estimation as a tool to reconstruct the conditional structure and to examine their asymmetry in a turbulent boundary layer for various levels of spanwise velocity perturbations near the wall. On the other hand, Bonnet *et al.* (1994) introduced a linear stochastic estimation (LSE)/Proper Orthogonal Decomposition (POD) complementary technique for identifying structures in an axisymmetric jet and a 2-D mixing layer. Furthermore, Glauser *et al.* (1999) used the LSE/POD as a low-dimensional model to estimate the large-scale unsteadiness of the reattachment region in an axisymmetric sudden expansion.

Estimating the flow field features using their wall-pressure signatures has been also sought by a few investigators. Naguib *et al.* (2001) were the first to seek to understand the interrelation between the flow field structures and the turbulent wall-pressure through stochastic estimation. They assessed the ability of stochastic estimation to capture the conditionally averaged flow field associated with negative and positive

wall-pressure peaks by conducting simultaneous measurements of the wall-pressure at a single-point and velocity in a turbulent boundary layer. The comparison between the conditional and stochastic estimation (linear and quadratic) results showed that the linear stochastic estimation based on the wall-pressure did not converge to the conditional average, and that it was necessary to include the quadratic term. The latter was inconsistent with the findings of earlier investigations employing stochastic estimation e.g., Adrian *et al.* (1987) and Guezennec *et al.* (1987). However, the discrepancy was attributed by Naguib *et al.* (2001) to the use of the wall-pressure as the estimation condition. Specifically, Naguib *et al.* demonstrated that the need for the inclusion of the quadratic term in the estimation was attributed to the effect of the TT pressure source term.

Recently, Murray and Ukeiley (2003) have demonstrated the potential for multi-point stochastic estimation, based on wall pressure, to accurately capture the instantaneous flow field in a resonating cavity flow. The success of the estimation in the cavity flow is believed to be due to the highly organized nature of this kind of flow and the well-defined phase relationship between the pressure and the vortical structures in the shear layer, which dominate the flow. In particular, feedback of the pressure disturbances due to periodic vortex impingement on the downstream lip of the cavity to the upstream lip sets the entire flow field in a highly organized resonant state. In a latter work, Murray and Ukeiley (2004) also employed the same estimation procedure in a non-resonating cavity flow. Although no direct comparison with the instantaneous flow field was provided in this case, the authors demonstrated that the estimation captured the essential features of the instantaneous flow structure.

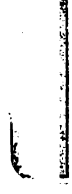

estim

Thes

techr

array

the i

On t

gauge

field

1.2. N

flow

separa

(1986)

separa

only t

measu

the ve

and ve

1.

Two other example studies that employ surface measurements for flow field estimation are those by Taylor and Glauser (2002) and Schmit and Glauser (2004). These studies employ a combined LSE/Proper Orthogonal Decomposition (POD) technique for estimating the flow field above the wall. In the first work, wall-pressure-array measurements were successfully employed to capture low-frequency fluctuations of the instantaneous velocity field associated with the flow over a backward-facing ramp. On the other hand, Schmit and Glauser (2004) employed an array of dynamic strain gauges mounted on the wing of a Micro Air Vehicle to estimate the instantaneous flow field in the immediate wake behind the wing.

1.2. Motivation

This work was motivated by the interest to understand the relation between the flow field and wall-pressure in the non-equilibrium flow downstream of a separating/reattaching flow. In particular, with the exception of Farabee and Casarella (1986), no other study of the wall-pressure beneath the flow downstream of a separating/reattaching flow was found. Furthermore, Farabee and Casarella employed only two-point measurements in their work. In the current investigation, *simultaneous* measurements of the wall-pressure field $p'(x,t)$, using a sixteen-microphone array, and the velocity field, employing an X-hotwire sensor, will be undertaken. The coupled array and velocity measurements will allow:

1. Determination of the space-time characteristics, including the frequency-wavenumber spectrum, of the wall pressure field. The documentation and understanding of such characteristics is important to flow-induced noise and vibration problems since it is the *combined* spatial and temporal characteristics

2.

1.3. C

1.

2.

3.

4.

5.

that determine if the wall-pressure field excitation of the wall will lead to substantial vibration and noise generation.

2. Multi-point Linear Stochastic Estimation (LSE) of the velocity field based on wall measurements. The estimation is motivated by examining the flow structure and wall-pressure sources associated with various types of wall-pressure signature. Ultimately, such examination may aid in developing structure-based models of the flow pressure sources, allowing simplified computations of the wall-pressure field in engineering calculations of flow-induced noise and vibration problems downstream of appendages and other separated flows in engineering devices.

1.3. Objectives

The specific objectives of this work may be listed as follows:

1. Construct a 16-point fluctuating-wall-pressure-sensor array and develop an appropriate calibration procedure. Integrate the sensor array into the fence-with-splitter-plate setup of Hudy (2001) beneath the non-equilibrium boundary layer downstream of reattachment.
2. Characterize the wall-pressure field through one- and two-point statistics as well as the wavenumber-frequency spectrum.
3. Conduct simultaneous measurements of the wall-pressure and flow velocity using the microphone array and X-hotwire sensor, respectively.
4. Examine the velocity-field characteristics and its relation to the wall-pressure field utilizing various conventional and conditional statistical analyses.
5. Estimate the "pseudo-instantaneous" flow field associated with typical instantaneous spatial wall-pressure patterns using multi-point wall-pressure based

descri

preser

bound

results

recom

LSE. The estimation is expected to not only provide some sense of the variability in the characteristics of the flow structures associated with typical wall-pressure signatures, but also to lead to better understanding of the physical nature and relative importance of the flow pressure sources. It is noted here that such a detailed study into the nature and significance of the wall-pressure-generating flow structures have not been conducted to date in the flow field considered here.

The remainder of this work consists of four main chapters. Chapter 2 provides a description of the experimental set-up and methodology, Chapter 3 contains a presentation of the wall-pressure results, while Chapter 4 includes a discussion of the boundary layer characteristics, pressure-velocity correlations and stochastic estimation results. Lastly, Chapter 5 highlights the main conclusions of the present work and recommended future work.

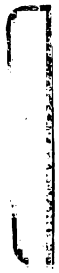

2. EXPERIMENTAL SET-UP AND METHODOLOGY

This chapter describes the experimental set-up, techniques and methodology used in the present work. Four measurement techniques were used to investigate the flow field of interest: static-pressure taps, flow visualization using tufts, microphones and single/X-hotwire probes. Two different sets of data-acquisition hardware were used to acquire the experimental data resulting from application of these various techniques. A full description of the set-up, methodology and data-acquisition hardware is provided in subsequent sections.

2.1. Experimental Set-up

The experimental set-up consisted of a fence-with-splitter-plate model, an open-circuit wind-tunnel facility, the sensing instrumentation and data-acquisition systems. Each of these constituents is described in details in this section.

2.1.1 Wind Tunnel Facility

The present experiments were conducted in a low-speed open-circuit indraft wind tunnel[1] facility in the Flow Physics and Control Laboratory (FPaCL) at Michigan State University. The wind tunnel consisted of four main sections (see Figure 2.1): the turbulence-manipulation section, contraction section, test section and diffuser and blower section. The overall dimensions of the wind tunnel were approximately 7.5 m long by 2.0 m high and 1.2 m wide.

The turbulence-manipulation (TM) section directed and conditioned the air flow to the contraction section. The main purpose of this section is to produce uniform mean velocity profile and to break up the large-scale eddies in the flow into smaller ones so that

[1] The wind tunnel was originally designed and built at Northwestern University by Steve Snarski and Richard Lueptow, and was moved to MSU in 1999.

they can dissipate prior to entering the contraction section. The overall dimensions of the TM unit were 1.15m x 1.15 m in cross section by 1.06 m in length. It consisted of 10 separable wooden frames. Each of the first five frames supported an 18-mesh aluminum window screen while each of the last five ones supported 30-mesh stainless steel screen. A 25,000-cell aluminum honeycomb element (6.0 mm cell size, 50.0 mm length) was also housed in the fifth section with the 18-mesh screen.

The contraction section accelerated the flow through a contraction ratio of 10.8:1. The section had a 1.15 m-wide square inlet cross-section and a 0.35 m-wide square outlet cross-section. The total length of the contraction section was about 1.5 m and it was built of plywood and fiberglass with a Formica inner surface.

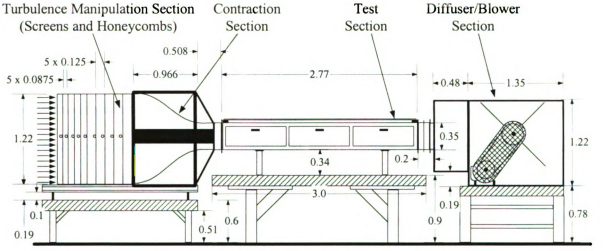

Figure 2.1. Schematic[2] of the wind facility (dimensions in meters)

The test section was 2.77 m long with inlet cross-section matching that at the exit of the contraction. The walls of the test section had a divergence angle of 0.13 degrees with respect to the centerline. The angle was selected to compensate for the displacement thickness of the boundary layer growing on the test-section walls in order to minimize the

[2] Done by Chad Stimson, Michigan State University, East Lansing, MI 48824

streamwise pressure gradient for most of the wind tunnel operating velocity range. The test section was made of plywood with a Formica inner surface supported by an aluminum external frame. One of the test section walls contained three windows that were made out of clear plexiglass. Each window was 0.9 m long, 0.3 m high and 12.5 mm thick. The windows were mounted such that their inner faces were flush with the inner test-section wall.

The fourth, and the last, component was the diffuser/blower section. The section was used to decelerate and turn the flow horizontally by 90 degrees towards the blower. The section was made out of 14 gage steel exterior case with perforated 22 gage galvanized steel interior flow surface and fiberglass acoustical wool inserted between the two. The relatively high contraction ratio (10.8) combined with the 90-degree bend and the perforated steel/acoustical lining were responsible for reducing the frequency and the strength of the blower noise, which is a potential source of contamination of the wall-pressure measurements. The high contraction ratio helped to reduce the blower rotation speed for a given wind tunnel velocity, and hence reduce the frequency of the noise generated due to the passage of the blower blades. On the other hand, the geometry and sound-absorption lining of the diffuser helped to attenuate the upstream-propagating noise resulting from the blower-blade passage.

The air flow in the tunnel is induced by an airfoil-vane centrifugal blower, type 27 SQA from Chicago Blower Corporation. The blower was driven by a dual belt drive and Minarik 180 Volt, 3hp permanent magnet DC motor, model number 504-36-043A with speed range of 30-1800 rpm. The speed control was provided by General Electrical rheostat controlled AC motor-DC generator set with variable frequency controller of the

blow

indic

Pitot

2.1.2

(see

symr

were

plate

two

regar

blower speed. The controller has a remote-operating keypad with a digital frequency indicator. The frequency indication was calibrated against flow velocity measured by a Pitot tube in the test section to facilitate setting of the freestream velocity.

2.1.2. Test Model

The fence-with-splitter-plate model of Hudy (2001) was used in the present work (see Figure 2.2). The design of the model, which was constructed from aluminum, was symmetric with respect to top and bottom. The total length and the width of the model were 160h and 44h, respectively; where h = 8 mm is the fence height above the splitter plate (or "step" height). In order to improve the two dimensionality of the mean flow, two endplates were attached to the two sides of the splitter-plate (for more details regarding the model design, see Hudy 2001).

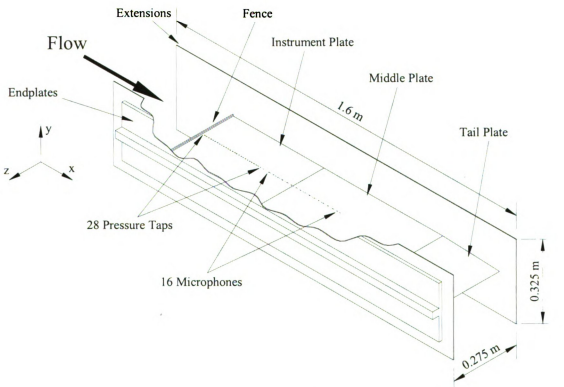

Figure 2.2. A schematic of the test model

The total fence height (2H = 2h + splitter plate thickness) was 35 mm. This fence height was selected to produce reasonable flow blockage while maintaining a long reattachment length to "stretch" the flow field and facilitate spatial resolution of the measurements in the x direction. Smits (1982) defined a blockage ratio (h/D_t) representing the ratio between the step height (h) and half of the test section height (D_t). He found that the blockage ratio resulted in flow acceleration around the fence, which decreased the mean reattachment length as the blockage ratio increased. The blockage ratio of the present model was 4.5% (see Figure 2.3 for visual illustration). As will be explained later, the reattachment length (X_r) of the present work was estimated using tuft measurements, which produced an X_r value of 180 mm (22.5h). This is slightly shorter than X_r of Hudy *et al.* (2003) because their blockage ratio (2%) was lower than the present study.

For the current study, an array of 16 microphones and 56 pressure taps (28 on each side of the model) were mounted in the splitter plate. The splitter plate consisted of a half-inch skeleton sandwiched between 3.175 mm-thickness aluminum plates. These plates included an instrument plate (I-plate) and a middle plate (M-plate) on each side. The I-plate was 51h (406 mm) long while the M-plate was 76h (610 mm) long. The tail plate (T-plate) was used to reduce plate-wake disturbances by gradually reducing the model thickness to zero. The T-plate length was 32h (254 mm). The volume within the skeleton was used for microphones insertion, as well as wires and tubes connections. Figure 2.4 shows schematic drawing of the "top" view of the model. A corresponding picture of the model installed in the wind tunnel is shown in Figure 2.5. Note that,

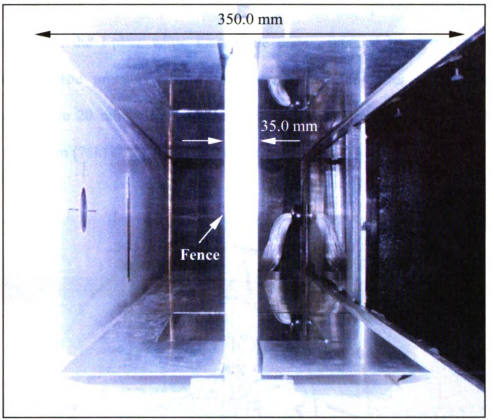

Figure 2.3. A frontal picture of the model showing the blockage effect of the fence

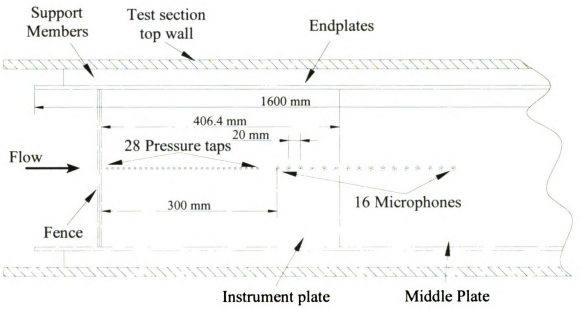

Figure 2.4. A schematic of the instrument and middle plates depicting the locations of the pressure taps and microphones

images in this thesis are presented in color. The 28 pressure taps and six microphones were installed in the I-plate while the middle plate contained the rest (10) of the microphones. The pressure taps were 9.5 mm center-to-center apart while the microphones were 20 mm apart with the microphone array stretching from 300 mm (37.5h) to 600 mm (75h) downstream of the fence.

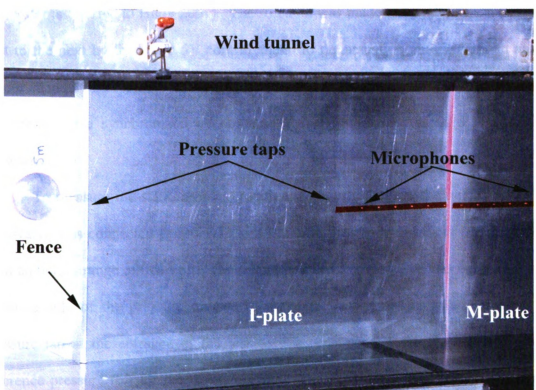

Figure 2.5. A picture of the fence-with-splitter-plate model inside the wind tunnel

2.1.3. Instrumentation

I. Static pressure

Static pressure measurements were used to align the model with the flow direction in order to achieve flow symmetry on both sides of the splitter plate. As mentioned earlier, there were 56 pressure taps (28 on each side) mounted flush with the I-pate

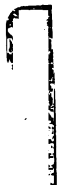

surfa
appr
pneu
man
ports
with
the r
port
outp
algo
prog

scan
with
nega
press
refer
open
press
press
posi
press
the t

surface. The inner diameter of each tap was 1 mm and the outer diameter was approximately 1.5 mm. Each of the taps was connected with a long Urethane tube to a pneumatic connector (48D9M-1/2) of a pressure scanner. The scanner, designed and manufactured by Scanivalve Corporation (48D9-1/2 Scanner Oiless Design with 48 ports), had a 100-psi range and was driven by a rotary solenoid (48D9M-1/2) coupled with a homemade solenoid-actuation circuit (for more detail regarding the circuit design the reader is referred to Hudy 2001). The solenoid was made to "step" from one pressure port to the next by feeding a 5V control signal to the actuation circuit from an analog-output channel of a PC-based D/A converter. The stepping and pressure-data-acquisition algorithms were synchronized by containing them within the same data acquisition program.

To measure the static pressure relative to some reference, the output port of the scanivalve was connected to a 0-1.33 kPa Baratron pressure transducer (model 223BD) with an output range of 0-1 Volt. The output port of the scanivalve was connected to the negative side of the pressure transducer while the positive side was connected to a pressure tap at the entrance of the test section, upstream of the model, to provide a reference pressure (p_r) for the measurements. The first port of the scanivalve was left open to the atmosphere while the following ones were connected to the tubes from the pressure taps. In this manner, the "home position" of the scanivalve gave the differential pressure between the atmospheric and reference pressure (p_{atm} - p_r) while the following positions yielded the differential pressure between that acting at the corresponding pressure tap and the reference pressure (p_s - p_r). Forty of the 56 pressure taps (28 taps on the top side and 12 on bottom) were used to align the model with the flow direction.

II. T

estir

dime

blac

in th

yarn

the t

captu

II. Tufts Visualization

Tufts were used to visualize the flow direction close to the wall in order to estimate the reattachment length, which is a relevant length scale for non-dimensionalizing the investigated flow quantities (e.g., Ruderich and Fernholz 1986). A black-yarn tuft was attached to the surface of the I-plate at different streamwise locations in the reattachment zone. The tuft was constructed from a 10 mm-long piece of black yarn attached to a short thread that was in turn attached to the I-plate using a tape, freeing the tuft to follow the flow. An image of the tuft is shown in Figure 2.6.

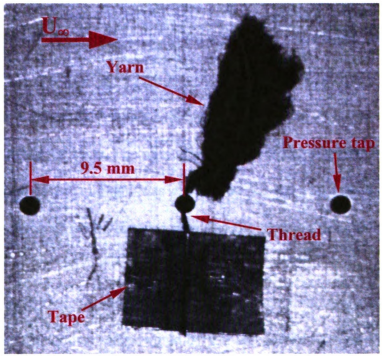

Figure 2.6. An image of a tuft attached to the I-plate

A CCD camera (Sony XC-75) coupled with a frame grabber system was used to capture the tuft image. The camera had a ½- inch CCD image sensor with a resolution of

768 x 494 pixels. The frame grabber was a National Instruments IMAQ PCI-1408 board (for more information regarding the board specifications, the reader is referred to the subsection V below in the current section, 2.1.3). The idea was to capture enough number of images in order to statistically determine the dominant flow direction from the percent of the time that the tuft is imaged in the up or downstream direction. Because of the high reflectivity of aluminum, *black* yarn was used to increase the contrast of the images and make it easier to determine the tuft location by looking for a dark area against a bright background.

III. Microphones

A microphone array consisting of 16 Panasonic microphones was used to measure the wall pressure fluctuations downstream of the separating/reattaching flow. The Panasonic microphone (WM-60AY) was an omnidirectional back electret condenser microphone cartridge. Figure 2.7 shows an image that illustrates the geometry of one of the microphones used in the array. The microphone was 6.0 mm in diameter and 5.0 mm in thickness. The sensing diaphragm was exposed to the flow through a 2 mm round sensing hole. The nominal sensitivity was specified by the manufacturer to be –42 ± 3 dB for a bandwidth of 20 – 20,000 Hz.

Figure 2.8 shows a schematic of a homemade circuit that was used to drive each of the microphones. The circuit was powered by 9 V DC power supply connected with a resistance of 2.2 kΩ in parallel with the microphone. The output of the microphone was then high-pass filtered to remove any DC component in the output (V_o). The capacitor (C) and the resistor (R_2) of the high-pass filter were selected for a cut-off frequency of 0.16

Hz, which was sufficiently low to block the DC without removing any significant fluctuating-pressure energy.

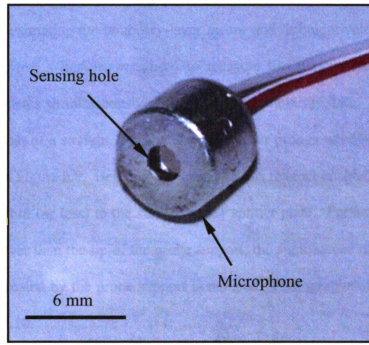

Figure 2.7. An image of one of the microphones used in the array

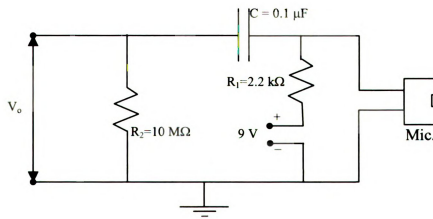

Figure 2.8. A schematic of the microphone driving circuit

IV.

inve

com

the

velo

was

30°,

as c

the b

that

seen

IV. Hotwire

Single- and X-hotwire probes were used to measure the velocity in the investigated flow. The single hotwire was used to measure the streamwise (u) velocity component for estimating the boundary-layer mean- and turbulent-velocity profiles. On the other hand, the X-hotwire was used to measure the streamwise and wall-normal velocity components simultaneously with the microphone-array data. The probe design was similar to that of a straight X-probe except the four prongs were bent by an angle of 30^{o}, as shown in Figure 2.9. Bending the prongs in this manner enabled positioning them as close as 0.5 mm (or less) to the surface of the splitter plate. Furthermore, by making the bent part lower than the tip of the probe support, the significance of any disturbances that might be created by the probe support is reduced. Photographs of the probe can be seen in Figure 2.10.

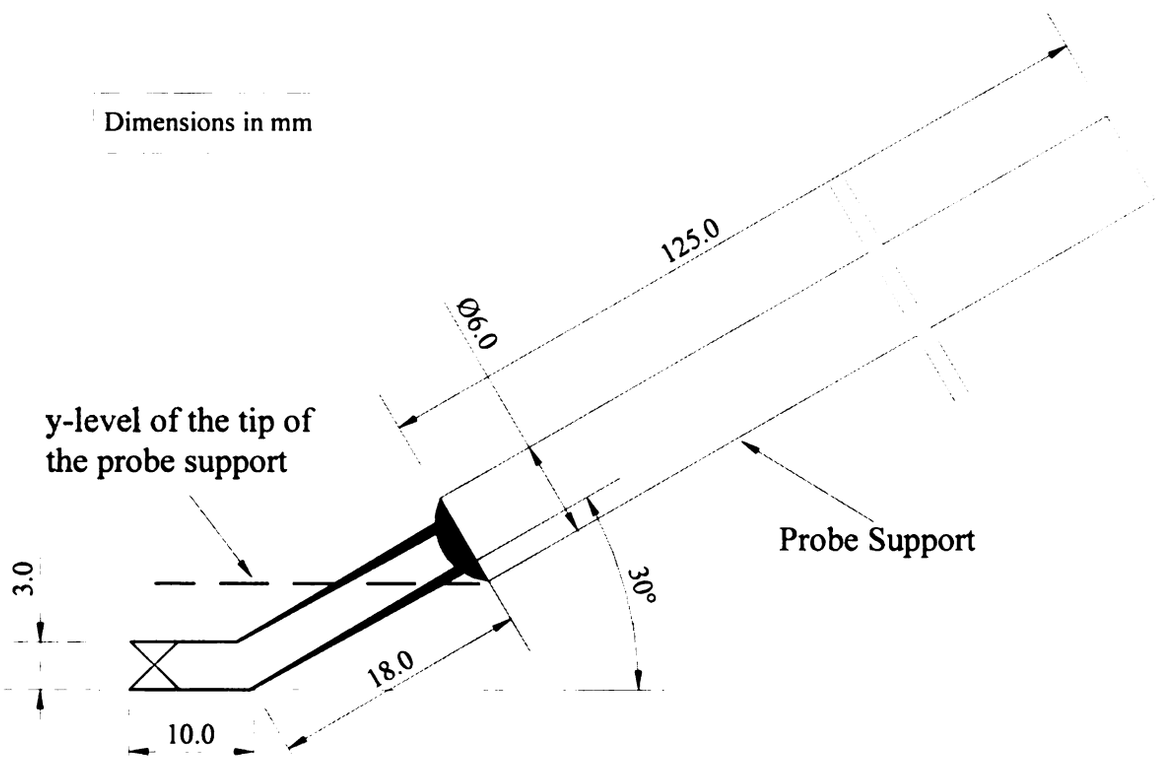

Figure 2.9. A schematic of the X-probe

from

signa

norm

consi

brack

frame

horiz

rod in

custo

wave

traver

was f

stepp

motor

resolu

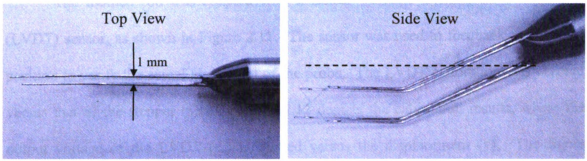

Figure 2.10. Images showing top and side views of the X-probe

The hotwire probes were operated by a Constant Temperature Anemometer, CTA, from DANTEC (Model 54T30) with an Over Heat Ratio (OHR) of 1.6. The output signal was low pass filtered using a built-in filter with a 10 kHz cut-off frequency.

A traversing mechanism was used to traverse the hotwire probes in the wall normal (y) direction. Figure 2.11 shows an image of this traversing mechanism, which consists of a toothed rod geared with a stepper motor and assembled to an aluminum bracket. The figure illustrates how the traversing mechanism was fixed to a supporting frame that was built out of uni-strut structural elements next to the test section. A horizontal slot was machined in the Plexiglass window to allow protrusion of the toothed rod into the test section. The hotwire probe was clamped at the end of this rod using a custom adapter. The position of the probe was then controlled by feeding TTL square wave pulses to the stepper motor from a digital I/O controller interfaced with a PC. The traversing mechanism was calibrated against a dial-gauge to determine its resolution. It was found that the probe translated a distance of 58.8 mm for each revolution of the stepper motor. This corresponded to a traversing resolution of approximately 74 μm per motor step (since 800 pulses, or steps were required to complete one full motor resolution).

The toothed rod was coupled with a Linear Variable Differential Transformer (LVDT) sensor, as shown in Figure 2.11. The sensor was used to feedback the hotwire position to verify the actual movement of the probe. The LVDT calibration was verified versus that of the stepper motor. Figure 2.12 depicts the calibration results, where the output voltage of the LVDT (e_o) is plotted versus the displacement (y). The figure reveals the linear character of the sensor over a range of about 50 mm. This range was large enough to accommodate the full movement of the hotwire probe in the y direction. The slope of the calibration line represents the LVDT sensitivity, which was 0.35 V/mm.

V. Data Acquisition Hardware

Three different data-acquisition systems were used in the present work. The first one was used throughout the experimental procedure of the wall-pressure measurements, including aligning the model, calibrating the microphones and acquiring data from the 16 microphones. This was accomplished using a National Instruments AT-MIO-16E-10 data acquisition A/D card with 16-single-ended analog-input channels and maximum sampling rate of 100,000 samples/s (corresponding to 6,250 samples/s per channel). This sampling rate resulted in 10 μs inter-channel time delay.

The second data acquisition card was also a National Instruments A/D card (NI 6024E-ADC), which was employed for driving the stepper motor, hotwire calibration procedure, measurement of the boundary-layer velocity profiles, and acquiring the simultaneous velocity and pressure data. The card also had 16-single-ended analog-input channels with a maximum sampling frequency of 200,000 Hz. It was necessary to switch to the second A/D board because the stepper motor had to be synchronized with the velocity measurements for automated operation of the traverse/acquire procedure. This

was not possible with the first board, which did not have the hardware provisions necessary to control the motor.

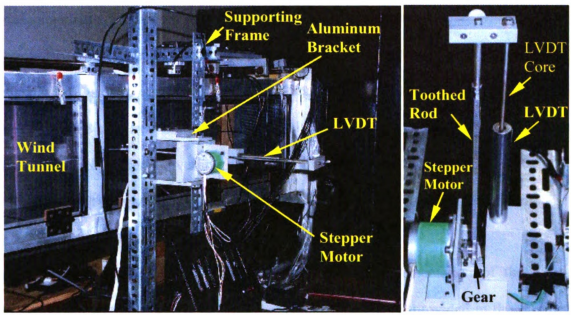

Figure 2.11. Images of the traversing mechanism and the LVDT: overall (left) and close-up (right) views

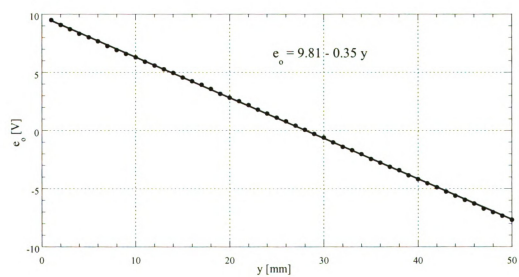

Figure 2.12. LVDT calibration

tuft

mor

vide

four

char

The

syst

anal

2.2.

mea

sub

2.2.

mer

mod

desc

I. A

para

were

after

The third and last computer-based-acquisition board was used for grabbing the tuft images. The board was an NI IMAQ PCI-1408 board, which was a high-accuracy, monochrome, PCI-based IMAQ board that supported RS-170, CCIR, NTSC, and PAL video standards. The board was connected to a BNC break-out terminal, which included four video-input channels and four corresponding I/O triggering channels. The triggering channels are used to start/stop sampling of images or indicate the status of acquisition. The PCI-1408 acquired image frames in real time and transferred them directly to the system memory after converting their data into digital formats using an 8-bit flash analog-to-digital converter (ADC).

2.2. Experimental Methodology

A full description of the procedures used in implementation of the various measurement techniques in the experiments conducted here is provided in the following subsections.

2.2.1. Static pressure system

Static pressure was only measured in the separating/reattaching flow region. As mentioned earlier, static pressure measurements were used for the purpose of aligning the model parallel to the freestream inside the test section. This subsection gives a description of the alignment procedure.

I. Acquisition Settings

The acquisitions settings were selected after considering the flow features and the parameters of the static-pressure measuring system. The main settings of the acquisition were the sampling time to converge to the average static pressure, and the time needed after each step of the scanivalve for the pressure inside the pressure-measuring system

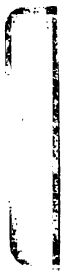

(connecting tubing, scanivalve and transducer) to stabilize. Tests conducted by Hudy (2001) using the same setup had shown that 10 seconds and one second, respectively, were more than sufficient for these parameters. Therefore, 1000 samples of pressure were acquired at a sampling rate of 100 Hz before triggering the scanivalve to step. After the trigger, the program waited for one full second before commencing with data sampling. The procedure was then repeated for all static-pressure ports to complete the experiment.

II. Model Alignment

Model alignment was done in two steps: a coarse alignment and a fine one. The model was coarsely aligned by connecting the tubes of pressure tap # 18 (x/h = 21.4 and x/X_r = 0.95) on opposite sides of the model to the positive and negative ports of the pressure transducer. The "angle of attack" of the model was then adjusted till the readout of the pressure transducer became zero, indicating rough alignment of the model with the flow direction.

For fine alignment, 40 of the 56 pressure taps (28 on top and 12 on bottom) were used in the alignment procedure. The taps were used to obtain a "fuller" picture of the pressure distribution on each side of the splitter plate. By matching the static pressure distributions on both sides of the model, the fine alignment of the model was achieved.

Figure 2.13 shows the top and bottom static-pressure distributions after the model was aligned. It is evident that both the top and bottom mean-pressure-coefficient (C_p) distributions match well, where:

$$C_p = \frac{p_s - p_r}{\frac{1}{2}\rho U_\infty^2}, \qquad (2.1)$$

p_s is the surface pressure at location x, p_r is a reference pressure measured with a static pressure tap located at the exit of the contraction, ρ is the fluid (air) density, and U_∞ is the freestream velocity upstream of the model. The results in Figure 2.13 indicate that the model is satisfactorily aligned with the direction of the flow. In fact the largest deviation between the two curves is 3.5% of the total C_p variation ($C_{p,\,max}$ - $C_{p,\,min}$), with the RMS deviation being 2.5%.

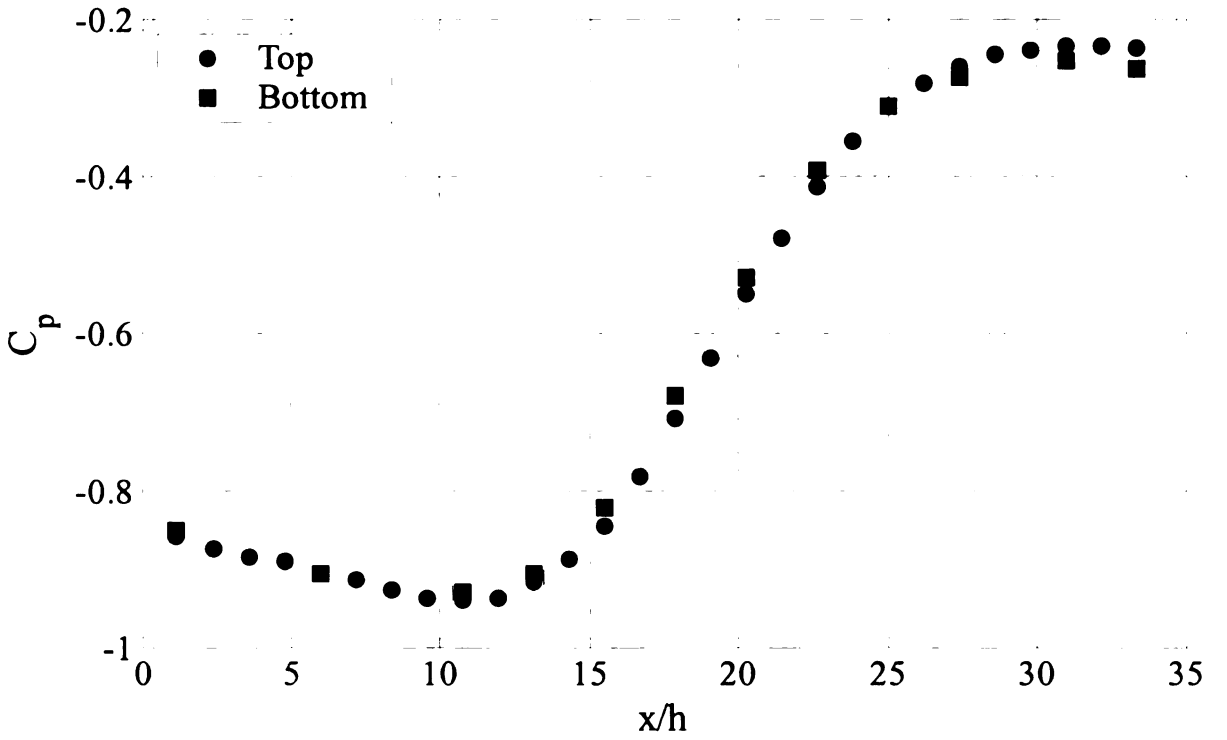

Figure 2.13. Mean-pressure-coefficient distribution for the top and bottom sides of the splitter plate

2.2.2. Microphones

As mentioned in section 2.1.3, Panasonic microphones were used to measure the wall-pressure fluctuations. The microphones installation, their calibration, time-delay check and cross-talk check are discussed here.

I. Installation

Figure 2.14 shows the installation of one of the microphones. To mount the microphones, counter-bored through holes were made on the back face of the instrument and middle plates. The smaller diameter of the counter-bored holes matched the microphone sensing diameter (2 mm), while the bigger diameter matched the diameter of the microphone casing. The idea was to make the sensing holes completely flush with the surface, which was achieved by inserting the microphone from the backside of the instrument and the middle plates.

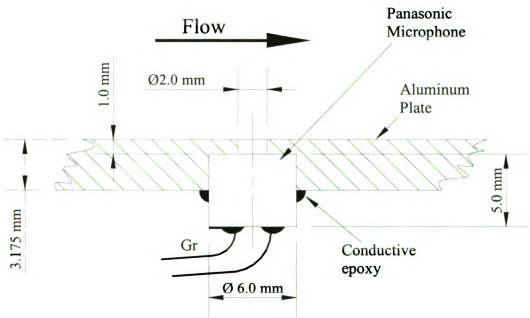

Figure 2.14. Microphone installation in the Instrument and Middle plates

The microphones were held in place using conductive epoxy (see Figure 2.14). The epoxy was applied around the perimeter of the microphone casing, electrically connecting the latter in the process to the model, which acted as a ground plane. Using the conductive epoxy guaranteed that all microphones had a common ground. All

microphone wiring was fed through the space between the top and the bottom plates of the splitter-plate.

II. Calibration

Although the Panasonic microphones had a nominal sensitivity of -42 ± 3 dB for a bandwidth of 20 – 20,000 Hz, they had to be calibrated to determine the frequency response of each microphone individually after their installation in the I- and M-plate. The calibration yielded two important pieces of information. The first was the determination of the mean sensitivity and phase response of each microphone. The second was to check that each microphone was mounted properly without a gap between the microphone face and the counter-bored hole, which could result in a Helmholtz-type resonance during measurements.

A Plane Wave Tube (PWT) was used to determine the frequency response of the Panasonic microphones. Basically, a PWT produces plane sound waves that travel parallel to the axis of a tube or a duct. This one-dimensional planar wave propagation is achievable if the width of the duct is small in comparison to the acoustic wavelength, λ_a. Specifically, for a square duct with rigid walls and side length of 2a, planar wave propagation is accomplished when $\lambda_a > 4a$, or $f < c/4a$ (where f is the sound frequency and c is the speed of sound); e.g., Kinsler et al. (1982). Thus, $f = c/4a$ establishes the upper limit, or cut-off, frequency of the PWT. In the current investigation, the PWT width selected is 12.7 mm, which gives an upper frequency limit of approximately 13.5 kHz for a speed of sound of 350 m/s.

A picture of the acoustic-wave-guide setup may be seen in Figure 2.15. The tube was made of 1.8 m long aluminum square duct with a cross-section of 12.7 x 12.7 mm^2

and a wall thickness of 3.175 mm. The centers of the microphones were located along the centerline of the PWT. Opposite to each microphone, a plug for mounting a reference Larson & Davis (L&D) 1/4-inch microphone (with known response) was made in the upper wall of the PWT (see Figure 2.15). A sound generating system (function generator, amplifier and speaker) was used to calibrate the Panasonic microphones. The system was used to excite the microphones over a broad range of frequencies using white noise containing frequencies up to the highest frequency of interest in the experiments ($\approx$ 3.5 kHz).

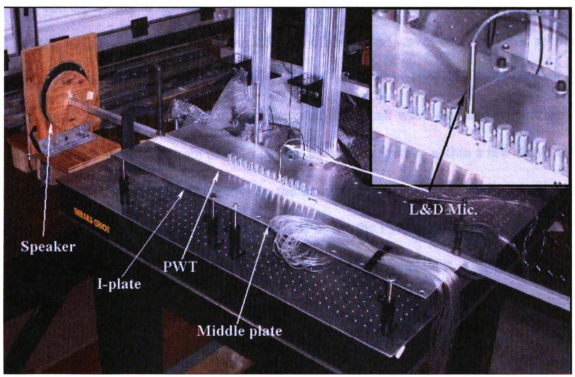

Figure 2.15. A picture of the microphone-calibration setup

Before using the PWT for calibration purposes, it was necessary to check the accuracy of the calibration procedure. The test was conducted using two L&D microphones, where the first microphone was mounted at the upper wall of the PWT,

while the second was mounted in a plug in the side of the PWT. In this manner the pressure ratio (R_p) and the phase shift (θ) between the acoustic pressures acting on the top and sidewalls of the PWT could be determined, where:

$$R_p = \frac{(p'_{rms})_{top}}{(p'_{rms})_{side}} \tag{2.2}$$

$(p'_{rms})_{top}$ and $(p'_{rms})_{side}$ are the RMS values of the pressure fluctuations on the top and side wall of the PWT, respectively.

The results provided in Figure 2.16 are the average for two locations along the PWT, corresponding to the beginning and end positions of the microphone array. Figure 2.16 (top plot) shows the amplitude uniformity of the sound waves over the cross section of the PWT, as demonstrated by the R_p value of one (within 10%) for frequency range extending up to 10 kHz. The planar character of the sound wave can also be confirmed from the phase shift, θ (bottom plot). The plot shows that θ stays within a few degrees in the same frequency range. Collectively, the amplitude and phase results show that the desired planar sound waves have been achieved inside the PWT.

Using the above calibration procedure, the frequency response of the microphone/hole assemblies could be determined. Figure 2.17 depicts the frequency response of one of the assemblies. The top plot in the figure shows that the sensitivity of the microphone (K) was flat and fell within ±2 dB of the estimated mean sensitivity (K_m, which is obtained by averaging over all frequencies within the calibration range) over the frequency range $50 < f < 5000$ Hz. In addition, the plot of the phase shift between the Panasonic and reference (L&D) microphone depicts a negligible phase delay. The results

v

it

of

of

R

0 [degree]

verify the appropriateness of the frequency response of the microphone after embedding it in the counter-bored holes of the I- and M-plates.

Figure 2.18 (top plot) shows the mean sensitivities of all microphones. The range of sensitivities extends from 8.5 to 12.5 mV/Pa (–41.4 to –38 dB relative to a sensitivity of 1.0 V/Pa; the nominal value reported by the manufacturer is –42 ± 3 dB).

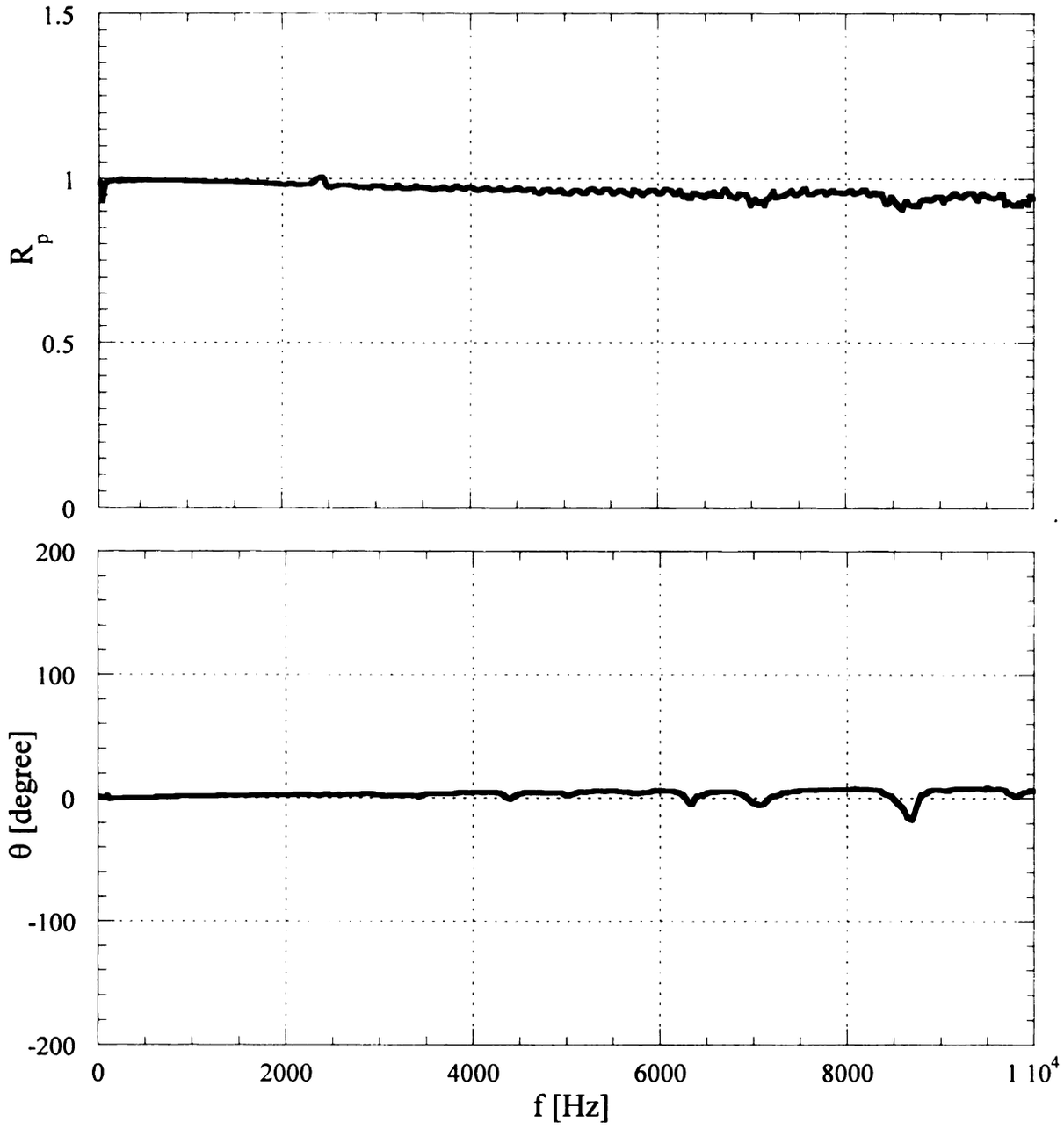

Figure 2.16. PWT calibration results: pressure ratio (top) and phase shift (bottom)

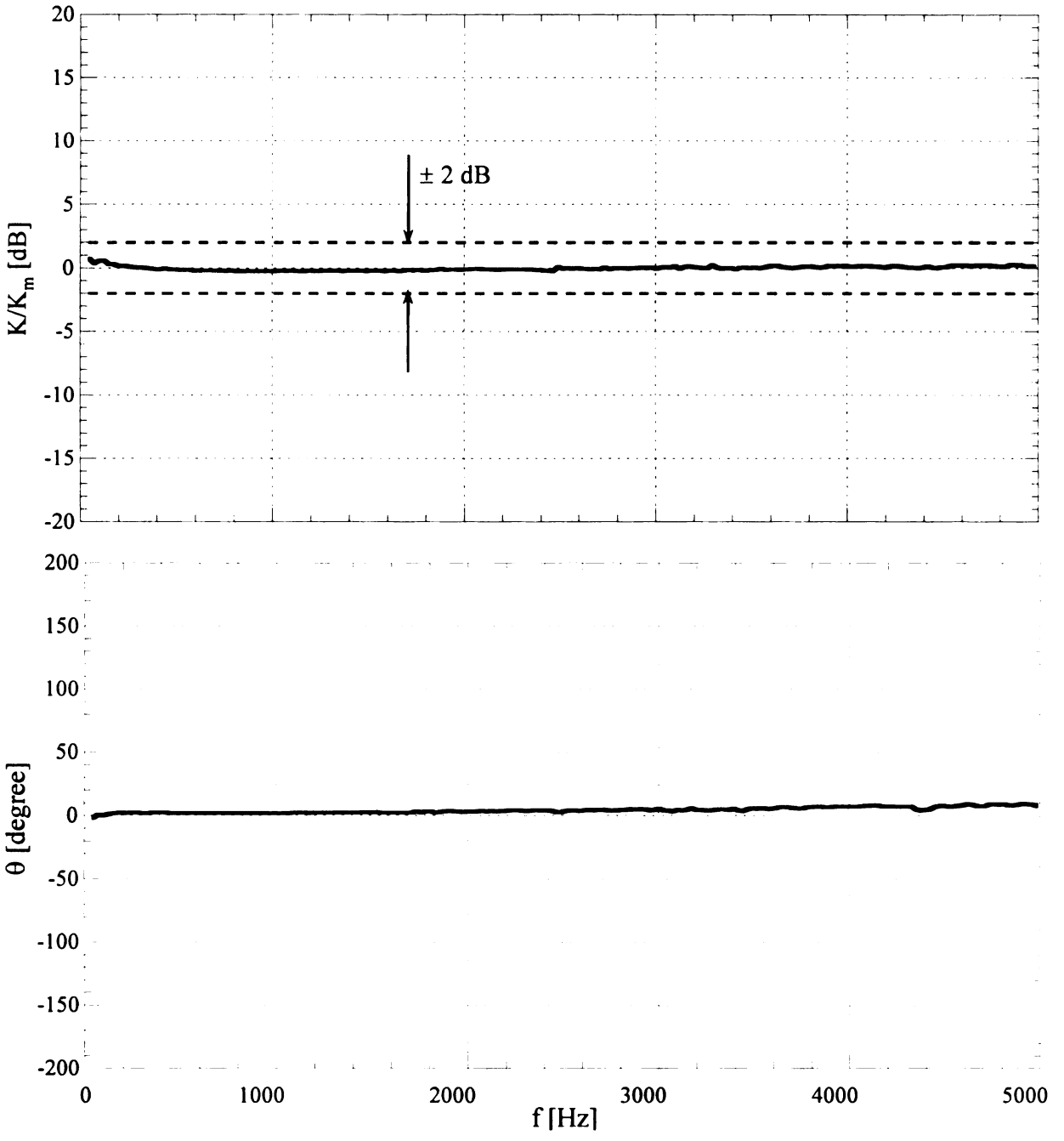

Figure 2.17. Frequency response of a microphone/hole assembly

III. Time-Delay Check

The time-delay of the microphone output voltage relative to the measured pressure was deduced from the phase shift information (see Figure 2.17; bottom plot) using the following equation:

$$\tau_d = \frac{d\theta}{d\omega} \tag{2.3}$$

where, τ_d is the time-delay in seconds, $\omega = 2\pi f$ (f is the frequency in Hz) and θ is the phase shift angle in radians.

The deduction of the time-delay was based on estimating the average slope $\left(\frac{d\theta}{d\omega}\right)$ in the plot of the phase shift versus frequency. The estimation indicated that τ_d was ≈ 10 μs, which was more than an order of magnitude (≈ 66 times) smaller than the average convection time between two successive microphones (≈ 667 μs), calculated based on the highest U_∞ of 30 m/s. Figure 2.18 shows the time delays of all microphones.

IV. Cross-Talk Check

Because of the relatively large number of signals acquired simultaneously in this study, checking the cross-talk among different acquisition channels was necessary before sampling data. The cross-talk check was conducted by exciting only one of the microphones by a sound source and determining the square of the RMS pressure measured by all other microphones relative to the square of the RMS pressure measured by the excited channel. The procedure, which utilized a Larson and Davis (L&D) hand-held calibrator (model CAL 200), was repeated for all microphones in the array. The calibrator was capable of generating sound waves at a frequency of 1 kHz and one of two

Sound Pressure Levels (SPL) selectable by a switch: 94 and 114 dB (relative to a reference pressure of 20 μPa). To ensure that sound was only applied to a single microphone, a short, flexible Urethane tube was connected to the cavity of the L&D calibrator on one end, while the other end was pressed against the top of the excited microphone only. Note that the test conducted in this manner enabled assessment of the cross-talk of the whole system end to end; i.e., including the microphones while embedded in the I- and M-plates, the driving/conditioning circuitry, the data acquisition terminal block, and the A/D card.

Figure 2.19 shows the cross-talk test results for the case when microphone # 13 was excited. This case is presented here because it had the most (i.e., worst) cross-talk amongst all 16 microphones. The data used in the plot was obtained by exciting microphone # 13 using the calibrator, as mentioned earlier, while simultaneously acquiring data from all 16 channels. A signal attenuation ratio (SAR) was then calculated by dividing the square of the RMS pressure measured at each channel by that of channel 13. The plot shows that the ratio is zero dB (decibels) at microphone # 13, which is consistent with the fact that microphone # 13 is the excited microphone. The strength of the signals measured by the other channels was at least two orders of magnitude (SAR < -40 dB) less than the source-signal. That indicated that the cross-talk among channels was negligible.

2.2.3. Tufts

Tufts were used to visualize the near-wall flow in order to estimate the reattachment length (X_r). As mentioned earlier, X_r is considered an important length

scale for characterizing separating/reattaching flows. The procedure employed for using tufts to evaluate X_r is presented here.

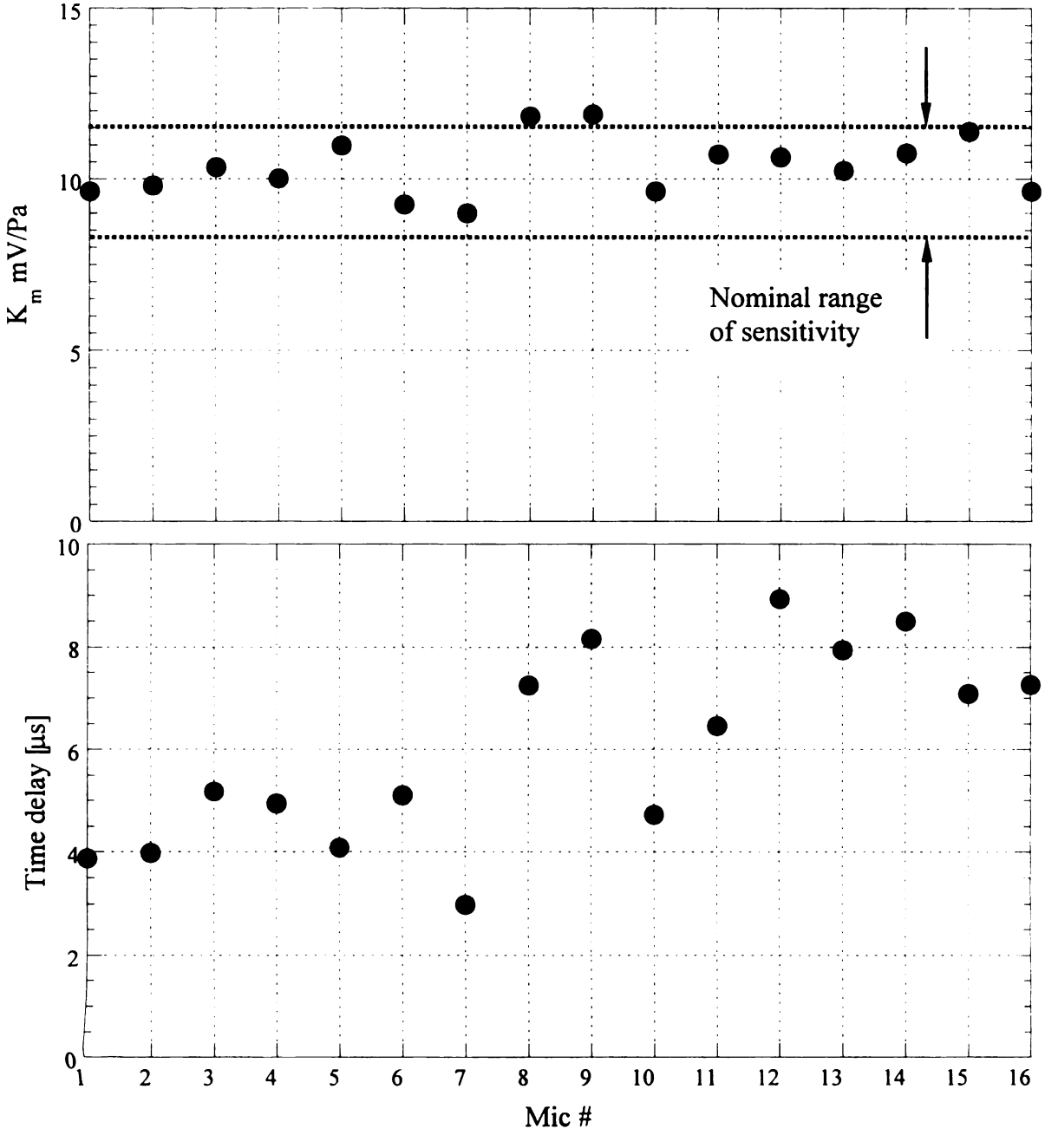

Figure 2.18. Mean sensitivity (K_m) of the microphones (top) and corresponding time-delay (bottom). Microphone #1 is the most upstream microphone

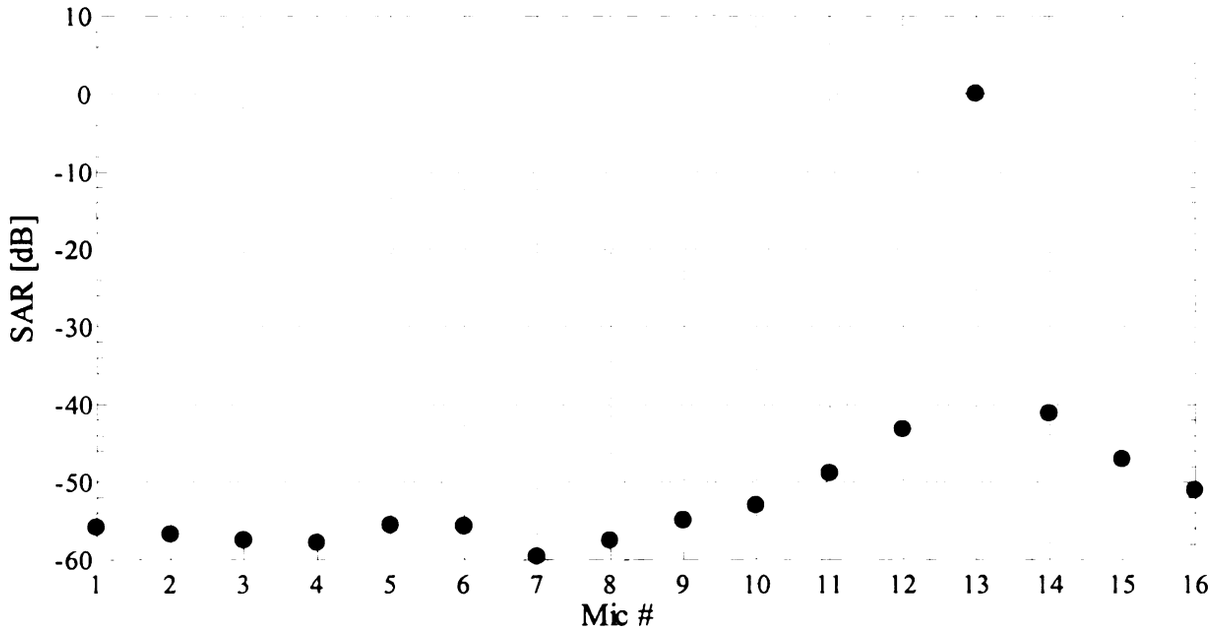

Figure 2.19. Cross-talk check of Microphone # 13 (Mic. # 1 is the most upstream one)

I. Procedure

A 10 mm-long black-yarn tuft was attached to the surface of the I-plate using tape at different streamwise locations in the reattachment zone. The streamwise location of the point of attachment (root) of the tuft was determined using the image shown in Figure 2.6. The root point was defined as the point at which the free part of the thread intersected with the edge of the tape. The corresponding x location of that point could be determined from knowing the x location of the closest pressure taps captured in the image (see Figure 2.6).

The required number of tuft images was determined by testing the effect of the number of the acquired images on the estimated Forward Flow Probability, FFP (to be explained later). The test results showed that 5000 images were enough for the FFP to converge within 5% percent, which was determined by acquiring 10,000 images. During recording, the tuft was illuminated using a fiber-optic strobe light synchronized with the

frame grabber system, while the shutter of the CCD camera was set to "always-open" mode. The synchronization was accomplished by triggering the strobe light using a signal generated from the image-grabbing LabView program through the triggering channel of the image acquisition board. This enabled "freezing" of the tuft location in each image.

A sample image of the tuft is shown in Figure 2.20. The image was captured after enlarging the aperture of the CCD camera lens relative to that used to capture the image shown in Figure 2.6. The idea was to force the background of the image (the aluminum surface) to be completely bright, leaving the black tuft highly visible in the foreground. In processing the images, the main idea was to determine to which side the tuft was located, relative to a "splitting line", which passes through the root of the tuft, as exemplified in Figure 2.20. If the tuft was to the left of the line, this would indicate a backward (upstream) flow, and vice versa. By using a MatLab program, each image was split into right and left "halves" based on the splitting line. Then, the average intensity of pixels in each half was calculated. The program was then able to indicate on which side the tuft was located by detecting the image half with lower mean intensity. The information from all 5000 images was used to determine the mean flow direction.

II. Forward Flow Probability (FFP)

Forward Flow Probability (FFP) is defined as the probability of; i.e., the fraction of the time that, the flow is in the forward (downstream) direction. If FFP equals 1.0, the flow is always forward. A zero FFP, on the other hand, reflects a flow direction that is always in the upstream direction. Accordingly, the mean point of reattachment is located by finding the x location where FFP equals 0.5.

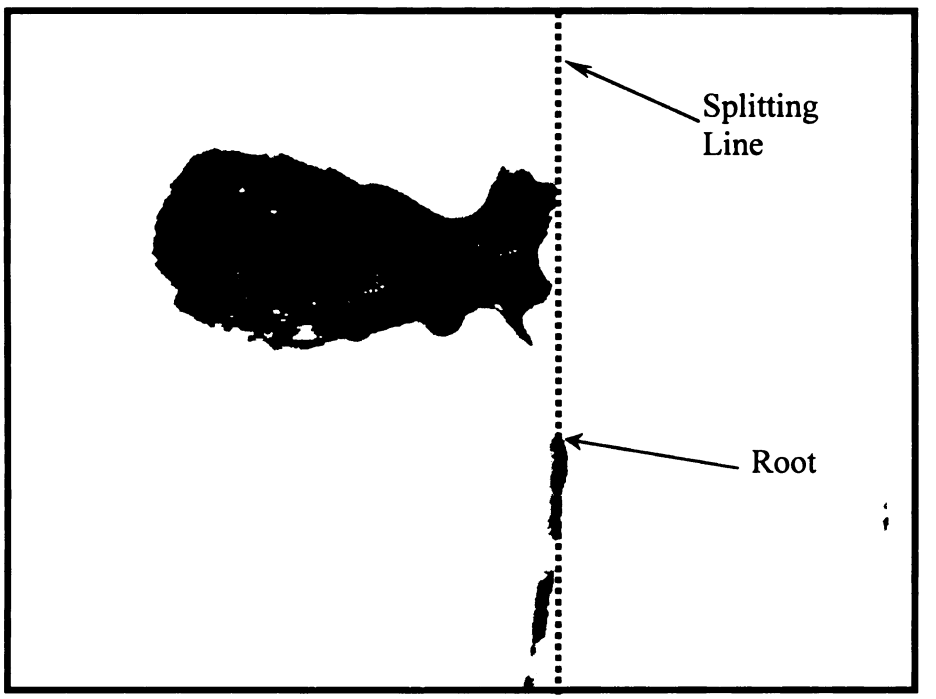

Figure 2.20. A sample wide-aperture tuft image

The FFP information was obtained for eight different x locations and the results are shown in Figure 2.21. The FFP value varies from around 0.1 to 0.9 at x locations extending from 161 mm to 199 mm downstream of the fence. The data for all eight locations were curve-fitted using a third-order polynomial function (the solid line in Figure 2.21) and the location of FFP = 0.5 on the fitting curve was found at approximately 180 mm downstream of the fence. For comparison purposes, the reattachment length was also estimated from the data presented by Smits (1982) for X_r versus blockage ratio for a similar flow geometry. This yielded an X_r value of 168 mm (which is 7% less than that obtained from the tuft data). Additionally, similar data from a shorter 5-mm tuft yielded an X_r value of 183 mm, which is within 2% of the value found from Figure 2.21. Considering all three values, it appears that the uncertainly in the estimated X_r value is of the order of 5-10%.

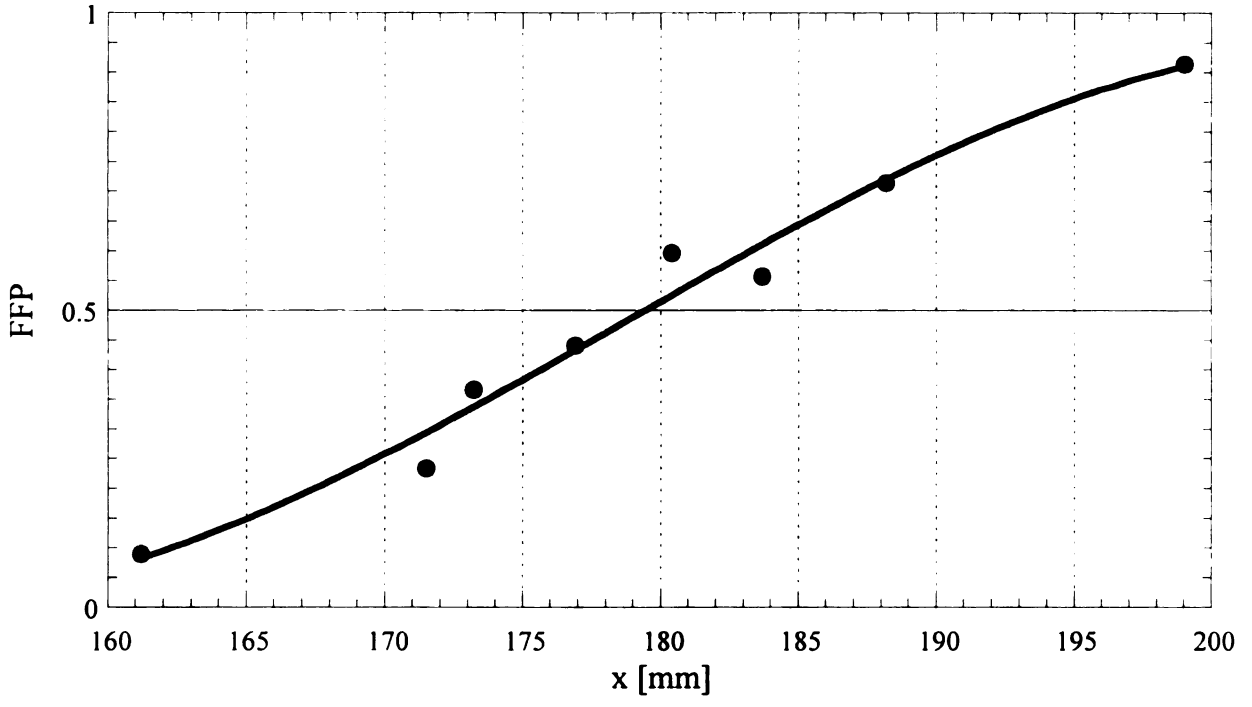

Figure 2.21. FFP of the reattaching flow versus the x-location of the tuft

2.2.4. Hotwire Sensors

Both a single- and X-hotwire probes were used to measure the flow velocity in the developing boundary layer at a single x location downstream of the reattachment point. The procedures for the magnitude and yaw calibration as well as for determination of the probe height above the wall are presented below.

I. Procedure

A 5 μm-diameter annealed tungsten wire was used to construct the hotwire sensors. First, a short length of the wire (≈ 50 mm) was electroplated with copper in a copper sulfate solution, except for a short bare length in the middle that formed the sensing length of the wire. This sensing portion was 1 mm long, resulting in a length-to-diameter ratio (l/d) of 200. After plating, the wire was directly soldered to the probe prongs, resulting in a typical sensor resistance of around 5 ohms.

The procedure adopted to measure the flow velocity using the hotwire probes may be summarized as follows (note: for the single wire, only procedure steps 2 through 5 are pertinent):

1. Conducting yaw calibration of the X-wire probe to determine the angle $\alpha_1+\alpha_2$ between the two wires forming the X configuration (see Figure 2.22 for definition of the angles), and identify the relation between the effective cooling velocity (U_e) for each of the wires and the velocity components u and v.
2. Positioning the probe at the desired y location above the wall and determining the angles of the wires of the X-probe relative to the x axis
3. Calibrating the probe in-situ at the specific streamwise location where measurements are to be conducted (pre-calibration)
4. Conducting velocity measurements
5. Calibrating the probe after measurements (post-calibration)

II. Yaw Calibration

Yaw calibration means determining the relation between the effective wire cooling velocity magnitude, on one hand, and the magnitude of the velocity vector and its angle relative to the wire, on the other. Such a calibration can be accomplished by changing the yaw angle of the X-wire probe over a certain range in a known-velocity (direction and magnitude) flow and recording the output of both wires at every angle. Using the resulting voltage versus angle information, the sought relation can be determined. For a single-wire probe, the wire is aligned perpendicular to the flow direction, experiencing the most cooling influence and resulting in the maximum output voltage for the given velocity magnitude. In this case, the angle between the velocity

vector and the normal to the wire (in a plane containing both the wire and velocity vector) is zero. If there is an angle between the flow direction and the normal to the wire, the wire primarily 'feels' the cooling effect of the component normal to the wire, with very little cooling resulting from the component parallel to the wire axis. The velocity corresponding to the *net* cooling influence is referred to as the effective cooling velocity (U_e). Ideally, for a wire with an infinite length-to-diameter (l/d) ratio, the cooling effect of the velocity component parallel to the wire is zero and the relation between U_e and the actual velocity is a "cosine law". For example, under ideal conditions, wire #1 of the X-probe shown in Figure 2.22 experiences a cooling velocity of u $\cos(90-\alpha_1)$ associated with the x component of the velocity (u).

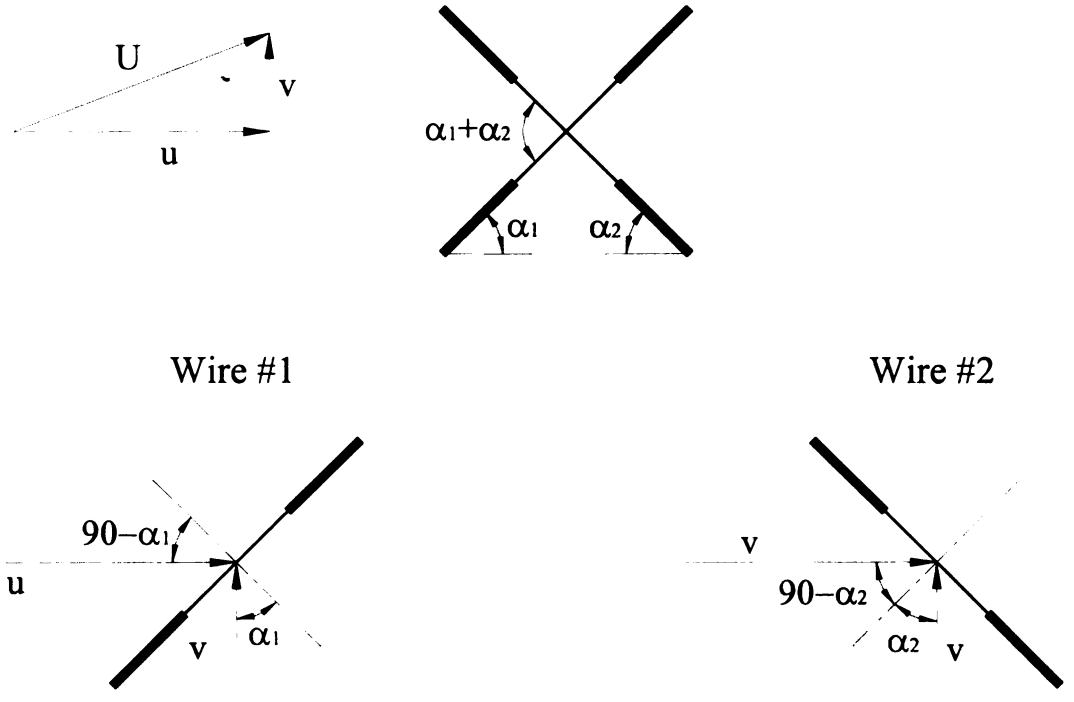

Figure 2.22. A schematic of the X-wire probe and angles definition

In reality, the length-to-diameter (l/d) ratio is finite and the cooling influence of the velocity component parallel to the wire causes a deviation from the cosine law. In this case, the effective velocity should be related to the actual velocity by a more general yaw response function ($F^2(90-\alpha)$; the square exponent of F indicates positive definiteness) instead:

$$U_e = U F^2(90-\alpha) \tag{2.4}$$

Where, U is the flow velocity magnitude and α is the angle between the wire axis and the velocity direction.

The form of the yaw-response function used in the present study is that proposed by Champagne (1965):

$$F^2(90-\alpha) = [\cos^2(90-\alpha) + k^2 \sin^2(90-\alpha)]^{1/2} \tag{2.5}$$

where, k is a constant that is determined from yaw calibration. Note that when k equals zero, the cosine law is recovered.

Figure 2.23 shows an image of the yaw-calibration setup that was used in the present study. The setup included a rotating stage with an angle indication of one degree resolution. The rotating stage, which was used to control the yaw angle of the probe, was installed above the upper wall of the wind tunnel test section, and was connected to the probe holding fixture in the wind tunnel via a 1/4" threaded rod that passed through a slot in the test section ceiling. The fixture holding the probe mainly consisted of a horizontal aluminum bar and a vertical cylindrical rod that were almost of the same length of 0.15 m. Together with the X-wire probe, these elements formed a U shape, as evident in Figure 2.23. The main purpose of the U-shape design was to keep the X-wire sensing part on axis with the rotating stage, thus allowing a change in the yaw angle while keeping the

center of the X-wire at the same location. This is demonstrated more clearly in Figure 2.24.

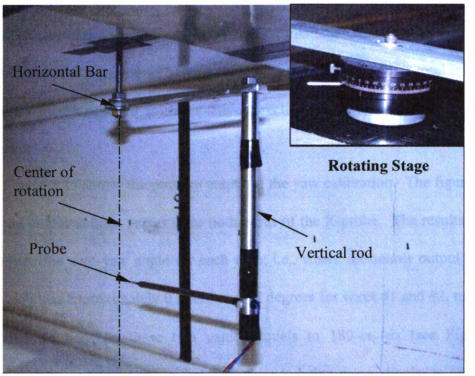

Figure 2.23. An image of the yaw calibration setup

Figure 2.24 provides a schematic of the setup for yaw calibration. The angle θ shown in the figure is that between the flow direction and a line drawn from the center of the X-wire to the center of the vertical rod. θ is used here to indicate the rotation of the wire relative to the freestream. Note that because of the bending angle of the sensor prongs, discussed earlier, when $\theta = 0$, the axis of the cylindrical body of the probe makes a very shallow angle relative to the flow direction. Also note that θ does not represent the yaw angle (which is that between the normal to the wire and the flow velocity vector), but θ increments equal yaw angle increments for both wires, with the largest wire output voltage at a given freestream velocity corresponding to a yaw angle of zero. In

implementing the yaw calibration procedure, the setup was initially adjusted such that the readout of the rotating stage was zero when the horizontal rod was visually aligned with the x direction (flow direction). The stage was then rotated through a large negative angle (−110 degrees) to start the calibration. At this angle, the corresponding hotwire output voltage was recorded. The procedure was then repeated for a total of 55 angles obtained by incrementing θ in the positive direction in increments of 5 degrees up to +160 degrees.

Figure 2.25 shows the primary output of the yaw calibration. The figure depicts a plot of the output voltage versus θ for both wires of the X-probe. The results were used to determine the zero-yaw angle for each wire; i.e., where the sensor output reaches its peak, which was approximately $\theta = -15$ and 75 degrees for wires #1 and #2, respectively. The difference between these two values equals to $180-\alpha_1-\alpha_2$ (see Figure 2.22), showing that the two wires are in fact very close to being perpendicular to each other as intended in the construction of the probe (note that the angle between the two wires is $\alpha_1+\alpha_2$).

To determine the value of the constant k in equation 2.5, each wire had to be calibrated individually at zero yaw angle (i.e., $\theta = -15^\circ$ for wire #1 and 75° for wire #2, as discussed above). The hotwire calibration was conducted by recording the mean wire voltage (E) at different known values of the flow velocity (U). The data, a sample of which is shown in Figure 2.26, were fitted using a fourth-order polynomial fit of the form: $u = a_0+a_1E+...$ (further details of the calibration process is given below). Using these polynomials, it was then possible to convert the voltages shown in Figure 2.25 to velocity

and replot the results as U_e/U_∞ (or effective to actual velocity ratio, where U_∞ is the freestream velocity in this case) versus θ in Figure 2.27.

Figure 2.28 shows the data points from Figure 2.27 replotted as U_e/U_∞ versus $(90-\alpha)$ for wires #1 (top plot) and #2 (bottom plot). This is accomplished by subtracting the θ value corresponding to the peak wire output from all θ values. Plotted in this format, the data in Figure 2.28 can then be fitted with an equation of the form given by equation 2.5. The equation has a single adjustable parameter: k. A second parameter, α_o, representing an angle offset error in determination of the θ value corresponding to the peak wire output (zero yaw) was also added in order to determine the zero-yaw angle with resolution better than the 5-degree increment used in the yaw calibration. The best values of these two parameters were found by varying each of them independently over a predetermined range, and calculating the corresponding average absolute error between the data points and the fitting curve. The pair of values corresponding to minimum error for each of the wires was then selected for the best fit. For reference, the resulting fits are displayed in Figure 2.28 with the data. The corresponding parameters are: $k_1 = 0.04$, $k_2 = 0.0$, and $\alpha_1+\alpha_2 = 93$.

Once k_1 and k_2 were determined, the following equations were used to calculate the streamwise and wall-normal velocity components from the effective cooling velocities of the two wires, respectively (for derivation of the equations see Appendix A):

$$u = \frac{U_{e2}\,F_1^2(\alpha_1) + U_{e1}\,F_2^2(\alpha_2)}{F_1^2(90-\alpha_1)\,F_2^2(\alpha_2) + F_1^2(\alpha_1)\,F_2^2(90-\alpha_2)}$$

$$v = \frac{U_{e2}\,F_1^2(90-\alpha_1) - U_{e1}\,F_2^2(90-\alpha_2)}{F_1^2(90-\alpha_1)\,F_2^2(\alpha_2) + F_1^2(\alpha_1)\,F_2^2(90-\alpha_2)} \qquad (2.6)$$

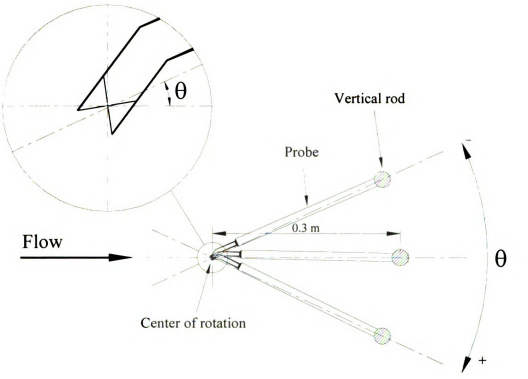

Figure 2.24. Schematic of the yaw calibration setup

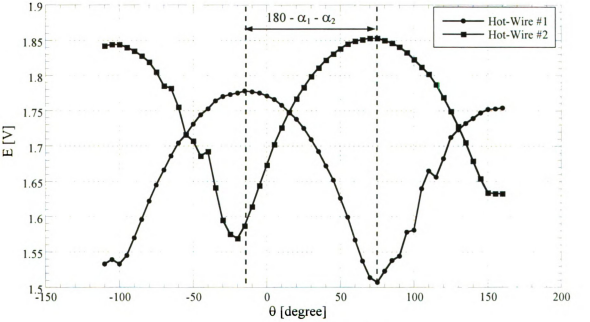

Figure 2.25. Yaw calibration: voltage results

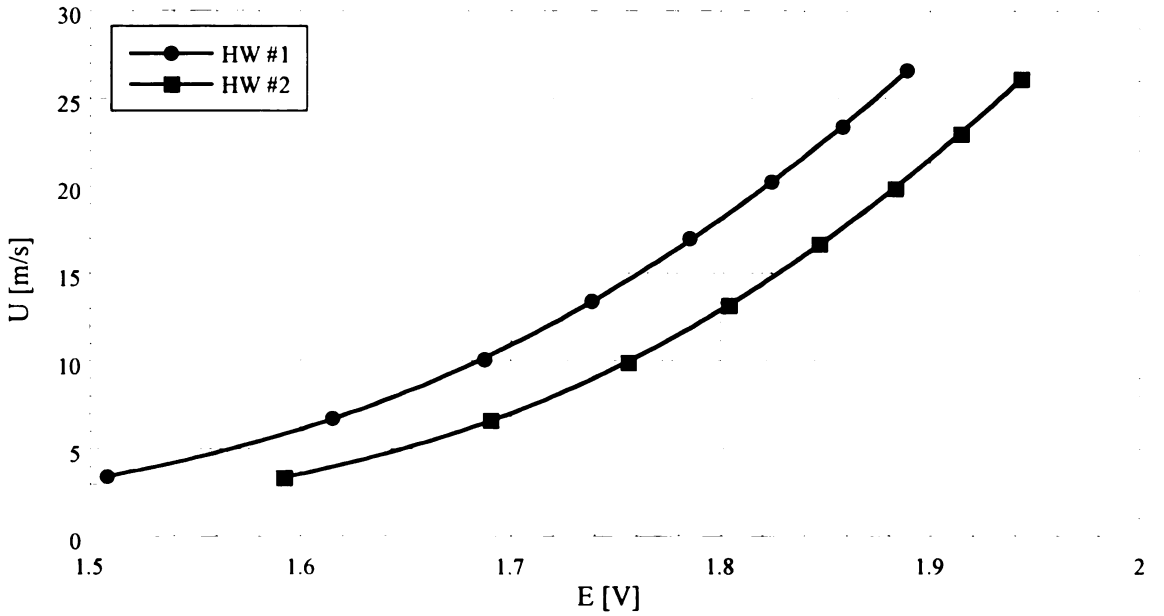

Figure 2.26. Sample calibration data for the X-probe hotwires

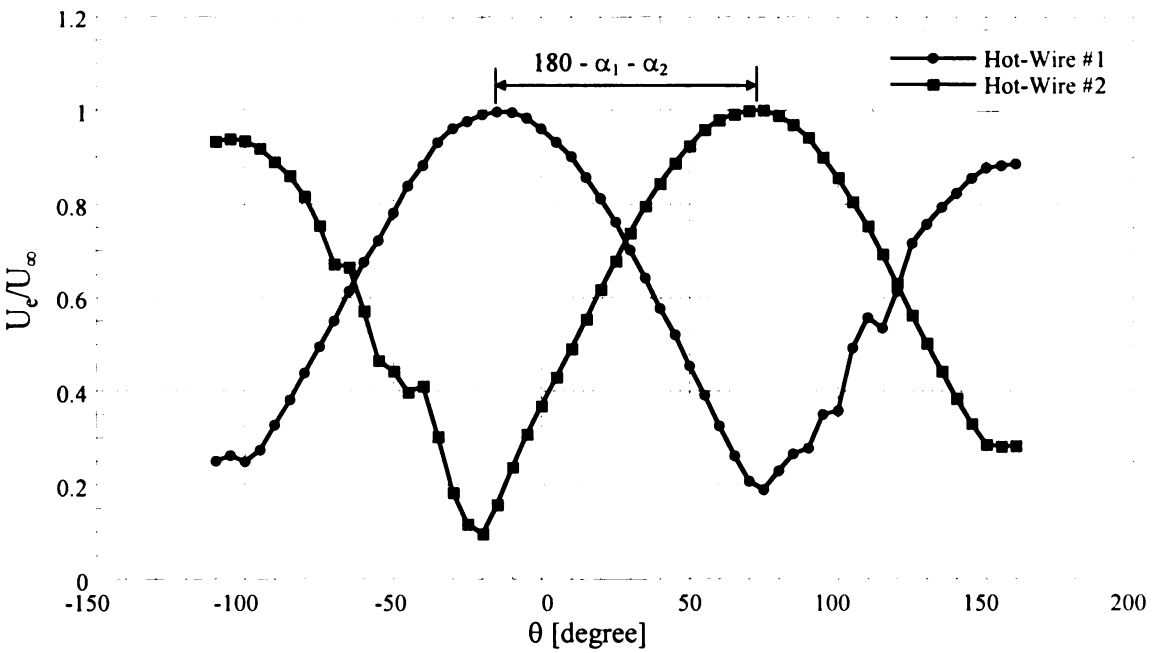

Figure 2.27. Yaw calibration data after conversion of voltage to velocity

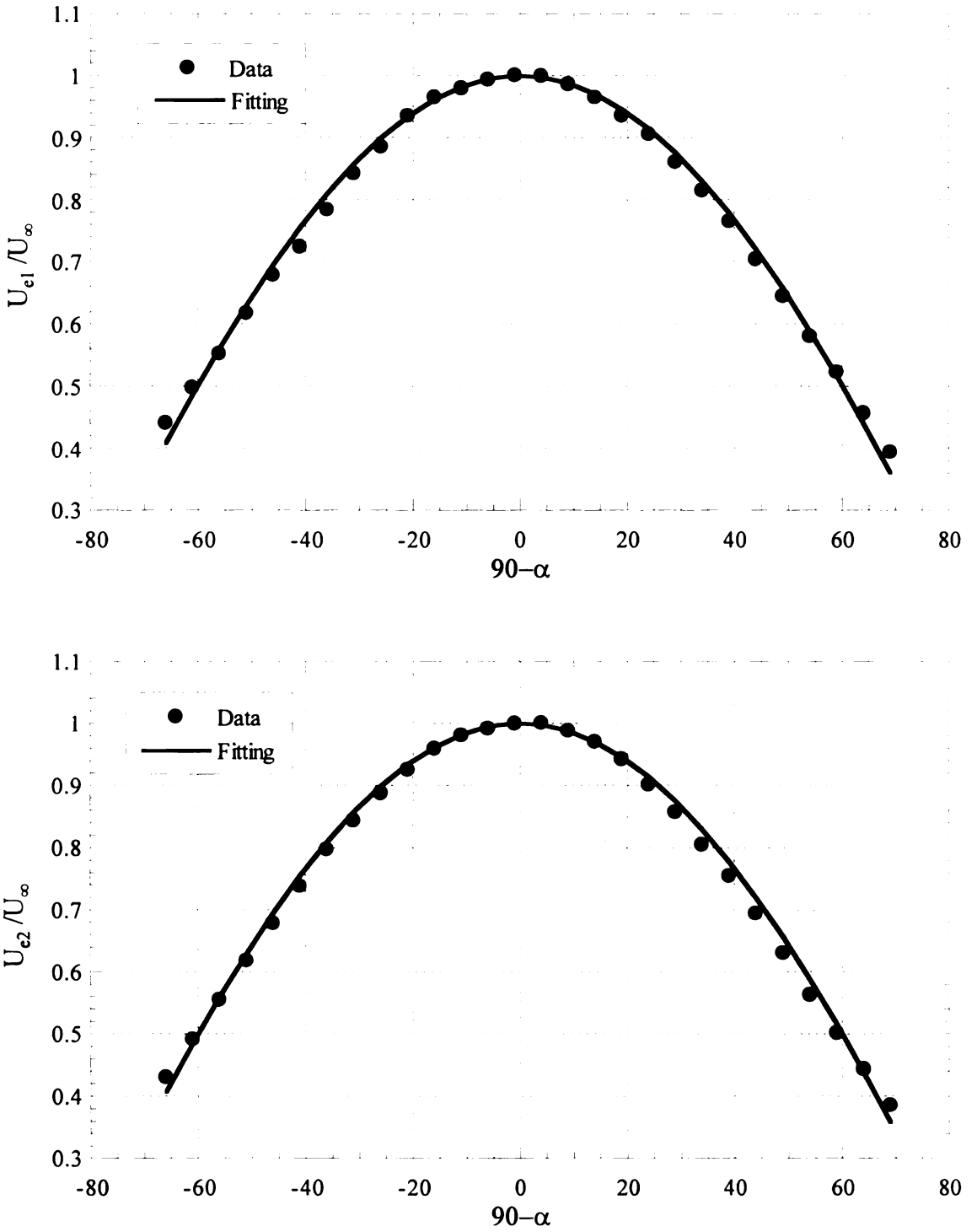

Figure 2.28. Yaw-calibration data and corresponding curve fits for hotwire #1 (top plot) and hotwire #2 (bottom plot)

where, U_{e1} and U_{e2} are the effective cooling velocities measured by wires #1 and #2, respectively, and F_1^2 and F_2^2 are given by:

$$F_1^2(\alpha_1) = [\cos^2(\alpha_1) + k_1^2 \sin^2(\alpha_1)]^{1/2} \quad (2.7)$$

$$F_2^2(\alpha_2) = [\cos^2(\alpha_2) + k_2^2 \sin^2(\alpha_2)]^{1/2} \quad (2.8)$$

The method used to determine α_1 and α_2 will be discussed below.

III. Probe Installation

The main purpose of the probe installation procedure was to position the probe at the desired location (between microphones #13 and 14, or 550 mm (3.05 X_r), downstream of the fence), and to adjust/determine the angle (in the x-y plane) between the wires of the X-probe and the x direction. The alignment of the probe prongs parallel to the splitter plate at that location was achieved with the aid of a small piece (approximately 25 mm by 25 mm) of a 23 μm-thick polymer foil with a thin layer of aluminum deposited on one side. The polymer side of the foil was adhered to the splitter plate surface directly below the probe to provide a mirror image of the prongs. Figure 2.29 shows a sample of the bent probe prongs and their reflected image. By adjusting the probe till the real prongs and their reflected image were parallel, the probe alignment was achieved.

After the alignment of the prongs, their image was also used to position the probe at the desired starting y location. The main idea was to measure the distance between one of the bottom prongs (the one closest to the wall) and its reflected image. Hence, the corresponding y location of the prong was the difference between half the measured distance and the thickness of the foil (23 μm). To measure the distance between the prong and its image, each image had to be calibrated (estimating how many pixels in the image per mm in real dimensions). The image was calibrated by causing the traversing

mechanism of the hotwire to move a known distance (typically 1 mm) and measuring the corresponding prong displacement in pixels, yielding an image scale factor in pixels per mm. This scale factor was then combined with the measured distance between the prong and its reflected image in pixels to position the bottom prongs 0.5 mm above the splitter plate surface. Given the geometry of the X-wire probe, the corresponding y location of the center of the sensing parts of the wires was 2.0 mm (0.5 + 1.5 mm). For the single wire probe, the same procedure was used to position the single wire at a starting y location of 0.5 mm. Because the wire of the single hotwire was parallel to the splitter plate, it was used as a reference to determine the y location of the probe.

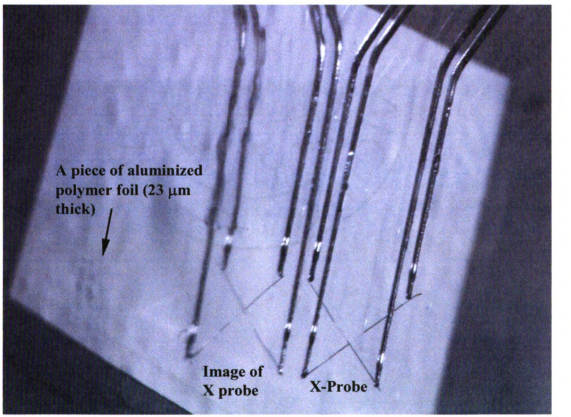

Figure 2.29. A photograph of the X-wire probe and its reflection in the splitter plate

Figure 2.30 shows a zoomed-in image of the X-wire sensor. The image was used to measure α_1 and α_2 (required for evaluation of equations 2.6 and 2.7). Once the probe was aligned as explained in the previous paragraph, the prongs of the probe became parallel to the x-direction. Thus, it was possible to determine α_1 and α_2 by measuring the angle between the wires and the prongs as depicted in Figure 2.30. The figure demonstrates how the angles were calculated by determining the pixel coordinates of the three points (1, 2 and 3 for α_1, and 1, 4 and 3 for α_2) for each of the angles. The measured values of α_1 and α_2 were 47° and 46°, respectively. Note how the sum of these two geometrically determined angels equals to 93 degrees, which is in very good agreement with the value determined earlier of the angle between the two wires from yaw calibration.

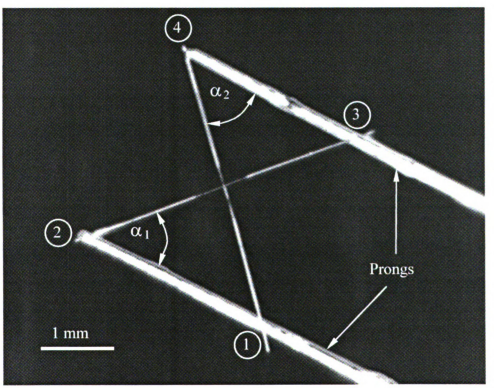

Figure 2.30. A close-up image of the X sensor

IV. Hotwire Calibration

In every test, the hotwire probes had to be calibrated before (pre-calibration) and after (post calibration) velocity measurements. It was desired to accomplish this in-situ by positioning the probe in the freestream above the re-developing boundary layer, where the flow is steady and laminar and the velocity is known. However, the thickness of the boundary layer (which was about 80 mm, as will be explained later in section 2.2.5) was larger than the farthest possible position the traversing mechanism can reach away from the wall. Thus, it was not possible for the probe to reach the freestream with the existing experimental setup. This problem was overcome by replacing the fence with a sharp (V-shaped) leading edge during calibration to reduce the boundary layer thickness by eliminating the bluff-body effect of the fence.

An actual image, along with a schematic diagram, of the "v-attachment" used in the calibration may be seen in Figure 2.31. The image provides a side view while the schematic yields a frontal view of the attachment. The modification of the leading edge resulted in diminishing the thickness of the boundary layer to approximately 25.0 mm. In order to measure the freestream velocity (which is used as a reference in the hotwire calibration) at the specific x location where the hotwire measurements were conducted, a pitot-static probe located in the freestream at this x location was calibrated against a static-pressure tap in the sidewall of the test section upstream of the model prior to installation of the hotwire. During the actual calibration procedure, the static pressure tap was then used to infer the freestream velocity "seen" by the wire.

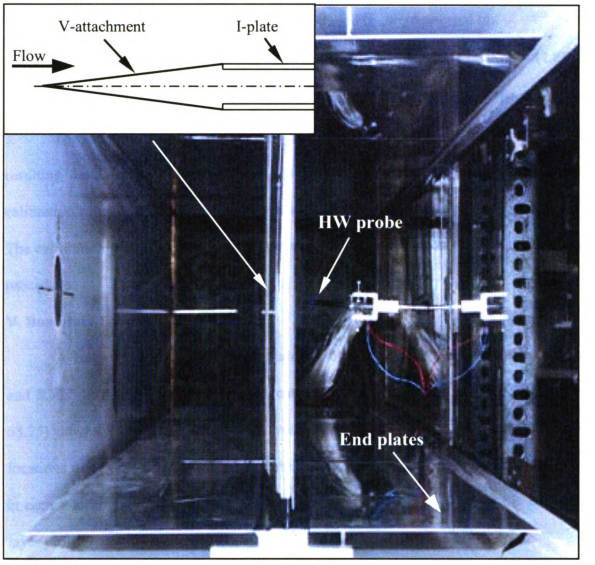

Figure 2.31. Leading edge for X- and single-wire in-situ calibration

The procedure for the hotwire calibration was as follows:

1. The wire mean output voltage was acquired at eight different wind tunnel freestream velocities. The corresponding velocity magnitude was measured using the output pressure of the reference pressure tap.

2. To deduce the effective velocities of both wires (U_{e1} and U_{e2}) at each calibration point, U_∞ together with the known values of α_1 and α_2, were plugged in:

$$U_{e1} = U_\infty F_1^2(90-\alpha_1) \quad (2.8)$$

$$U_{e2} = U_\infty F_2^2(90-\alpha_2) \quad (2.9)$$

3. The effective velocity of each wire was plotted versus the output voltage and the resulting data were curve-fitted using a 4^{th} order polynomial to provide an analytic calibration equation for converting the wire output voltage to effective cooling velocity. The calibration procedure of the single hotwire only included steps 1 and 3 of the above procedure.

V. Boundary Layer Profiles

A single hotwire was used to obtain the boundary-layer velocity profiles (mean and RMS) at the selected streamwise location of x = 550 mm (x/X_r = 3.05 and x/h = 68.75) downstream of the fence. The velocity was measured at 182 wall-normal (y) locations from y = 0.5 to 91 mm in increments of 0.5 mm. 10,000 samples were acquired at each y location with a sampling frequency of 1000 sample/s to construct the boundary layer profiles as shown in Figures 2.32 and 2.33.

Figure 2.32 depicts the mean-velocity profile of the boundary layer. The ordinate is the mean velocity in the x direction (u) normalized by the local freestream velocity (U_∞ = 16.2 m/s), while the abscissa is the physical y locations of the hotwire normalized by the boundary-layer thickness based on $0.99U_\infty$ (δ = 80 mm). The shape of the profile generally agrees with the typical shape of a developing boundary layer downstream of a reattaching shear layer (a detailed discussion of the profile and comparison to the literature may be found in section 4.1.1). For verification of the X-wire measurement

procedure, which is substantially more elaborate than the single wire, data from the X-wire are also plotted using open circles in Figure 2.32. The X-wire was traversed from a y location of 2 mm to 51.5 mm ($y/\delta = 0.025$ to 0.64) in steps of 0.5 mm ($\Delta y/\delta = 0.00625$). The figure depicts a generally good agreement between the two profiles with a maximum error of 3% of U_∞.

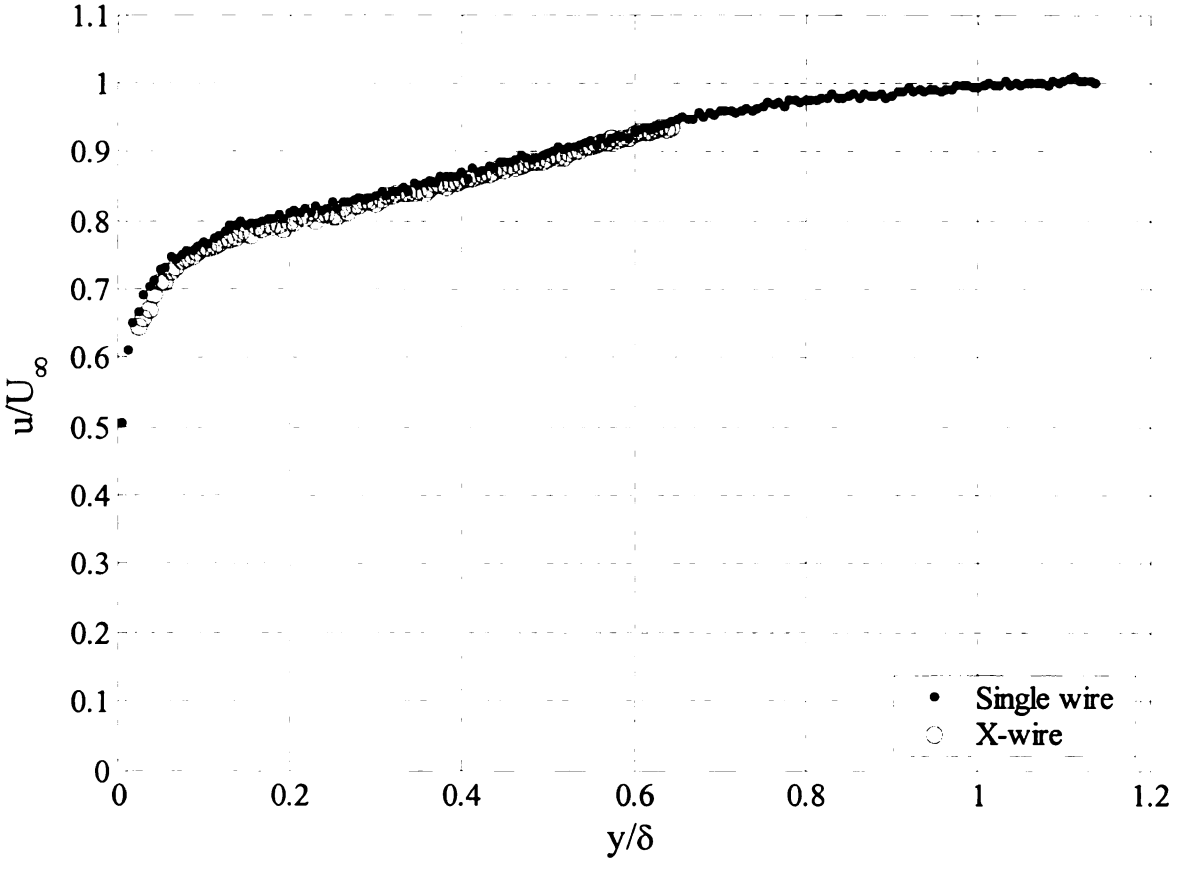

Figure 2.32. Boundary-layer mean-velocity profiles from single- and X-wire measurements at $x/X_r = 3.05$

Figure 2.33 shows the RMS values of the flow velocity in the x direction. The ordinate represents the RMS velocity normalized by U_∞ and the abscissa is the same as Figure 2.32. The RMS profile shows a plateau of high RMS value of approximately

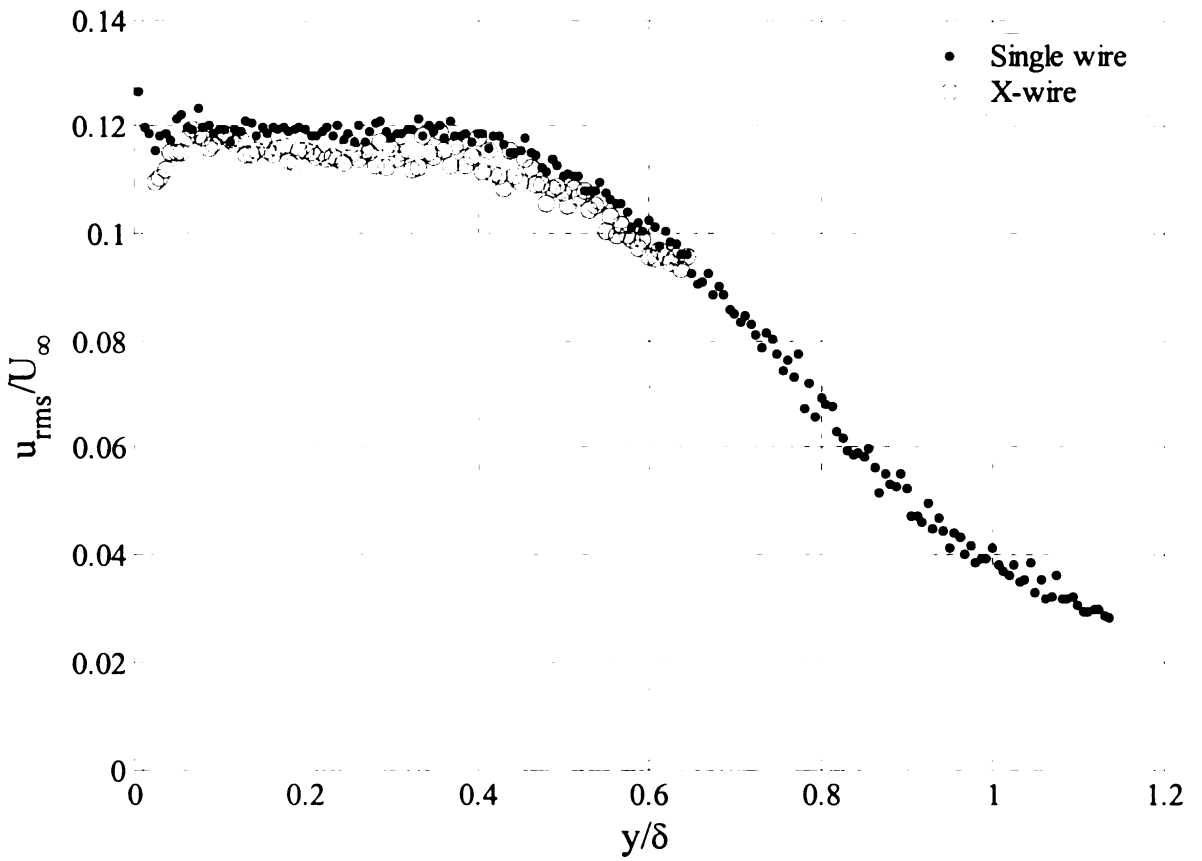

Figure 2.33. Boundary-layer RMS streamwise-velocity profiles from single- and x-wire measurements at $x/X_r = 3.05$

$0.12U_\infty$. Beyond a certain height, the RMS value decays as the probe moves away from the wall. Very close to the wall, within a narrow region of $y/\delta < 0.025$ or so, there is a rise in the RMS value above that given by the plateau. The RMS values calculated from the X-wire data are also plotted in Figure 2.33. The figure depicts that the two profiles agree fairly well. The estimated maximum deviation between the two profiles is less than 1% of U_∞. This deviation, which depicts the X-wire data to be consistently lower than that of the single-wire data, is not surprising since the X-wire averages the measurements over a spatial sensing volume of approximately 1 mm^3, while the single wire averages the measurements over a 1 mm length in the spanwise direction (the wire dimensions in x

and y directions may be neglected relative to the flow scales). The larger sensor volume of the X-wire, particularly in the y direction results in attenuation of the small-scale energy. This is most evident near the wall, where the X-wire data decreases in value as y approaches the wall, while the single-wire RMS data rise.

VI. X-Probe Disturbance Check

Because of the simultaneous wall-pressure and velocity measurements, it was necessary to check if any significant disturbances caused by the presence of the X-probe in the flow contaminated the wall-pressure data. The check was done by examining the microphones output when the X-wire probe resided at different y locations. Figures 2.34 depicts the power spectra of the microphone voltage output for three different heights of the X-probe (y = 4, 10 and 50 mm). It should be noted that these three locations indicate the height of the center of the probe (the sensing part), while the corresponding locations of the closest prong to the splitter plate were 2.5, 8.5 and 48.5 mm, respectively. Figure 2.34 shows the spectra of the pressure measured by the microphone closest to the hotwire location ($x/X_r = 3.0$) on the upstream side. In interpreting the data, the farthest y location was considered as the *no disturbance* case. The figure depicts good agreement among the three spectra, which indicates that the microphone measurements are insensitive to the hotwire location, suggesting that the presence of the probe in the flow does not create any undesired contamination of the microphone data.

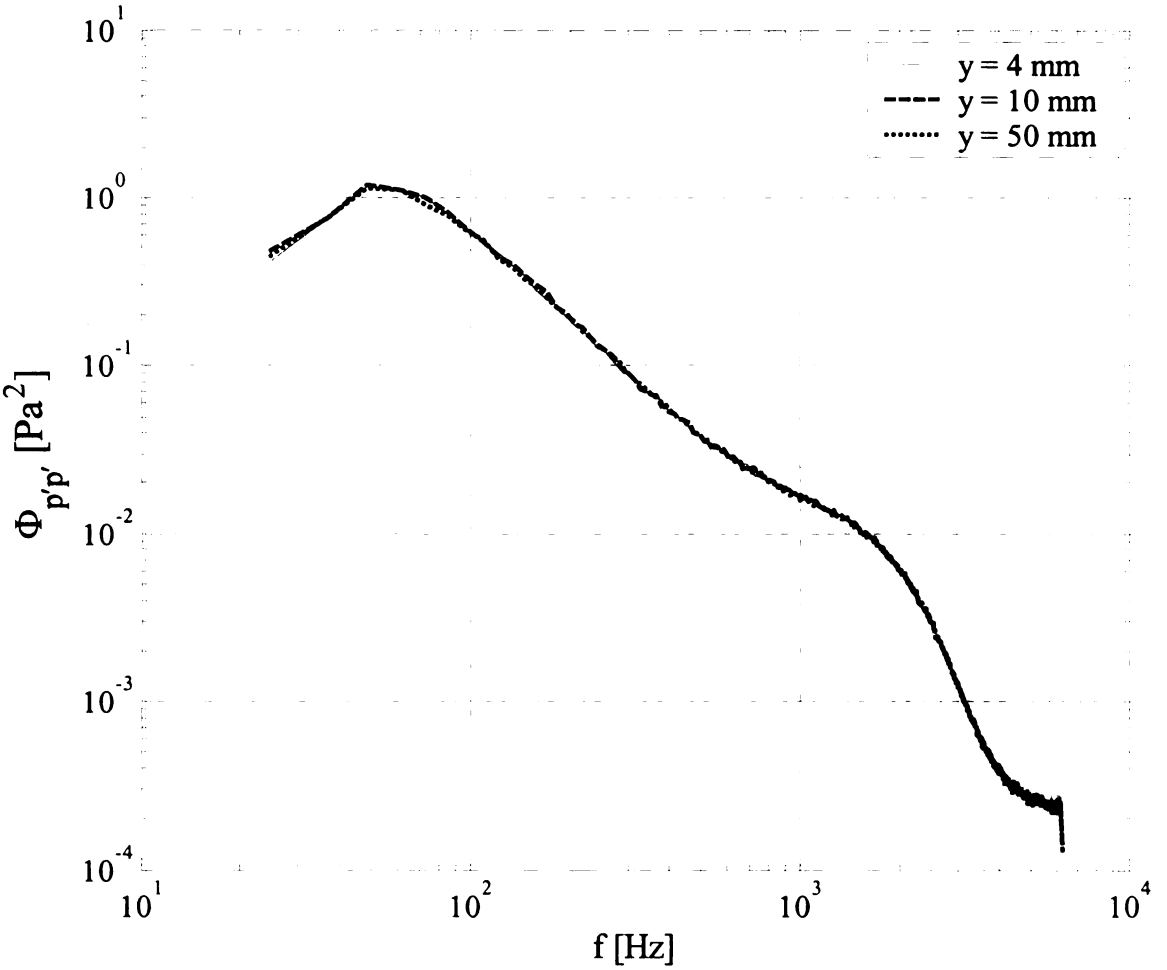

Figure 2.34. Pressure spectra of the microphone immediately upstream ($x/X_r = 3.0$) of the X-wire for three y locations of the wire

Moreover, the same test was done for a microphone immediately downstream of the hotwire. The test results are shown in Figure 2.35. The data confirm that the hotwire probe effects on the pressure data can be neglected for the range of frequency of interest. Note that the same test was conducted for all of the microphones, but only the data for microphones #13 and #14 were presented because they were the closest microphones to the hotwire probe, and hence they should suffer the most from any interfering effects of the X-probe.

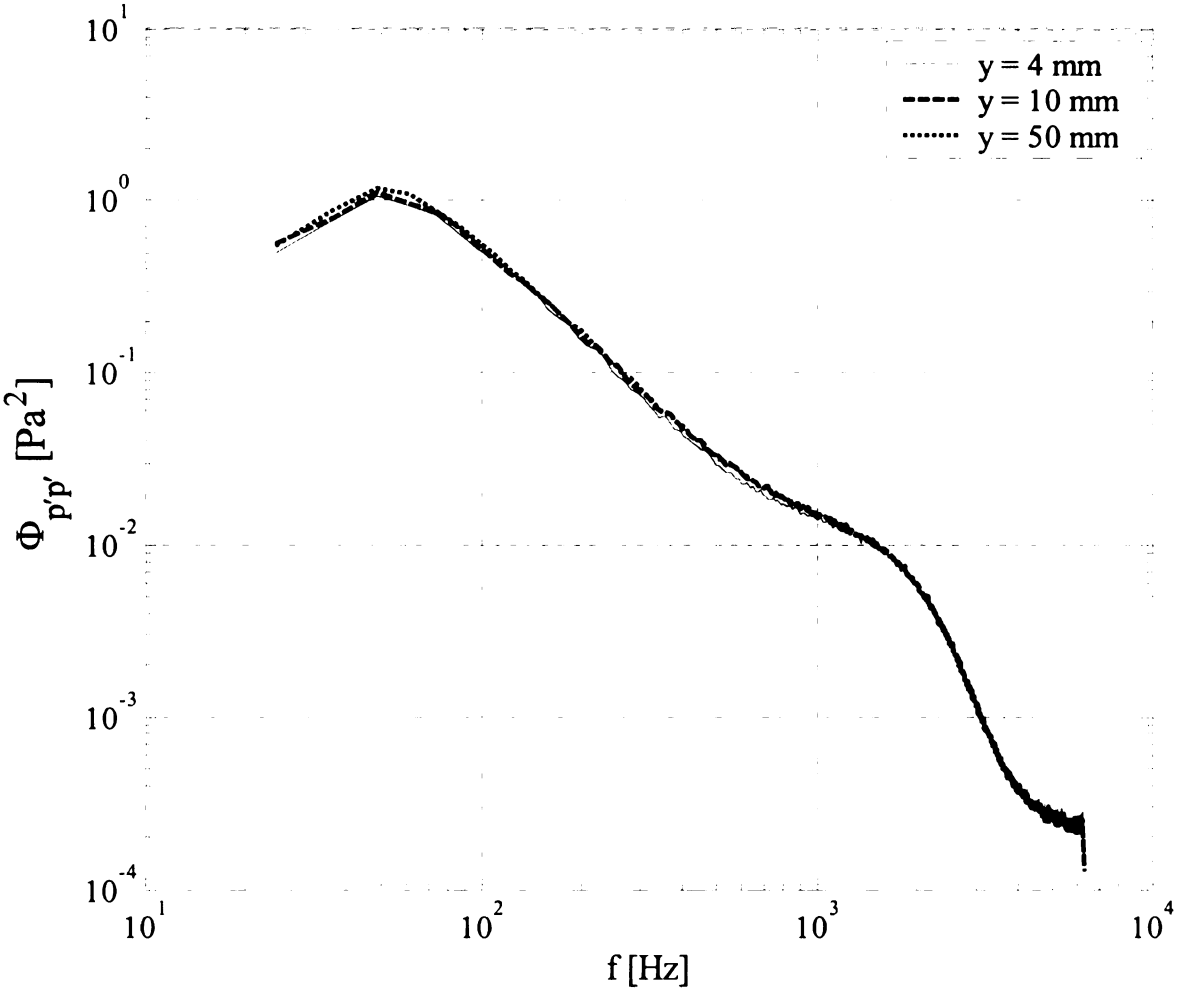

Figure 2.35. Pressure spectra of the microphone immediately downstream (x/X_r = 3.11) of the X-wire for three y locations of the wire

3. WALL-PRESSURE RESULTS

This chapter focuses on the results of the wall-pressure measurements only. This focus is important for two reasons: (1) one of the primary goals of this work is to understand the nature of the wall-pressure field beneath the *recovering* boundary layer and compare this to the *fully-developed* boundary layer, on one hand, and the *separating/reattaching* flow, on the other; (2) because in the following chapter the velocity field will be estimated using Linear Stochastic Estimation (LSE) based on wall-pressure data, understanding of the characteristics of the latter is an important precursor to proper interpretation of the estimated velocity field. Of course, an understanding of the wall-pressure/velocity field relationship is also important for interpretation of the LSE results. This relationship will be explored in detail in Chapter 4 prior to implementation of the LSE procedure.

As explained in Chapter 2, the mean wall-pressure was measured using 28 pressure taps located on the center of the splitter plate, while the fluctuating wall-pressure signature underneath the flow was captured using a 16-microphone array downstream of the reattachment point. It should be noted that due to the lower limit of the microphones' operating frequency range (20Hz), all microphone data are high-pass filtered at 20Hz. This removes any ambiguity concerning the magnitude and phase of p' in the analyzed data. As will be demonstrated herein, the wall-pressure spectral peak is in fact captured within the analyzed band of frequencies. Moreover, there is negligible amount of fluctuating-pressure energy lost because of the filtering process. In the following subsection, data-processing details and results will be presented concerning the mean-

and fluctuating-pressure streamwise variation, autocorrelation, power spectra, cross correlation, and wavenumber-frequency spectrum.

3.1. Mean-pressure distribution and the reattachment length

Figure 3.1 shows a comparison between the mean-wall-pressure coefficient (C_p, see equation 2.1) distribution from the present work and that from Hudy *et al* (2003). The ordinate represents the pressure coefficient while the abscissa represents the streamwise location of the pressure taps (x) in mm with respect to the fence. The test model used in Hudy *et al.* (2003) was the same as the current one except that their blockage ratio was 1.94% versus 4.5% in the present work. This blockage ratio is defined based on the fence height (h). The actual blockage in the present flow (based on the total fence height, 2H) was 9.9% (compared to 4.26% in Hudy *et al.*). Because of the higher blockage ratio and consequent flow acceleration, the distribution of C_p from the present data shows a more pronounced negative valley downstream of the fence (note that in both studies the reference pressure in C_p is taken at the beginning of the test section, or upstream of the model). Furthermore, the pressure recovery is less than that of Hudy *et al.* (2003). This pressure recovery is faster in the present study, resulting in a shorter reattachment length (180mm, 22.5h, as found using tufts, compared to 205mm, 25.5h, in Hudy *et al.* 2003).

The observation that the mean reattachment length of the present work is shorter than that of Hudy *et al.* (2003) agrees well with the results of Smits (1982), who investigated the effect of the blockage ratio on the mean reattachment length. Smits' results showed that the reattachment length decreased for larger blockage ratio. Furthermore, when the blockage ratio of the present model is used in conjunction with

Smits' data to estimate the mean reattachment length, an X_r value of approximately 21h is found, which is shorter than, but falls within 7% of, the measured reattachment length.

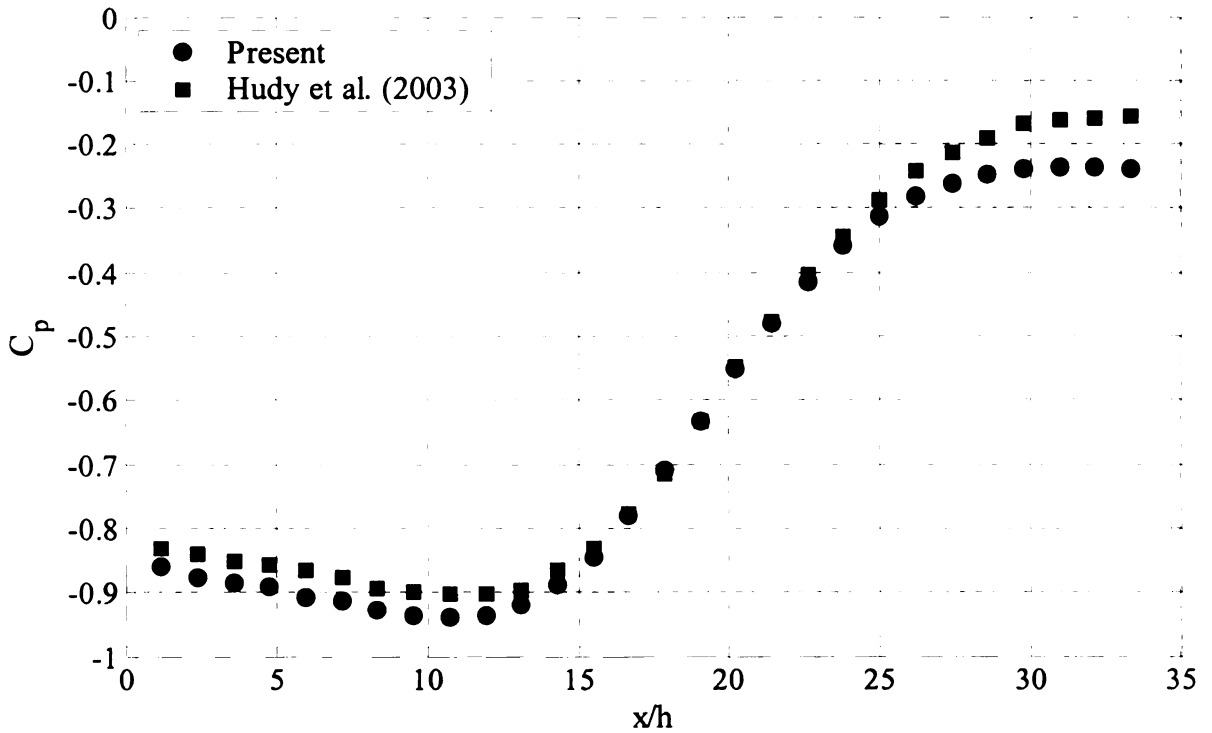

Figure 3.1. Streamwise distribution of the mean pressure coefficient from the present study compared to Hudy *et al.* (2003)

Ruderich and Fernholz (1982) also used a fence-with-splitter-plate model with two fence heights above the splitter plate (h) of 11 and 22mm. The cross-section height of the wind tunnel used with their experiments was 0.5m, while the splitter plate thickness was 6.3mm, which resulted in total fence heights (2H) of 28.3 and 50.3mm. Consequently, the blockage ratios based on h = 11 and 22 mm were approximately 4.4% and 8.8%, while the actual blockage ratios based on 2H were approximately 5.7% and 10%, and the corresponding mean reattachment lengths were 22.6h and 17.2h, respectively. Therefore, Ruderich and Fernholz's results depict an agreement with that of Smits that the mean reattachment length decreases for higher blockage ratio.

Furthermore, the mean reattachment length of the present work agrees well with that of Ruderich and Fernholz (1986) for the case of h = 22mm, which approximately have the same blockage ratio based on h as the current work. Additionally, Castro and Haque (1987) reported a mean reattachment length of 19.2h with a 6.2% blockage ratio based on h.

Note that due to the flow acceleration caused by the blockage effect of the model, the *local* (at the location of hotwire measurements) freestream velocity will be used as U_∞ for the remainder of this thesis. This local value is approximately 14% higher than the approaching freestream velocity.

3.2. Fluctuating pressure distribution

Figure 3.2 shows the streamwise distribution of the fluctuating-pressure coefficient ($C_{p'} = \frac{p'_{rms}}{\frac{1}{2}\rho U_\infty^2}$, where p'_{rms} is the root mean square (RMS) of the fluctuating pressure). The figure depicts the profiles of $C_{p'}$ versus ξ, where $\xi = (x-X_r)/X_r$, for Reynolds numbers 7600 and 15700 based on step height. The distributions depict a decay in the pressure fluctuation with increasing distance from the reattachment point. This suggests that the flow structures dominating the wall-pressure generation are continually loosing energy as they travel downstream of the reattachment point. This is consistent with the relaxation process of the shear layer vortices in zone VI (see Figure 1.1) referred to in the Chapter 1. More specifically, the high mean shear stress energizing those vortices during their earlier development in the free shear layer (before reattachment) slowly gives way to a much weaker mean shear as the attached shear layer gets thicker with increasing x. Thus, the source of turbulent energy received by these vortices becomes weaker and weaker and so does their energy as well as their wall-

pressure signature. Furthermore, the plot in Figure 3.2 shows that at the higher Reynolds number p′ is more energetic and its rate of decay is slightly higher than that at the lower Reynolds number. This decay presumably continues monotonically till p′ reaches a level corresponding to that of an equilibrium turbulent boundary layer.

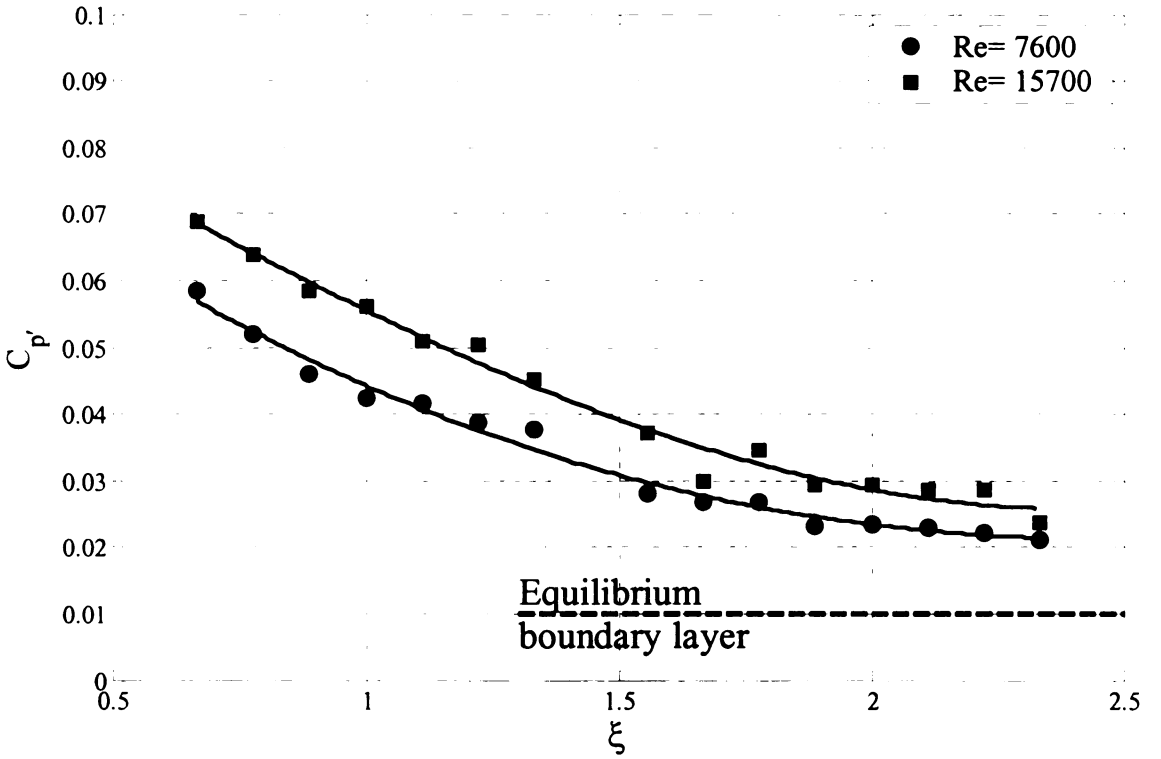

Figure 3.2. Streamwise distribution of the coefficient of the RMS pressure fluctuation

Figure 3.3 depicts the full streamwise distribution of $C_{p'}$ in both the separating/ reattaching and redeveloping flow zones at Reynolds number of 7600. The solid squares represent data obtained in the separating/reattaching flow by Hudy *et al.* (2003), while the solid circles show those from the present work. A polynomial fit is also added to the plot for the purpose of showing the general trend in the streamwise profile of $C_{p'}$. The profile shows the typical behavior of p' in a separating/reattaching flow before and after reattachment, which is represented by a rise in the wall-pressure fluctuation till it reaches

a peak slightly upstream of reattachment, followed by a decay during the relaxation process downstream of reattachment.

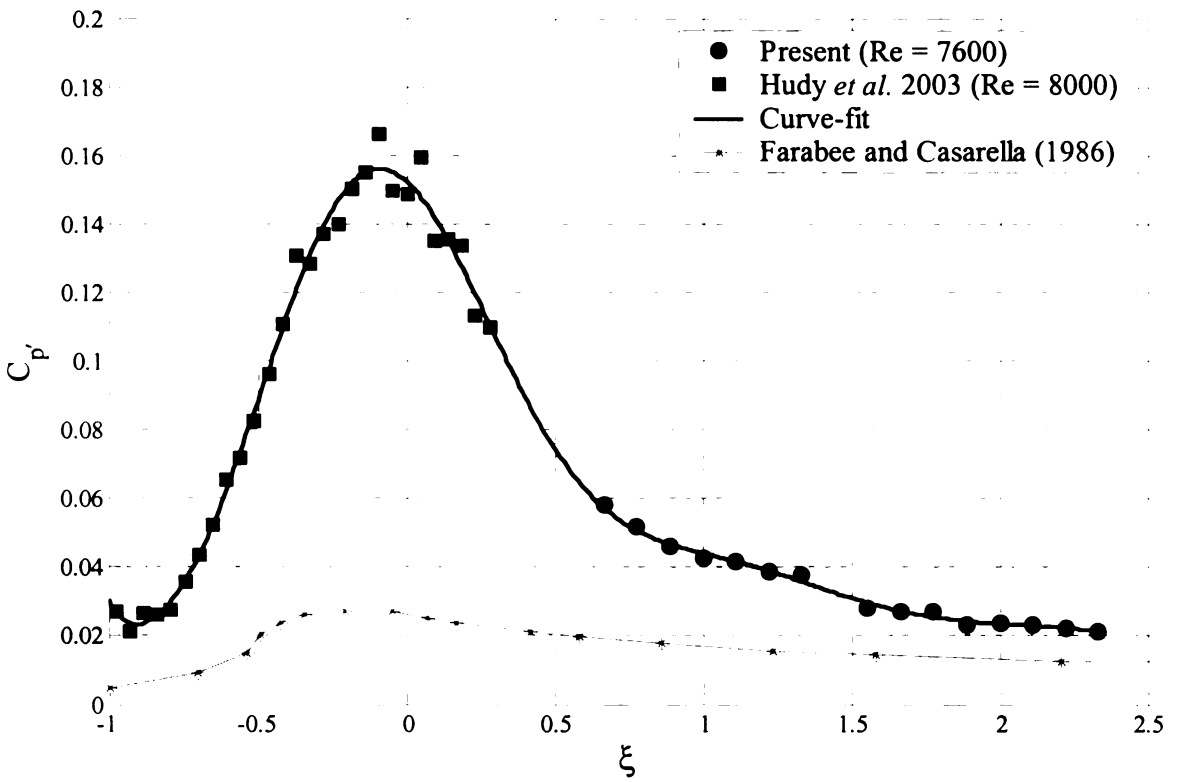

Figure 3.3. A comparison between the $C_{p'}$ streamwise distribution of Hudy *et al.* (2003) and the present work with that of Farabee and Casarella (1986)

Figure 3.3 also depicts a comparison between the $C_{p'}$ streamwise distribution of the fence-with-splitter-plate model used in the present work with that of a backward-facing step flow from Farabee and Casarella (1986). Both distributions exhibit the same qualitative behavior. However, the present flow exhibits much more energetic wall-pressure fluctuations than that of the typical backward-facing step. This is believed to be caused by the much stronger shear across the very thin, laminar boundary layer at separation in the fence flow, in comparison to that experienced across the much thicker turbulent boundary layer of Farabee and Casarella (1986). Considering that the stronger

the shear ($\frac{du}{dy}$) the higher the turbulent energy production term ($-\overline{u'v'}\frac{du}{dy}$), the strong shear in the investigated flow results in more energetic vortices resulting from the roll-up of the shear layer and their associated wall-pressure signature.

3.3. Autocorrelation

In order to analyze the time scales of the flow structures producing the most energetic pressure fluctuation, the autocorrelation of p′ time records was evaluated. The autocorrelation, $R_{p'p'}$, is defined as:

$$R_{p'p'}(\tau, x) = \frac{\overline{p'(x,t)\,p'(x,t-\tau)}}{(p'_{rms}(x))^2} \tag{3.1}$$

where the overbar denotes time averaging and τ is a time delay. The discrete form of equation (3.1) that is implemented in the processing of the discrete-time data is given by:

$$R_{p'p'}(m, x) = \frac{N}{N-|m|}\frac{\sum_{n=0}^{N-m-1} p'(x,n)\,p'(x,n-m)}{\sum_{n=0}^{N} p'^2(x)} \tag{3.2}$$

where N is the total number of data points in the time series and m is the time delay in data samples. The corresponding time delay in seconds is estimated from $\tau = m/f_s$, where f_s is the sampling frequency in samples/sec. To calculate the autocorrelation, each pressure data series, is split into records of 4096 samples each. Since $N = 2^{23} = 8{,}388{,}608$ and $2^{20} = 1{,}048{,}576$ samples for Re = 7600 and 15700, respectively, 2048 and 256 data records are obtained for the low and high Reynolds numbers, respectively. The autocorrelation is finally calculated by averaging the inverse Fast Fourier Transforms (FFT) of the product of the FFT and its conjugate for all records.

Figure 3.4 shows the autocorrelation coefficient ($R_{p'p'}$) plotted versus the non-dimensional time delay ($\tau U_\infty/X_r$) for the two Reynolds numbers examined here at five sparse locations covering the streamwise range of the measurements: ξ = 0.67, 1.11, 1.56, 2.0 and 2.33. Generally speaking, there is very little change in $R_{p'p'}$ for all x positions. This is more evident in the color contour maps in Figure 3.5. These maps represent $R_{p'p'}$ values for all x positions using color contours. The constant-shade contours are almost parallel to the τ axis, revealing a practically "frozen" auto-correlation function.

In Figure 3.4, a "preferred" time scale corresponding to the negative peak in $R_{p'p'}$ is suggested. This time scale represents a quasi-periodic disturbance with a period of $\frac{\tau U_\infty}{X_r} \approx 1.3$ (peak-to-peak time delay). The dominance of this disturbance decays somewhat with increasing ξ. This is evident from the small decay in the largest negative $R_{p'p'}$ value with downstream distance. On the other hand, Figure 3.6 depicts a plot enlarging the region around the autocorrelation peak for the lower Reynolds number and all five x locations. The figure shows an increasing curvature of the auto-correlation at zero time delay with increasing ξ, which implies a decrease in the Taylor microscale. This suggests that the smaller scale turbulence is increasingly contributing to the wall-pressure fluctuation with increasing downstream distance from X_r. Finally, it is noted here that $R_{p'p'}$ results seem to be affected very little by the Reynolds number (at least for the small Re range covered here).

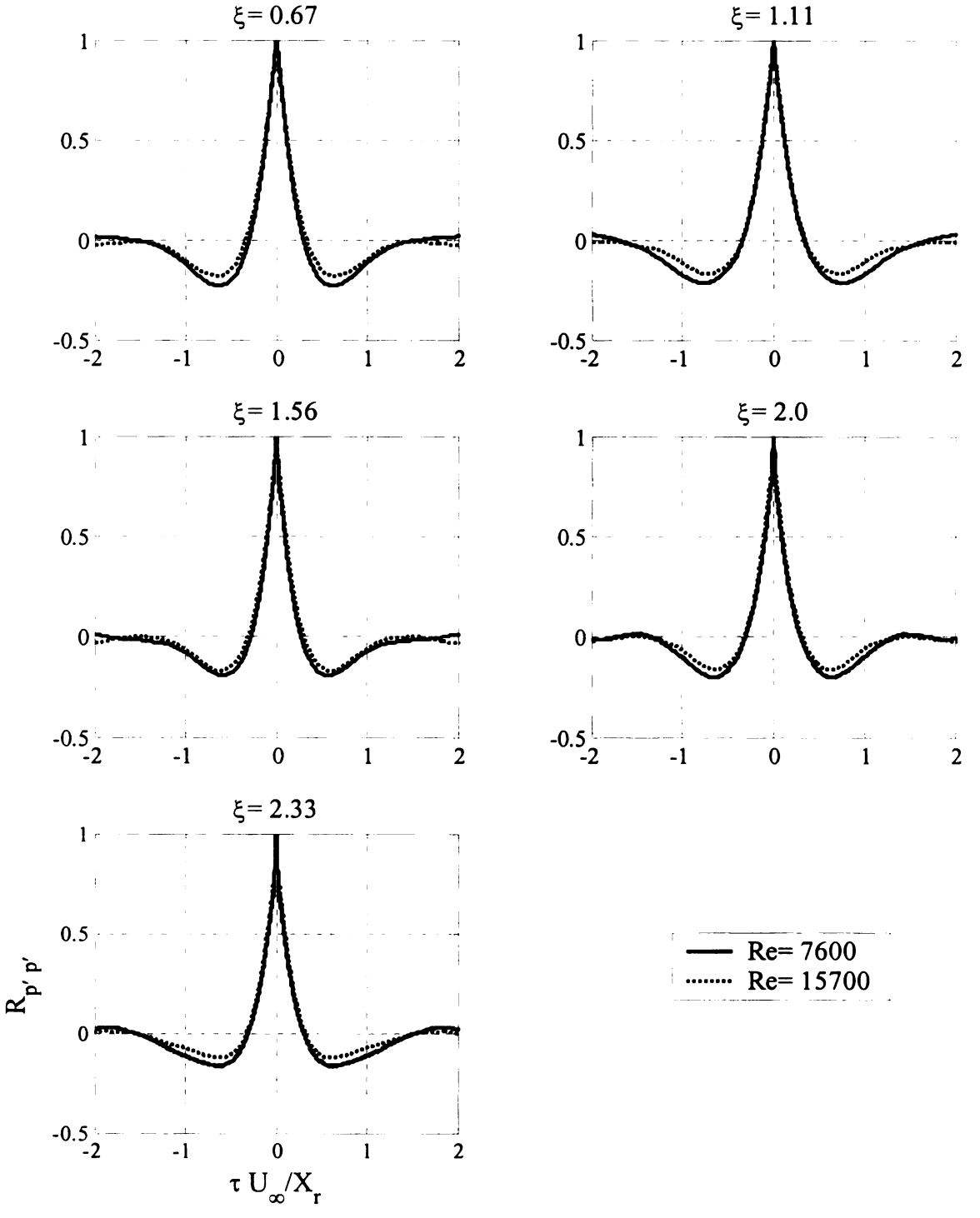

Figure 3.4. Autocorrelation coefficient at five different streamwise locations downstream of the reattachment region for Re = 7600 and 15700

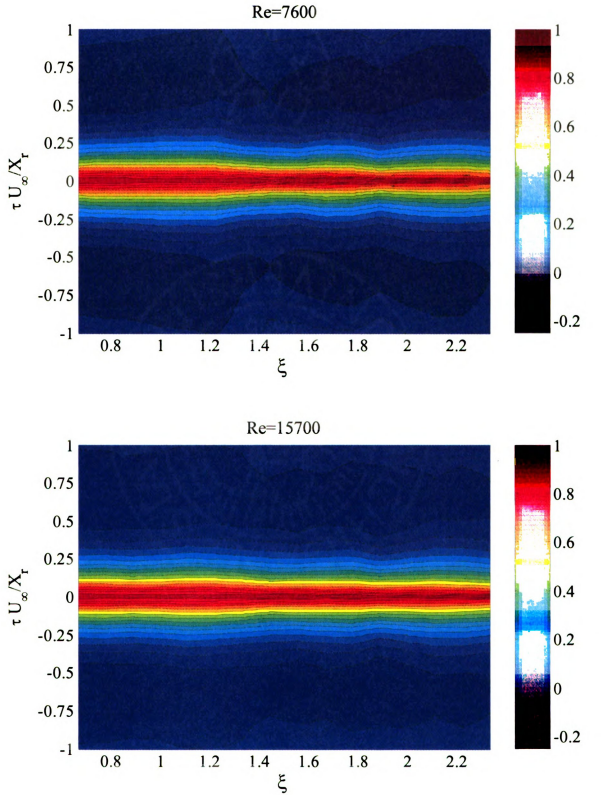

Figure 3.5. Contour maps of the autocorrelation coefficient for all 16 microphones and the two Reynolds numbers; Re = 7600 and 15700

Figure 3.7 depicts the color contour map of the autocorrelation coefficient for the flow upstream and downstream of reattachment. The results show combination of those from the separating/reattaching flow region obtained by Hudy *et al.* (2003), $\xi < 0.3$, at Re = 8000, and the present results. The map shows that the auto correlation width, and hence the dominant time scale of the wall-pressure-generating structures, remain practically unchanged with increasing x downstream of $\xi \approx -0.5$. This suggests that the flow structures dominating p' generation within the development zone trace their origin upstream to the middle of the separation bubble: an observation that is consistent with the idea proposed earlier that the vortices originating in the separating shear layer do in fact dominate the wall-pressure signature in the non-equilibrium boundary layer within the streamwise extent investigated here. The persistence of the shear-layer vortices downstream of reattachment has been reported by Bradshaw and Wong (1972), Farabee and Casarella (1986) and Ruderich and Fernholz (1986).

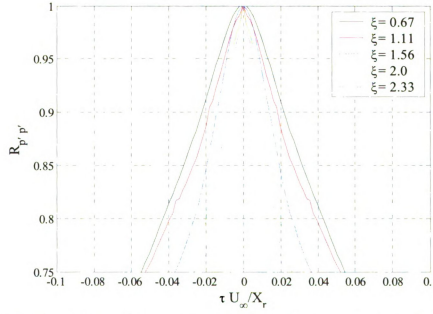

Figure 3.6. A comparison of the auto-correlation results at zero time delay and five different streamwise locations downstream of the reattachment region for Re = 7600

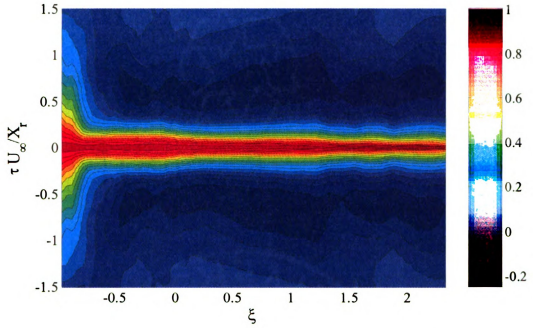

Figure 3.7. A full contour map of the p' autocorrelation coefficient for the separating/ reattaching (Hudy *et al.* 2003) and the present recovering flows

Upstream of $\xi = -0.5$, the dominant p' disturbances posses a substantially larger time scale, as indicated by the significantly larger width of the auto-correlation. In addition to Hudy *et al.* (2003), the larger-time-scale or lower-frequency has been reported in different investigations and attributed to shear-layer flapping; e.g., Castro and Haque (1987), Farabee and Casarella (1986) and Lee and Sung (2002); see Chapter 1.

3.4. Power Spectra

The wall-pressure power spectrum, $\Phi_{p'p'}$, is used for characterizing the frequency content of the pressure signature at the wall. $\Phi_{p'p'}$ is calculated by multiplying the FFT of the wall-pressure signal by its complex conjugate and then dividing the product by the square of the number of samples in the spectrum. To reduce the random uncertainty error, $\Phi_{p'p'}$ is calculated as the average of the power spectra of individual data records obtained

from partitioning the pressure time series. Each record contained 4096 samples, resulting in a spectral resolution of 12.2 Hz. The total number of records was 2048 and 256, resulting in random uncertainty error of 2.2% and 6.3%, for the low and high Reynolds numbers, respectively. The specific equation that is used to calculate $\Phi_{p'p'}$:

$$\Phi_{p'p'}(f) = \left[\frac{1}{N_j} \left(\sum_{j=1}^{N_j} P_j(f) P_j^*(f) \right) \right] \frac{1}{N^2} \qquad (3.3)$$

where P and P^* are the FFT of the wall-pressure data record and its complex conjugate, respectively, f is the associated frequency, f_s is the sampling frequency, N is the total number of samples in each record, N_j is the total number of records, and j is the record index.

Non-dimensional power spectra for the low and high Reynolds numbers, at the same five locations of the autocorrelation results in Figure 3.4, are plotted in two different forms in Figures 3.8 and 3.9, respectively. The top graph in both figures depicts the non-dimensional power spectrum of the wall-pressure, β (where $\beta = \Phi_{p'p'}/(1/2\ \rho\ U_\infty^2)^2$), versus the non-dimensional frequency ($f\ X_r/U_\infty$) using logarithmic scale for both the ordinate and abscissa. For both Reynolds numbers, the top spectrum shows concentration of the pressure fluctuations at low frequency as depicted from the broad spectral peak close to $\frac{f\ X_r}{U_\infty} = 0.7$. This frequency value is consistent with that documented in the literature to correspond to the passage of the vortical structures generated in the separated shear layer upstream of reattachment. For example, the top graph in Figure 3.8 shows a comparison between the spectrum of the present data and

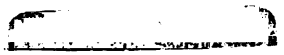

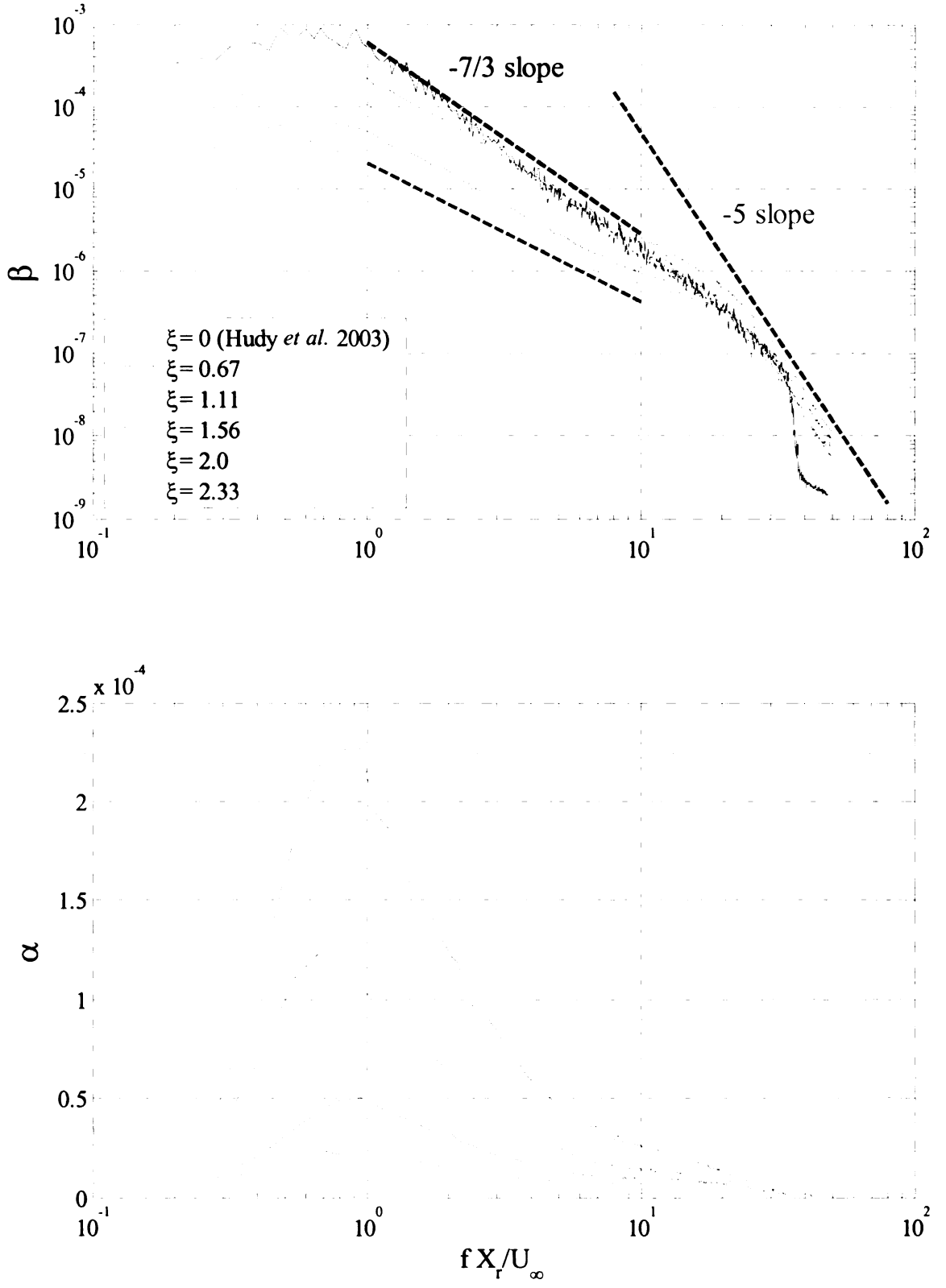

Figure 3.8. Spectra of the wall-pressure fluctuation for Re = 7600: logarithmic (top) and semi-logarithmic (bottom) plots

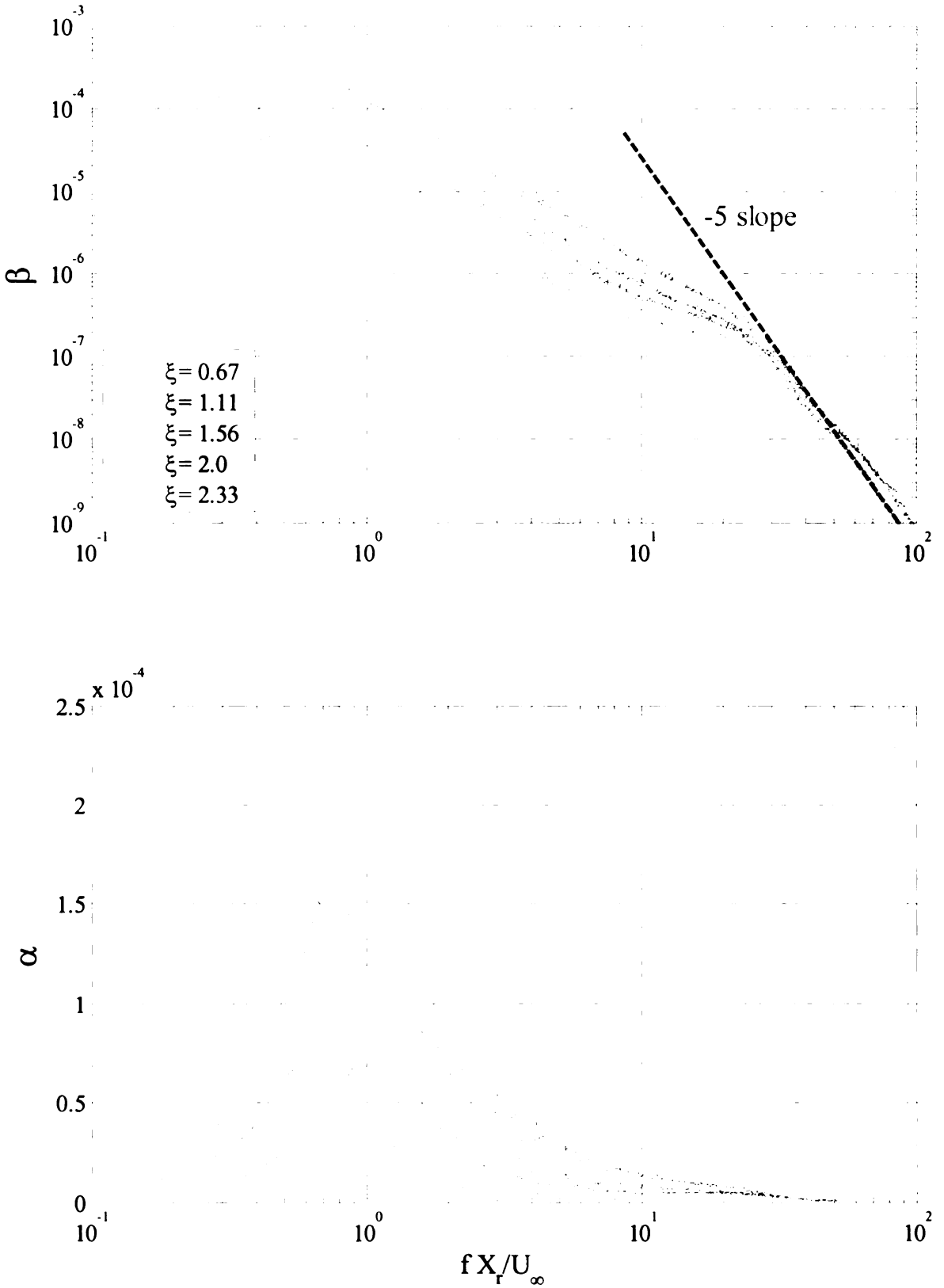

Figure 3.9. Spectra of the wall-pressure fluctuation for Re = 15700: logarithmic (top) and semi-logarithmic (bottom) plots

that of Hudy *et al.* (2003) at reattachment. The comparison shows that the pressure-fluctuation-peak frequency found at reattachment is similar to that found farther downstream beneath the redeveloping boundary layer, which is consistent with the auto-correlation results discussed earlier. Similar values of the dimensionless frequency of the wall-pressure spectral peak were also reported by a number of studies focused on the separation/reattachment zone e.g., Cherry *et al.* (1984), Farabee and Casarella (1986) and Lee and Sung (2001).

As the vortices are advected downstream by the mean flow, they appear to decay as evident from the attenuation in the spectrum peak with increasing ξ. In contrast, the spectral level at the high-frequency end is maintained by the smaller-scale turbulence. Blake (1986) showed that the high-frequency end of the wall-pressure spectrum beneath turbulent boundary layers is characterized by a slope of -5 on a log-log plot. The slope of -5 (within approximately 5% uncertainty) is also found here at the high-frequency end of the spectra shown in the top plot of Figures 3.8 and 3.9, respectively. Based on Blake's analysis, the flow structures responsible for the -5 spectral region are those residing in the buffer layer of a fully developed turbulent boundary layer. Thus, it is possible that the existence of a -5 region in the spectra measured here is a manifestation of the redevelopment of the inner region of the boundary layer downstream of reattachment; i.e., that associated with the sub-boundary layer.

On the other hand, George *et al.* (1984) found that the turbulent-turbulent (TT) source terms of pressure result in the establishment of a power-low-type spectral characteristics of p' with exponent of -7/3; i.e., corresponding to a frequency range with slope of -7/3 on a log-log plot of the spectrum. The top graph in both Figures 3.8 and 3.9

depict that the slope of the wall-pressure spectra is slightly shallower than -7/3 for $1 < \frac{f X_r}{U_\infty} < 10$ beneath the redeveloping boundary layer. However, the wall-pressure spectrum of Hudy *et al.* (2003) at reattachment does posses a slope of -7/3 within the same range of frequencies. Furthermore, Lee and Sung (2001) observed a slope of -7/3 in the wall-pressure spectra near reattachment, and a shallower slope downstream of reattachment ($\xi \approx 0.35$). Thus, it appears that within the separation/reattachment zone, the wall-pressure signature reflects spectral characteristics similar to those found in a free-shear layer. As the shear layer reattaches, and the vortical structures continue to decay with increasing x, these characteristics gradually change, ultimately disappearing and giving way to boundary-layer-like characteristics as x approaches infinity.

The bottom graph in both Figures 3.8 and 3.9 shows a plot of the spectral information plotted with the ordinate α represented on linear scale ($\alpha = f \beta X_r / U_\infty$). The rationale for plotting the spectra in this manner may be seen when integrating the spectrum to obtain the fluctuating wall-pressure energy:

$$\overline{p'^2} = \int_0^\infty \Phi_{p'p'}\, df = \int_0^\infty f\, \Phi_{p'p'}\, d[\log(f)] \qquad (3.4)$$

Equation (3.4) shows that when using a logarithmic frequency axis, the *geometrical* area under the spectrum curve corresponds to the pressure fluctuations energy only if $\Phi_{p'p'}$ is multiplied by f and plotted on a linear scale. The corresponding non-dimensional quantity is then α instead of β. The abscissa still represents the non-dimensional frequency $\frac{f X_r}{U_\infty}$. The figures confirm that the maximum contribution to p′ occurs within a non-dimensional frequency band centered around 0.7-0.9, which corresponds to the

passage frequency of the separated shear layer vortices obtained in previous literature within the separation/reattachment zone as discussed above. The center of this range, $fX_r/U_\infty = 0.8$, corresponds to a non-dimensional time scale of 1.25, which agrees quite well with the dominant time scale of 1.3 identified from the auto-correlation results earlier. Moreover, visual extrapolation of the data towards lower frequencies than those shown in the plot suggests that only very small fraction of the overall p' energy is not captured because of the low cut-off frequency of the microphones (20 Hz).

The semi-log plots also verify the growth of the boundary-layer fractional contribution to p' energy. This may be examined by considering the ratio of the area under the spectrum curve at high frequencies to that at low frequencies $(p'_h/p'_l)^2$. This ratio is estimated by splitting the spectrum of the wall-pressure fluctuation into two portions. One is for low frequencies (due to the large vortical structures originating in the separated shear layer) and the second is for boundary-layer contribution at high frequencies (or small turbulent eddies). This idea of the p' spectrum beneath the non-equilibrium flow being a composite of two spectra separated in frequency, one associated with the outer-shear layer and the other with the sub-boundary layer, may be examined further in Figure 3.10. The figure depicts a comparison of typical p' spectra in separating/reattaching (Hudy *et al.* 2003) and equilibrium boundary layer (Gravante *et al.* 1995) flows. To superpose the spectrum from Gravante et al. (1995) and the present spectrum at $\xi = 2.33$ on the same plot, the start of the -5 region of the two spectra were made to overlap[3]. On the other hand, the spectrum of Hudy *et al.* (2003) was re-scaled

[3] As a side note: the equilibrium-boundary-layer literature shows the -5 region to start at $f\nu/u_\tau^2 \approx 0.13$, where ν is the kinematic viscosity and u_τ is the friction velocity. Using this value suggests that u_τ for the current flow is 0.5 m/s

such that its peak coincides with the present spectrum to facilitate comparison of the spectral shapes.

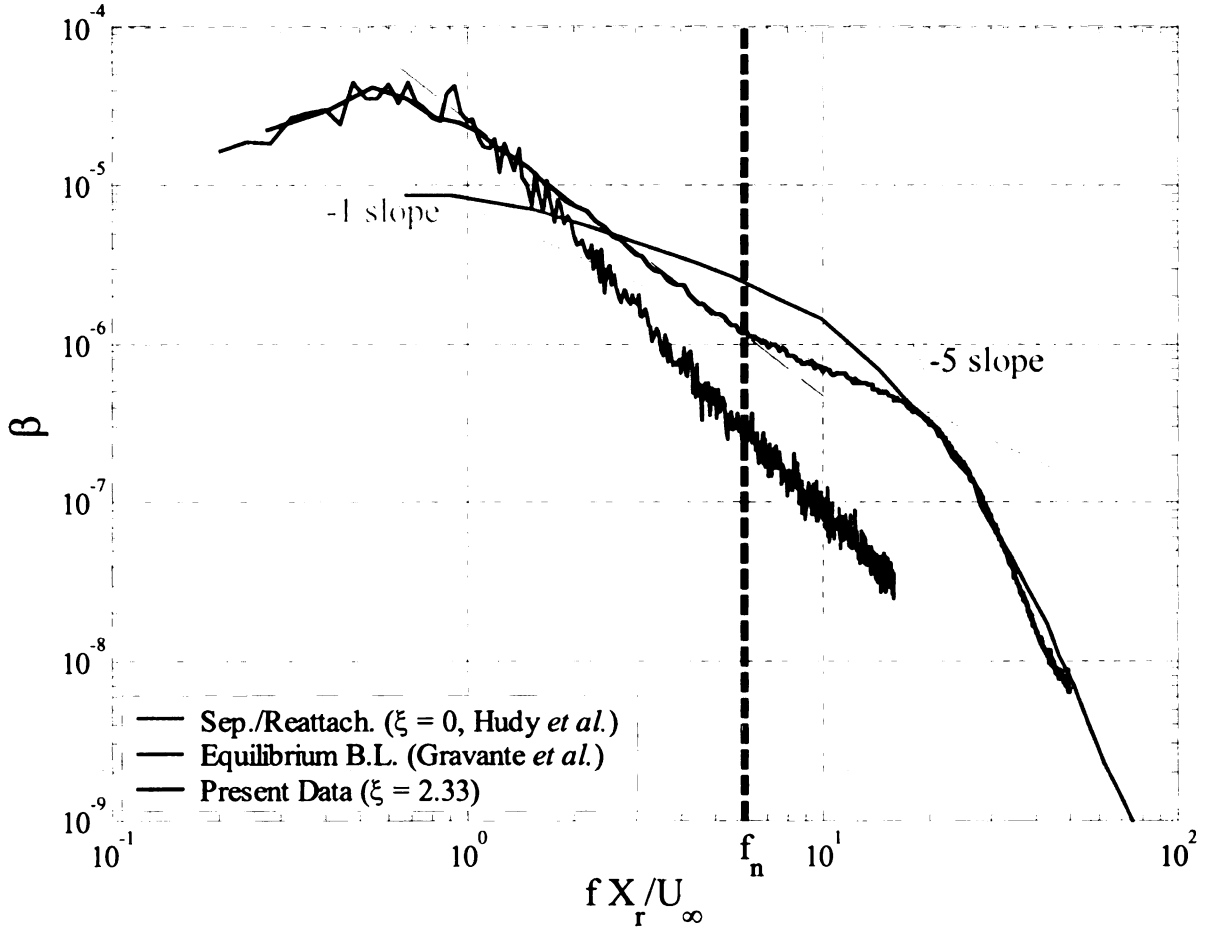

Figure 3.10. Definition of the frequency used in the splitting procedure of p′ spectrum

Based on the comparison in Figure 3.10, the splitting of the spectral energy into out-shear-layer and sub-boundary-layer components was based on the frequency at which the spectrum changes its slope, which is indicated by f_n in Figure 3.10. The choice of f_n is somewhat heuristic since the demarcation between the two frequency ranges is likely to be not sharply defined, and one would expect a gradual switch from one spectrum to the other with the middle range of frequencies receiving contribution from both the smallest scales of the outer-shear layer and the largest of the sub-boundary layer.

However, f_n does coincide with the point at which the spectrum slope switches from the value typical of the middle frequency range in turbulent boundary layers (≈ -1, see Blake, 1986) to a more negative value that has never been observed in boundary layers at low frequencies.

The streamwise variation of the ratio $(p'_h/p'_l)^2$ is provided in Figure 3.11 for the two Reynolds numbers examined here. The results verify that the boundary layer contribution to the wall-pressure fluctuation becomes increasingly important with increasing x. Moreover, Figure 3.11 shows that the initial contribution of the small-scale turbulence to p′ energy increases as Reynolds number increases, which is consistent with known turbulence physics. Note that the two solid curves in the figure are plotted to aid in visualizing the trend of the data.

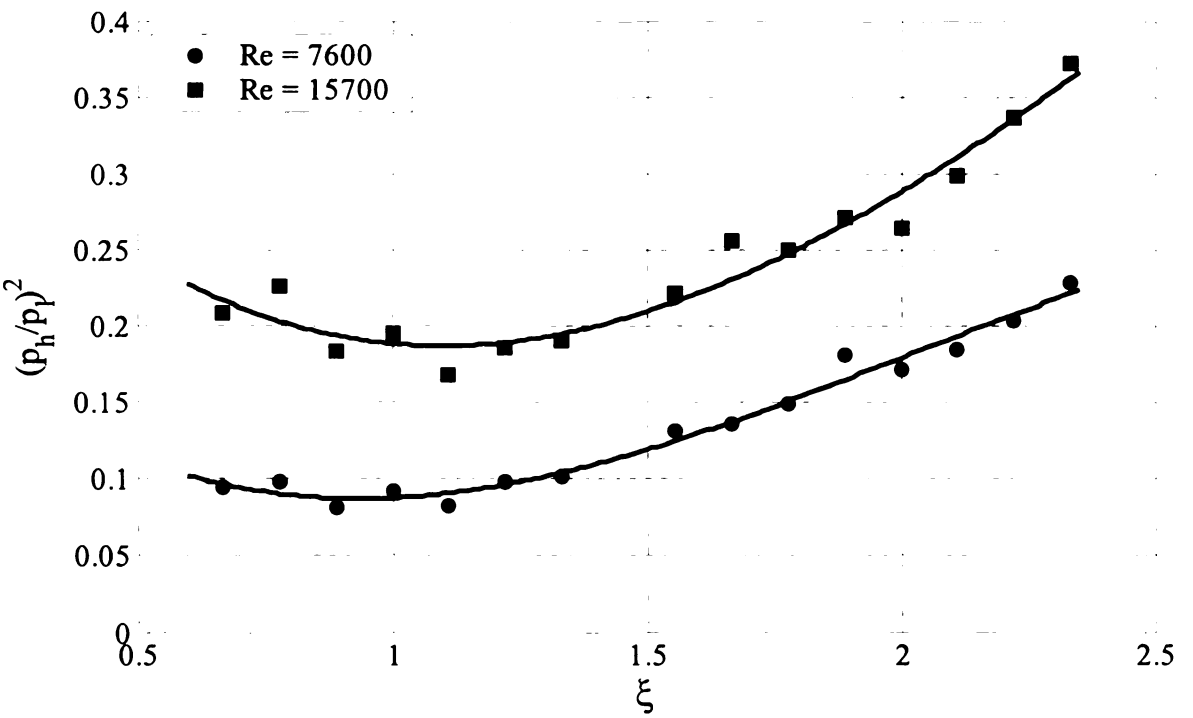

Figure 3.11. The ratio between high- and low-frequency pressure fluctuations energy

3.5. Cross Correlation

The cross-correlation coefficient ($C_{p'p'}$) is defined as:

$$C_{p'p'} = \frac{\overline{p'(x_o,t)\,p'(x_i,t-\tau)}}{p'_{o,\,rms}\,p'_{i,\,rms}} \tag{3.5}$$

where subscript "o" refers to a reference microphone location (ξ = 0.67), subscript "i" refers to a variable microphone location, the overbar denotes time averaging and τ is the time delay. The discrete form of equation (3.5) that is used to calculate $C_{p'p'}$ from the computer-sampled time series is given by:

$$C_{p'p'}(m, x_i; x_o) = \frac{N}{N-|m|} \frac{\sum_{n=0}^{N-m-1} p'(x_o,n)\,p'(x_i,n-m)}{\sqrt{\sum_{0}^{N-1} p'^2(x_o)}\ \sqrt{\sum_{0}^{N-1} p'^2(x_i)}} \tag{3.6}$$

where N is the total number of samples and m is the time delay between the two pressure time series in data samples. Similar to the calculation of $R_{p'p'}$, $C_{p'p'}$ is calculated as the inverse FFT of the cross-spectrum of the two wall-pressure signals. The calculations include the same length and number of records as those used with the autocorrelation calculation in section 3.3. Unlike the autocorrelation where the peak correlation is found at zero time delay, the cross-correlation peak typically exists at some time delay corresponding to the duration needed for a given wall-pressure signature to travel from the reference to the variable microphone. Thus, the cross correlation provides valuable information concerning the convection characteristics of the dominant wall-pressure-generating motion.

The cross-correlation, $C_{p'p'}$, between the time series obtained from five sparsely-positioned microphones (ξ = 0.67, 1.11, 1.56, 2.0 and 2.33) and that captured by the most

upstream microphone (ξ = 0.67) for Reynolds numbers of 7600 and 15700, are plotted in Figure 3.12. In the figure, the cross-correlation coefficient $C_{p'p'}$ is the ordinate and $\frac{\tau U_\infty}{X_r}$ is the abscissa. Note that the results at ξ = 0.67 represent the autocorrelation of the microphone at that position. The five plots in Figure 3.12 reflect the streamwise convective nature of the dominant wall-pressure-generating motion. This is seen from the shift in the time delay corresponding to maximum positive (or negative) correlation with increasing ξ. More specifically, as the x location of the variable sensor increases, the correlation peak is located at an increasing negative time delay (i.e., increasing time advance). This corresponds to a disturbance whose signature reaches sensors that are farther downstream later in time. It is also noteworthy that the dominant time scale (i.e., the period between the two negative $C_{p'p'}$ peaks) of the convective quasi-periodic disturbance depicted in Figure 3.12 is the same as that observed earlier in Figure 3.4 in the autocorrelation plot.

Figure 3.13 provides a fuller picture of the convection motion of the dominant vortical structures for the two different Reynolds numbers. The figure depicts plots of $C_{p'p'}$ for all 16 microphones where the ordinate and abscissa are exactly as those of Figure 3.12. The figure shows that the $C_{p'p'}$ peak shifts by about 0.15 on the non-dimensional time-scale axis between each two consecutive microphones. This time shift is estimated to be almost the same for both Reynolds numbers. To estimate the corresponding convection velocity (U_c), Figure 3.14 depicts a plot of the dimensionless time shift of the peak of $C_{p'p'}$ ($\frac{\tau_p U_\infty}{X_r}$) versus the dimensionless distance between the corresponding

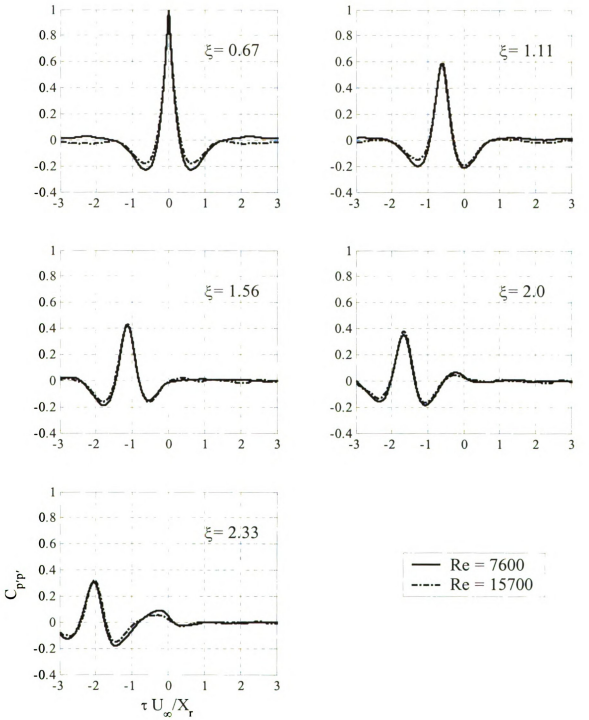

Figure 3.12. Cross-correlation results at five different locations for Re = 7600 and 15700

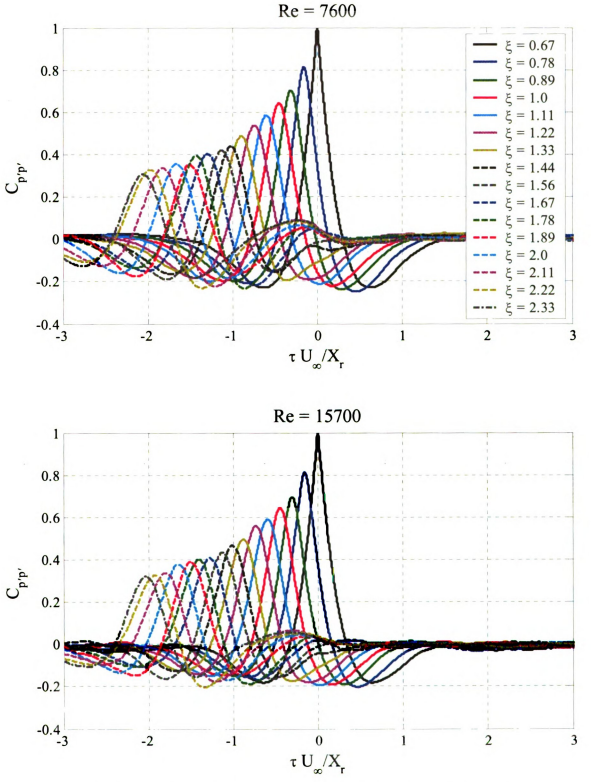

Figure 3.13. Cross-correlation results for all 16 microphones and Re = 7600 (top); and 15700 (bottom)

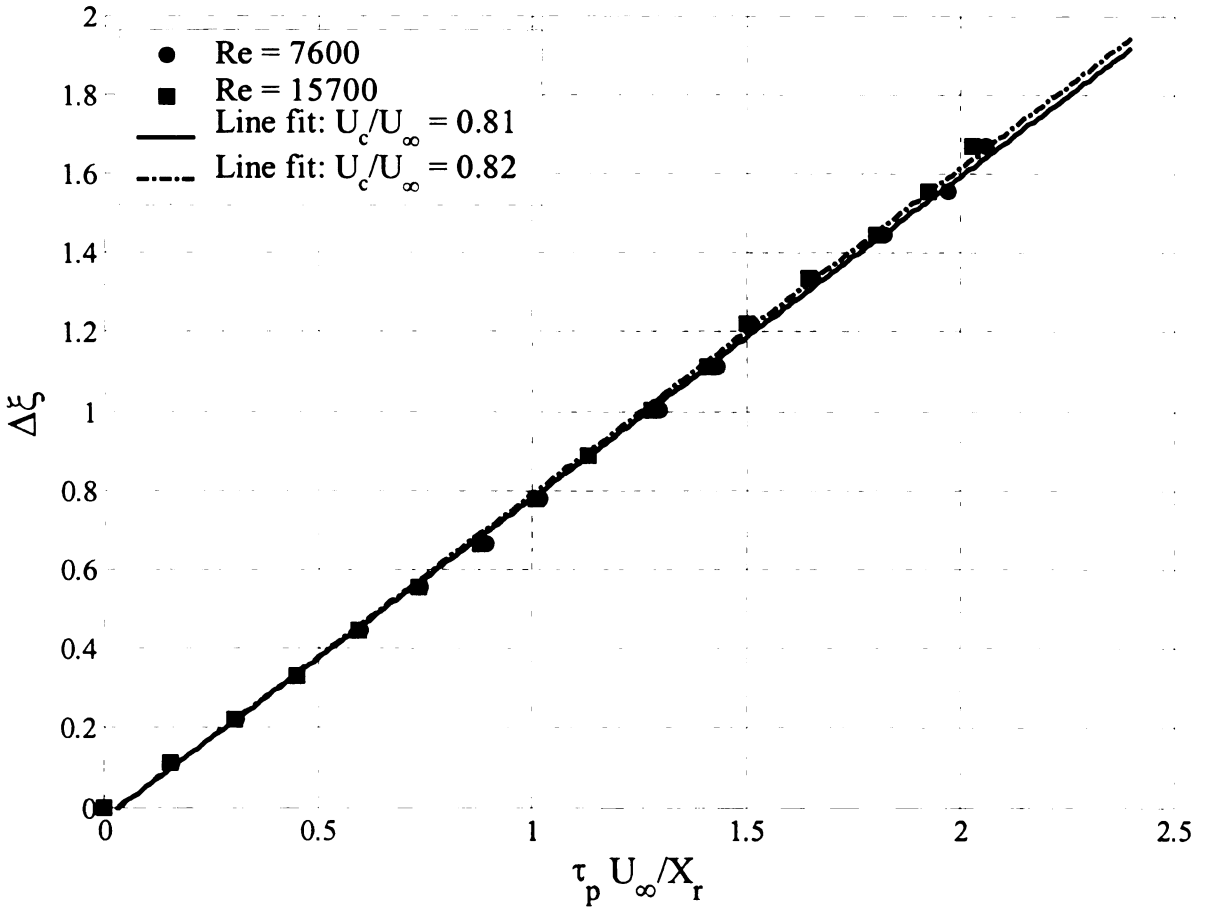

Figure 3.14. Plot for extraction of the convection velocity for the two Reynolds numbers of 7600 and 15700

microphone and the reference (the most upstream) microphone, $\Delta\xi$. In this manner, the *local* U_c/U_∞ value is given by the slope of the $\Delta\xi$ versus $\frac{\tau_p U_\infty}{X_r}$ curve, and an overall average convection velocity may be obtained through a linear fit to the data over the whole range. The results depict a local slope that seems invariant with $\Delta\xi$, which shows that U_c/U_∞ is constant along the whole x range and equal to 0.81 and 0.82 for Re = 7600 and 15700, respectively. Those velocities are higher than the velocities reported in the literature within the upstream separation/reattachment region. For example, Cherry *et al.* (1984) reported convection speeds of approximately $0.5U_\infty$ and

$0.63U_\infty$ from the pressure-pressure and -velocity cross-correlation and, recently, Hudy *et al.* (2003) and Lee and Sung (2002) reported a mean convection velocity of $0.6U_\infty$ in their separating/reattaching flows. This indicates that the convection speed of the vortices originating in the separating shear layer increases as they travel from the separation to the redevelopment zone. These conclusions are qualitatively consistent with those of Farabee and Casarella (1986). However, quantitatively, Farabee and Casarella showed that the convection velocity at similar locations downstream of the reattachment point was 0.6–0.7 U_∞. The reason for the higher value found in the current study is elaborated on in section 4.2.2.

The cross-correlation information of all 16 microphones are also plotted in color contour maps in Figures 3.15 and 3.16. The map yields the cross- correlation of all 16 microphones with respect to the most upstream microphone ($\xi = 0.67$) for Re = 7600 and 15700, respectively. The maps show an inclined positive-correlation lobe with a peak value at zero time-shift at the location of the reference microphone. The inclination of the main lobe in this spatiotemporal plot provides another representation of the convection of the vortical structures downstream of the reattachment region. In fact, the slope of the broken line in Figure 3.15, which is aligned with the center of the positive-correlation lobe, represents the ratio U_c/U_∞. This slope value is found to be approximately 0.81, in agreement with the earlier results for Re = 7600. The results for the higher Reynolds number of 15700, displayed in Figure 3.16, yield approximately the same ratio of $U_c/U_\infty = 0.81$.

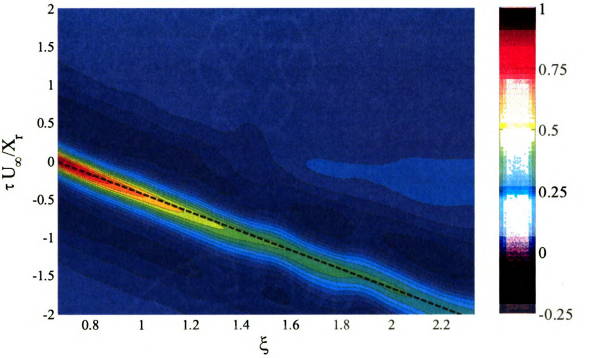

Figure 3.15. Contour map of the cross-correlation coefficient for all 16 microphones and Re = 7600

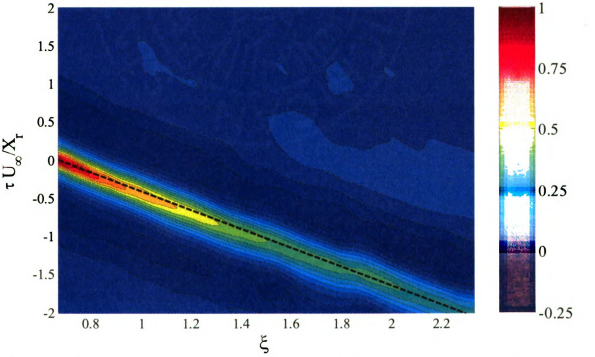

Figure 3.16. Contour map of the cross-correlation coefficient for all 16 microphones and Re = 15700

3.6. Wavenumber-Frequency Spectrum

The wavenumber-frequency (k_x-f) spectrum of the wall-pressure data was calculated for Re = 7600. The spectrum was obtained by calculating the two-dimensional Fourier transform of the spatiotemporal wall-pressure data, p'(x,t), of all 16 microphones. 1048576 samples of wall-pressure were acquired from each microphone at a sampling frequency of 6250 samples/sec. Therefore, the wall-pressure data set could be represented by a two dimensional array of 1048576×16 in size. This 2D array was then broken up into 2048 sub-arrays (records) of 512×16 in size, which produced a random uncertainty error of 2.2% in the spectral estimation. The wavenumber-frequency spectrum of each record was calculated by multiplying the two-dimensional FFT of each record by its complex conjugate, then averaging the spectra of all records. The 2D FFT operation is accomplished by doing a one-dimensional FFT transformation of the columns of the 2D record, to transform time into frequency, followed by another 1D FFT operation of the rows, to transform x to k_x. The resulting resolution of the dimensionless frequency and wavenumber were 0.14 and 0.6, respectively. To obtain smoother contour plots of the outcome, the spectrum was interpolated along the wavenumber axis by zero-padding each record in the x direction to be 512×64 in size. Thus, the increment in the dimensionless wavenumber became 0.15.

The physical interpretation of the wavenumber-frequency spectrum may be clarified by considering propagating harmonic waves. Since the propagation velocity (U_c) of any harmonic wave is the product of its frequency and wavelength ($1/k_x$), then the slope, or f/k_x, of a line connecting the coordinates of the spectrum peak corresponding to the wave to the origin of the k_x-f spectrum equals U_c. Accordingly, if the disturbance

being characterized contains waves with different frequencies and wavenumbers, but propagate with the same speed, the disturbance energy will be distributed along a straight line emanating from the origin in the k_x-f plane, Wills (1964).

Figure 3.17 depicts a color contour map of the k_x-f spectrum. The abscissa represents the dimensionless wavenumber ($k_x X_r$) while the ordinate represents the dimensionless frequency ($\frac{f X_r}{U_\infty}$). Also, the slope of a straight line drawn on the map from the origin gives the ratio between the convection velocity and the freestream velocity, $\frac{U_c}{U_\infty}$.

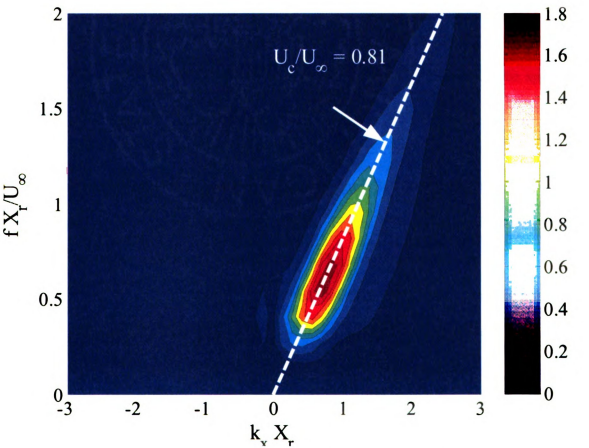

Figure 3.17. Wavenumber-frequency spectrum for Re = 7600

Figure 3.17 depicts an inclined ridge of peaks where most of the fluctuating pressure energy is concentrated. The highest point of the ridge corresponds to a dimensionless frequency of about 0.6-0.7 and a dimensionless wavenumber of 0.8-0.9. Furthermore, the broken line plotted in the figure represents the peak locus of the spectrum ridge. This line passes through the origin indicating that all dominant wall pressure disturbances propagate downstream with the same convection velocity regardless of scale; i.e., the wall-pressure modes are not dispersive. This observation along with the narrowness of the ridge suggests that a good representation of the frequency spectra could be obtained from the wavenumber spectra by using U_c to transform x to t. Thus, it appears that Taylor's hypothesis of frozen turbulence may be used acceptably to obtain spatial statistics from temporal ones in the late stages of the developing boundary layer ($\xi > 2$), where the RMS and spectra change very little and the statistics reflect a fair degree of homogeneity in the streamwise direction. The specific convection velocity value was found from the slope of the broken line to be 0.81. This agrees quite well with the value estimated from the cross-correlation analysis.

It is interesting to compare the results in Figure 3.17 to similar type of results obtained upstream beneath the separation bubble. Figure 3.18 depicts the wavenumber-frequency spectrum from Hudy *et al.* (2003). The spectrum shows an inclined ridge similar to that in Figure 3.17. However, the peak locus of the ridge in this case does not pass through the origin of the plot. This produces a wavenumber dependent convection velocity, which indicates that the flow structures upstream of reattachment are dispersive; i.e., flow structures of different scales travel with different speeds. Finally, it is also noted that at very low frequencies, Figure 3.18 depicts both upstream and downstream

propagating disturbances. This signature, which is absent in the spectrum obtained beneath the redeveloping boundary layer, was attributed by Hudy *et al.* (2003) to the shear-layer flapping, or expansion/contraction of the separation bubble.

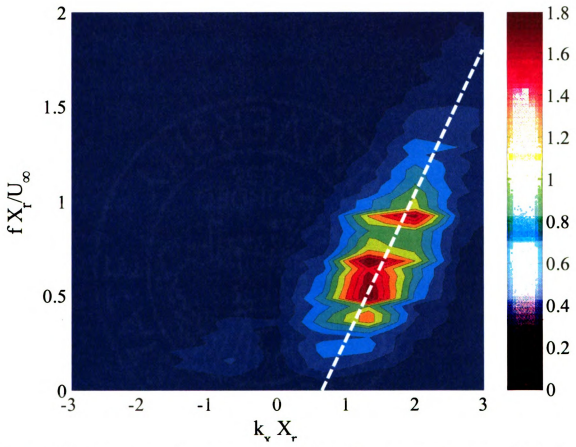

Figure 3.18. Wavenumber-frequency spectrum from the separating/reattaching flow of Hudy *et al.* (2003)

4. VELOCITY-PRESSURE ANALYSIS AND STOCHASTIC ESTIMATION

This chapter presents an analysis and discussion of the results obtained from the simultaneous velocity and pressure data and their usage to stochastically estimate the velocity field from the wall-pressure signature. The chapter has three main sections. The first section provides a presentation of mean, turbulent and spectral characteristics of the velocity measurements at $\xi = 2.05$, while the second one illustrates a scenario, that has been established in the present study of the relation between the wall-pressure and flow structures. Analysis of the stochastic estimation work including its principle and results, may be found in the last section.

4.1. Velocity Characteristics

Here, various characteristics that are derived from the velocity measurements within the non-equilibrium boundary layer are analyzed and compared with the corresponding published results for separating/reattaching, free-shear-layer and equilibrium-boundary-layer flows.

4.1.1. Characteristics of the Boundary-Layer Mean and Turbulent Velocity Profiles

Figure 4.1 depicts the mean streamwise velocity profile obtained from single-hotwire measurements. The profile has been normalized using inner (or viscous) boundary-layer scaling and is compared with the data of Ruderich and Fernholz (1986), Bradshaw and Wong (1972), and Farabee (1986). The abscissa represents the dimensionless height ($y^+ = \frac{y u_\tau}{\nu}$); where y is the hotwire distance above the wall, u_τ is the friction velocity and ν is the kinematic viscosity of air, while the ordinate represents

the dimensionless mean streamwise velocity ($u^+ = u/u_\tau$). The solid line shows the "log-law" of an equilibrium boundary layer. Ruderich and Fernholz (1986) conducted their measurements on a fence-with-splitter-plate model with a fence height of 22 mm and freestream velocity of 9.6 m/s, resulting in an Re of 1.4×10^4. The present data are compared with theirs at ξ = 1.86, which is the most downstream location of their measurements. The thickness and friction velocity of their boundary layer at that location were approximately 130 mm and 0.4 m/s, respectively. Note that the friction velocity of the present measurements (0.64 m/s) was estimated for the best visual agreement between the present mean streamwise velocity profile and that of Ruderich and Fernholz. This is done in order to provide a comparison between the profile shapes. It should also be mentioned that the same u_τ value is used for normalization of the turbulent velocity and Reynolds stress profiles below. On the other hand, Bradshaw and Wong, and Farabee's investigations were of a backward-facing step. The step height, freestream velocity and corresponding Re of Bradshaw and Wong (1972) were 25 mm, 24.5 m/s and 40835 while those of Farabee (1986) were 12.5 mm, 15.3 m/s and 12750, respectively. The friction velocities of the former and latter studies were approximately 1.0 and 0.6 m/s, respectively.

Before proceeding further, it is important to highlight a fundamental distinction between the backward-facing step and the present model, fence-with-splitter-plate. In the case of a backward-facing step, a boundary layer develops over a generally long surface upstream of separation to a laminar or turbulent state. Once the flow separates, a free shear layer forms downstream of the step. For a laminar boundary layer condition, the initial velocity profile is typically that of a Blasius boundary layer at the step and due to

the Kelvin-Helmholtz instability of the flow, vortical structures are created and energized by the mean-velocity gradient of the free shear layer, resulting in the *whole* laminar boundary layer quickly becoming a free shear layer. However, in the case of a separating turbulent boundary layer, the recent study of Morris and Foss (2003) showed that the free shear layer contributing to the Kelvin-Helmholtz instability develops *only* from a thin layer within the inner layer of the boundary layer with no contribution from the outer layer and its large-scale structures. The latter were also found to persist unchanged for a large distance downstream of the separation point, before the much-smaller shear-layer structures grow sufficiently in scale to contaminate the entire width of the separating flow.

Based on the above, it is anticipated that the flow in the separation/reattachment region of a turbulent boundary layer consists of three main layers on top of one another: a recirculation bubble, a free shear layer and the outer layer of the original boundary layer (in order, from bottom to top). Such a three-layer structure may be depicted in the measurements of Bradshaw and Wong (1972), Farabee (1986) and Song and Eaton (2002). Downstream of the reattachment zone, the layers become: the growing sub-boundary layer, the remanence of the free shear layer that contains the vortical structures that were generated in the separating shear layer upstream of reattachment, and the outer layer that contains the large-scale structures of the original boundary layer. It is obvious that, unlike laminar separation, in this case the upstream boundary layer has a direct fingerprint on the characteristics of the turbulence structure downstream of the step.

In the case of the fence-with-splitter-plate, a very thin laminar boundary layer is formed at the point of separation. As a result, downstream of reattachment the recovering boundary layer is expected to consist of two, rather than three, layers: the sub-boundary

layer and the remanence of the separating shear layer; i.e., similar to the case of laminar separation over a back step.

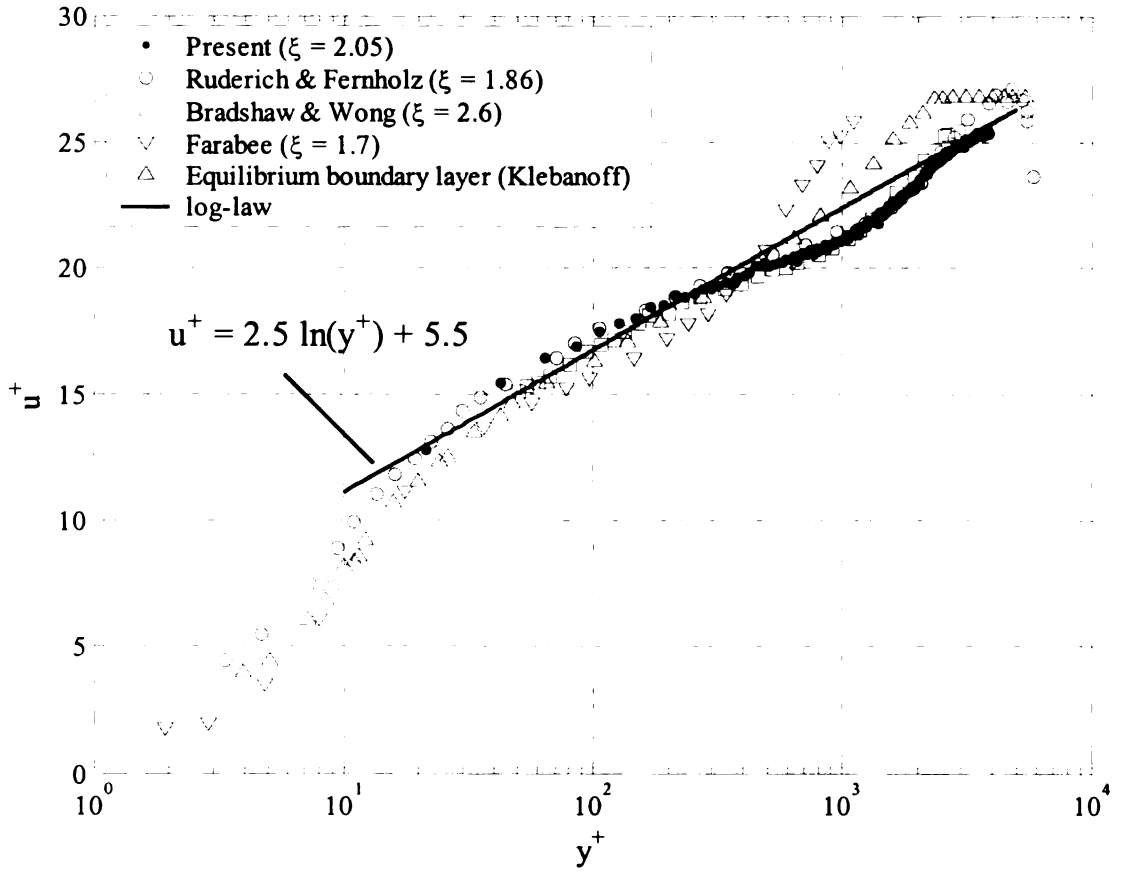

Figure 4.1. Wall scaling of boundary-layer mean-velocity profile

Comparing with the equilibrium boundary layer, the current velocity profile deviates from the log-law and the mean-velocity profile of an equilibrium turbulent boundary layer (Klebanoff 1954) as depicted in Figure 4.1. In particular, the data is seen to overshoot the log-law for $y^+ < 300$ and undershoot it for $y^+ > 300$. This is in agreement with the data of Ruderich and Fernholz (1986), and Bradshaw and Wong (1972), as evident from Figure 4.1. These two studies included velocity measurements at different streamwise locations, and hence they were able to track the redevelopment process of the mean-velocity profile due to the growth of the sub-boundary layer

originating from the new viscous sublayer downstream of reattachment. They showed that the development process continued with a slow build-up of the logarithmic law with increasing x. Initially, closer to reattachment, the velocity profiles undershot the log-law. As x increased, the observed undershoot moved farther away from the wall, with an overshoot region developing closer to the wall, as seen in Figure 4.1. The authors provided two reasons for the observed deviation from the log-law: the rapid change of the turbulence structure near reattachment and the non-proportionality of turbulent length scales to height above the wall.

Although the profile of Farabee (1986) in Figure 4.1, who used a backward-facing step, does not quantitatively agree with the rest of the profiles, it qualitatively behaves in the same way for $y^+ < 300$. In this range, Farabee's mean velocity profile exhibits a viscous-sublayer-like profile near the wall, followed by a log-law undershoot farther away from the wall. For $y^+ > 300$ Farabee's profile significantly deviates from the others both quantitative and qualitatively. The most important difference between Farabee's profile and that of the other studies is that it exhibits the overshoot above the log-law characteristic of the wake region of a fully-developed turbulent boundary layer. The amount of overshoot above the log-law is classically known as the wake strength, Coles (1956). It is clear that the present data along with those from Ruderich and Fernholz and Bradshaw and Wong do not possess such a wake region. A reasonable physical explanation of the disagreement could be related to the fact that in Farabee's study, a fully developed turbulent boundary layer was established at the point of separation, instead of the laminar boundary layer employed in all of the other studies. As reasoned earlier in this section, the flow downstream of separation/reattachment of a fully developed

turbulent boundary layer consists of three layers, and therefore the difference may be attributed to the existence of an outer boundary layer originating from the equilibrium turbulent boundary layer upstream of the step in Farabee's investigation.

Castro and Epik (1998) presented measurements in the flow downstream of the mean reattachment location of the separated flow at the edge of a blunt flat plate. Their results showed that the developing boundary layer downstream of reattachment exhibited the same behavior as that of the present flow. More specifically, Castro and Epik's mean-velocity profile depicted that the log-law behavior was absent immediately downstream of reattachment. However, they observed that the mean-velocity profile started to build up a "logarithmic region" with increase in x through an overshoot and undershoot similar to that of the present mean-velocity profile. Although their results showed that the log-law was established by $\xi \approx 10$, they stated that the turbulence structures did not develop fully even at a streamwise location of $\xi \approx 19$.

Song and Eaton (2002) studied the flow of a fully developed turbulent boundary layer over a backward-facing convex ramp. In spite of the geometrical difference from the canonical separating/reattaching flow models (e.g. backward facing step, forward facing step, etc.), their flow exhibited similar physics. At streamwise location of $\xi \approx 2.0$, similar to that where the present data are acquired, their mean-velocity profile showed a similar redeveloping behavior represented by an overshoot and undershoot of the log-law. Also, because the boundary layer upstream of the ramp was turbulent, the profiles exhibited a wake region in the outer portion of the flow. Furthermore, Song and Eaton's results showed that the flow downstream of reattachment reasonably reached the condition of an equilibrium boundary layer farther downstream at $\xi \approx 9.0$. This suggests

that the current mean-velocity profile represent the state of the boundary layer some 25% or so of the distance required to reach an equilibrium state.

The results in Figure 4.1 are normalized in a manner that is consistent with the boundary-layer component of the "two-layer" structure of the present flow. Another way to normalize the results that reflects the free-shear-layer like flow in the outer portion of the flow would be using classical shear layer normalization. For this purpose, the y location of the shear-layer center needs to be determined. Typically, this location coincides with the position at which the mean velocity is the average of two velocities on the low- and high-speed sides of the shear layer, which corresponds to half of the freestream velocity for a single-stream shear layer. This also coincides with the location where the mean streamwise-velocity gradient, the velocity fluctuations, the Reynolds stress, and therefore the turbulent energy production term are maximal, e.g., see Ho and Huang (1982). In the current flow, the mean streamwise-velocity gradient is maximal at the wall, and hence it can't be used to locate the center of the "free" shear layer. Instead, the position of the maximum shear Reynolds stress ($\overline{u'v'}$) is taken as the outer-shear-layer center. This location also agrees roughly with that of the maximum v_{rms}, as will be seen later. It is also noted here that the peak $\overline{u'v'}$ within the sub-boundary layer may be the strongest across the whole layer. However, because of the size of the X-hotwire used to conduct u and v measurements, it is not possible to capture this region of the flow. Thus, the identified peak is that corresponding to the center of the outer-shear layer.

Figure 4.2 depicts a plot of the mean streamwise-velocity in shear-layer coordinates. The abscissa is $(y-y_{ref})/x$; where y_{ref} is the y location of the Reynolds stress peak (y = 38 mm, or y_{ref}/δ = 0.48). The ordinate is the streamwise mean velocity

normalized by the mean velocity at y_{ref} (u_{ref}), where $u_{ref}/U_\infty = 0.89$. The figure shows the comparison between the present mean profile with that of Ruderich and Fernholz (1986). The two profiles show good agreement in the outer portion of the flow. The agreement reinforces the earlier observation that the free-shear-layer vortical structures still dominate the outer part of the boundary layer.

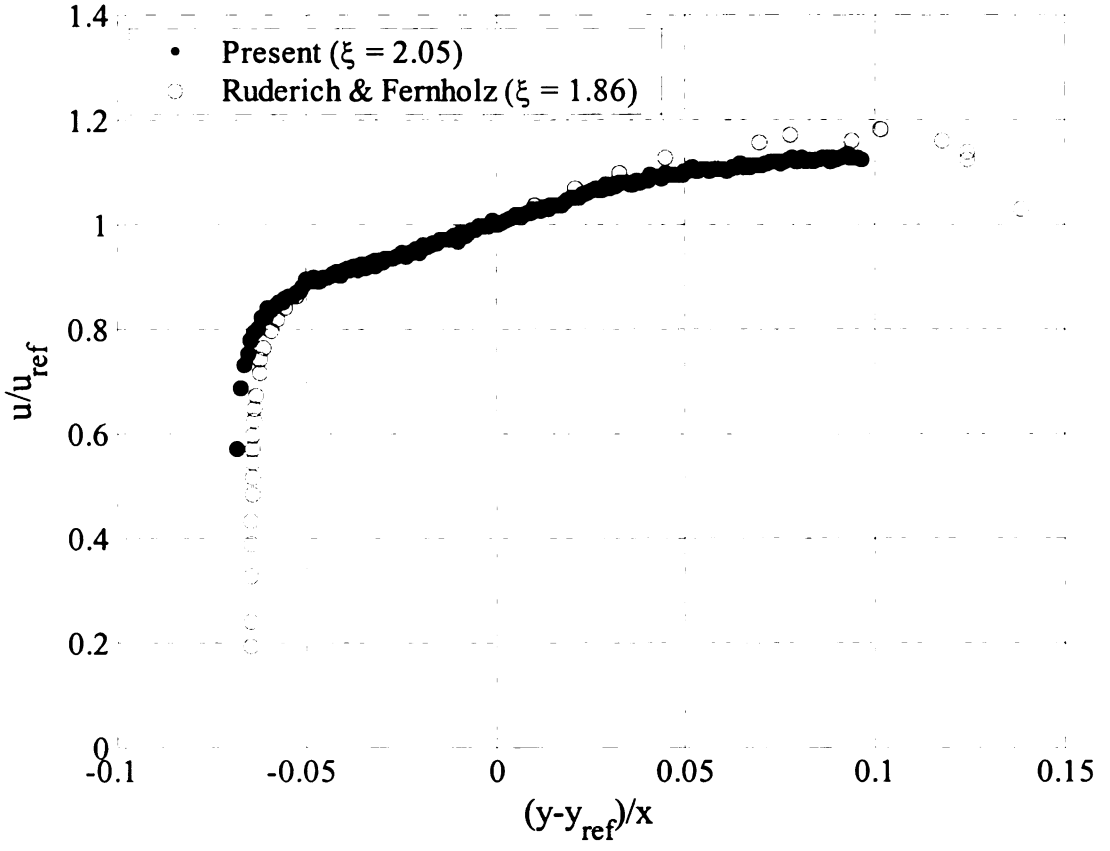

Figure 4.2. Shear-layer scaling of the boundary-layer mean-velocity profile

Figure 4.3 shows the root mean square, RMS, profile of the streamwise velocity fluctuations (u_{rms}) in boundary layer coordinates. The abscissa is y^+ and the ordinate is u_{rms} normalized by the friction velocity. The figure shows a reasonable agreement between the present data and that of Ruderich and Fernholz for $y^+ < 300$. Although the

present data could not resolve the peak of u_{rms} near the wall, they exhibit a rise in u_{rms} with decreasing y^+ for $y^+ < 70$, consistent with the existence of such a peak. Ruderich and Fernholz's results show the peak near the wall to be located in the buffer layer of the sub-boundary layer ($y^+ \approx 10$). The profile also shows a flat region of velocity fluctuation in the range of $70 < y^+ < 1500$ apparently associated with the outer-shear-layer structures.

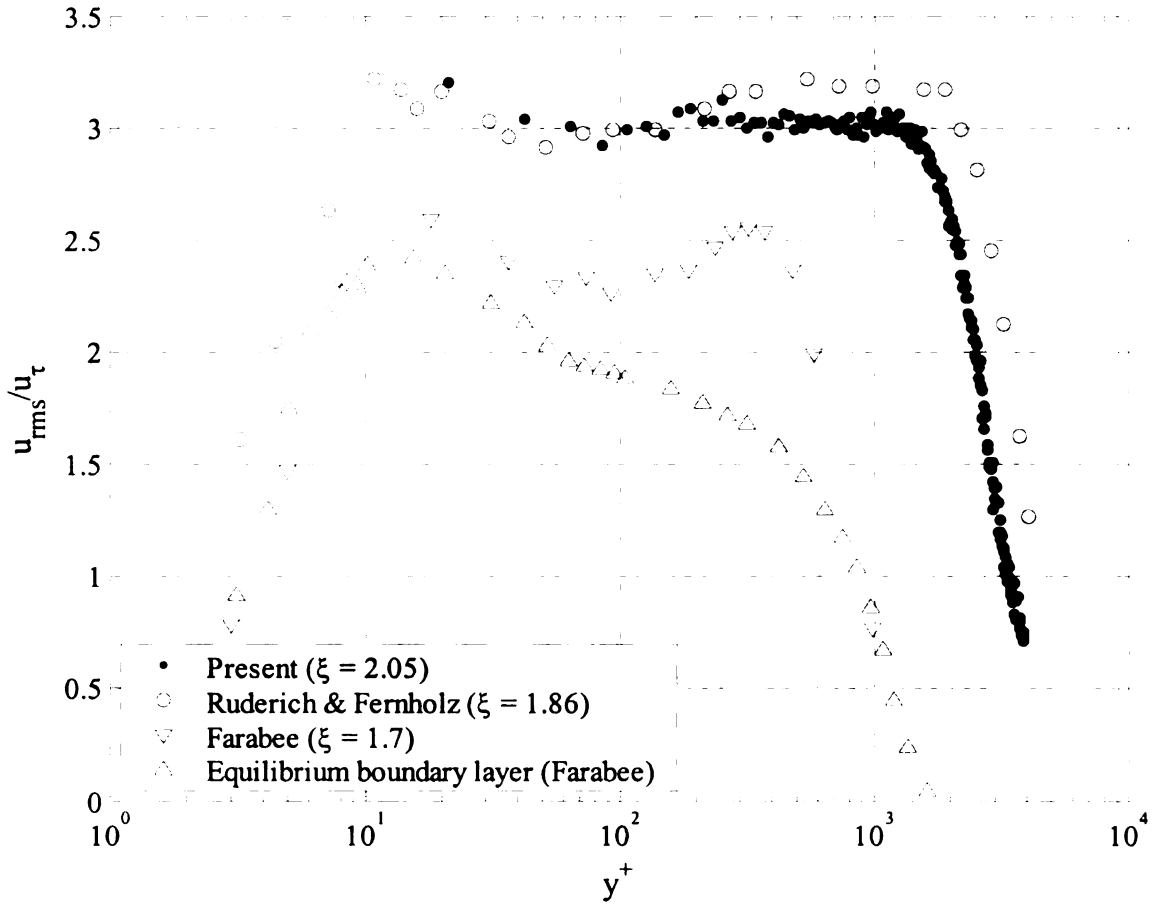

Figure 4.3. Wall scaling of the boundary-layer u_{rms} profile

As discussed above, the present data and that of Ruderich and Fernholz show good quantitative agreement near the wall and disagreement in the outer part of the boundary layer. On the other hand, when including Farabee's data, there is a qualitative agreement between the three data sets in the sense that all results reflect the existence of a

near-wall sub-boundary-layer peak and an away-from-the-wall free-shear-layer peak. The latter is most well defined in Farabee's results because the peak is less broad. This is apparently caused by the narrower extent of the shear layer in the case of Farabee (1986). Moreover, the distance between the near-wall and outer u_{rms} peaks is smaller for Farabee's data: a manifestation of the smaller Reynolds number of that boundary layer in comparison to the other two data sets, where the Reynolds number based on the boundary layer momentum thickness, Re_θ, is 8000, 11284 and 4027 for the present study, Ruderich and Fernholz (1986) and Farabee (1986), respectively.

Finally, although the current data set does not resolve the buffer region of the sub-boundary layer, the data from Ruderich and Fernholz (1986) as well as those from Farabee (1986) do. It is expected that both data sets should collapse given the viscous scaling of the data. However, there is discrepancy between the two data sets with that from Farabee agreeing well with the equilibrium boundary layer. This raises a question concerning the inner-portion of the sub-boundary layer and how quickly it reaches equilibrium conditions downstream of reattachment for the two different flows of Ruderich & Fernholz (1986) and Farabee (1986). Further investigation of this issue is beyond the scope of the current work. Finally, it is useful to note here that both investigations of Ruderich and Fernholz, and Farabee reported the relaxation effect of the flow to an equilibrium boundary layer, showing a decay of the outer peak of u_{rms} with increasing x till the profiles monotonically reach the shape of the canonical boundary layer profile, exhibiting only one peak near the wall.

The data in Figure 4.3 are rescaled and plotted in shear-layer coordinates in Figure 4.4. The abscissa is the same as that in Figure 4.2 and the ordinate represents u_{rms}

normalized by U_∞. The figure shows that all three profiles almost collapse in the outer portion of the flow, above the location of the peak of the Reynolds stress; i.e., the shear-layer center. On the other hand, the present data exhibit good agreement with the data of Ruderich and Fernholz (1986) for all heights but very near the wall ($\frac{(y - y_{ref})}{x} < -0.05$). Moreover, both profiles reveal a region of flat turbulence intensity ($u_{rms}/U_\infty \approx 0.12$) that extends well below the shear-layer center.

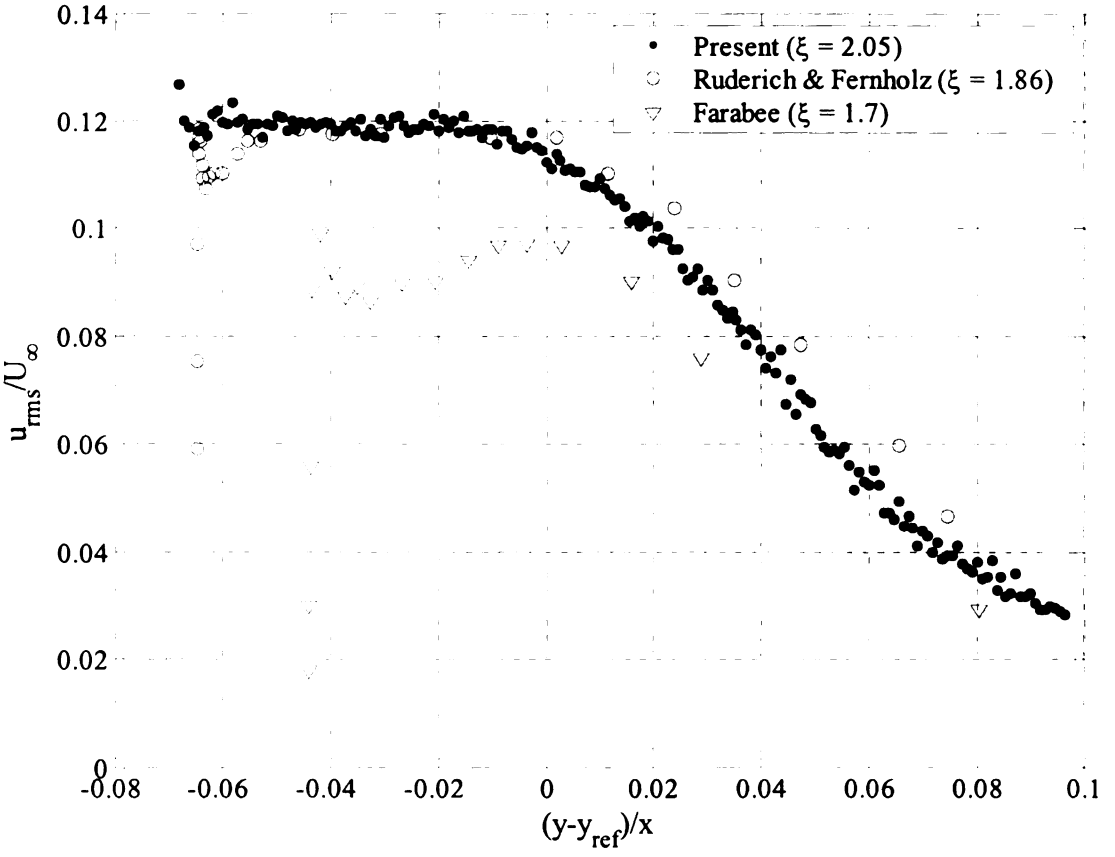

Figure 4.4. Shear-layer scaling of the boundary-layer u_{rms} profile

The root mean square profile of the normal velocity fluctuations (v_{rms}) is plotted in boundary-layer coordinates in Figure 4.5. Note that hereafter all results are based on

velocity data measured using the X-hotwire probe as described in section 2.2.4. Unlike u_{rms}, v_{rms} profile exhibits a clear peak in the outer part of the flow. The v_{rms} fluctuations are also attenuated with y change from the shear-layer centerline towards the wall more strongly than away from the wall. This is another feature that differs from that of u_{rms} where a flat region of u_{rms} fluctuations was observed on the lower side of the shear-layer center. For a truly *free* shear layer, velocity fluctuations are expected to be damped as one moves away from the center of the shear layer. The stronger damping of v_{rms} on the lower side of the shear layer in this case is consistent with the anticipated wall-damping effect of v'.

The present v_{rms} profile is also compared with those of Ruderich and Fernholz (1986), and Farabee (1986) in Figure 4.5. It is evident that the present data agree well with Ruderich and Fernholz's v_{rms} profile for $y^+ < 800$. On the other hand, the profiles don't collapse farther away from the wall, but they show qualitatively the same trend and approximately the same peak location. The discrepancy is consistent with the expectation that the outer portion of the boundary layer cannot be scaled with wall coordinates. On the other hand, Farabee's data show significant disagreement with both the present data and that of Ruderich and Fernholz. Farabee's profile shows the same trend of Figure 4.3, in which his boundary layer is thinner than the present one in wall-coordinates by approximately and order of magnitude. As discussed previously, this is consistent with Farabee's lower Reynolds number which is proportional to the ratio of the outer and inner scales of the boundary layer, or δ^+.

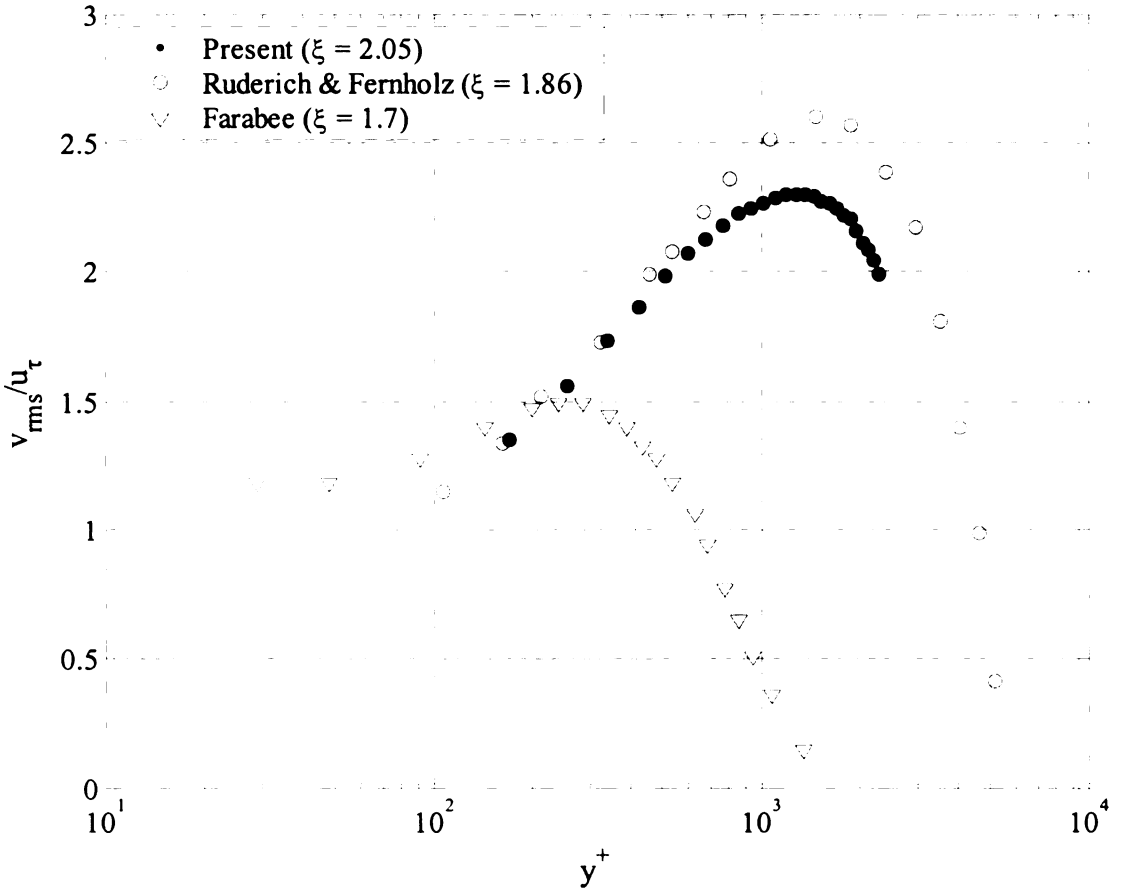

Figure 4.5. Wall scaling of the boundary-layer v_{rms} profile

Figure 4.6 depicts the same data in Figure 4.5 after they are rescaled and plotted in shear-layer coordinates; i.e., in the same manner as in Figure 4.4. The figure shows that the peak of v_{rms} falls on the negative side of the abscissa which is below the peak of the Reynolds stress. Moreover, all profiles exhibit a peak approximately at the same location in shear-layer coordinates. Generally, Figure 4.6 shows that the present data agrees better with Ruderich and Fernholz's than that of Farabee, although all data sets show the same trend. The level of v_{rms} for both the current and Ruderich and Fernhotz (1986) studies is approximately twice that of Farabee (1986), showing that the vortical structures are more energetic in the fence-with-splitter-plate flow. This is believed to be resulting from the more intense mean shear stress from which the vortices originate at

separation in the case of the fence flow, which is the same reasoning used to explain the larger level of pressure fluctuations found in the fence flow relative to that of the back-step flow (see Figure 3.3 and associated discussion).

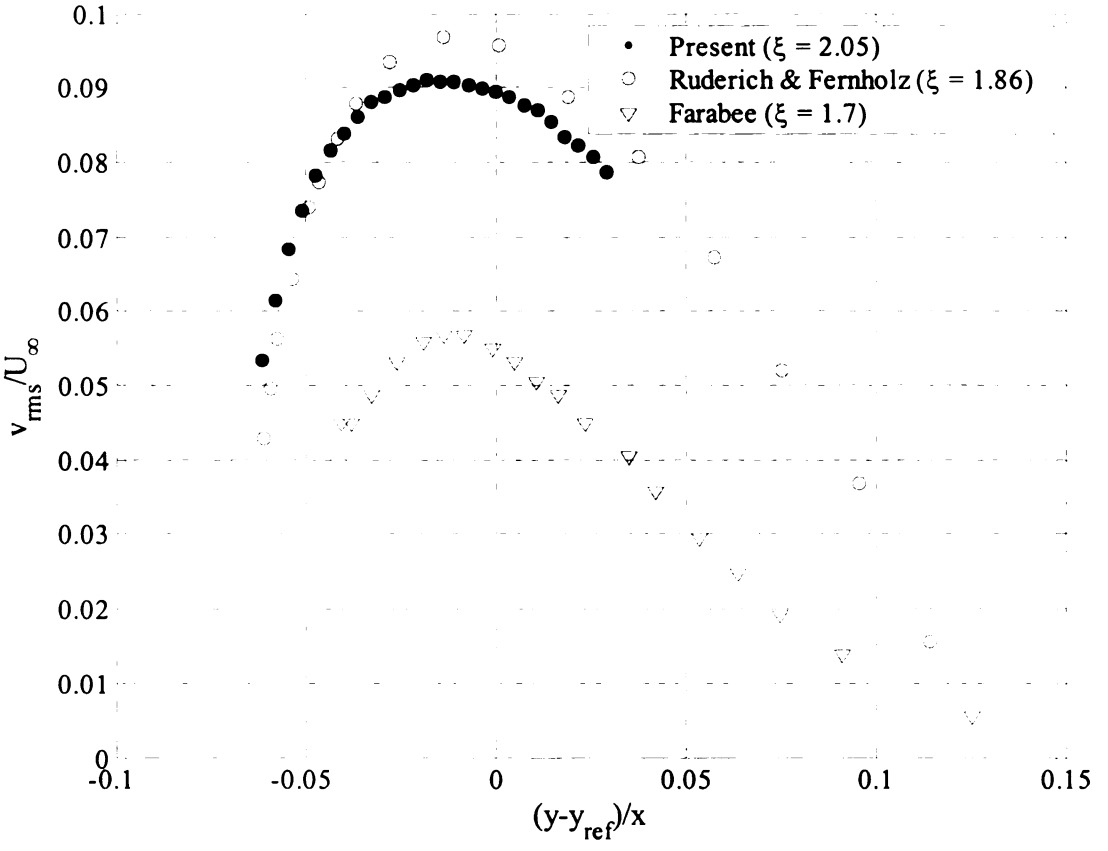

Figure 4.6 Shear-layer scaling of the boundary-layer v_{rms} profile

Another notable observation from Figure 4.6 is the fact that the data from Ruderich and Fernholtz (1986) do not collapse completely with the current data in the outer part of the flow, even with the employment of shear-layer scaling. The fairly small deviation (~10%) may be caused by differences in the streamwise freestream pressure gradient due to flow blockage by the model and wind tunnel boundary layers. Finally, by

comparing Figures 4.4 and 4.6, it can be shown that the peak of v_{rms} coincides with the outer edge ($\frac{(y - y_{ref})}{x} \approx -0.02$) of the y range where u_{rms} profile is flat.

The boundary-layer Reynolds stress profile ($-\overline{u'v'}$) is plotted in wall and shear-layer coordinates in Figures 4.7 and 4.8, respectively. Figure 4.7 shows the qualitative consistency between the present data and Ruderich and Fernholz's, which exhibit the same trend and peak location ($y^+ \approx 2000$). Furthermore, general comparison of the two profiles shows that the turbulence in Ruderich & Fernholz's flow is more energetic than in the present one, possibly due to pressure-gradient differences as discussed above. The smaller y^+ location and lower $-\overline{u'v'}$ values for Farabee's results are consistent with the same observations concerning v_{rms} and associated discussion made earlier.

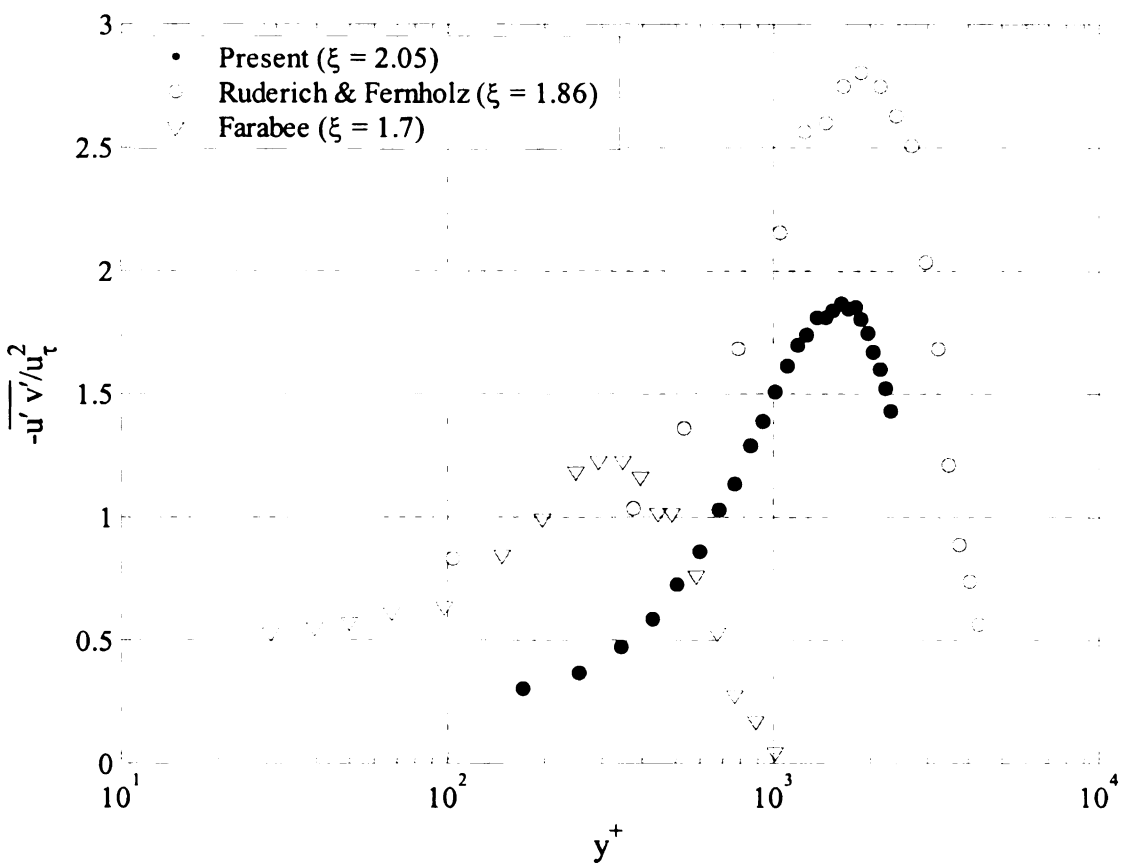

Figure 4.7. Wall scaling of the boundary-layer Reynolds stress profile

Figure 4.8 depicts the $-\overline{u'v'}$ profile in shear-layer coordinates. As stated earlier, y_{ref} is the locus of the $-\overline{u'v'}$ peak, which means that all three profiles are forced to have the same peak location. Data comparison in the figure shows that there is a trend similarity among the three profiles with quantitative differences as clarified before.

In summary, the boundary layer profiles show that the non-equilibrium boundary layer in the redevelopment zone studied here mainly consists of a growing sub-boundary layer near the wall and outer-shear layer that exists above it. The characteristics of the investigated boundary layer exhibit a discrepancy with those of the fully-developed turbulent boundary layer, as demonstrated by the shape of the u_{rms}, v_{rms} and $-\overline{u'v'}$ profiles. The maxima of those profiles for an equilibrium boundary layer fall in the buffer layer ($y^+ < 30$) as reported in the literature (e.g. Wei and Willmarth 1989). In contrast, the boundary layer at $\xi = 2.05$ predominantly exhibits free-shear-like characteristics, associated with the existence of u_{rms}, v_{rms} and $-\overline{u'v'}$ peaks in the outer layer. Those maxima, which clearly differ from those described for the equilibrium boundary layer, are related to the energetic large-scale vortical structures that were generated and energized upstream in the separating free-shear layer. As was concluded from the pressure data in Chapter 3, those vortical structures seem to dominate the flow especially in the outer layer of the boundary layer. Although a few authors investigated the flow downstream of separating/reattaching flows (e.g. Ruderich & Fernholz 1986, Farabee 1986 , Farabee & Casarella 1986, Castro and Epik 1998 and Song and Eaton 2002), they observed that the vortical structures could be seen at downstream locations as far as six reattachment lengths ($6X_r$). These authors also stated that the equilibrium boundary layer state could be reached at the location where the sub-boundary layer had

propagated all the way through the non-equilibrium boundary layer. Moreover, Farabee (1986) indicated that the distance needed to reach the equilibrium boundary layer stage was approximately $20X_r$. However, the results of Castro and Epik (1998) and Song and Eaton (2002) showed that their non-equilibrium boundary layer relaxed to the equilibrium behavior at $10X_r$ downstream of separation.

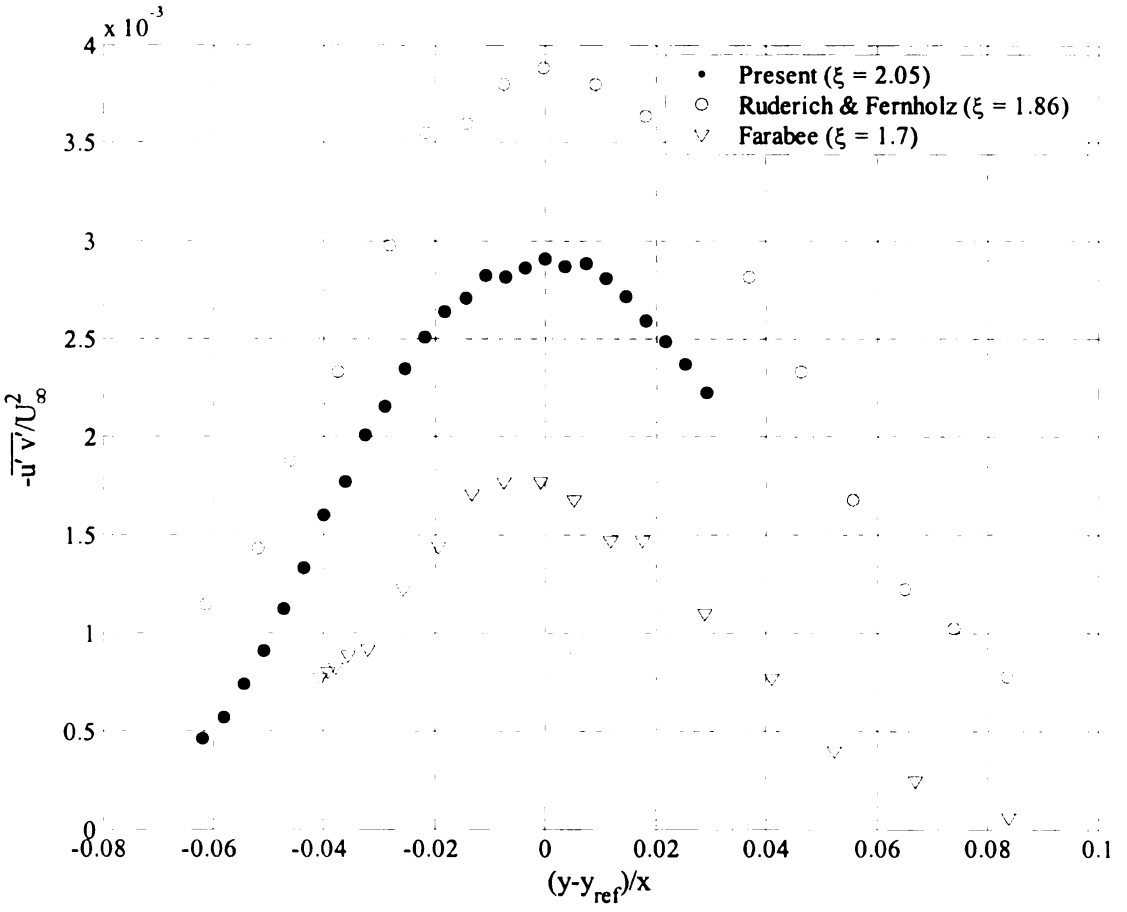

Figure 4.8. Shear-layer scaling of the boundary-layer Reynolds stress profile

4.1.2. Velocity Spectra

Here, the turbulent velocity and shear-Reynolds-stress spectra in the non-equilibrium boundary layer at $\xi = 2.05$ are presented and analyzed in order to obtain more

information of the turbulent flow features during the boundary-layer relaxation process. In order to show the effect of height on the spectral characteristics of the flow, the dimensionless auto-spectra and cross-spectrum of the streamwise and normal velocities (Φ_{uu}, Φ_{vv} & Φ_{uv}) are plotted at six different heights (y/δ = 0.05, 0.125, 0.25, 0.375, 0.5 & 0.625) that approximately cover the y range of velocity measurements. Furthermore, each spectrum is plotted in both logarithmic and semi-logarithmic scales. As explained earlier based on equation 3.2, the reason for using the semi-log scale is that the geometrical area under the spectrum represents the spectral distribution of the turbulence energy in this case.

The spectra are calculated by dividing the time series of velocity into 2048 records of 1024 samples each. The Fourier transform of each record is then calculated and multiplied by its conjugate, except in the case of the cross-spectrum, where the Fourier transform of the u component is multiplied by the conjugate of the Fourier transform of the v component. Subsequently, the products of all records are averaged to give the average auto- or cross-spectrum of the velocity components of interest. The resulting frequency resolution is 12.2 Hz ($\frac{f X_r}{U_\infty} = 0.136$) with a random-error uncertainty of about 2%.

Figure 4.9 depicts the streamwise-velocity spectra at the six different heights, plotted using logarithmic scale. The abscissa is the dimensionless frequency ($f X_r/U_\infty$), while the ordinate is the velocity spectrum (Φ_{uu}) normalized by U_∞^2. The spectra show that with the exception of y/δ = 0.625, corresponding to the lowest spectrum, the energy content of all other spectra is quite similar. This is consistent with the uniform

distribution of u_{rms} shown in Figure 4.3 for $70 < y^+ < 1500$ ($0.02 < y/\delta < 0.5$). The spectra also depict that the closer the location to the wall the more the contribution from high-frequency fluctuation to the velocity spectra. This observation, which is more evident in the semi-log plot in Figure 4.10, is presumably a manifestation of the increasing importance of the small-scale turbulence associated with the sub-boundary layer as one approaches the wall. It is noted though that, for the y values considered, the overall contribution of these small scales to u_{rms} is negligible compared to the lower-frequency larger-scale structures.

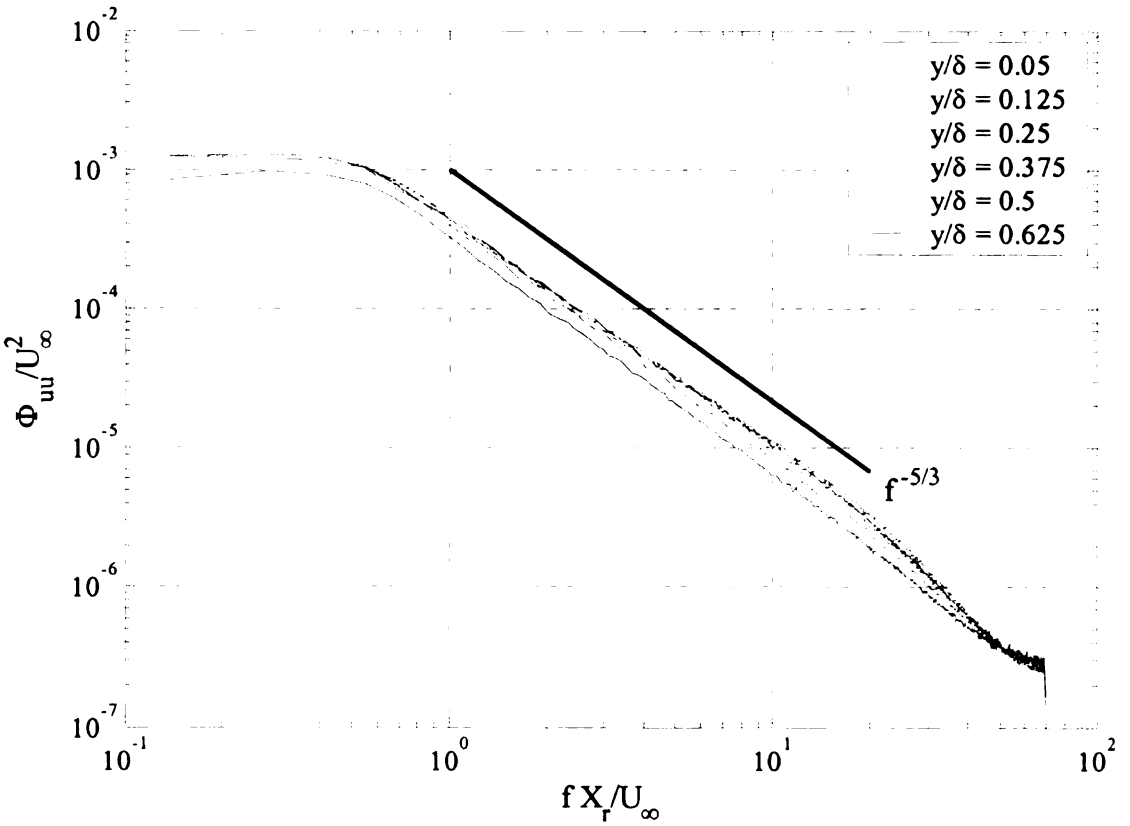

Figure 4.9. Streamwise-velocity spectra at y/δ = 0.05, 0.125, 0.25, 0.375, 0.5 and 0.625 and ξ = 2.05

The practically-uniform u_{rms} energy found at five of the presented heights (y/δ = 0.05, 0.125, 0.25, 0.375 & 0.5) can be related to the mean-velocity and Reynolds-shear-

stress profiles presented earlier and their influences on the turbulence-energy-production term ($-\overline{u'v'}\frac{du}{dy}$). Near the wall, the $\frac{du}{dy}$ term is large which compensates for the low Reynolds stress term ($-\overline{u'v'}$). As the height increases, $\frac{du}{dy}$ decreases while $-\overline{u'v'}$ increases, keeping the whole term approximately the same. This scenario seems to be valid up to the location of the Reynolds stress peak location, above which the energy production term decreases because the $\frac{du}{dy}$ term remains practically constant while $-\overline{u'v'}$ decreases with height. As a result, u_{rms} decreases with further increase in y resulting in the drop in the spectrum seen at $y/\delta = 0.625$.

Another notable feature of the spectra in Figure 4.9 is the existence of a more than a decade wide $f^{-5/3}$ range, implying the sustenance of an inertial sub-range. The width of this range increases with increase in height in the boundary layer. Farabee (1986) and Castro and Epik (1998) reported the same slope at similar streamwise location and heights above the wall. Furthermore, Ruderich & Fernholz (1986) observed the same trend in the dimensionless streamwise-velocity spectra, which showed similarity at different heights in the boundary layer.

To study the distribution of u_{rms} energy among different frequency ranges, Φ_{uu} is plotted in semi-log coordinates as shown in Figure 4.10. The ordinate is the product between the dimensionless frequency and streamwise-velocity spectrum ($\frac{f X_r}{U_\infty}\frac{\Phi_{uu}}{U_\infty^2}$), while the abscissa is the dimensionless frequency ($\frac{f X_r}{U_\infty}$). The spectra are all grossly

similar qualitatively and quantitatively except at the highest location ($y/\delta = 0.625$), which is consistent with what is observed earlier in Figure 4.9. From the general inspection of the spectra, it can be observed that there is a frequency range, centered around $\frac{f X_r}{U_\infty} \approx$ 0.55, where most of the u' fluctuations are concentrated. This dominant frequency range, which encompasses the signature of the low-frequency shear-layer vortical structures (based on the analysis of the pressure data in Chapter 3) persists at all heights, even near the wall. However, closer to the wall, there is also more contribution from small-scale structures within the high frequency range, which is reflected in the growth of a small hump in the spectra for $\frac{f X_r}{U_\infty} > 5$ and the lowest height.

Figure 4.11 depicts the normal-velocity spectra, which are plotted at the same heights as in Figure 4.9. The spectra show that the normal-velocity energy increases significantly as the height increases in the region near the wall ($y/\delta = 0.05$ & 0.125), which highlights the attenuation effect of the wall on the normal velocity fluctuations. This is consistent with what is deduced from the v_{rms} profile shown in Figures 4.5 and 4.6. In addition, Figure 4.11 depicts that the spectra for $y/\delta > 0.25$ start to show a peak at a frequency of $\frac{f X_r}{U_\infty} \approx 0.75$, which is approximately the same frequency as that found in the wall-pressure spectra earlier, but higher than the frequency range of the u' flat spectral peak in Figure 4.9. These observations further supplement the earlier conclusions that the energy-generating flow-features are still dominated by the vortical structures generated upstream in the separating free-shear layer.

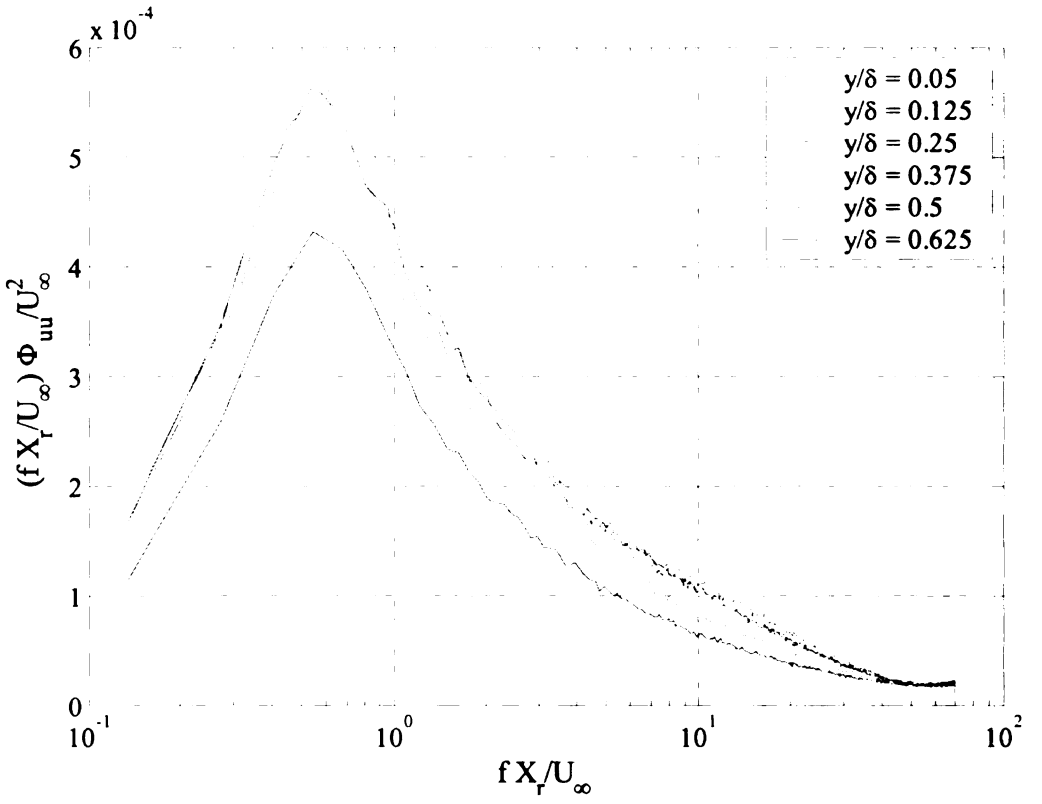

Figure 4.10. Semi-log plots of the streamwise-velocity spectra at $y/\delta = 0.05$, 0.125, 0.25, 0.375, 0.5 and 0.625 and $\xi = 2.05$

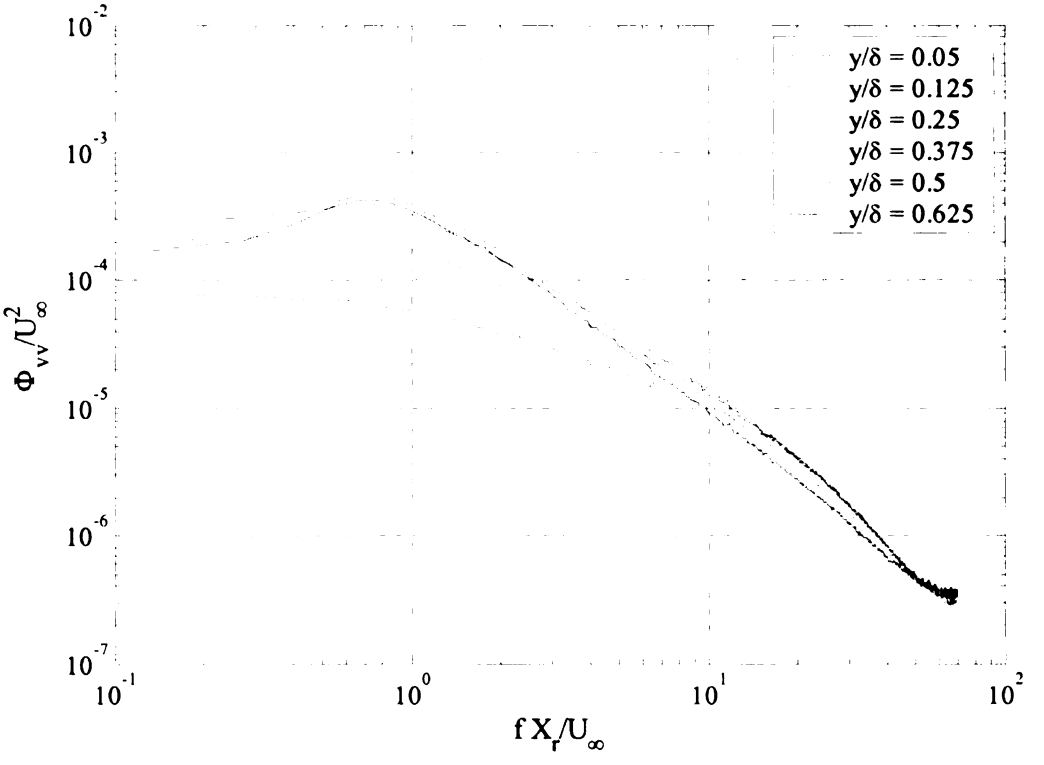

Figure 4.11. Normal-velocity spectra at $y/\delta = 0.05$, 0.125, 0.25, 0.375, 0.5 and 0.625 and $\xi = 2.05$

Figure 4.12 provides the dimensionless semi-log normal-velocity spectra. Grossly, the spectra show significant dissimilarity with the semi-log streamwise velocity spectra shown in Figure 4.10 for $\frac{f X_r}{U_\infty} < 20$. For higher frequencies ($\frac{f X_r}{U_\infty} > 20$), the normal-velocity spectra exhibit more or less the same behavior as u', reflecting an increase in the contribution of the high-frequency fluctuations to the normal-velocity energy near the wall.

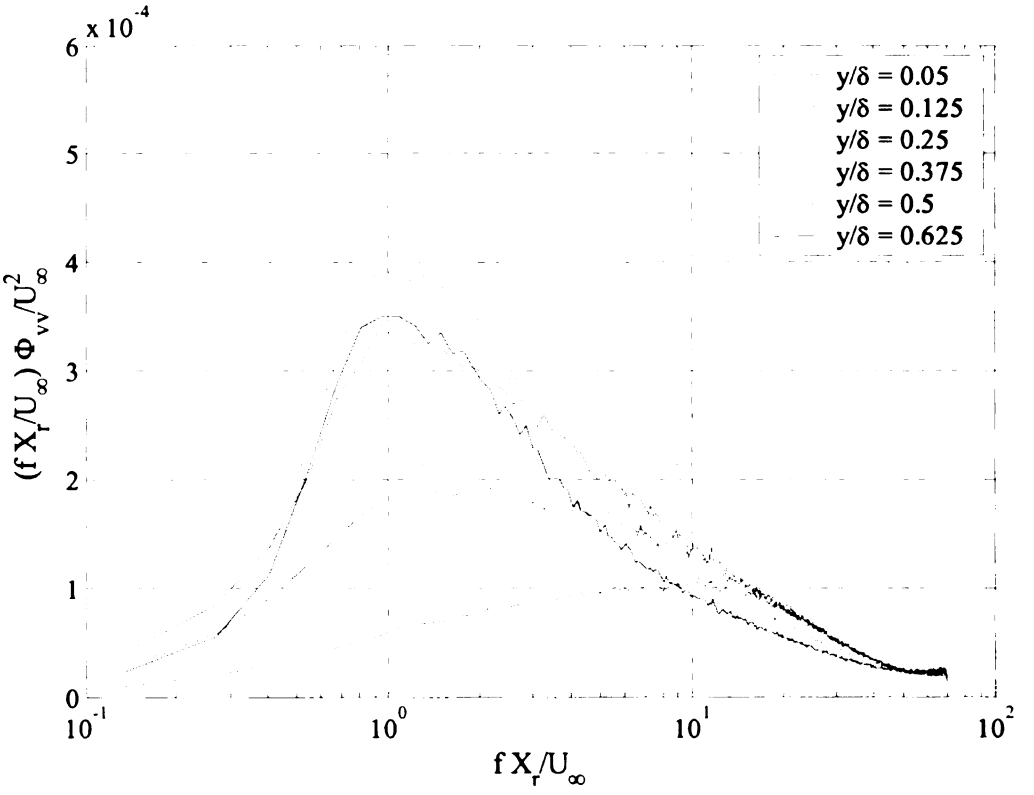

Figure 4.12. Semi-log normal-velocity spectra at y/δ = 0.05, 0.125, 0.25, 0.375, 0.5 and 0.625 at ξ = 2.05

The collapse of the spectra for y/δ < 0.375 and $\frac{f X_r}{U_\infty} > 20$ in Figure 4.12 implies that the energy contribution of the flow structures within that frequency range is independent of the height above the wall. On the other hand for $\frac{f X_r}{U_\infty} < 20$, the spectra

reveal a strong evidence of the dependency of spectral distribution of v' on height. Particularly at $y/\delta = 0.05$, the spectrum shows that the contribution of the low-frequency shear-layer vortical structures to v' fluctuations at that height is minimal in contrast with the contribution of the high-frequency small-scale structures. The spectrum at $y/\delta = 0.05$ emphasizes this observation by showing a peak at approximately $\frac{f X_r}{U_\infty} = 10$, which is at least one order of magnitude higher than the reported passage frequency of the shear-layer vortices.

On the other hand, Figure 4.12 also shows that as y increases the contribution of the large-scale shear-layer vortical structures increases, which is implied from both the growth and the shift to lower-frequency of the spectrum peak. More specifically, the frequency of the spectrum peak drops by almost a factor of five as y/δ goes from 0.05 to 0.125. Furthermore, the area under the spectra (which represents the energy) for $\frac{f X_r}{U_\infty} <$ 20 increases significantly as the height increases. At higher locations ($y/\delta > 0.25$) the spectra show that the energy of the normal-velocity fluctuations is mainly provided by the shear-layer vortical structures. Furthermore, for the same height range, the spectra show more or less the same level of energy with a peak at $\frac{f X_r}{U_\infty} \approx 1.0$. However, the energy contained in the spectrum at $y/\delta = 0.375$ is maximal since v_{rms} reaches its peak at that height.

Next, the shear Reynolds stress ($\overline{u'v'}$) spectra, or the cross-spectra of the streamwise and normal fluctuating velocities (Φ_{uv}) are evaluated. Figure 4.13 shows the Φ_{uv} spectra in the same dimensionless coordinates of Figures 4.9 and 4.11. The spectra

shown in Figure 4.13, which depict the spectral characteristics of $\overline{u'v'}$ at different heights, reveal that at all heights except $y/\delta = 0.05$ (the closest to the wall), the cross-spectra are similar and the peak contribution to the Reynolds stress is at a non-dimensional frequency of 0.55. At $y/\delta = 0.05$, there is a reduction in the level of the Reynolds-stress contribution at that frequency relative to the other heights. Additionally, a substantial increase in Reynolds stresses associated with the high-frequency end is seen at this location closest to the wall. This most likely reflects the build up of small-scale energetic turbulence within the growing sub-boundary layer near the wall.

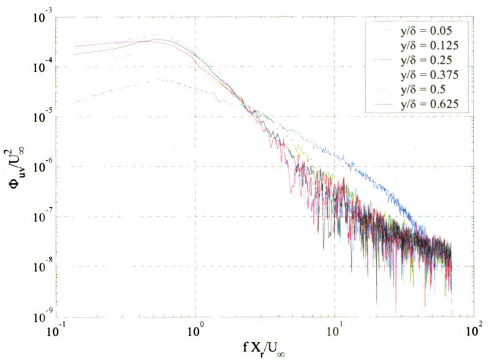

Figure 4.13. Boundary-layer velocity cross spectra at $y/\delta = 0.05$, 0.125, 0.25, 0.375, 0.5 and 0.625 and $\xi = 2.05$

The semi-log plot of Φ_{uv} in Figure 4.14 also depicts the same trends as those of Figure 4.12, but it shows more clearly that the contribution of the flow structures with

non-dimensional frequencies higher than 6 to the shear Reynolds stress is practically negligible for $y/\delta > 0.05$. That is, the shear Reynolds stress for $y/\delta > 0.05$ is solely associated with the large-scale motion in the free shear layer. The peak magnitude of the corresponding cross-spectrum increases with height till it reaches a maximum at $y/\delta = 0.5$, before dropping down again at $y/\delta = 0.625$. This behavior follows the trend of the $-\overline{u'v'}$ profiles displayed in Figures 4.7 and 4.8. Additionally, Figure 4.14 shows that the frequency band containing most of $\overline{u'v'}$ is centered around the same frequency at which the wall-pressure fluctuation exhibit a peak i.e., $\frac{f X_r}{U_\infty} \approx 0.7$.

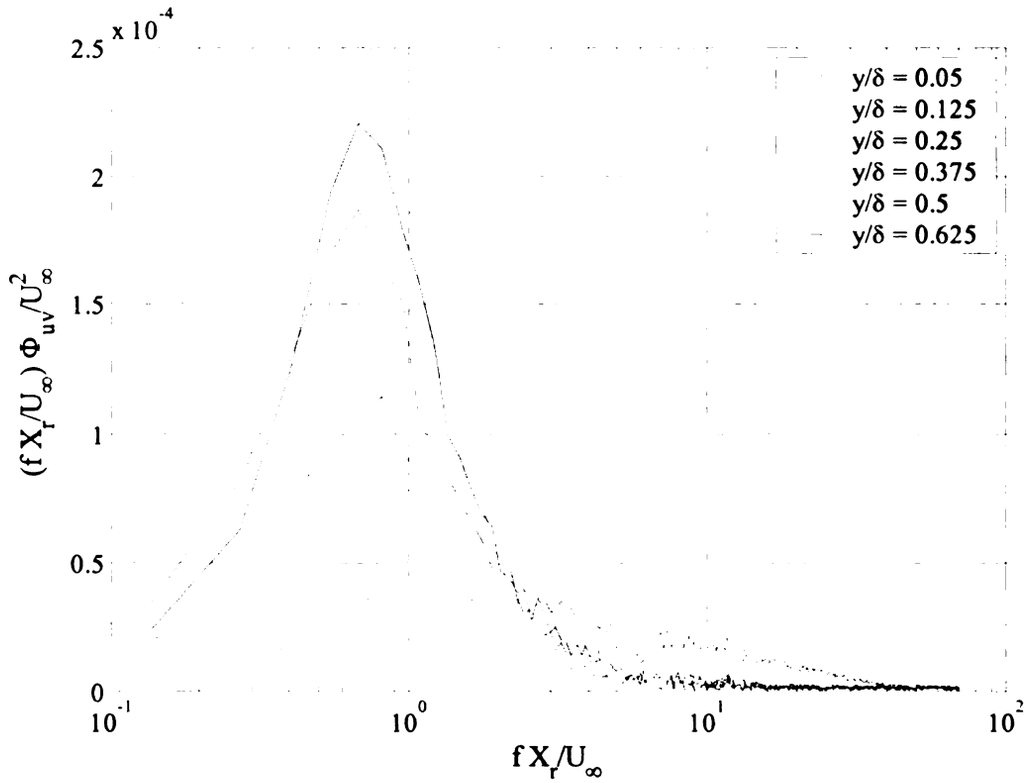

Figure 4.14. Semi-log plot of the boundary layer velocity cross spectra at $y/\delta = 0.05$, 0.125, 0.25, 0.375, 0.5 and 0.625 and $\xi = 2.05$

The collective observations of the velocity and $\overline{u'v'}$ spectra may be interpreted from the perspective of Townsend's hypothesis of *active* and *inactive* motions, Townsend

(1961), which was extensively studied by Bradshaw (1967) using zero- and adverse-pressure-gradient boundary layers. Basically Townsend defined the *inactive* motion as that of the large-structures that do not contribute to the Reynolds shear stress near the wall while contributing to u′. This was verified by the measurements of Bradshaw (1967) who reported that the large-scale structures produced Reynolds shear stress in the outer layer but not in the inner layer. A good explanation of the reason for the inability of the large-scale motion to contribute to the near wall $\overline{u'v'}$ generation is offered by the structures-based model of Perry *et al.* (1986). These authors envisioned the turbulence structures of equilibrium turbulent boundary layers to consist of a hierarchy of scales of hair-pin eddies. Treating these vortices as potential vortices, they argued that the heads of the hair-pin eddies, which are similar to an x-y section of a spanwise vortex, contribute to v′ only at heights above the wall that are similar to the vortex center location. Away from the center, the vortices only contributed to the u′. Hence, because locations near the wall would be far away from the large-scale vortex centers that reside in the outer-layer, these vortices contribute very little to v′, and consequently to $-\overline{u'v'}$, while contributing substantially to u′ near the wall. That is, the large-scale vortices are *inactive* near the wall.

This analysis is consistent with the current results where Figures 4.10, 4.12 and 4.14 imply that the large-scale structures are *active* in the outer layer as they contribute to both the streamwise and normal velocity fluctuations and consequently to the Reynolds shear stress. Those structures, however, become *inactive* near the wall because they only produce the streamwise velocity fluctuations while their v′ and $\overline{u'v'}$ contributions are attenuated substantially. Similarly, the analysis of the small-scale structures

demonstrates that they are *active* near the wall because they contribute to the fluctuations of both velocity components and the Reynolds shear stress.

Finally, it is important to note that the physical nature of the inactive motion here is different from that referred to by Townsend (1961) and proposed by Perry *et al.* (1986). In particular, Townsend's inactive, or large-scale, structures are those that occupy the wake region of an equilibrium boundary layer. As discussed in section 4.1.1 the non-equilibrium boundary layer investigated here does not have a wake region. Instead, the inactive motions here are those originating in the free shear layer at separation. It is also emphasized that whereas Townsend's inactive motion contribute, but does not necessary dominate, the wall-pressure fluctuations, the inactive motion here does dominate the wall-pressure generation process. The physical mechanism(s) by which it does so will be elaborated upon in section 4.3.3.

4.2. Velocity-Pressure Characteristics

To investigate the relationship between the velocity field and its wall-pressure signature, the simultaneous velocity/pressure data are explored in this section. The exploration includes analyses of the cross-spectra and cross-correlations of the velocity and wall-Pressure data. Furthermore, the average velocity field that is conditioned on the occurrence of strong positive and negative wall-pressure events is obtained and analyzed for additional insight.

4.2.1. Velocity/Wall-Pressure Cross-Spectra

The velocity/wall-pressure cross-spectrum is the Fourier transform of their cross-correlation. Therefore, in this section the cross-spectra are investigated to better understand the spectral properties of the velocity/wall-pressure cross-correlations; i.e., to

identify the frequencies at which strong velocity-pressure correlation is found. The cross-spectra are calculated between the flow velocities at $\xi = 2.05$ and the wall-pressure at three streamwise locations $\xi = 1.33$, 2.0 and 2.33. The microphones at those locations are the 1st, 7th and 10th microphones, where the 1st microphone is the most upstream one, and therefore, p_1, p_7 and p_{10} will be used to denote the corresponding pressure at these respective locations. The procedure for the velocity/wall-pressure cross-spectra calculation is the same as that used for the velocity cross-spectra, given earlier in 4.1.2.

The cross-spectra between u′ and p′ at $\xi = 1.33$, 2.0 and 2.33 (Φ_{up_1}, Φ_{up_7} & $\Phi_{up_{10}}$, respectively) are shown in Figures 4.15 through 4.20. Figures 4.15, 4.17 and 4.19 show the logarithmic plots of the dimensionless cross-spectra, while Figures 4.16, 4.18 and 4.20 depict the semi-logarithmic ones. Figures 4.15 and 4.16 show that the only correlation between u' at $\xi = 2.05$ and p' at $\xi = 1.33$ is produced by the passage of the large-scale vortical structures, which correspond to the low-frequency range, while no correlation is evident due to the small-scale structures near the wall (corresponding to the high-frequency end). This is not too surprising given that p′ measurements are more than one boundary-layer thickness ($\approx 1.6\delta$) upstream of that of u′.

In contrast, the logarithmic and semi-logarithmic cross-spectra of the microphone closest to the hotwire ($\xi = 2.0$), Figures 4.17 and 4.18, show a rise in the contribution of the small-scale structures to the cross-spectra near the wall. This may be deduced from inspecting the spectrum at $y/\delta = 0.05$, which exhibits a rise in the spectra at high frequencies ($\frac{f X_r}{U_\infty} > 1.5$). At higher y locations, the data still resemble those in Figures 4.15 and 4.16 at the same heights, but with a decrease in magnitude of the cross-spectrum.

The observed reduction in the spectrum magnitude seems to oppose intuition that the correlation should increase as the distance between the microphone and the hotwire decreases. However, the reduction mainly results from the decay of the vortical structures energy with increasing x due to their relaxation process, which is documented in Chapter 3 as a decay in the p'_{rms} in the streamwise direction. That is, if the cross-spectra were normalized by using u_{rms} and p_{rms}, there would be an increase in the cross-spectra levels at $\xi = 2.0$ relative to $\xi = 1.33$ instead of attenuation.

The cross-spectra corresponding to p'_{10} or $\xi = 2.33$, which is downstream of the hotwire location, are presented in Figures 4.19 and 4.20. The results in both figures are generally similar to those obtained in Figures 4.17 and 4.18 for $\xi = 2.0$, including evidence of some small-scale ($\frac{f X_r}{U_\infty} > 1.5$) contribution to u'-p' correlation near the wall. Unlike the data at $\xi = 2.0$, though, this contribution is not only evident at $y/\delta = 0.05$, but also at $y/\delta = 0.125$. It is interesting to note that the range of frequencies corresponding to the small-scale signature ($1.5 < \frac{f X_r}{U_\infty} < 10$) is actually at the low-frequency end of the range that has been identified to correspond to the sub-layer pressure fluctuations. Thus, it is believed that the flow structures corresponding to this range of frequencies although small in scale relative to the shear-layer vortical structures, they represent the largest of the sub-boundary layer turbulence. Since the sub-boundary layer thickens with increase in x, these structures are expected to grow in size with downstream distance. This is likely why the small-scale contribution to the cross-spectrum at $\xi = 2.33$ is felt as high as

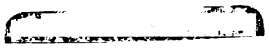

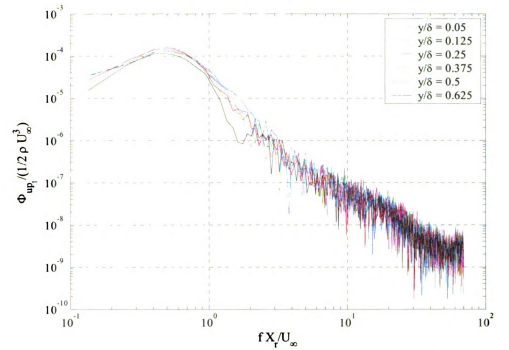

Figure 4.15. Cross-spectra between the streamwise velocity (at ξ = 2.05) and wall-pressure (at ξ = 1.33) for y/δ = 0.05, 0.125, 0.25, 0.375, 0.5 and 0.625

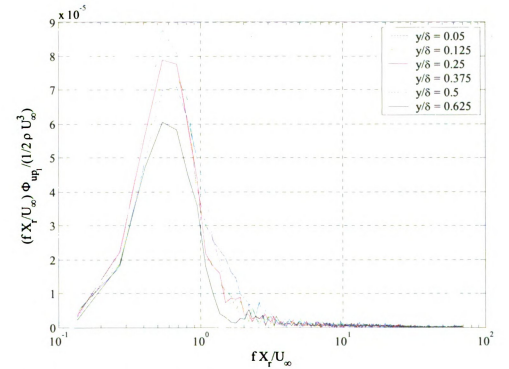

Figure 4.16. Semi-log plot of the cross-spectra between the streamwise velocity (at ξ = 2.05) and wall-pressure (at ξ = 1.33) for y/δ = 0.05, 0.125, 0.25, 0.375, 0.5 and 0.625

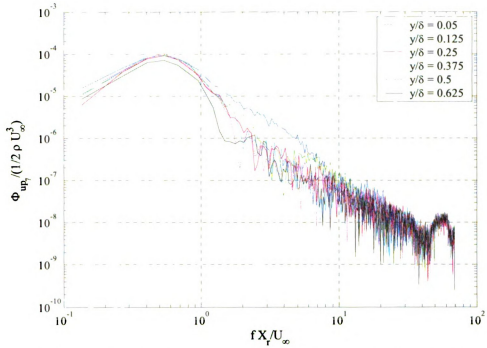

Figure 4.17. Cross-spectra between the streamwise velocity (at ξ = 2.05) and wall-pressure (at ξ = 2.0) for y/δ = 0.05, 0.125, 0.25, 0.375, 0.5 and 0.625

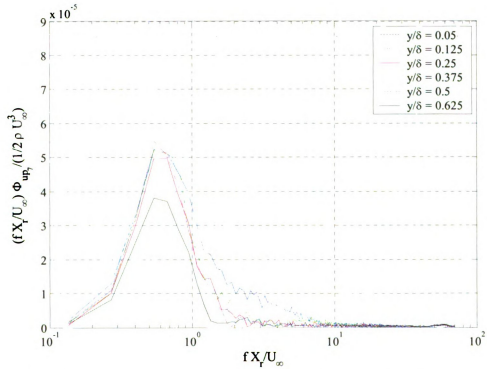

Figure 4.18. Semi-log plot of the cross-spectra between the streamwise velocity (at ξ = 2.05) and wall-pressure (at ξ = 2.0) for y/δ = 0.05, 0.125, 0.25, 0.375, 0.5 and 0.625

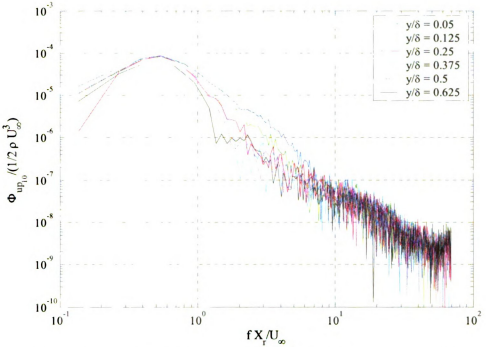

Figure 4.19. Cross-spectra between the streamwise velocity (at ξ = 2.05) and wall-pressure (at ξ = 2.33) for y/δ = 0.05, 0.125, 0.25, 0.375, 0.5 and 0.625

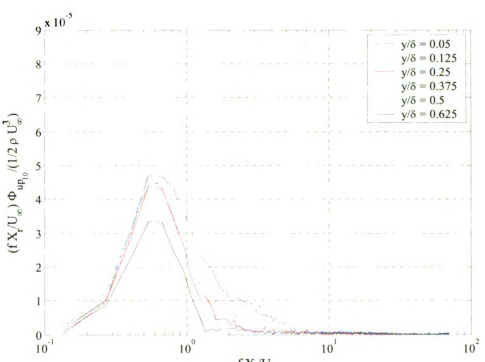

Figure 4.20. Semi-log plot of the cross-spectra between the streamwise velocity (at ξ = 2.05) and wall-pressure (at ξ = 2.33) for y/δ = 0.05, 0.125, 0.25, 0.375, 0.5 and 0.625

$y/\delta = 0.125$ in comparison to $y/\delta = 0.05$ at $\xi = 2.0$. On the other hand, the disappearance of small-scale effects in the results at $\xi = 1.33$ (Figure 4.16) is an indication of the short "life-time" of these structures such that after registering a small-scale-pressure signature at $\xi = 1.33$, they decay and dissipate prior to reaching the hotwire at $\xi = 2.05$.

The cross-spectra Φ_{vp_1}, Φ_{vp_7} & $\Phi_{vp_{10}}$ are presented in Figures 4.21 through 4.26. Figures 4.21 and 4.22 depict the cross-spectra calculated at $\xi = 1.33$ in logarithmic and semi-logarithmic scales, respectively. The cross-spectra are dominated by the large-scale vortices with no evidence of small scale contribution even at $y/\delta = 0.05$. This implies the same observation as the u′-p′ cross-spectra at the same streamwise location, that the "life-time" of the small-scale structures near the wall is not long enough for the structures to travel the distance between the locations of the microphone at $\xi = 1.33$ and the hotwire at $\xi = 2.05$ ($\Delta\xi = 0.72$, or $\Delta x \approx 1.6\delta$). The spectra in Figure 4.22 also show the attenuation effect of the wall on the normal velocity fluctuation as a decrease in the spectral peak at locations near the wall. In addition to the peak attenuation, the cross-spectra exhibit a peak at $\frac{f X_r}{U_\infty} \approx 0.7$. This value is consistent with the frequency of the peak pressure fluctuations found in Chapter 3. In contrast, the peak of u'-p' cross-spectra is found at $\frac{f X_r}{U_\infty} \approx 0.55$ (e.g., see Figure 4.17). This shift to lower frequency of $\Phi_{u'p'}$ peak is a manifestation of the higher u' energy at normalized frequencies lower than 0.7 (see $\Phi_{u'u'}$ in Figure 4.9). Additionally, in contrast to the u′-p′, the v′-p′ cross-spectra depict the strongest correlation is at the highest location of $y/\delta = 0.625$.

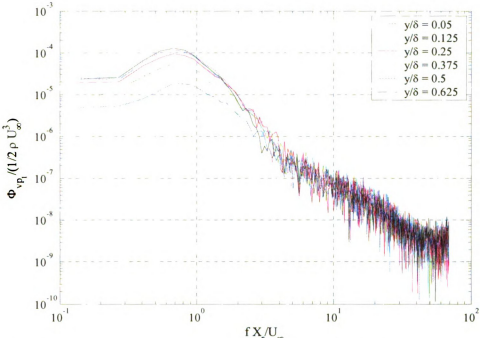

Figure 4.21. Cross-spectra between the normal velocity (at $\xi = 2.05$) and wall-pressure (at $\xi = 1.33$) for $y/\delta = 0.05, 0.125, 0.25, 0.375, 0.5$ and 0.625

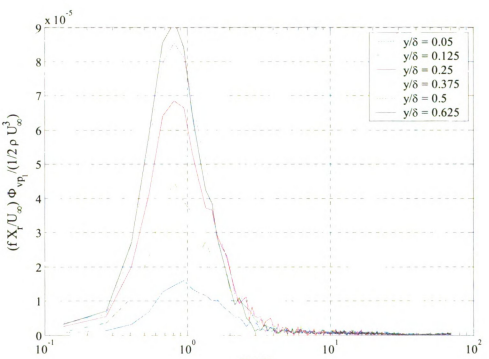

Figure 4.22. Semi-log plot of the cross-spectra between the normal velocity (at $\xi = 2.05$) and wall-pressure (at $\xi = 1.33$) at for $y/\delta = 0.05, 0.125, 0.25, 0.375, 0.5$ and 0.625

The cross-spectra at ξ = 2.0, shown in Figures 4.23 and 4.24, depict a pronounced contribution of the small-scale structures to the cross-correlation at heights of y/δ = 0.05 and 0.125, which is consistent with the fact that the corresponding microphone location is the closet to the X-wire. As a result, the frequency range of $\Phi_{v'p'}$ extends to a frequency as high as $\frac{f X_r}{U_\infty} \approx 20$ and 10 at y/δ = 0.05 and 0.125, respectively. Finally, the spectra in Figures 4.23 and 4.24 seem to follow the same trend of those at ξ = 1.33 in terms of the spectral peak attenuation near the wall and the increase in the cross-spectrum peak with increase in y. Moreover, there is a slight shift of the spectrum-peak's frequency from 0.7 to 0.8 at y/δ = 0.05. The peak is also seen to become progressively broader with decreasing y. This is consistent with the earlier discussion that as one approaches the wall the largest scales become more inactive, contributing less to v', and hence to v'-p' correlation, while the smaller scales become more active, producing a "flatter" spectral distribution where a broader range of scales is involved in generating v', and v'-p' correlation.

Because the spectra in Figures 4.25 and 4.26 correspond to ξ = 2.33, which is farther from the hotwire location than ξ = 2.0 but not as far as ξ = 1.33, they exhibit an intermediate behavior between that of $\Phi_{v'p'}$ at ξ = 1.33 and ξ = 2.0. In general the analysis of the cross-spectra between the wall-pressure and the normal-velocity component reinforces the conclusion made in Chapter 3 that the p′ fluctuations are dominated by the vortical structures in the outer part of the boundary layer. Specifically, the semi-logarithmic plots of the cross-spectra reveal that the wall-pressure is mainly

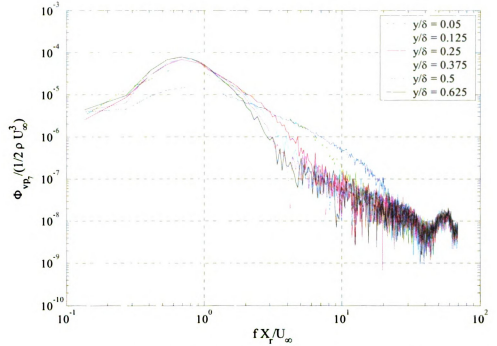

Figure 4.23. Cross-spectra between the normal velocity (at $\xi = 2.05$) and wall-pressure (at $\xi = 2.0$) for $y/\delta = 0.05$, 0.125, 0.25, 0.375, 0.5 and 0.625

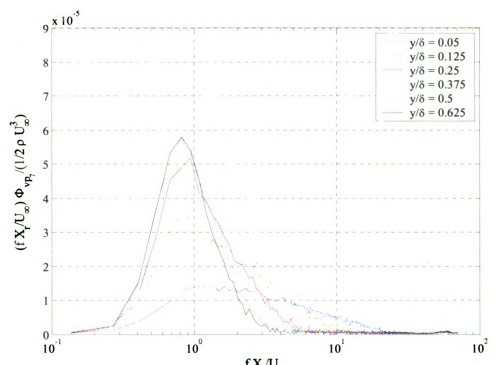

Figure 4.24. Semi-log plot of the cross-spectra between the normal velocity (at $\xi = 2.05$) and wall-pressure (at $\xi = 2.0$) for $y/\delta = 0.05$, 0.125, 0.25, 0.375, 0.5 and 0.625

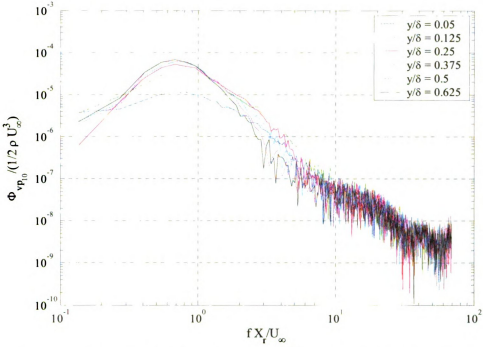

Figure 4.25. Cross-spectra between the normal velocity (at ξ = 2.05) and wall-pressure (at ξ= 2.33) for y/δ= 0.05, 0.125, 0.25, 0.375, 0.5 and 0.625

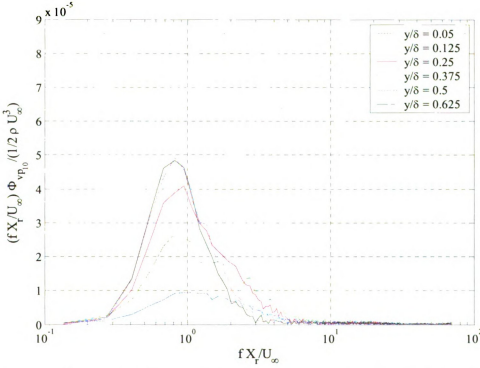

Figure 4.26. Semi-log plot of the cross-spectra between the normal velocity (at ξ = 2.05) and wall-pressure (at ξ = 2.33) at for y/δ = 0.05, 0.125, 0.25, 0.375, 0.5 and 0.625

correlated with the normal velocity in the frequency range corresponding to the passage of the vortical structures in the outer-shear layer even at heights near to the wall at which the normal-velocity fluctuations generated by those structures are significantly attenuated due to the bounding-wall effect. Furthermore, the velocity illusively seems to correlate better with p′ farther upstream, which is a direct reflection of the vortical structure being more energetic upstream than downstream as they undergo a relaxation process while traveling.

4.2.2. Velocity/Wall-Pressure Cross-Correlations

In this section, the relationship between the wall-pressure and velocity fields is investigated further in terms of their space-time cross-correlation coefficient. The spatial cross-correlation coefficient is calculated at zero time-shift (τ) between the measured velocities at ξ = 2.05 and the wall-pressure at all streamwise locations using the equations:

$$R_{up_o}(\xi, y; \xi_o) = \frac{\overline{u'(\xi_o, y, t)\, p'(\xi, t)}}{u_{rms}\, p_{rms}} \tag{4.1}$$

$$R_{vp_o}(\xi, y; \xi_o) = \frac{\overline{v'(\xi_o, y, t)\, p'(\xi, t)}}{v_{rms}\, p_{rms}} \tag{4.2}$$

where ξ_o is a parameter representing the streamwise location of the hotwire, ξ is the streamwise location of the microphone and the overbar refers to the time average. On the other hand, the corresponding temporal cross-correlation coefficient is calculated using:

$$R_{up}(y, \tau; \xi_i) = \frac{\overline{u'(\xi_o, y, t+\tau)\, p'(\xi_i, t)}}{u_{rms}\, p_{rms}} \tag{4.3}$$

$$R_{vp}(y, \tau; \xi_i) = \frac{\overline{v'(\xi_o, y, t+\tau)\, p'(\xi_i, t)}}{v_{rms}\, p_{rms}} \tag{4.4}$$

where ξ_i is a parameter indicating the streamwise location of a selected microphone.

The cross-correlation is calculated from the discrete-time data using the Fast Fourier Transform (FFT). Data are divided into 2048 records, each containing 1024 samples, then the cross-correlation is calculated from the average of the inverse-FFT of the products between the FFT of each velocity record with the conjugate of the concurrent pressure record.

Color contour maps of the spatial cross-correlation coefficients between the wall-pressure fluctuations, and the streamwise- and normal-velocity components (R_{up_o} & R_{vp_o}) are illustrated in the top and bottom plots in Figure 4.27, respectively. The abscissa is the dimensionless streamwise location of the microphones and the ordinate is the height of the hotwire normalized by the boundary-layer thickness. In interpreting the results in Figure 4.27, the reader is reminded that at a given height, the results represent an *average* spatial wall-pressure pattern associated with the passage of flow structures past the location of the hotwire. If the structures registering at the probe were not responsible for any p' generation, their velocity signature would have no specific relationship to p', and hence the correlation would be zero everywhere, resulting in a vanishing pressure pattern. For example, consideration of R_{up_o} results at $y/\delta = 0.4$ show that on *average* p' is in phase with u' directly beneath the hotwire and that the peak in the pressure pattern is also found immediately below the velocity probe (since this is where the highest correlation is found for the probe height considered). In contrast, an out-of-phase pressure signature is found on average at a location that is approximately $0.5X_r$ upstream of the hotwire location. The combination of the p' peak and valley forms

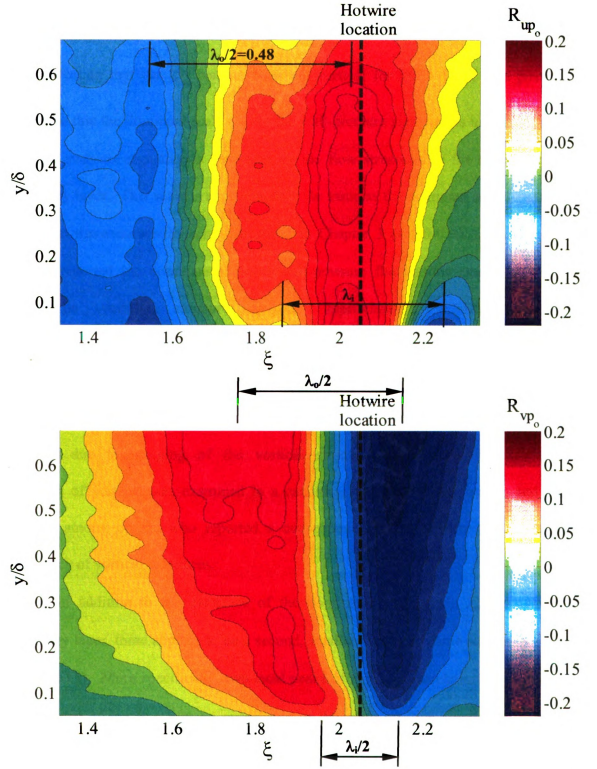

Figure 4.27. Contour plots of the cross-correlation coefficient at zero time shift between the streamwise (top plot) and normal (bottom plot) velocity and the wall-pressure at the location of the ten downstream most microphones (from ξ = 1.33 to 2.33)

a spatial wall-pressure signature with wavelength λ_o of approximately $0.96X_r$ (see Figure 4.27 for illustration).

Noting that the R_{up_o} contour lines are vertical for $y/\delta > 0.15$, it is possible to conclude that the dominant scale (λ_o) of the wall-pressure signature is invariant provided that the pressure signature is generated by the flow structures in the outer part of the boundary layer. This scale is approximately the same as the dominant wavelength found from the wavenumber-frequency spectrum in Chapter 3 ($\approx 0.8\text{-}0.9X_r$). Lee and Sung (2002) reported the dominant scale of wall-pressure fluctuations associated with the large-scale vortical structure to be approximately $0.54X_r$ within the separation/reattachment zone of a backward-facing step. This was slightly smaller than that reported by Kiya & Sasaki (1985), $0.6X_r$. The difference between the scale found in the present flow and the flow upstream of reattachment could be a result of the increase in size due to merging of the vortical structures as they travel downstream. Merging of vortices was examined in a canonical free shear layer by Ho and Huang (1982), among others, who reported a consequent increase in size and decrease in frequency of vortical structures.

In addition to the existence of the dominant length scale λ_o throughout the boundary layer, there appears to be a second, smaller, distinguishable scale near the wall ($y/\delta < 0.15$). More specifically, two local peaks of negative correlation are found at the lower edge of the R_{up_o} plot on either side of the main positive correlation lobe. The streamwise spacing of the two peaks gives rise to a length scale (λ_i; see Figure 4.27) that is about $\frac{1}{2}\lambda_o$. This suggests that the near-wall ($y/\delta < 0.15$) velocity fluctuations are on average associated with a p' signature of smaller scale than that associated with the outer-

shear layer motion. This hints to the existence of a smaller-scale wall-pressure-generating mechanism that is different in nature than being the direct footprint of the outer-shear layer structures (which are presumably associated with the λ_o scale). This mechanism, however, is expected to somehow still be related to the outer-shear layer structures since the analysis of the velocity-pressure cross spectra clearly revealed the negligible contribution of the sub-boundary layer structures to the velocity-pressure correlations even at the lowest y position (this was especially true when considering the u component of the flow velocity). It is noted here that this is the first occasion in this work that evidence of an important near-wall pressure source is identified. Subsequent analysis in this chapter will clarify the nature of this source and its relation to the large-scale vortices.

The R_{vp_o} results shown in the bottom plot of Figure 4.27 are consistent with the R_{up_o} results in revealing two characteristic streamwise length scales. These scales are reflected in the spacing between the negative and positive correlation lobes that dominate the correlation map. The spacing (λ_o) is large and fairly uniform throughout most of the y range, but it narrows down near the wall, as demonstrated by the labels in the figure. The value of λ_o obtained from the R_{vp_o} results is somewhat shorter ($\sim 0.8X_r$) than that estimated from the R_{up_o} data. On the other hand, the R_{vp_o} results seem to be "90 degrees out of phase" with the R_{up_o} results. In particular, when R_{up_o} shows a strong positive correlation, R_{vp_o} is zero. Similarly, when R_{vp_o} has a strong positive or negative correlation, R_{up_o} is zero. Additionally, unlike R_{up_o}, R_{vp_o} magnitude attenuates

quickly with decreasing height near the wall. This is consistent with the wall attenuation of v', referred to earlier in 4.1.2 and 4.2.1. Overall, the cross-correlation maps shown in Figure 4.27 show good qualitative match with those presented by Lee and Sung (2002) for the flow within the separation/reattachment zone of a backward-facing step.

The temporal cross-correlation between the streamwise and normal velocity components and wall-pressure fluctuations at three microphone locations similar to those selected for the cross-spectrum results earlier (ξ = 1.33, 2.0 and 2.33) are shown in Figures 4.28 and 4.29, respectively. Both figures depict color contour maps of the cross-correlation results. Note that positive time difference (τ) means that the occurrence of the velocity disturbance at the hotwire lags that of the corresponding pressure signature. In other words, positive τ refers to the past of the pressure data, and vice versa. The R_{up} plots in Figure 4.28 reflect the signature of a quasi-periodic disturbance with a dimensionless time scale (τ_o) of 1.8. This value is consistent with the frequency of the peak in the semi-log Φ_{up} plots shown in Figures 4.16, 4.18 and 4.20. That is, the frequency of the cross-spectrum peak was found to be approximately 0.55 which equals 1/1.8. On the other hand, the R_{vp} results (Figure 4.29) depict a somewhat smaller τ_o of 1.4. This value is also consistent with the somewhat higher-frequency ($\frac{f X_r}{U_\infty} \approx 0.7$) peak of the semi-log Φ_{vp} results given in Figures 4.22, 4.24 and 4.26. Moreover, the results are in agreement with the larger λ_o value found from the spatial R_{up_o} in comparison to that found from R_{vp_o}. It is also interesting to note that, consistent with the spatial

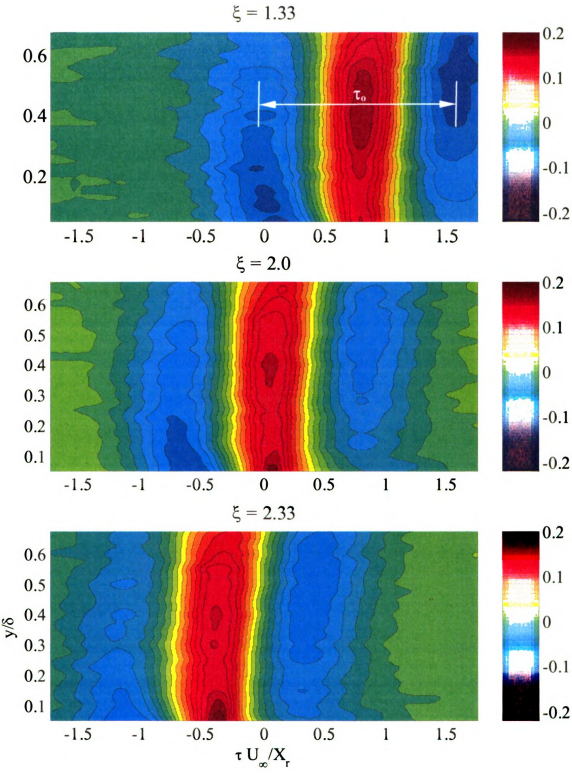

Figure 4.28. Maps of the cross-correlation coefficient between the streamwise velocity at $\xi = 2.05$ and wall-pressure at $\xi = 1.33$ (top plot), $\xi = 2.0$ (middle plot) and $\xi = 2.33$ (bottom plot)

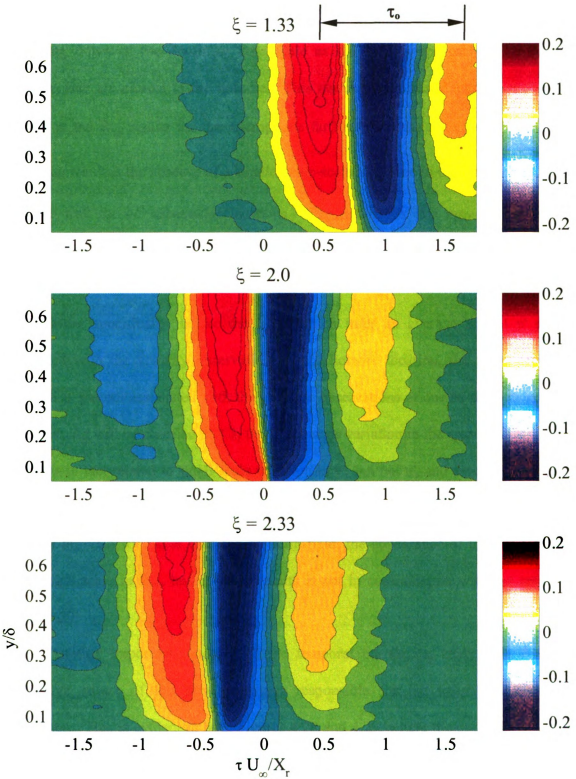

Figure 4.29. Maps of the cross-correlation coefficient between the normal velocity at ξ = 2.05 and wall-pressure at ξ = 1.33 (top plot), ξ = 2.0 (middle plot) and ξ = 2.33 (bottom plot)

correlation observation, the temporal correlation data of R_{vp} (Figure 4.29) do reveal a narrowing down of the dominant time scale as the wall is approached for the two locations that are closest to the hotwire. This narrowing of scale near the wall is not evident in the R_{vp} results for the microphone farthest from the hotwire (ξ = 1.33). A surprising result is the absence of a smaller time-scale signature in the temporal R_{up} data near the wall for *all* streamwise locations. The reason for this may be clarified by realizing that the physical interpretation of the temporal correlation results in Figures 2.28 and 2.29 is fundamentally different from that of the spatial correlation data in Figure 2.27. More specifically, unlike the latter which infer an average spatial p' pattern associated with the velocity observations at the hotwire location, the former reveal a temporal u' pattern associated with the pressure observations at one of three streamwise locations. As will be clarified in 4.3, the small-scale variation in the spatial wall-pressure pattern is in fact related to small-scale variation in v', but not u', and associated variation in near-wall, pressure sources. Thus, since Figures 4.28 and 4.29 should be interpreted in terms of the velocity rather than the pressure field, the appearance of the smaller near-wall length scale in R_{vp}, but not R_{up}, results is not in contradiction with the results in Figure 4.27.

Another important outcome of the temporal correlation analysis is the clear convective nature of the flow structures responsible for the velocity/wall-pressure correlation. This is evident in both Figures 4.28 and 4.29, where the correlation contour map retains the same shape while shifting towards negative time delay with increasing streamwise location of p' observation. Thus, one may estimate the convection velocity

of these structures by tracking the time delay ($\frac{\tau U_\infty}{X_r}$) at which a particular feature of the correlation map appears in the temporal R_{up} results for two microphones spaced by distance $\Delta\xi$. In this manner, the convection velocity would be estimated as $\Delta\xi$ divided by the change in the time delay. To choose a suitable feature in the correlation results, it is noted that correlation peaks tend to be broad and difficult to pin-point with good accuracy. Therefore, the zero-crossing of the R_{vp} results was selected as the feature to track since the gradient of the correlation results (with respect to τ) is substantially sharper than that associated with the R_{up} correlation. To demonstrate, the R_{vp} correlation results averaged over the heights $y/\delta = 0.375$ to 0.625 are shown in Figure 4.30 for three microphone locations of $\xi = 1.67$, 1.89, and 2.11. The averaging in y is employed to reduce any data scatter that may influence the ability to identify the zero crossing. Moreover, this average is conducted over a y range that is centered around the center of the outer shear layer (i.e., where $-\overline{u'v'}$ is max., or $y/\delta \approx 0.48$). Thus, the resulting convection velocity should be that of the large-scale vortices.

To obtain an average convection velocity over the streamwise extent of the ten most downstream microphones, the ξ location of each microphone is plotted versus the normalized time delay of the zero-crossing of the corresponding R_{vp} in Figure 4.31. The slope of a straight-line fit through the data yields a convection velocity value of $0.82U_\infty$. This agrees quite well with the convection velocity values extracted in Chapter 3 using various spatiotemporal statistical measures of the wall-pressure field, providing additional evidence that the convection velocity of the wall-pressure signature is in fact a direct reflection of the convection velocity of the outer-shear layer structures.

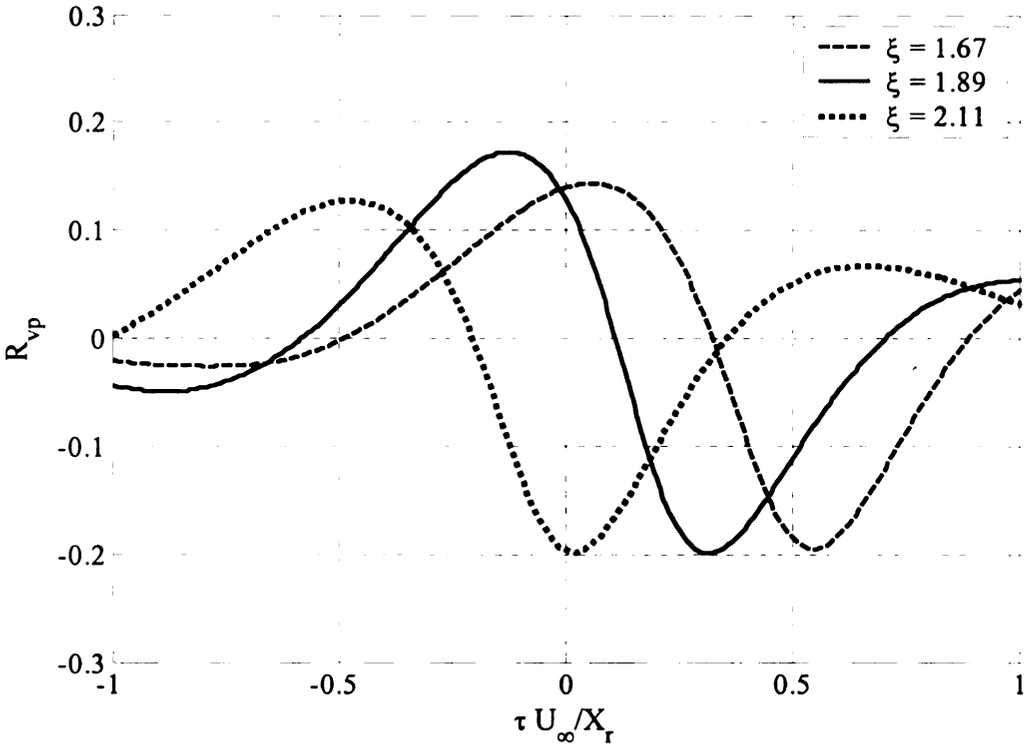

Figure 4.30. The average cross-correlation between the normal-velocity and wall-pressure in the range of $y/\delta = 0.375$ to 0.625, for $\xi = 1.67$, 1.89 and 2.11

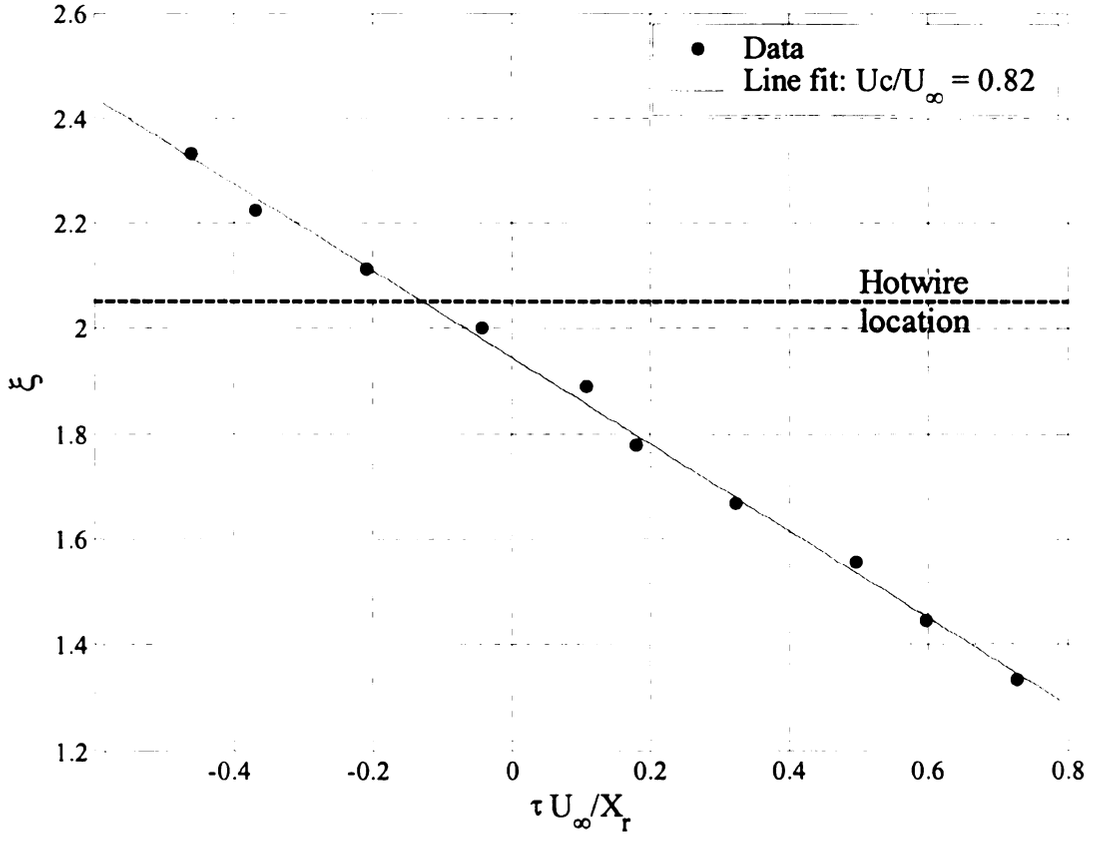

Figure 4.31. Plot for extraction of the convection velocity from R_{vp} results

4.2.3. Conditionally-Averaged-Data Analysis

To gain an understanding of the type of flow structures that produce the correlation results presented in the previous section, the conditionally averaged velocities (< u′ > & < v′ >) and wall-pressure fluctuations (< p′ > are examined here); where < > denotes the conditional, or ensemble, average of the quantity. Specifically, the interest here is in obtaining the conditionally averaged velocity vector measured by the X-hotwire when strong positive and negative pressure events occur at the microphone closest to the hotwire ($\xi = 2.0$). Because there is a small offset in the streamwise direction between the positions of the two sensors ($\Delta\xi = 0.05$), the pressure time series was delayed by an amount equal to $0.05/U_c$ ($U_c = 0.81U_\infty$) to approximate the wall-pressure information directly below the X-wire; i.e., at ξ location 0.05 farther downstream. Note that hereafter, all pressure and velocity time series will be low-pass filtered below $\frac{f X_r}{U_\infty} \approx 2.2$ to focus only on the structures in the frequency range that is most significant to the pressure fluctuations. Filtering was implemented in post processing using the "filtfilt" function of MatLab version 6.5. This routine filters the time series in the time-forward and -reverse directions to ensure that the filter response does not result in any phase lag of the filtered data. Additionally, both velocity and pressure time series were filtered.

To demonstrate the influence that the filtering process has on the p'-related flow features, the spatial and temporal cross-correlation results shown in Figures 4.27 through 4.29 were obtained again after low-pass filtering the data and the outcome is shown in Figures 4.32 through 4.34. Comparison between the results before and after filtering shows that with the exception of some smoothing of the contour plots and higher

correlation values, the overall correlation shape does not change as anticipated. Thus, the filtering will only aid in emphasizing the flow features that are most relevant to the wall-pressure generation process while removing the influences of the sub-boundary layer flow structures, which are insignificant for p' generation in the current flow field as demonstrated thus far.

The top and the bottom plots in Figure 4.35 illustrate the conditionally averaged mean-removed velocity fields associated with positive and negative wall-pressure peaks, respectively. The abscissa represents the dimensionless time ($\frac{\tau U_\infty}{X_r}$) whose zero-reference is the instant of the pressure peak occurrence. A plot of the conditionally averaged pressure $< p' >$ normalized by p_{rms} is provided directly below each of the vector fields for reference. The positive and negative pressure peaks where identified using the following process: whenever the p' time series value exceeded an arbitrarily selected threshold of $1.5p'_{rms}$, above or below zero, the time of occurrence of the closest local positive or negative peak, respectively, that exceeded the threshold was found. This corresponded to a time offset of zero, and the average of all velocity vectors occurring at all such instants for the entire velocity data record represents the result at $\frac{\tau U_\infty}{X_r} = 0$ in Figure 4.35. Other positive, or negative, values of τ represent the average velocity at the corresponding time delay, or advance, from the occurrence of the peak.

The top plot in Figure 4.35 depicts that the positive wall-pressure peak coincides with "inrush" of high-speed fluid towards the wall. The plot also illustrates that <u'> is positive in the vicinity of the positive wall-pressure peak but starts to switch to negative

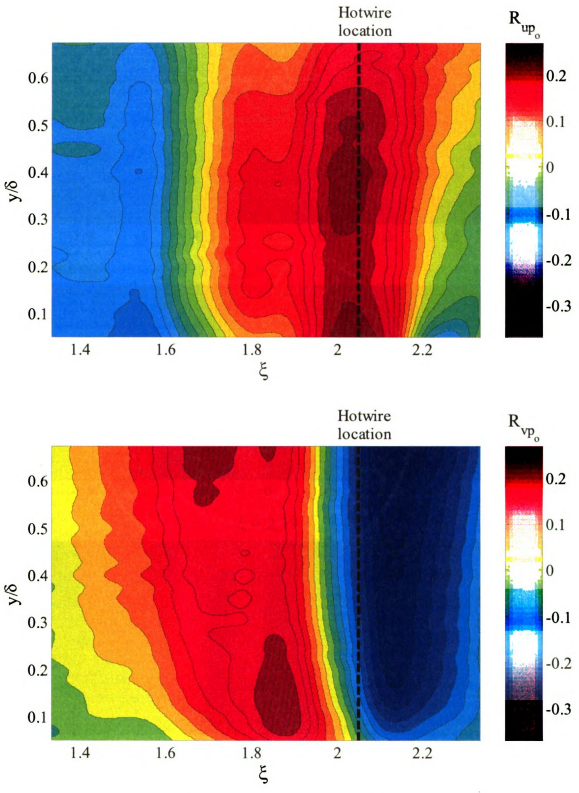

Figure 4.32. Contour plots of the cross-correlation coefficient at zero-time shift between the low-pass filtered streamwise (top plot) and normal (bottom plot) velocity and the wall-pressure at the ten downstream most microphones (from $\xi = 1.33$ to 2.33)

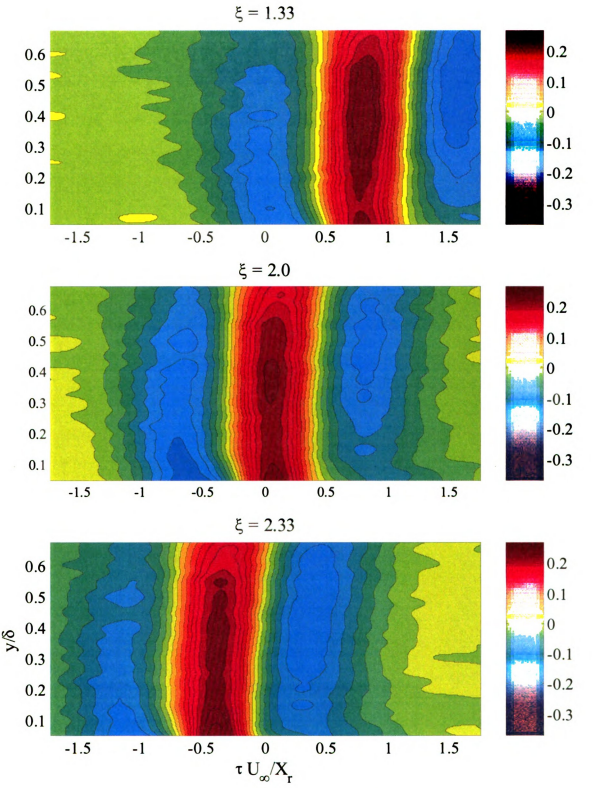

Figure 4.33. Maps of the cross-correlation coefficient between the low-pass filtered streamwise velocity at $\xi = 2.05$ and wall-pressure at $\xi = 1.33$ (top plot), $\xi = 2.0$ (middle plot) and $\xi = 2.33$ (bottom plot)

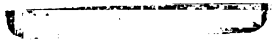

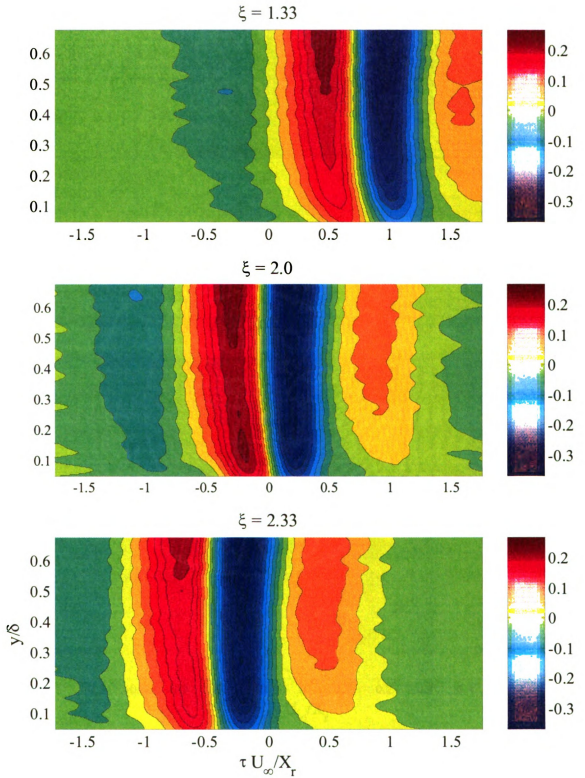

Figure 4.34. Maps of the cross-correlation coefficient between the low-pass filtered normal velocity at $\xi = 2.05$ and wall-pressure at $\xi = 1.33$ (top plot), $\xi = 2.0$ (middle plot) and $\xi = 2.33$ (bottom plot)

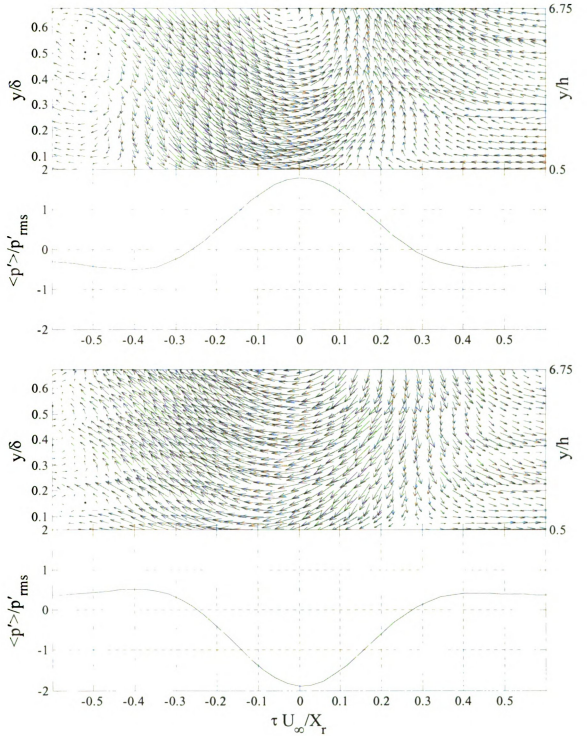

Figure 4.35. Wall-pressure, <p'>, and conditionally-averaged mean-removed velocity-vector field associated with positive (top plot) and negative (bottom plot) wall-pressure peaks at $\xi = 2.05$

values at $\frac{\tau U_\infty}{X_r} \approx 0.3$ and -0.5. In the flow over blunt flat plate, Kiya *et al.* (1982) and Kiya & Sasaki (1985) reported positive u′ fluctuation near the wall between successive vortices. They attributed the instantaneous excess in streamwise momentum near the wall to the penetration of the irrotational freestream fluid close to the wall in between the vortical structures. They also associated this region of the flow with the formation of saddle point, when viewed in a frame of reference that is translating with the convection velocity of the vortices.

The bottom plot in Figure 4.35 shows the conditional-velocity-vector field associated with negative wall-pressure peaks. As seen in the plot, the negative wall-pressure fluctuations seem to coincide with negative u′ fluctuation. This was also observed by Kiya *et al.* (1982) and Kiya & Sasaki (1985) who also indicated that the negative pressure coincided with the passage of a spanwise-vortex center, which is a significant source of low pressure.

The above discussion leads to the following simple scenario for the successive generation of positive and negative wall-pressure peaks. As the large-scale vortical structures of the outer-shear layer travel downstream, they entrain irrotational freestream fluid in between each pair of successive vortices. Accordingly, the accompanying interface between the irrotational flow in the freestream and the vortical structures moves up and down in the direction normal to the wall in synchronization with the passage of the vortices above a certain streamwise location. Specifically, when a vortex passes over a point of observation, it thickens the boundary layer leading to a streamwise momentum deficit across the boundary layer and associated negative wall pressure, as found above. On the other hand, the entrained irrotational flow between the vortices reduces the

boundary layer thickness and provides streamwise momentum excess. This coincides with the saddle points up and downstream of each vortical structure and is associated with the generation of positive wall pressure.

The x-momentum *deficit* and *excess* accompanying the passage of the vortex center and saddle point, respectively, are examined in Figure 4.36. The figure depicts a comparison between the mean streamwise-velocity profile and the conditionally averaged streamwise-velocity profiles at the instant of occurrence of the positive and negative p' peaks. The plot shows that the conditionally averaged streamwise-velocity profile associated with the positive wall-pressure peak has higher velocity at all heights included in the present measurements, which confirms the fact that positive pressure coincides with x-momentum excess across the boundary layer. On the other hand, the conditionally averaged profile synchronized with the negative wall-pressure peaks drops below the mean-velocity profile at all heights. The above results clarify some of the features of the spatial correlation results in Figure 4.32. In particular, the top plot in the figure shows a vertical positive R_{up} correlation lobe that extends across the entire y range at a ξ location of 2.05. Based on the analysis of the conditional streamwise-velocity profiles it is now clear that positive p' is associated with positive u' across the whole y range and vice versa, thus resulting in the vertical positive correlation lobe seen in Figure 4.32. The corresponding feature in the R_{vp} correlation (bottom of Figure 4.32) is a strong streamwise gradient of the correlation value that is associated with a switch in the correlation sign from positive to negative. This would be consistent with the scenario identified above that associates the pressure generation with vortex centers and saddle points. Both of these features are characterized with a switch in the direction of the v'

component from the upstream side of the source to the downstream one. In the following, the association of vortex centers and saddle points with wall-pressure peaks will be established more convincingly.

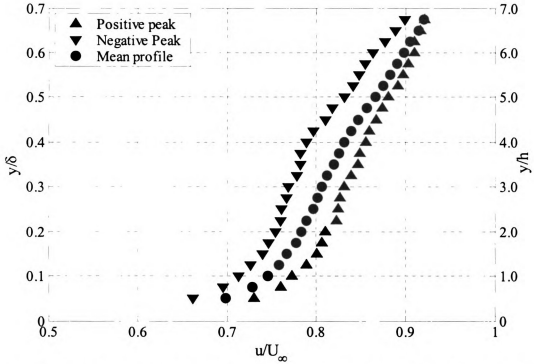

Figure 4.36. Comparison between the mean streamwise-velocity profile and the conditionally-averaged streamwise-velocity profiles associated with positive and negative wall-pressure peaks

Although Figure 4.35 illustrates the main features of the conditional velocity field and associated wall-pressure signature, it does not show the real physical picture of the flow structures. To obtain such a picture, the velocity vector field has to be viewed from a coordinate frame that moves with the convection velocity of the flow structures (Fiedler 1988). Fielder (1988) investigated this issue extensively and referred to the vector-field representation in Figure 4.35 as *triple-decomposition*, which is obtained by looking at the mean-removed velocity vector field in laboratory coordinates. However, he argued that

in order to obtain the velocity vector field that represents the real physical picture of the flow structures, one has to do a double-decomposition of the flow by viewing the total velocity vector field (mean + fluctuation) relative to an observer moving with the convection velocity of the flow structures. The top and the bottom plots of Figure 4.37 show the same results as in Figure 4.35 after adding the mean velocity and viewing the result in a frame of reference that is moving with a convection speed of $0.81U_\infty$. The top plot of the figure shows clear evidence of a saddle point that is synchronized with the positive wall-pressure peak directly below it, while the bottom plot provides a clear physical picture of a vortical structure with a center located directly above the negative wall-pressure peak. This provides a strong support for the central role played by the vortex structures and saddle points in the scenario of wall-pressure generation outlined earlier. Note that strictly speaking, because the abscissa in Figure 4.37 represents time rather than space, the results are indicative of the *passage* of the vortex structures and saddle points past the point of observation of the pressure, rather than the actual *spatial structure* of these features. However, as discussed in Chapter 3, it is believed that Taylor hypothesis of frozen turbulence holds fairly well for the large-scale vortices, and hence the results in Figure 4.37 are likely to represent well the actual spatial structure. A more quantitative assessment of this statement is provided in 4.3.

4.3. Stochastic Estimation

The above analysis has led to the identification of the quasi-periodic passage of the outer-shear layer vortices and saddle points resulting from their mutual interaction as the primary source of wall-pressure generation. Generally, the identification is based on

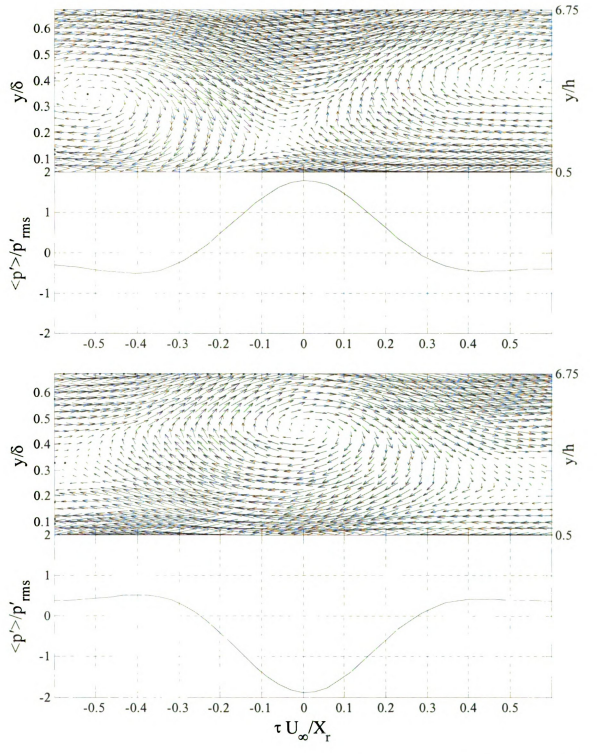

Figure 4.37. Wall-pressure, <p'>, and conditionally-averaged velocity-vector field associated with positive (top plot) and negative (bottom plot) wall-pressure peaks, viewed in a frame of reference moving with $0.81U_\infty$

time-averaged statistical information, which does not reveal an in-depth picture of the variation in the characteristics of the individual flow structures or the nature of the mechanism(s) leading to the wall-pressure generation. Hence, in this section an analysis is conducted using the stochastic estimation of the flow field based on the instantaneous p' signature across the ten most downstream microphones. As explained below, the procedure yields an estimate of the "quasi-instantaneous" velocity over the full y range of the measurements. Subsequent evolution in time of this estimate yields a picture of the quasi-instantaneous flow structures traveling past the streamwise location of the hotwire, which can be examined to reveal some of the variability in the individual flow structures and associated wall-pressure-producing mechanisms.

4.3.1. Principle and Equations

Application of the stochastic estimation technique for identification of organized, or coherent, motion in turbulent flows was first proposed by Adrian (1975) and then further refined by him and his coworkers (e.g. Tung and Adrian 1980). Since then, applications of stochastic estimation have expanded to range from the identification of the conditional eddies of isotropic turbulence, Adrian (1979) and Adrian & Moin (1988), to the extraction of the spatio-temporal flow field characteristics of turbulent boundary layer structures, Guezennec (1989) and Choi & Guezennec (1990). Classically, the stochastic estimation technique estimates any variable at one location in the flow from a known variable at some other location. However, and as pointed out in the objectives section, stochastic estimation is used in the present work to estimate the velocity field above the wall from its wall-pressure signature. In particular, the technique seeks to get the estimated velocity $u'_{i,s}(\vec{r}_o + \vec{r}, t + \tau)$ from a known wall-pressure $p'(\vec{r}_o, t)$;

where $\vec{r}_o$ is the position vector of the pressure-observation point, the components of which are x_o, 0 and z_o, in the streamwise, wall-normal and spanwise direction, respectively, $\vec{r}\,(x\text{-}x_o, y, z\text{-}z_o)$ and τ are the spatial-offset vector and time-shift between the estimated velocity and wall-pressure event, respectively, subscript i is the tensor index notation specifying the velocity component and subscript s is used to denote the stochastic estimate. Note that $u'_{i,s}(\vec{r}_o + \vec{r}, t+\tau)$ and $p'(\vec{r}_o, t)$ are the mean-removed values. The former is obtained from a Taylor-series expansion in terms of the latter as follows:

$$u'_{i,s}(\vec{r}_o + \vec{r}, t+\tau) = A_i(\vec{r}_o + \vec{r}, \tau)\, p'(\vec{r}_o, t) + B_i(\vec{r}_o + \vec{r}, \tau)\, p'^2(\vec{r}_o, t) + \cdots \qquad (4.5)$$

where, $A_i(\vec{r}_o + \vec{r}, \tau)$ and $B_i(\vec{r}_o + \vec{r}, \tau)$ are the estimation coefficients for the linear and quadratic terms in the expansion, respectively. Note that both coefficients depend on the location of observation of the event ($\vec{r}_o$) but not its time of occurrence (t). This is because the flow field considered is generally inhomogeneous and hence statistical properties of the flow in the vicinity of a particular event location ($\vec{r}_o$) will differ from those at another location. On the other hand, the flow is stationary in time, and therefore its statistical properties are independent of the time of occurrence of the event.

The primary goal of the stochastic estimation procedure is to obtain the coefficients A_i and B_i, so that the velocity field can be estimated from equation 4.5. If only the linear term in the equation is included in the estimation, it is known as Linear Stochastic Estimation (LSE). However, if the first two terms are included, the estimation is a Quadratic Stochastic Estimation (QSE). Note that both LSE and QSE can be implemented using wall-pressure conditions from multiple points in space

simultaneously, yielding a "multi-point" estimation. The multi-point estimate is generally more effective in capturing the "true" nature of the flow structures, and it is the one of primary focus here given the availability of multi-point information from the pressure-array data. The multi-point estimate will only be of the LSE type because of the complexity involved in obtaining a multi-point QSE. However, the results will be compared to those from single-point LSE and QSE. Derivation of the equations used to obtain the estimation coefficients for all of these cases is given below.

I. Single-Point LSE

As mentioned earlier, the single-point LSE (denoted by SL hereafter), provides a linear estimation of the conditional flow filed, $u'_s(\vec{r}_o + \vec{r}, t+\tau)$ from the wall-pressure, $p'(\vec{r}_o, t)$. For brevity, the following analysis will only consider the x-component of the velocity, but the resulting equations are the same for the y-component. The estimated u' is calculated from the following equation:

$$u'_s(\vec{r}_o + \vec{r}, t+\tau) = A_{u,\,lin}(\vec{r}_o + \vec{r}, \tau)\, p'(\vec{r}_o, t) \tag{4.6}$$

where, $A_{u,\,lin}$ is the coefficient of the linear estimate of u'. This is determined such that the long-time mean squared error between the velocity and its estimate, $e(\vec{r}_o + \vec{r})$, is minimized. This is the maximum likehood estimate, assuming a Gaussian distribution of the error about the estimate. Explicitly, at a specific location within the flow domain the mean squared error is:

$$\begin{aligned} e(\vec{r}_o + \vec{r}) &= \overline{\left(u'_s(\vec{r}_o + \vec{r}, t+\tau) - u'(\vec{r}_o + \vec{r}, t+\tau)\right)^2} \\ &= \overline{\left(A_{u,\,lin}\, p'(r_o, t) - u'(\vec{r}_o + \vec{r}, t+\tau)\right)^2} \end{aligned} \tag{4.7}$$

where, the overbar denotes time averaging. The value of $A_{u,lin}$ that minimizes the error may be found then by requiring:

$$\frac{de}{dA_{u,lin}} = \frac{d}{dA_{u,lin}}\left[\overline{\left(A_{u,lin}\, p'(\vec{r}_o,t) - u'(\vec{r}_o+\vec{r},t+\tau)\right)^2}\right] = 0 \tag{4.8}$$

Exchanging the order of the derivative and time integration operations:

$$\begin{aligned}
&\frac{d}{dA_{u,lin}}\overline{\left[\left(A_{u,lin}\, p'(\vec{r}_o,t) - u'(\vec{r}_o+\vec{r},t+\tau)\right)^2\right]} \\
&= \overline{2\left(A_{u,lin}\, p'^2(\vec{r}_o,t) - u'(\vec{r}_o+\vec{r},t+\tau)\times p'(\vec{r}_o,t)\right)} \\
&= \left(A_{u,lin}\,\overline{p'^2(\vec{r}_o,t)} - \overline{u'(\vec{r}_o+\vec{r},t+\tau)p'(\vec{r}_o,t)}\right) = 0
\end{aligned} \tag{4.9}$$

Equation 4.9 is satisfied if

$$A_{u,lin} = \frac{\overline{u'(\vec{r}_o+\vec{r},t+\tau)\,p'(\vec{r}_o,t)}}{\overline{p'^2(\vec{r}_o,t)}} = \frac{\overline{u'(\vec{r}_o+\vec{r},t+\tau)\,p'(\vec{r}_o,t)}}{p'^2_{rms}(\vec{r}_o,t)} \tag{4.10}$$

Inspection of Equation 4.10 shows that $A_{u,lin}$ equals the ratio between the cross-correlation of u' and p', at a time delay corresponding to the delay between the estimate and the event, and the square of the root-mean-square, or second PDF moment, of the wall-pressure. Equations 4.6 and 4.10 yield the final form of the equations employed for SL estimation:

$$u'_s = \left(\frac{\overline{u'(\vec{r}_o+\vec{r},t+\tau)\,p'(\vec{r}_o,t)}}{p'^2_{rms}(\vec{r}_o,t)}\right)p' \quad \& \quad v'_s = \left(\frac{\overline{v'(\vec{r}_o+\vec{r},t+\tau)\,p'(\vec{r}_o,t)}}{p'^2_{rms}(\vec{r}_o,t)}\right)p' \tag{4.11}$$

II. Single-Point QSE

Similar to the single-point LSE, SL, the single-point QSE will be denoted by SQ. Based on equation 4.5, the main equation for obtaining the SQ estimate is given by:

$$u'_s(\vec{r}_o+\vec{r},t+\tau) = A_{u,quad}(\vec{r}_o+\vec{r},\tau)\,p'(\vec{r}_o,t) + B_u(\vec{r}_o+\vec{r},\tau)\,p'^2(\vec{r}_o,t) \tag{4.12}$$

where, $A_{u,quad}$ and B_u are the unknown coefficients of the first- and second-order terms for the SQ method. Similar to SL, those coefficients are determined by a least square error minimization process:

$$e(\vec{r}_o + \vec{r}) = \overline{\left(A_{u,quad}\, p'(r_o,t) + B_u p'^2(r_o,t) - u'(\vec{r}_o + \vec{r}, t+\tau)\right)^2} \tag{4.13}$$

By taking the derivative of Equation 4.13 with respect to $A_{u,quad}$ and B_u individually and equating the result of each to zero, the error is minimized in a least-square sense:

$$\begin{aligned}\frac{de}{dA_{u,quad}} &= \frac{d}{dA_{u,quad}}\left[\overline{\left(A_{u,quad}\, p'(\vec{r}_o,t) + B_u p'^2(\vec{r}_o,t) - u'(\vec{r}_o + \vec{r}, t+\tau)\right)^2}\right] \\ &= \overline{\frac{d}{dA_{u,quad}}\left[\left(A_{u,quad}\, p'(\vec{r}_o,t) + B_u p'^2(\vec{r}_o,t) - u'(\vec{r}_o + \vec{r}, t+\tau)\right)^2\right]} \\ &= \overline{2\left(A_{u,quad}\, p' + B_u p'^2 - u'\right)\times p'} = \left(A_{u,quad}\,\overline{p'^2} + B_u \overline{p'^3} - \overline{u'p'}\right) = 0\end{aligned} \tag{4.14}$$

$$\begin{aligned}\frac{de}{dB_u} &= \frac{d}{dB_u}\left[\overline{\left(A_{u,quad}\, p'(\vec{r}_o,t) + B_u p'^2(\vec{r}_o,t) - u'(\vec{r}_o + \vec{r}, t+\tau)\right)^2}\right] \\ &= \overline{\frac{d}{dB_u}\left[\left(A_{u,quad}\, p'(\vec{r}_o,t) + B_u p'^2(\vec{r}_o,t) - u'(\vec{r}_o + \vec{r}, t+\tau)\right)^2\right]} \\ &= \overline{2\left(A_{u,quad}\, p'(\vec{r}_o,t) + B_u p'^2(\vec{r}_o,t) - u'(\vec{r}_o + \vec{r}, t+\tau)\right)\times p'^2(\vec{r}_o,t)} \\ &= \left(A_{u,quad}\,\overline{p'^3(\vec{r}_o,t)} + B_u \overline{p'^4(\vec{r}_o,t)} - \overline{u'(\vec{r}_o + \vec{r}, t+\tau)\, p'^2(\vec{r}_o,t)}\right) = 0\end{aligned} \tag{4.15}$$

Solving Equations 4.14 and 4.15 for $A_{u,quad}$ and B_u gives:

$$B_u = \frac{\overline{p'^2(\vec{r}_o,t)}\;\overline{u'(\vec{r}_o + \vec{r}, t+\tau)\, p'^2(\vec{r}_o,t)} - \overline{p'^3(\vec{r}_o,t)}\;\overline{u'(\vec{r}_o + \vec{r}, t+\tau) p'(\vec{r}_o,t)}}{\left(\overline{p'^3(\vec{r}_o,t)}\right)^2 - \overline{p'^4(\vec{r}_o,t)}\;\overline{p'^2(\vec{r}_o,t)}} \tag{4.16}$$

$$A_{u,quad} = \frac{\overline{u'(\vec{r}_o + \vec{r}, t+\tau)\, p'(\vec{r}_o,t)} - B_u \overline{p'^3(\vec{r}_o,t)}}{\overline{p'^2(\vec{r}_o,t)}} \tag{4.17}$$

Similarly, the coefficients for the v-component estimation are given by:

$$B_v = \frac{\overline{p'^2(\vec{r}_o,t)}\;\overline{v'(\vec{r}_o + \vec{r}, t+\tau)\, p'^2(\vec{r}_o,t)} - \overline{p'^3(\vec{r}_o,t)}\;\overline{v'(\vec{r}_o + \vec{r}, t+\tau)\, p'(\vec{r}_o,t)}}{\left(\overline{p'^3(\vec{r}_o,t)}\right)^2 - \overline{p'^4(\vec{r}_o,t)}\;\overline{p'^2(\vec{r}_o,t)}} \tag{4.18}$$

$$A_{v,quad} = \frac{\overline{v'(\vec{r}_o + \vec{r}, t+\tau)\, p'(\vec{r}_o,t)} - B_v \overline{p'^3(\vec{r}_o,t)}}{\overline{p'^2(\vec{r}_o,t)}} \tag{4.19}$$

III. Multi-Point LSE

Multi-point LSE, or ML, is essentially based on a weighted linear combination of wall-pressure events at multiple points in space. In the present study ML uses ten points on the wall, corresponding to the ten downstream most microphones. In this case, the relation between the estimated velocity and wall-pressure can be stated as:

$$u'_s = A_{u1}\, p'_1 + A_{u2}\, p'_2 + A_{u3}\, p'_3 + \cdots + A_{u10}\, p'_{10} \tag{4.20}$$

where, A_{u1}, A_{u2},...A_{u10} are the unknown coefficients of the estimation. Note that microphone #1 is located at $\xi = 1.33$ and microphone #10 is the most downstream one ($\xi = 2.33$). Similar to the procedure of SL and SQ, those coefficients are determined by minimizing the mean squared error, e, between the estimate and the actual velocity:

$$e = \overline{\left(A_{u1}\, p'_1 + A_{u2}\, p'_2 + A_{u3}\, p'_3 + \cdots + A_{u10}\, p'_{10} - u'\right)^2} \tag{4.21}$$

To obtain A_{u1}, the derivative of Equation 4.21 with respect to A_{u1} is set to zero, leading to:

$$\begin{aligned} \frac{de}{dA_{u1}} &= \frac{d}{dA_{u1}}\left[\overline{\left(A_{u1}\, p'_1 + A_{u2}\, p'_2 + A_{u3}\, p'_3 + \cdots + A_{u10}\, p'_{10} - u'\right)^2}\right] \\ &= \overline{\frac{d}{dA_{u1}}\left[\left(A_{u1}\, p'_1 + A_{u2}\, p'_2 + A_{u3}\, p'_3 + \cdots + A_{u10}\, p'_{10} - u'\right)^2\right]} \\ &= 2\overline{\left(A_{u1}\, p'_1 + A_{u2}\, p'_2 + A_{u3}\, p'_3 + \cdots + A_{u10}\, p'_{10} - u'\right) \times p'} = 0 \end{aligned} \tag{4.22}$$

Rearranging equation 4.22 and applying the same procedure to the rest of the microphones:

$$\begin{aligned} &\left(A_{u1}\, \overline{p'_1 p'_1} + A_{u2}\, \overline{p'_1 p'_2} + A_{u3}\, \overline{p'_1 p'_3} + \cdots + A_{u10}\, \overline{p'_1 p'_{10}}\right) = \overline{u' p'_1} \\ &\left(A_{u1}\, \overline{p'_2 p'_1} + A_{u2}\, \overline{p'_2 p'_2} + A_{u3}\, \overline{p'_2 p'_3} + \cdots + A_{u10}\, \overline{p'_2 p'_{10}}\right) = \overline{u' p'_2} \\ &\qquad\qquad \vdots \\ &\left(A_{u1}\, \overline{p'_{10} p'_1} + A_{u2}\, \overline{p'_{10} p'_2} + A_{u3}\, \overline{p'_{10} p'_3} + \cdots + A_{u10}\, \overline{p'_{10} p'_{10}}\right) = \overline{u' p'_{10}} \end{aligned} \tag{4.23}$$

The equation set 4.23 can be reorganized using matrix notation as follows:

$$\begin{bmatrix} \overline{p_1'p_1'} & \overline{p_1'p_2'} & \overline{p_1'p_3'} & \cdots & \overline{p_1'p_{10}'} \\ \overline{p_2'p_1'} & \overline{p_2'p_2'} & \overline{p_2'p_3'} & \cdots & \overline{p_2'p_{10}'} \\ \overline{p_3'p_1'} & \overline{p_3'p_2'} & \overline{p_3'p_3'} & \cdots & \overline{p_3'p_{10}'} \\ \vdots & \vdots & \vdots & \ddots & \vdots \\ \overline{p_{10}'p_1'} & \overline{p_{10}'p_2'} & \overline{p_{10}'p_3'} & \cdots & \overline{p_{10}'p_{10}'} \end{bmatrix} \begin{bmatrix} A_{u1} \\ A_{u2} \\ A_{u3} \\ \vdots \\ A_{u10} \end{bmatrix} = \begin{bmatrix} \overline{u'p_1'} \\ \overline{u'p_2'} \\ \overline{u'p_3'} \\ \vdots \\ \overline{u'p_{10}'} \end{bmatrix} \tag{4.24}$$

and then the coefficients can be calculated from:

$$\begin{bmatrix} A_{u1} \\ A_{u2} \\ A_{u3} \\ \vdots \\ A_{u10} \end{bmatrix} = \begin{bmatrix} \overline{p_1'p_1'} & \overline{p_1'p_2'} & \overline{p_1'p_3'} & \cdots & \overline{p_1'p_{10}'} \\ \overline{p_2'p_1'} & \overline{p_2'p_2'} & \overline{p_2'p_3'} & \cdots & \overline{p_2'p_{10}'} \\ \overline{p_3'p_1'} & \overline{p_3'p_2'} & \overline{p_3'p_3'} & \cdots & \overline{p_3'p_{10}'} \\ \vdots & \vdots & \vdots & \ddots & \vdots \\ \overline{p_{10}'p_1'} & \overline{p_{10}'p_2'} & \overline{p_{10}'p_3'} & \cdots & \overline{p_{10}'p_{10}'} \end{bmatrix}^{-1} \begin{bmatrix} \overline{u'p_1'} \\ \overline{u'p_2'} \\ \overline{u'p_3'} \\ \vdots \\ \overline{u'p_{10}'} \end{bmatrix} \tag{4.25}$$

Similarly the coefficients for ML estimation of v' are given by:

$$\begin{bmatrix} A_{v1} \\ A_{v2} \\ A_{v3} \\ \vdots \\ A_{v10} \end{bmatrix} = \begin{bmatrix} \overline{p_1'p_1'} & \overline{p_1'p_2'} & \overline{p_1'p_3'} & \cdots & \overline{p_1'p_{10}'} \\ \overline{p_2'p_1'} & \overline{p_2'p_2'} & \overline{p_2'p_3'} & \cdots & \overline{p_2'p_{10}'} \\ \overline{p_3'p_1'} & \overline{p_3'p_2'} & \overline{p_3'p_3'} & \cdots & \overline{p_3'p_{10}'} \\ \vdots & \vdots & \vdots & \ddots & \vdots \\ \overline{p_{10}'p_1'} & \overline{p_{10}'p_2'} & \overline{p_{10}'p_3'} & \cdots & \overline{p_{10}'p_{10}'} \end{bmatrix}^{-1} \begin{bmatrix} \overline{v'p_1'} \\ \overline{v'p_2'} \\ \overline{v'p_3'} \\ \vdots \\ \overline{v'p_{10}'} \end{bmatrix} \tag{4.26}$$

The inverse matrix in equations 4.25 and 4.26 (first matrix on the right hand side) is calculated from the wall-pressure measurements alone and it contains information on the two-point correlation among the data from all microphones. The second matrix on the right hand side of the equations represents the cross-correlation between the velocity component to be estimated and the wall-pressure at all microphones. The values of these cross-correlations at different heights are represented in the cross-correlation maps shown

in Figure 4.33. Note, though, that the values in the figure are normalized by the corresponding root-mean-square values of the velocity and pressure; i.e., they represent a correlation *coefficient*.

It is interesting to note that the estimation of the conditional velocity vector field, using any of the three stochastic estimation methods, is obtained from unconditional statistics, which are the p'-p', u'-p' and v'-p' two-point correlations. By comparing the conventional conditional average with stochastic estimation, it is found that the bulk processing in stochastic estimation, involving the calculation of the stochastic estimation coefficients, is conducted only once no matter what the number of conditions to be investigated is. This makes the method substantially more efficient than the conventional conditional average when dealing with large two- or three-dimensional databases (Guezennec 1989); though this gain in efficiency may be at the expense of some reduction in accuracy if the estimation does not converge to the conditional average using a linear or a quadratic estimation.

4.3.2. Comparison Between ML, SL and SQ

In order to assess their capability of estimating the velocity field, the results of three different estimation methods ML, SL and SQ are compared in this section. The assessment is based on correlation of the stochastically-estimated velocity vector field with that of the measured velocity. In addition, the auto-spectra of the measured streamwise- and normal-velocity are compared with those of their stochastically-estimated counterpart. Moreover, the effect of the microphone location on the estimation is examined for the cases involving single-point estimation. In this examination, the upstream (at ξ = 2.0) and downstream (at ξ = 2.11) microphones closest to the hotwire

location are used, and will be denoted hereafter by subscripts 1 and 2, respectively. Specifically, SL_1 and SL_2 refer to the single-point LSE based on the wall-pressure data at $\xi = 2.0$ and $\xi = 2.11$, respectively, while SQ_2 denotes the single-point QSE based on the data from the microphone located at $\xi = 2.11$.

To compare the different estimation methods, the correlation coefficient between the measured streamwise- (C_u) and normal-velocity (C_v) time series and the corresponding stochastically estimated time series are evaluated at all heights for the four different estimation methods (ML, SL1, SL2 and SQ2). The results are shown in the top and bottom plots in Figure 4.38, respectively. In general, the distributions depict the streamwise- and normal-velocity estimated using ML to be better correlated with the measured values than those obtained using single-point estimation. On the other hand, comparison among the single-point methods reveals that whereas SL_1 provides the best estimation results of u' (i.e., highest C_u value), the corresponding v' estimation is poor across the boundary layer. This is caused by the low v'-p' correlation for the pressure data obtained at $\xi = 2.0$, as seen from Figure 4.32. By utilizing the microphone at $\xi = 2.11$ in the estimation (SL_2 results), where the v'-p' correlation is higher, a significant improvement in the single-point estimation of v' is found, as reflected in the increase in C_v (see Figure 4.38, bottom). The enhancement in v' estimation is accompanied by a small deterioration in u' estimation, because of a decrease in the u'-p' correlation associated with the microphone at $\xi = 2.11$. These results highlight one of the main disadvantages of single-point estimation relative to that based on multiple points. More specifically, single-point estimations exhibit sensitivity to the location of observation of

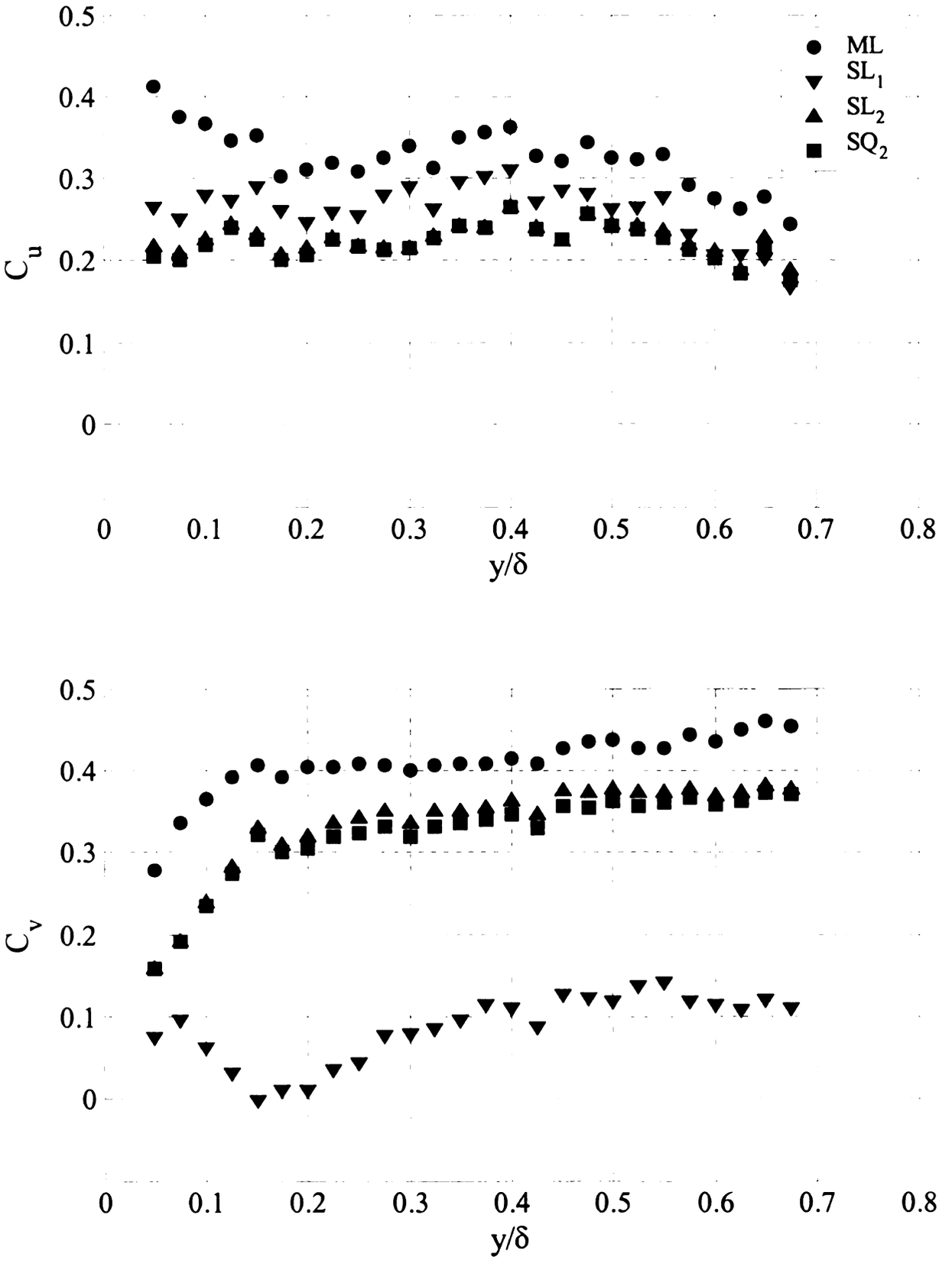

Figure 4.38. Correlation coefficient between the measured and stochastically-estimated streamwise- (top plot) and normal- (bottom plot) velocity using ML, SL_1, SL_2 and SQ_2

the event, and hence in order to obtain a good estimation one must select a location where a high u'-p' and v'-p' correlations are maintained simultaneously. In contrast, in ML, the estimations from all points of observations are superposed such that p' information at locations with high velocity-pressure correlations automatically compensate for information at points where the correlation is low.

Another point of interest in relation to the data shown in Figure 4.38 is the comparison between the SL_2 and SQ_2 results. As evident, both methods provide an equally good estimation, yielding similar C_u and C_v values across the flow. This suggests that the inclusion of the quadratic term does not provide substantial improvement in the estimation for the current flow. Therefore, it was not worth a while to pursue the substantially more complicated multi-point QSE in this study.

To examine the spectral agreement between the measured and stochastically-estimated streamwise- (u'_s) and normal-velocity (v'_s), a comparison between their spectra is presented in Figure 4.39 and 4.40, respectively, for y/δ = 0.05, 0.125, 0.25, 0.375, 0.5 and 0.625. The abscissa and ordinate represent the dimensionless frequency ($\frac{f X_r}{U_\infty}$) and the dimensionless velocity spectrum ($\frac{\Phi_{uu}}{U_\infty^2}$ and $\frac{\Phi_{vv}}{U_\infty^2}$), respectively. In general, the spectra in Figures 4.39 and 4.40 show that the spectra of the estimated velocities qualitatively posses the same shape as the actual spectra but with an attenuation in the energy content. The least attenuation is found in the ML case (particularly within the frequency range corresponding to the peak pressure fluctuations, $\frac{f X_r}{U_\infty} \approx 0.7$), giving

additional evidence for the ability of the multi-point estimation to provide a better estimation of the velocity field.

The above analysis, although highlighting the advantage of ML versus SL estimation, does not shed light on the accuracy of the estimation in calculating the conditional average of the velocity. In order to assess the accuracy of the estimates, one must compare the estimated values to those obtained from conditional averaging. For the ML estimation, it is practically impossible to achieve such a comparison. To elaborate, the reader is reminded that the ML estimation at a given point in time corresponds to the average velocity associated with the specific pressure pattern "seen" by the ten downstream most microphones. In order to obtain the conditional average corresponding to this pattern, one must search the wall-pressure data records for a large number of "exactly" similar pressure patterns with the same pressure values seen by each of the ten microphones, which would be quite difficult to achieve. Therefore, the estimation accuracy will only be assessed here for single-point estimation, with the understanding that the accuracy of the ML estimation is expected to be at least the same, if not better.

In order to examine the accuracy of the single-point estimates, the conditionally-averaged ($\langle u' \rangle$ & $\langle v' \rangle$) and the estimated streamwise (u_s) and normal (v_s) velocities using SL_2 and SQ_2 are calculated for different values of the pressure condition (p'). In particular, $\langle u' \rangle$ and $\langle v' \rangle$ are obtained by averaging u' and v', respectively, at times when the wall-pressure value falls within a window of $0.5p_{rms}$ centered around the p' condition value. By repeating this process for different values of p' that cover the whole range of wall-pressure fluctuations, the dependence of $\langle u' \rangle$ and $\langle v' \rangle$ on p' can be examined.

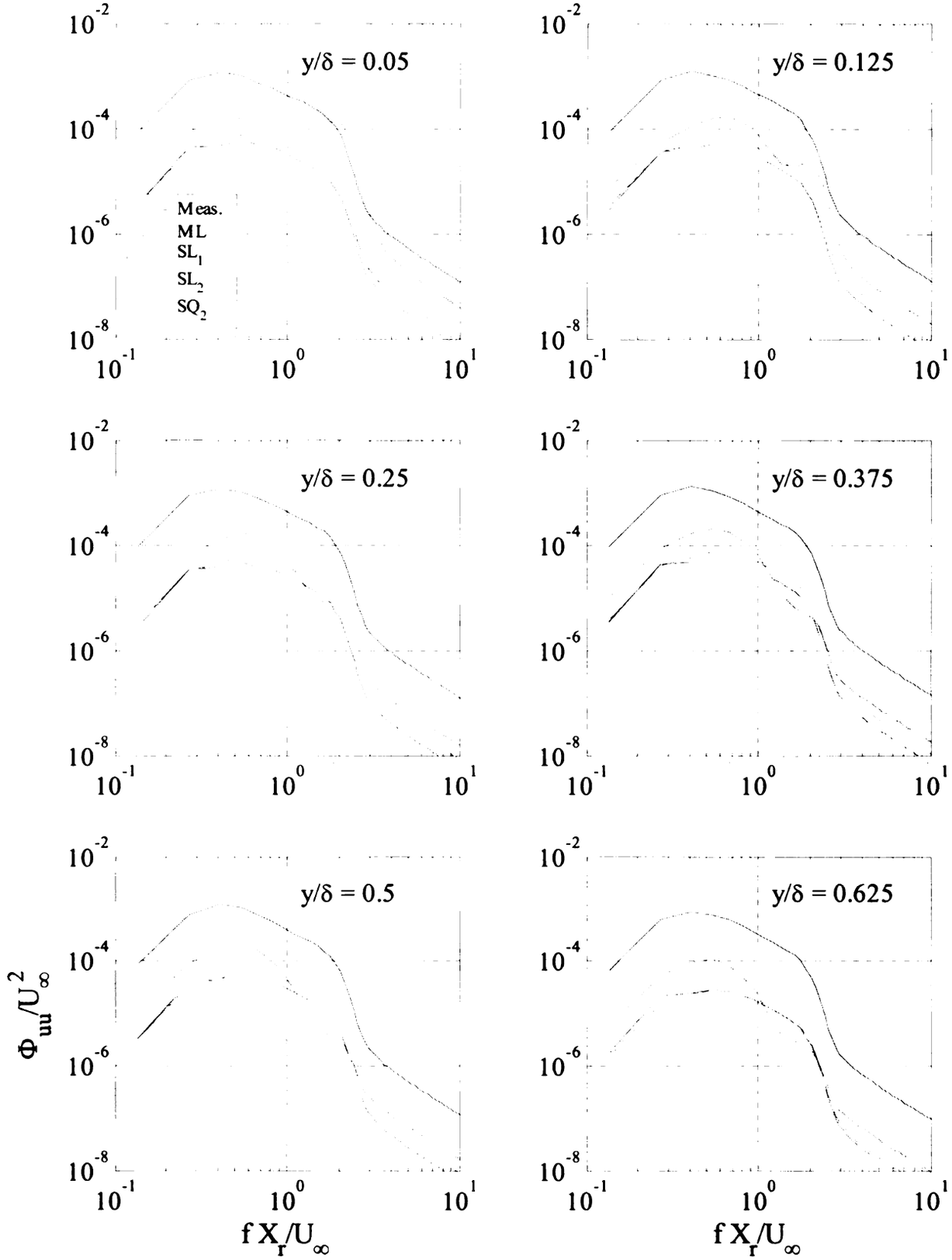

Figure 4.39. Comparison between the measured and stochastically-estimated streamwise-velocity spectra using ML, SL_1, SL_2 and SQ_2 for y/δ = 0.05, 0.125, 0.25, 0.375, 0.5 and 0.625

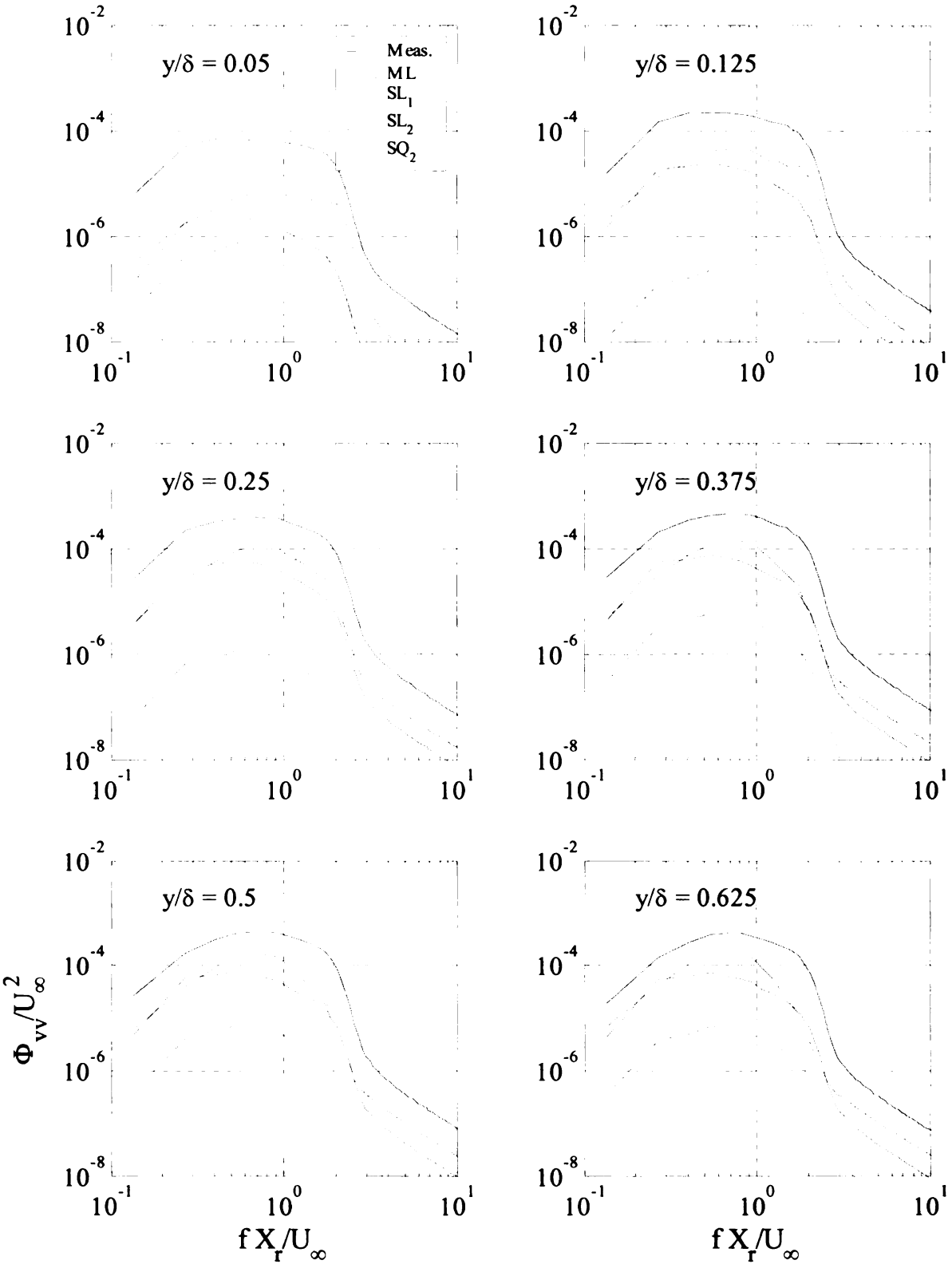

Figure 4.40. Comparison between the measured and stochastically-estimated normal-velocity spectra using ML, SL_1, SL_2 and SQ_2 for y/δ = 0.05, 0.125, 0.25, 0.375, 0.5 and 0.625

Figures 4.41 and 4.42 depict a comparison between <u'> and <v'>, and u_s and v_s calculated using the linear and quadratic estimation methods (SL_2 and SQ_2, respectively) as a function of the wall-pressure condition at $\xi = 2.11$ for $y/\delta = 0.05$, 0.125, 0.25, 0.375, 0.5 and 0.625. In Figure 4.41, the ordinate represents $<u'>/u_{rms}$ and u_s/u_{rms} while the abscissa is p'/p_{rms}. It should be noted that <u'> is calculated for a wall-pressure range of $\pm 2.25 p_{rms}$, which is found to contain more than 90% of the observed wall-pressure values. Generally, Figure 4.41 shows the attenuation in both the conditionally-averaged and estimated velocities; i.e., the largest positive or negative value of <u'> and u_s is approximately $0.5u_{rms}$. More importantly, the figure shows that, for a wall-pressure range of $\pm p_{rms}$, the values of u_s calculated using SL_2 and SQ_2 agree well with those of <u'> for all heights, and that SQ_2 does not provide any improvement in the accuracy of the estimate. On the other hand, when the magnitude of p' exceeds or drops below p_{rms}, a deviation is seen between the linear estimate and the conditional average. This deviation, however, does not exceed 20% of u_{rms}, which indicates that within the entire range of pressure conditions, the SL estimation accuracy is better than 80% of u_{rms}.

The deviation between the linear estimate and the conditional average when $|p'| > p_{rms}$ seems to be odd; i.e., the estimate overpredicts the average for $p' > p_{rms}$ and underpredicts it for $p' < -p_{rms}$. This odd deviation, which may be accounted for by the inclusion of a cubic term in the estimation, seems to increase as the height decreases. In other words, the results suggest that including a cubic term in the estimation should improve the accuracy of the results beyond the 80% obtained when truncating the estimation after the linear term. The inclusion of this higher order term will not be pursued here, however.

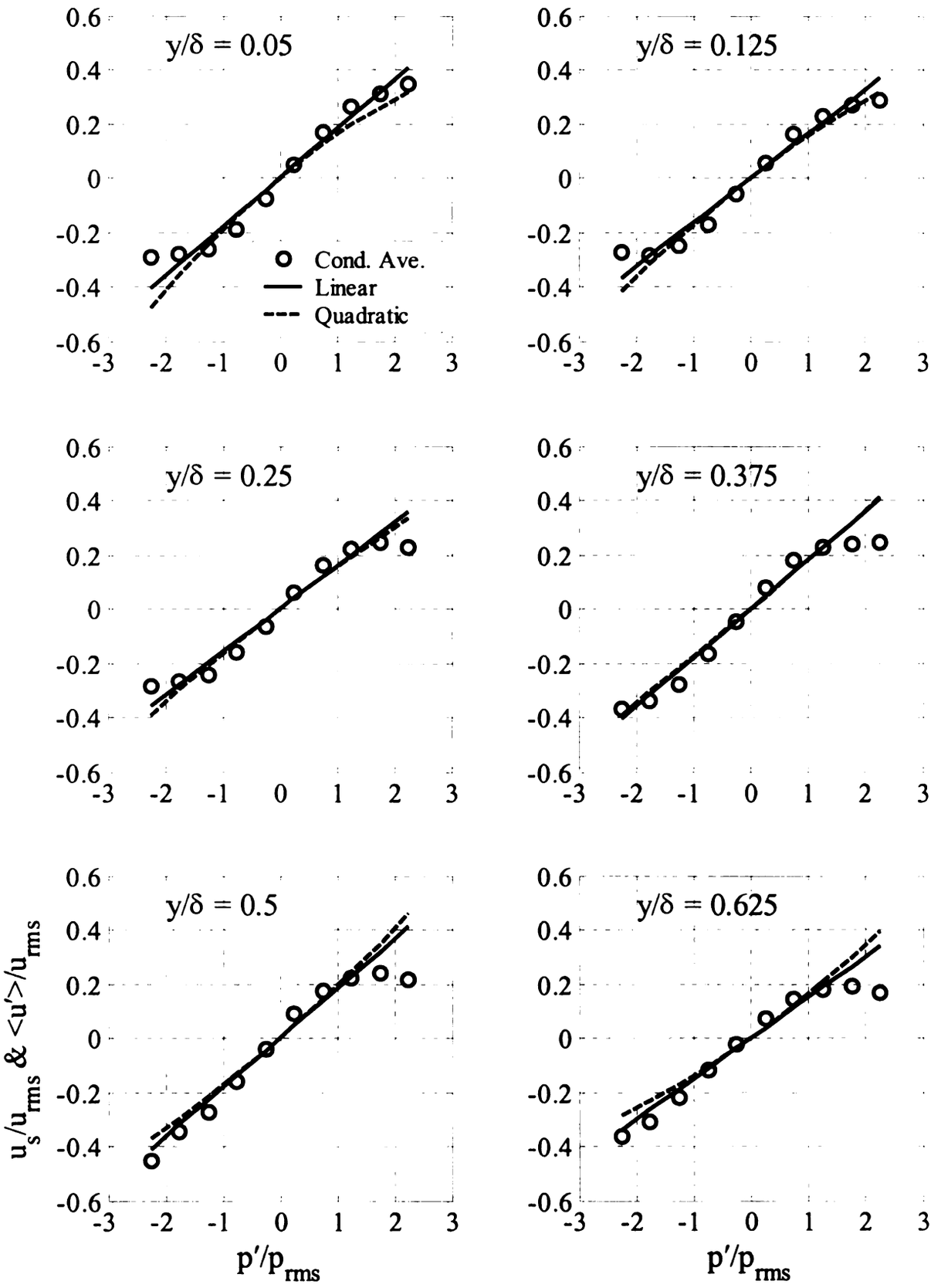

Figure 4.41. Comparison of the conditionally-averaged and stochastically-estimated streamwise-velocity using SL_2 and SQ_2 for $y/\delta = 0.05$, 0.125, 0.25, 0.375, 0.5 and 0.625

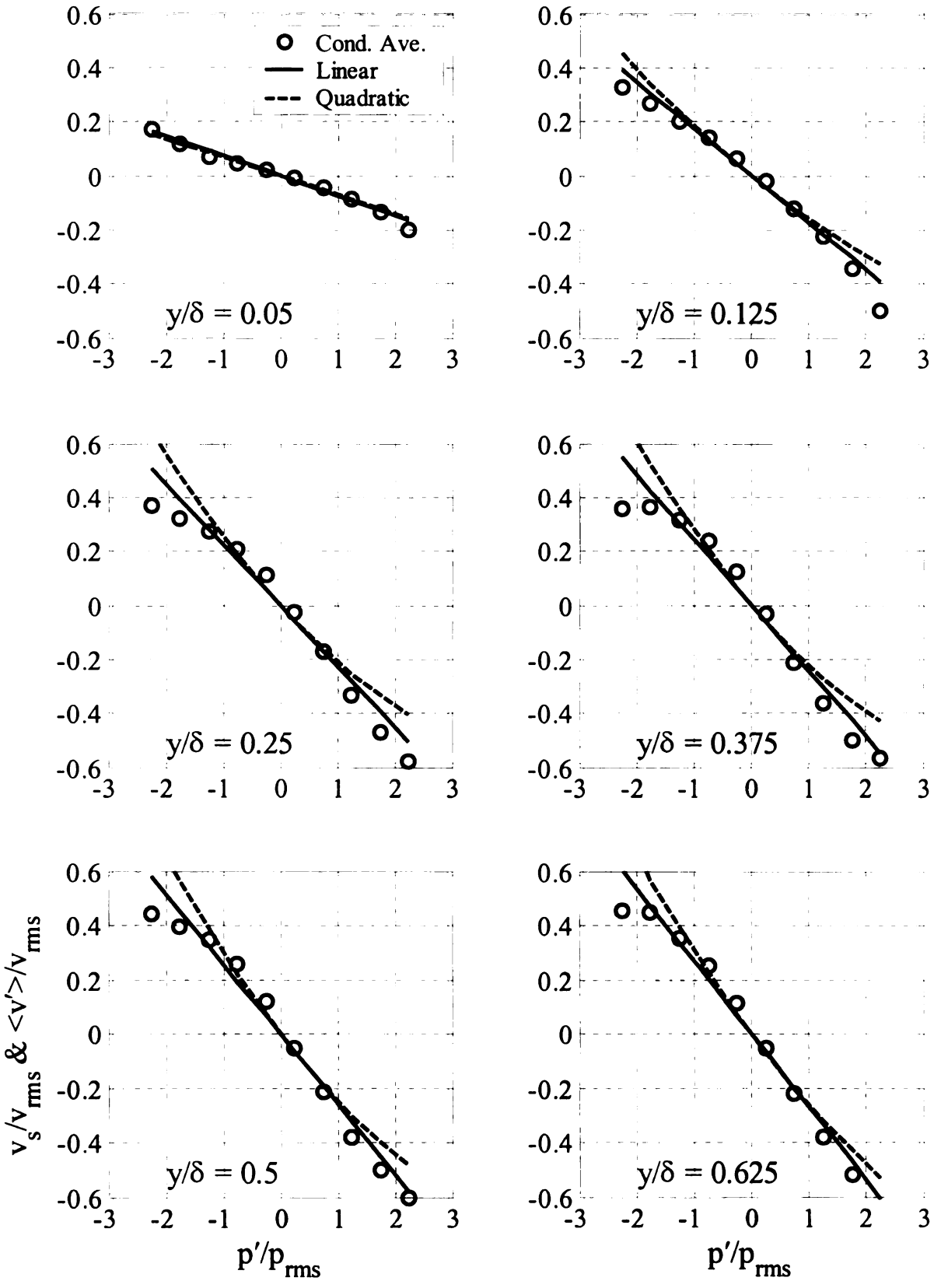

Figure 4.42. Comparison of the conditionally-averaged and stochastically-estimated normal-velocity using SL_2 and SQ_2 for y/δ = 0.05, 0.125, 0.25, 0.375, 0.5 and 0.625

Conclusions concerning the accuracy of the normal-velocity estimation may be drawn from Figure 4.42. The figure shows that, at the lowest y location ($y/\delta = 0.05$), SL_2 is capable of representing $\langle v' \rangle$ with good accuracy. For higher y locations, the three data sets show good agreement within the range: $|p'| < \pm p_{rms}$. Similar to the observations of Figure 4.41, Figure 4.42 depicts that the quadratic term does not include more information and, in contrast, the linear estimation seems to more accurately estimate $\langle v' \rangle$. Although the need for a cubic term is not as clear in the normal-velocity results as it is in the case of the streamwise velocity, Figure 4.42 reveals that the need for such a term is strongest at $y/\delta = 0.375$ (where the v' fluctuations are strongest).

In summary, the comparison of the velocities estimated using ML, SL_2 and SQ_2 with the instantaneous and conditionally averaged ones reveals that the quadratic term does not provide more information to the estimated results. Moreover, the multi-point estimation (ML) was found to represent the conditional velocity field better than single-point-based estimation, with an accuracy that is projected to be larger than 80% of the RMS velocity for both velocity components and at all heights examined here. Therefore, in the remainder of this thesis only ML results will be employed.

4.3.3. Stochastic Estimation Results and Wall-Pressure Sources

Figures 4.43 depicts the ML velocity vector field, along with the associated wall-pressure time series at $\xi = 2.0$ (corresponding to the microphone location immediately upstream of the hotwire) for three consecutive time windows plotted in three plots, one above the other. The vector fields are viewed in a frame of reference translating with a velocity of $0.81U_\infty$ in the downstream direction. Also, in the velocity vector field windows, two scales are shown for the ordinate: one giving the y location normalized by

the boundary layer thickness (displayed on the left side of the plot), and the other (shown on the right side) provides y/h values. For the wall-pressure plots, the ordinate is the fluctuating wall-pressure normalized by p_{rms}. The corresponding abscissa, which is common for the velocity vector field and wall-pressure plots, represents the non-dimensional time.

It should be noted that τ values displayed in the plot are folded (i.e., they increase in the time-backward direction) relative to an arbitrarily selected time offset (t_o); i.e., $\tau = -(t-t_o)$; $t < t_o$. By changing t_o, one can display different time windows from the data records. On the other hand, the time reversing operation orders the data in such a way that the progression of information with increasing time is from right to left. This facilitates viewing of the vector field in a frame of reference where increasing τ may be interpreted as increasing downstream distance by invoking Taylor's hypothesis of frozen turbulence. The intent here is not to claim that the vector fields displayed in Figure 4.43 represent the instantaneous spatial structure, but rather that the time evolution of the velocity vector field is consistent with the passage of the flow features shown in the figure. The degree to which the actual spatial structure of the flow features resembles that depicted in the vector plots as they sweep past the hotwire is actually quite reasonable as discussed in the following paragraph.

The stochastically-estimated data, shown in Figure 4.43, may be used to represent the spatial velocity field using *Taylor's hypothesis of frozen turbulent eddies* (Taylor 1938), which provides an approximation to obtain spatial information from temporal data and is, strictly speaking, only applicable to statistically stationary, homogenous, flows.

Lumely (1965) showed that the hypothesis gives adequate accuracy if $\frac{u_{rms}}{U_c} << 1$; where U_c is the mean convection velocity of the flow structures. Alternately, the hypothesis is reasonable over a time window (T) that is much smaller than an eddy "turn-over time" (ℓ/u_{rms}; ℓ being a characteristic length scale of the dominant eddies). That is, there is very little time for the eddy to evolve and change state during T. This implies: $T << \ell/u_{rms}$. The dominant length scale of the structures related to the wall-pressure generation may be estimated from the wavenumber-frequency spectral peak in Figure 3.17 as approximately $\ell = X_r$ ($k_x \approx 1/X_r$). On the other hand, the u_{rms} plot in Figure 4.4 shows that u_{rms} is of the order of $0.1U_\infty$ (note lower u_{rms} values improve the applicability of the hypothesis). Thus, if the reader wishes, it appears reasonable to interpret the structural features (not the vector field as a whole) in Figure 4.43 as being spatial structures over a time window $T\ U_\infty/X_r << 10$; i.e., $T\ U_\infty/X_r \approx 1$. For guidance, this time window is demonstrated in the vector plots in Figure 4.43. Additional support for the reasonableness of Taylor hypothesis in such interpretation is provided by the practically invariant pressure fluctuation level in the streamwise direction in the vicinity of the hotwire location (see $C_{p'}$ in Figure 3.2), and the constant convection velocity associated with all frequencies and time scales of the wall-pressure field as found earlier from the wavenumber-frequency analysis.

Overall, the velocity-vector field snap shots displayed in Figure 4.43 are dominated by quasi-periodic vortical structures. These vortices are large in scale and have cores (as identified visually) that appear mostly within a small y range in the

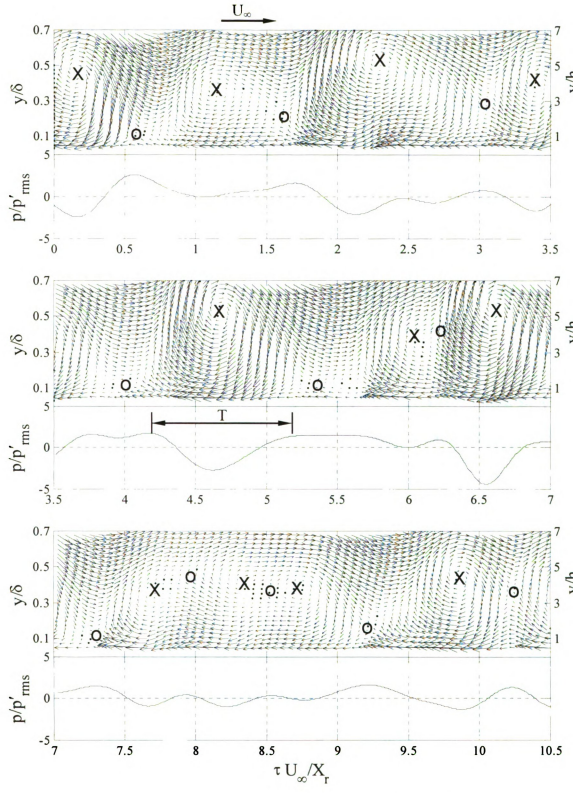

Figure 4.43. Wall-pressure time series at $\xi = 2.0$ (bottom of each plot) and the associated stochastically-estimated velocity vector field (top of each plot) using ML for three consecutive time windows, viewed in a frame of reference translating with velocity of $0.81U_\infty$ (largest vector = $0.25U_\infty$)

neighborhood of $y/\delta \approx 0.5$. One can also depict saddle points inbetween the vortices, associated with the interaction between successive vortical structures. These observations are consistent with the picture drawn above from the previous statistical analyses. However, the stochastically estimated velocity fields based on the instantaneous spatial wall-pressure footprint reveal the richness in variability in the characteristics of the flow structures: something that can't be discerned from the earlier results. This variability includes structure scales, locations, temporal (and hence spatial) spacing, and interactions (including variability in saddle point locations and apparent vortex merging). Some observations concerning these characteristics are discussed in the following paragraph.

In the first (top-most) window in Figure 4.43, four successive vortical structures, the centers of which are marked using "x", are evident. Note that at this stage, a vortex is identified whenever the vector field locally reflects a circulatory flow pattern around a zero-velocity center. Of course, the appearance of such pattern is highly sensitive to the selection of the translation velocity of the frame of reference. The dependency of the vortex identification on the velocity of the frame of reference may be seen in Figure 4.44. The figure depicts that varying the velocity of the frame of reference by $\pm 0.05U_\infty$ greatly affects the visual identification of the locations of vortical structure centers. Therefore, the observations discussed here require substantiation by some other frame-independent measure, which is done immediately following this discussion. The non-dimensional temporal spacing between the three right-most vortices in the top vector plot of Figure 4.43 is approximately 1.3, which is equal to the dominant time scale identified earlier in

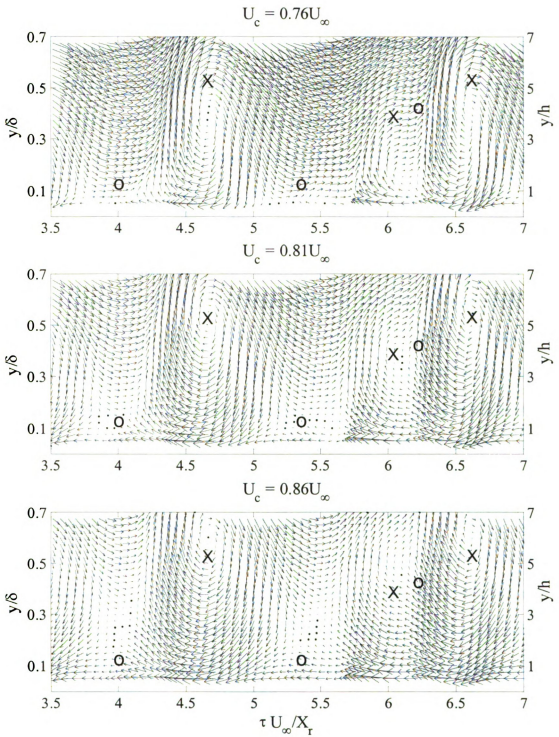

Figure 4.44. The stochastically-estimated velocity vector field using ML viewed in frames of reference translating with three different velocities of $0.76U_\infty$ (top plot), $0.81U_\infty$ (middle plot) and $0.86U_\infty$ (bottom plot); largest vector = $0.25U_\infty$ (note that the "x" and "o" locations are fixed for all three plots to help identify the variability in the vortex and saddle-point locations, respectively)

the autocorrelation of the wall-pressure and the cross-correlation between the normal-velocity and wall-pressure, while that between the two left-most vortices seems to be shorter (approximately equal to 1.0). In the middle window, three vortices are also captured over the same time frame. These vortices, also, appear not to be separated uniformly; i.e., their centers are located at time instants of 4.7, 6 and 6.6. Therefore, the left-most and middle vortices are $\frac{\tau U_\infty}{X_r} = 1.3$ apart while the separation between the middle and right-most ones, which appear to be undergoing a vortex-merging process, is 0.6, reflecting the variability in the temporal separation between successive vortices, and hence the quasi-periodic nature of the vortical structures. Finally, the bottom-most window in the vector-field sequence depicts three consecutive small vortices that are possibly undergoing a merging process, in addition to a separate fourth vortex at the right side of the window. The reader is cautioned that the identification of vortex merging from a single snap shot of the vector field is somewhat speculative since space-time velocity information, which is not available in the present study, is required to examine the time evolution of the vortices and ascertain that a merging process is in fact taking place. In-between the vortex structures, saddle, or stagnation, points (marked by "o") that result from mutual-vortex interactions are observed. Some of the saddle points are observed as close to the wall as $y/\delta \approx 0.13$, signifying the fairly deep penetration into the boundary layer of the high-speed momentum fluid from the freestream associated with these saddles.

Overall, the depicted vector field corroborates the idea that the wall-pressure generation process is in fact dominated by the passage of quasi-periodic vortices and their mutual interaction. As the vortex cores convect past a point on the wall, they produce

negative pressure, followed by positive-pressure generation associated with the passage of the saddle points. This scenario, which was suggested earlier from examination of the conditional-average of the velocity vector field in 4.2.3, can be further examined using the plots of the simultaneous velocity vector field and wall-pressure signature presented in Figure 4.43. Generally, the three time windows in the figure confirm that the negative and positive p' peaks are synchronized with the passage of the vortex cores and saddle points, respectively. Practically all time instants of observing vortex cores ($\frac{\tau U_\infty}{X_r} = 0.2$, 1.15, 2.3, 3.4, 4.7, 6.0, 6.6, 7.7, 8.35, 8.7 & 9.9) coincide with the occurrence of a negative peak or local minimum in the wall-pressure. There is a small time offset between the observation of the negative p' peak at the microphone, and the passage of the vortex center past the hotwire. This offset is due to the fact that the microphone is located slightly ($\Delta\xi = 0.05$) upstream of the hotwire, and hence the p' peak occurs slightly ahead of the passage of the vortex core past the hotwire. On the other hand, positive wall-pressure peaks evidently coincide with the occurrence of saddle points (e.g. $\frac{\tau U_\infty}{X_r} = 0.6$, 1.6, 3.0, 4.0, 5.4, 6.2, 7.3, 8.0, 8.5, 9.2 & 10.2).

The aforementioned flow features are consistent with the study of Kiya *et al.* (1982), who used a discrete-vortex model to simulate the free-shear-layer flow above a separation bubble formed by the flow past the nose of a thick splitter plate. Their results show negative pressure peaks in the vicinity of vortical structures and positive peaks when the vortices are absent. In addition, the above observations are consistent with the recent study of Naguib and Koochesfahani (2003) in which it was shown that for a vortex ring interacting with a flat wall, the primary source of negative pressure was associated

with the high vorticity in the vortex core. On the other hand, positive-pressure generation was dominated by the straining motion caused by the interaction of the vortex with the wall or with other secondary vortices that are produced from such interaction.

The above analysis presumes that a coordinate-frame translation velocity of $0.81U_\infty$ is appropriate based on the convection velocity information obtained earlier from statistical analysis of the pressure and velocity information. Based on the observations of Figure 4.44, the reasonableness of identifying certain flow structures as vortices needs to be verified here, and therefore we examine the vorticity field associated with the estimated velocity field. It should be understood that the existence of regions of high vorticity does not necessarily imply the existence of a vortex (e.g., Blasius boundary layer contains vorticity but no vortices). Nevertheless, vortex cores are expected to be associated with localized high-level vorticity. Hence, the association of the vortex structures identified above with locally high vorticity at the core is required to justify the above discussion. It is also noted here that unlike the velocity vector field, vorticity is independent of the selection of the coordinate-frame translation velocity.

The spanwise vorticity, $\omega_{z,s} = \frac{\partial v'_s}{\partial x} - \frac{\partial u'_s}{\partial y}$, is calculated from the estimated velocity vector field using a central-finite-difference method and plotted using a color contour map that is superimposed on top of the corresponding velocity vector field as shown in Figure 4.45. In order to concentrate only on regions with significant vorticity, the vorticity contours are shown for values that exceed 50% of the highest vorticity in the figure. Figure 4.45 reveals that the vortex cores identified earlier are in fact associated with locally high values of vorticity. In particular, the top-most window

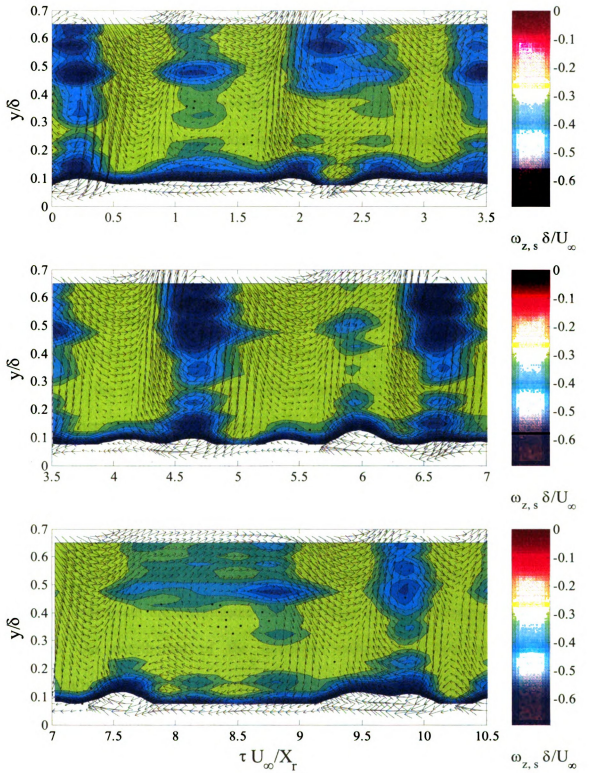

Figure 4.45. Vorticity and associated stochastically-estimated velocity vector field at three consecutive time windows, viewed in a frame of reference translating with $0.81U_\infty$

depicts four main high-vorticity cores, which coincide with the occurrence of the identified cores of vortical structures and their associated wall-pressure negative peaks. However, the middle window depicts only two spots of locally high negative vorticity, but significantly stronger than those found in the first window, which represent the left-most vortex and the two right-most merging vortices. Similarly in the bottom-most window, the existence of a broad ($7.5 \leq \frac{\tau U_\infty}{X_r} \leq 9.3$) and concentrated ($\frac{\tau U_\infty}{X_r} \approx 9.9$) regions of high negative vorticity seem to correspond well to the three merging vortices and the right-most vortex identified earlier in Figure 4.43. The three windows also show a thin but extended layer of negative vorticity concentration near the wall. This layer is clearly associated with the high mean velocity gradient near the wall, modulated by the passage of the outer-shear layer vortical structures. The above suggests the appropriateness of the selected frame of reference for viewing the structure of the flow. It should also be noted that in this frame of reference, the identified vortex cores are observed in the vicinity of $y/\delta \approx 0.48$, which agrees well with the identified outer-shear-layer center based on the peak shear Reynolds stress.

To attain a deeper understanding of the relationship between the wall-pressure signature underneath the investigated boundary layer and the pressure-generating flow structure, the distribution of the turbulent wall-pressure flow sources of the stochastically-estimated, or quasi-instantaneous, velocity field are investigated. As discussed in Chapter 1, Poisson's equation governs the pressure fluctuations in incompressible turbulent flows. For the flow considered here, which possesses a dominant mean shearing component, du/dy, the Poisson's equation may be simplified to:

$$\frac{1}{\rho}\nabla^2 p' = -2\frac{du}{dy}\frac{dv'}{dx} - u'_{i,j}\,u'_{j,i} = q \qquad (4.27)$$

where u is the mean velocity in the streamwise direction, q is the spatial distribution of wall-pressure sources, and the prime indicates a fluctuating (mean-removed) quantity. As described in 1.1.2, the first term on the right hand side of equation (4.27) is called the linear pressure source, while the second term is known as the nonlinear one.

In many investigations of the wall-pressure in turbulent wall-bounded flows, only the linear term is considered because of the obvious simplicity in measuring, analyzing, and modeling the linear relative to the non-linear term. This simplification is typically justified because of the large value of $\frac{du}{dy}$ in comparison to that associated with the turbulent-velocity gradients comprising the non-linear term. However, DNS computations by Kim (1989) and Chang *et al.* (1999) enabled calculation of both the linear and non-linear terms in fully-developed turbulent channel flow. Both studies did indicate that the non-linear contribution to the wall-pressure was at least as important as the linear one. The first indirect experimental verification of this conclusion was later provided by Naguib *et al.* (2001) who showed that for the stochastic estimation of the flow field based on single point wall-pressure events to converge to the conditional average, a quadratic stochastic estimation must be used. Considering an analysis based on the source terms of Poisson's equation, Naguib *et al.* found that the improvement to the stochastic estimation via inclusion of the quadratic or higher-order terms was attributed to the importance of the non-linear sources of the wall pressure.

The reasonableness of neglecting the non-linear source terms for the current flow may be substantiated using an order of magnitude analysis. Referring to the mean-

velocity profile in Figure 4.36, it is seen that $\frac{du}{dy}$ is almost uniform in the outer part of the flow (y larger than approximately 0.15δ) and is approximately equal to $0.3U_\infty/\delta$. As found earlier in the discussion of the spatial cross-correlation results in 4.2.2, the dominant length scale of the pressure-generating structures is of the order of X_r for $y/\delta > 0.15$. Thus, the ratio of mean-velocity gradient to any of the turbulent velocity gradients is of the order of $(0.3\ U_\infty/\delta)/(0.1\ U_\infty/X_r)$; note that the estimate of the velocity scale of the turbulent fluctuations as $0.1U_\infty$ is quite reasonable based on the u_{rms} and v_{rms} profiles (see Figures 4.3 through 4.6). This yields $3X_r/\delta \approx 7$. Closer, to the wall ($y/\delta < 0.2$), where the du/dy is of the order of U_∞/δ (within the measurement range) and a shorter length scale of $\lambda_i \approx X_r/2$ are found, the ratio becomes approximately 10. Thus, it is evident that the mean-velocity gradient across the layer is in fact substantially higher than the turbulent velocity gradient, providing some support of the dominance of the linear source of the wall pressure. It should be noted that this conclusion is not in conflict with the significance of the non-linear source terms found in canonical wall-bounded flow by Kim (1989), Chang *et al.* (1999) and Naguib *et al.* (2001), since the current flow is clearly a non-equilibrium one and the dominant p' sources are those originating in the separating shear layer and hence they bear no relation at all to the sources in the equilibrium wall-bounded flows.

Based on the above discussion, the following analysis of p' sources will only consider the first term on the right-hand-side of equation 4.27, which is the linear source, or q_L. The reader is reminded, though, that the analysis based on Figures 4.41 and 4.42 showed that one should include a cubic term in the stochastic estimation for a full

account of the conditional average, which provides a hint that the non-linear pressure source terms may not be totally negligible, based on the results of Naguib et al. (2001). Therefore, the analysis of the linear source alone should be viewed as an analysis of the leading-order term of the pressure-generating sources. Future studies, considering full 3D stochastic estimation of the flow can then quantitatively assess the relative importance of the linear and non-linear sources.

The time evolution of the y distribution of the dimensionless *linear* pressure sources ($q_L X_r\delta/U_\infty^2$) for the same three time windows considered in Figure 4.43 is shown in Figures 4.46. Note that because q_L is the product of $\frac{du}{dy}\frac{dv'}{dx}$, it is normalized by $\frac{U_\infty}{\delta}\frac{U_\infty}{X_r}$, where δ and X_r are the length scales in the y and x directions, respectively. The source distribution is shown using three color contour plots of q_L calculated from the stochastically-estimated velocity field. The associated wall-pressure time series is also provided in the figure below each of the contour plots. Note that in order to compute $\frac{dv'}{dx}$, the temporal variation of v' is converted to spatial variation using Taylor's hypothesis in conjunction with the local mean velocity over a very narrow time window (corresponding to the duration of acquisition of three successive data points that are used for implementation of a central finite-difference method to calculate the derivative. Note that this window width is $1/60^{th}$ of the period T shown in Figure 4.43, over which Taylor hypothesis was estimated to work reasonably well).

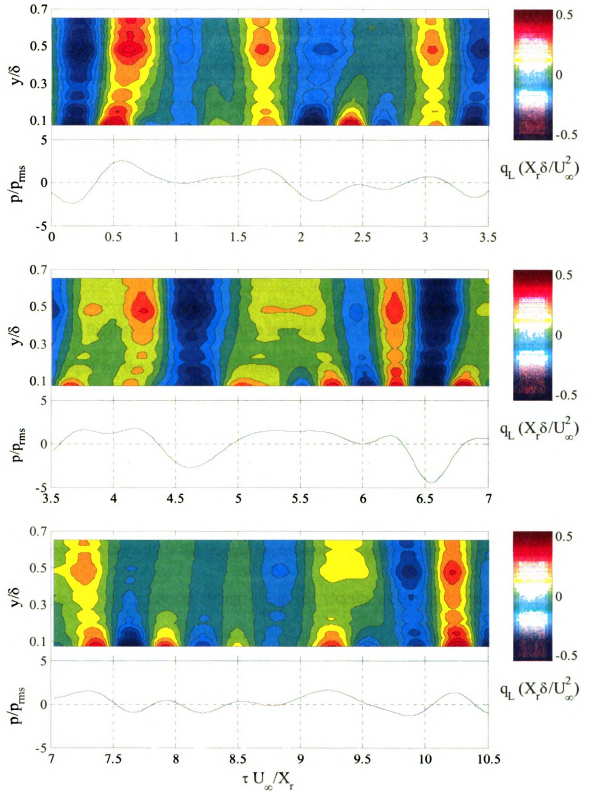

Figure 4.46. Pseudo-instantaneous *linear* pressure source (q_L) flooded contour maps and associated wall-pressure for three consecutive time windows

Inspection of Figure 4.46 shows that whenever a substantial negative pressure peak is observed, negative pressure sources are found directly above the peak. Although the sources are distributed across the entire y range, they exhibit two high-concentration spots, or localized peaks: one far from the wall in the outer-shear layer, near $y/\delta = 0.48$, where the Reynolds-shear-stress peak was found earlier, and the other close to the wall ($y/\delta < 0.2$). In a similar fashion, substantial positive pressure peaks are also associated with positive sources that are located directly above the positive pressure peak, with the highest sources also found in the vicinity of the outer-shear-layer center, and below $y/\delta = 0.2$.

The localized peaks of negative sources found in the outer-shear layer are located at the height of the vortex cores identified earlier in the vector plot in Figure 4.43. Comparison of this figure to Figure 4.46 shows good coincidence between these localized negative-pressure sources and the vortex-core locations. Positive-pressure sources are found immediately before and after the negative ones, but at the same height. This provides strong evidence for the ideas presented thus far that the passage of vortex cores past a point on the wall is the leading contributor to p' generation in the current flow. As the vortex travels it creates strong $\frac{dv'}{dx}$ in the vicinity of the core leading to pressure generation via the linear mechanism (or $\frac{du}{du}\frac{dv'}{dx}$). The $\frac{dv'}{dx}$ variation associated with the vortex passage is such that it creates a negative source at the core and positive ones upstream/downstream of the core. The alteration in the pressure source sign from positive to negative and back again to positive may be depicted by considering $\frac{dv'}{dx}$

variation associated with the conditional velocity field obtained earlier for negative pressure peak in Figure 4.37. Figure 4.47 shows a plot of v' normalized by U_∞ versus $\tau U_\infty/X_r$ extracted from Figure 4.37 at different heights. The associated $\frac{dv'}{dx}$ normalized by U_∞/X_r is also shown in the figure. The succession of positive/negative sources associated with the vortex passage is evident from the alternating sign of $\frac{dv'}{dx}$.

As y decreases below the vortex center, the source strength becomes weaker since $\frac{du}{dy}$ is practically uniform in the outer-shear layer and v' attenuates with decreasing height (see v_{rms} profiles and spectra in Figures 4.6 & 4.12). However, below $y/\delta \approx 0.2$, the mean-velocity gradient starts to increase substantially because of the no-slip condition. As a result, the creation of another significant source of pressure fluctuations is found near the wall. Physically, this source may be thought of as one that results from the modulation of the near-wall flow by the vortex passage; i.e., one that is the result of the indirect influence of the vortices. Unlike the outer-shear-layer source, this source is associated with weak $\frac{dv'}{dx}$ disturbances, the ability of which to produce p' is amplified by the strong near-wall shear.

It is interesting to note that whereas, localized peaks of q_L are always found below $y/\delta = 0.2$, whenever there are localized peaks near $y/\delta = 0.48$, the opposite is not true. That is, at certain instances, there are localized peaks near the wall that are not associated with localized peaks away from the wall. This gives rise to a pressure source near the wall that is associated with a time scale smaller than, about half, that characteristic of the

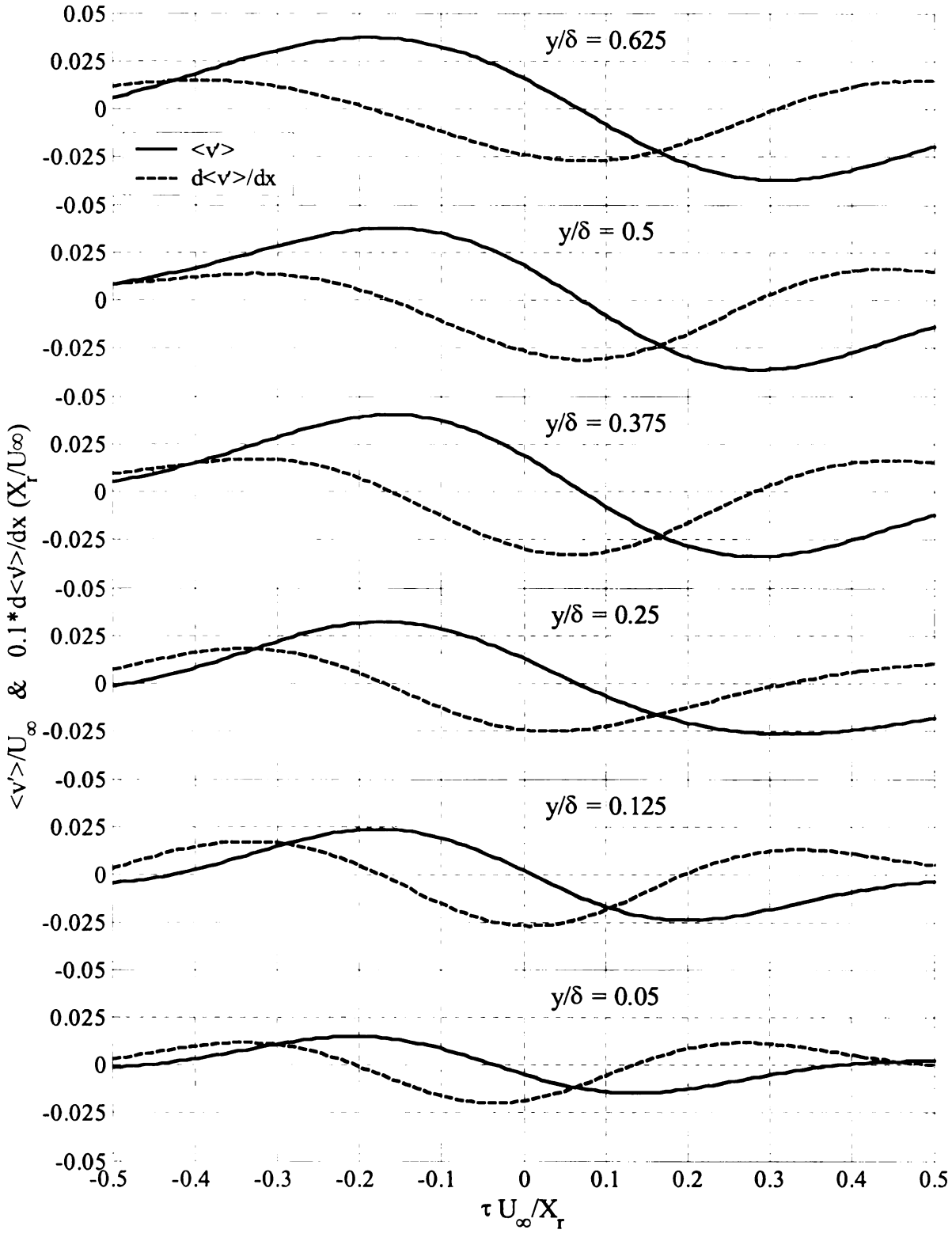

Figure 4.47. The conditionally-averaged normal velocity and its streamwise gradient associated with negative wall-pressure peak for y/δ= 0.05, 0.125, 0.25, 0.375, 0.5 and 0.625

vortex-vortex spacing away from the wall. Consequently, pressure sources near the wall are expected to generate wall-pressure signatures with both the smaller and larger characteristic scales. This observation is consistent with the spatial cross-correlation analysis presented earlier in the discussion associated with Figure 4.27.

The importance of the various flow sources of pressure to the wall-pressure generation depends not only on the strength of the source, but also on the distance between the source and the wall. The larger this distance is, the weaker is the source contribution to p'. This may be seen from the solution of equation (4.27), which is a volume convolution integration of weighted pressure sources over the flow domain given by (e.g., Kim 1989):

$$\frac{p'(x,y,z,t)}{\rho/2\pi} = -\iiint \frac{q(x_s,y_s,z_s,t)}{\sqrt{(x-x_s)^2+(y-y_s)^2+(z-z_s)^2}}\,dV_s \qquad (4.28)$$

where x_s, y_s and z_s are the coordinates of the pressure source, and x, y and z are the coordinates of the point in the flow of where the solution of p′ is sought. Thus, the denominator represents the distance between the source and a point on the wall in the case of the wall pressure. Moreover, the observed p' value is an integration, or superposition, of all sources within the domain. Thus, in order to assess the true significance of the sources identified in the discussion of Figure 4.46 above, the source strength must be weighted, i.e., divided by, its distance (r) to the point of observation of the pressure. This was done (accounting for the source height above the wall and the x offset between the hotwire location and that of the microphone for which p' data are shown below the source-distribution maps) and the outcome is shown in Figure 4.48. The figure shows that the importance of the *direct* pressure-source located at the height of

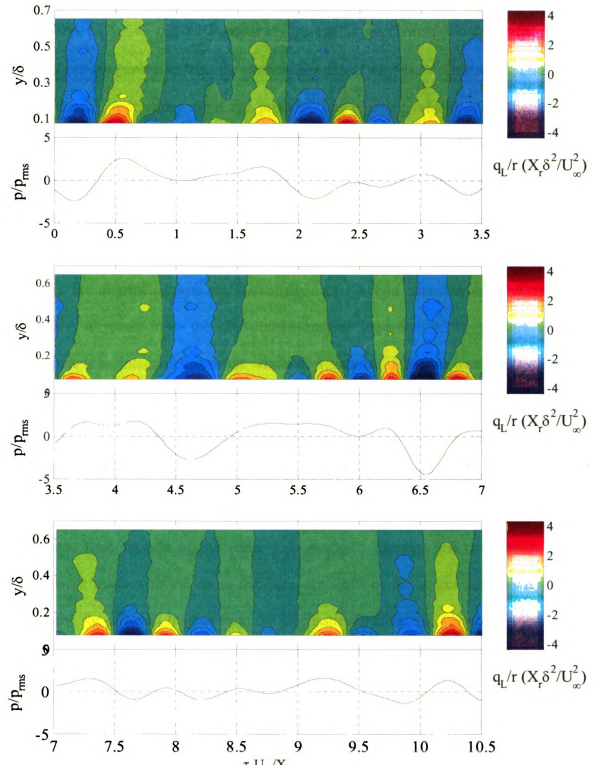

Figure 4.48. Pseudo-instantaneous *linear* pressure source (q_L/r) flooded contour maps and associated wall-pressure for three consecutive time windows

the vortex centers is greatly diminished, because of the larger distance to the wall. Therefore, as far as the wall-pressure signature is concerned, the strongest pressure fluctuations are generated from the near-wall sources ($y/\delta < 0.2$). This is quite surprising given that all indications from the pressure and pressure-velocity statistical analysis undoubtedly tie the wall-pressure to the outer-shear-layer vortices. However, the reader is reminded that the near-wall source is in fact an indirect consequence of the passage of the large-scale vortices, and if the outer-shear layer were to somehow disappear, the near-wall source would not exist. Moreover, the weaker outer-shear-layer sources of the *wall* pressure are distributed over a substantially larger height than the stronger near-wall sources. As seen from the convolution-integral (equation 4.28), the net pressure magnitude is an integration over the whole flow volume. Hence, a weaker source that is extended over large volume may be as important as one that is very strong, but also highly localized. Therefore, the results in Figure 4.48 do not necessarily indicate that the *direct* influence of the vortices, i.e., outer-shear-layer sources, is negligible.

The linear source analysis presented above is based on the observation of typical, but short, time records of the entire data set. To examine the consistency of the conclusions made with the entire database, the RMS of the source strength (q_{rms}) was calculated for different heights from the stochastically-estimated velocity and plotted in Figure 4.49. The abscissa is the RMS of the pressure source normalized by $\frac{U_\infty}{\delta}\frac{U_\infty}{X_r}$ while the ordinate is the height above the wall (y) normalized by the boundary-layer thickness (δ). The figure shows the profiles of q_{rms} calculated from both the measured and estimated velocity fields. Comparison between the two data sets shows a very good agreement in the qualitative trend of the data with, expected, attenuation of the results

based on the stochastic estimation relative to those based on the actual velocity. Consistent with the above analysis, the source RMS profile clearly depicts two localized peaks of large pressure generation: the first one is at $y/\delta = 0.48$, which is the same height of the maximum $-\overline{u'v'}$. The second peak is implied from the rise in q_{rms} magnitude below $y/\delta = 0.2$. Since v' goes to zero at the wall, q_{rms} must decay to zero at $y = 0$. Thus the near-wall q_{rms} peak is located somewhere between the lowest y value shown in Figure 4.46 and the wall.

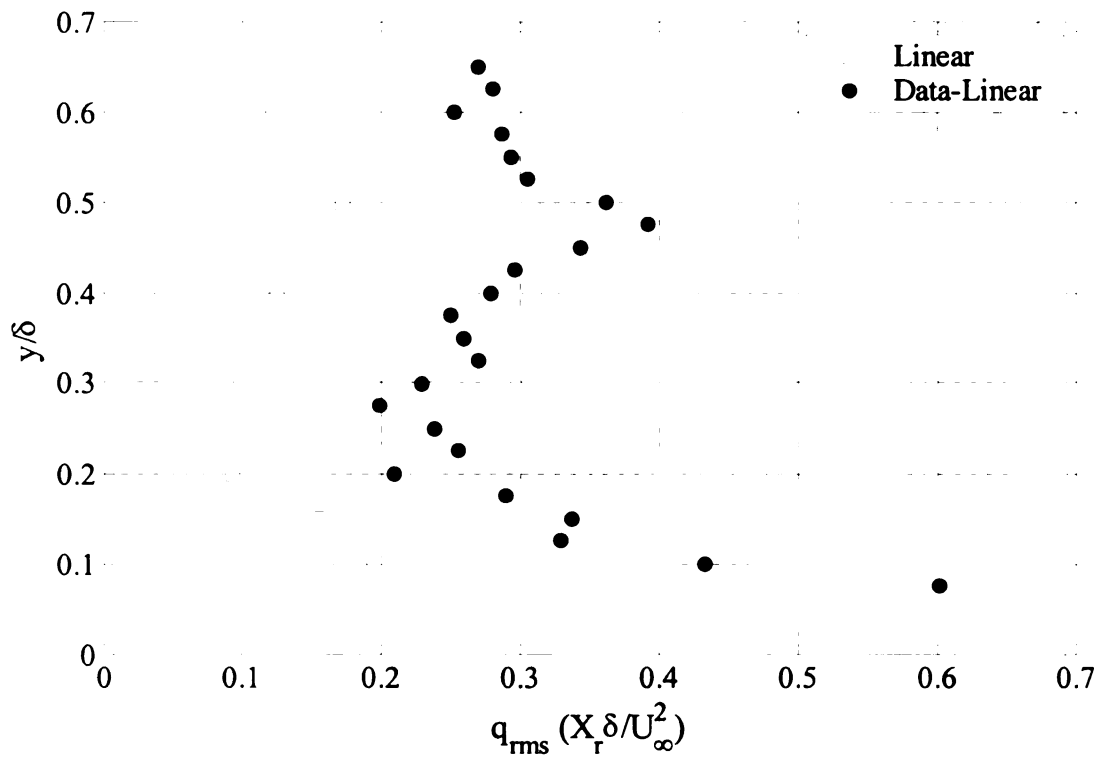

Figure 4.49. RMS profile of the linear pressure source calculated from stochastically-estimated and measured velocity time series

The results shown in Figure 4.49 do not account for the distance between the source and the wall. Figure 4.50 shows q_{rms} after proper weighting and normalization, by

$\frac{U_\infty}{\delta^2}\frac{U_\infty}{X_r}$, of the source strength to account for its location relative to the wall-pressure observation point. The outcome reflects a practically uniform distribution of source strength above $y/\delta \approx 0.2$. As discussed above, this distribution is substantially weaker than the largest value found near the wall (by about a factor of five). However, the corresponding y range of the uniform source is also five or more times that of the near-wall source. Hence, the direct influence of the vortices may in fact be of equal importance to their indirect influence in generation of the wall pressure.

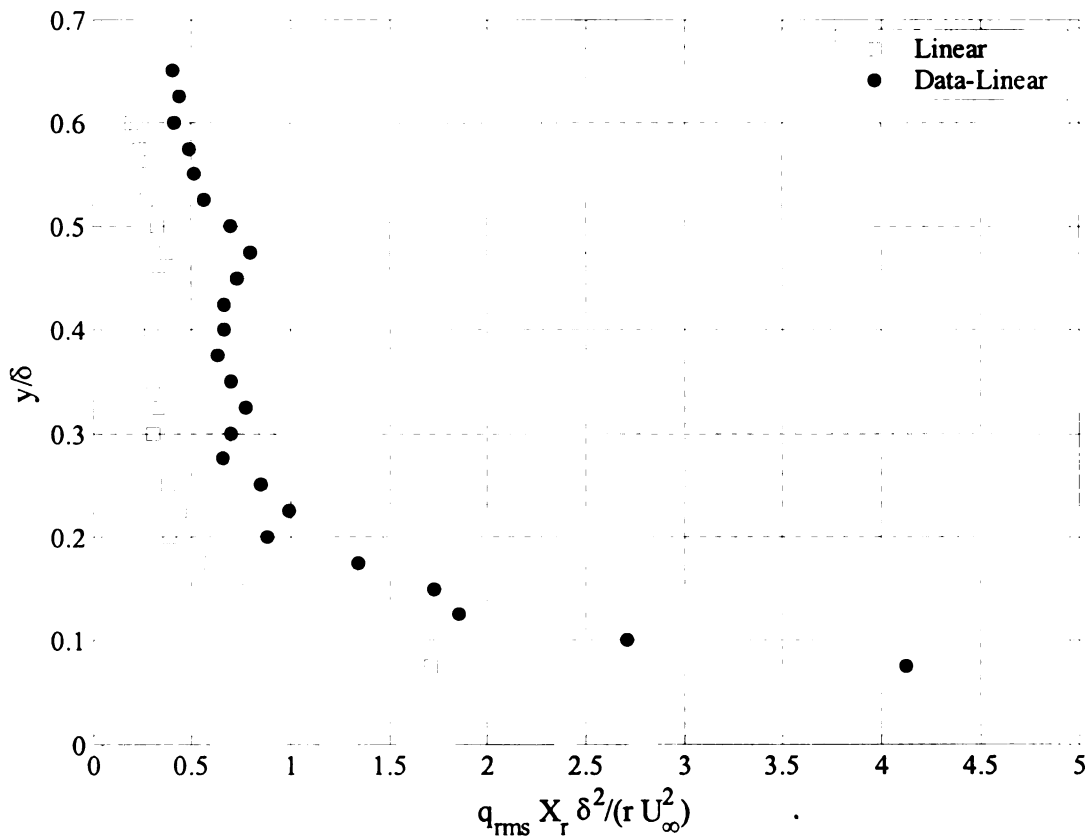

Figure 4.50. RMS profile of the linear weighted pressure source calculated from stochastically-estimated and measured velocity time series

5. CONCLUSIONS AND RECOMMENDATION FOR FUTURE WORK

5.1. Conclusions

In this investigation, a 16-microphone array has been constructed and used to acquire a wall-pressure database simultaneously with X-hotwire time series in a non-equilibrium boundary layer originating from a separating/reattaching shear layer. Data were acquired over a non-dimensional streamwise (ξ) range extending from 0.67 to 2.33. Characterization of the wall-pressure data alone showed that the wall-pressure fluctuations were dominated by large-scale downstream-traveling disturbances that were linked to the vortical structures generated upstream in the separated shear layer. Notwithstanding this dominance, the p' signature of these structures decayed with increasing downstream distance as the vortices underwent a relaxation process, gradually loosing their energy and associated p' signature.

In contrast, the contribution of eddies generated due to the boundary-layer-like shear near the wall became more significant with increasing ξ. This could be deduced from the increase in the energy at high frequencies in the wall-pressure spectra, which resulted from the growth of the inner sub-boundary layer near the wall. The dimensionless frequency of the most energetic wall-pressure fluctuations was found to be approximately $fX_r/U_\infty = 0.7$, which agreed well with the passage frequency of the separated-shear-layer vortices reported in studies concerned with the separating/reattaching flow upstream of the flow region examined here. In addition, wavenumber-frequency-spectrum results showed that pressure signatures of all wavenumbers and frequencies were associated with flow disturbances that travel downstream with the same convection velocity of approximately $0.81U_\infty$, which was

about 10% U_∞ higher than that reported by Farabee and Casarella (1986). The lower value in the latter study is attributed to the influence of the wake region of the separating turbulent boundary layer. Such a region exists in the study of Farabee and Casarella but not in the current study where a laminar boundary layer exists at separation.

The flow velocity was measured within the non-equilibrium boundary layer flow (at ξ = 2.05), simultaneously with wall-pressure data from the ten downstream-most microphones (ξ = 1.33 to 2.33). Those measurements were used to examine the velocity-field characteristics of the non-equilibrium boundary layer and the relationship between the flow structures and associated wall-pressure field.

The wall-normal profile of the mean streamwise velocity deviated from that of a canonical equilibrium turbulent boundary layer and its log-law, consistent with the earlier studies by Ruderich and Fernholz (1986), Farabee and Casarella (1986), Castro and Epik (1998) and Song and Eaton (2002). In addition, the present data showed that the non-equilibrium boundary layer did not possess a wake region, which could be related to the laminar separating boundary layer. On the other hand, the boundary layer at ξ=2.05 exhibited free-shear-like characteristics, associated with the existence of v_{rms} and $-\overline{u'v'}$ peaks in the outer layer at y/δ = 0.38 and 0.48, respectively, which were related to the energetic large-scale vortical structures that were generated and energized upstream in the separating free-shear layer. Unlike v_{rms} and $-\overline{u'v'}$, the u_{rms} profile exhibited a flat region of fluctuations in the range of $0.02 < y/\delta < 0.44$.

The dimensionless auto-spectra of the streamwise- and normal-velocity (Φ_{uu}, Φ_{vv}) revealed the increasing importance with increasing downstream distance of the small-scale turbulence associated with the sub-boundary layer near to the wall. The former

revealed the existence of a more than a decade wide $f^{-5/3}$ range, implying the existence of an inertial sub-range, while the latter depicted a peak similar to that of the wall pressure at a frequency of $\frac{f X_r}{U_\infty} \approx 0.7$. The cross-spectrum between the streamwise- and normal-velocity (Φ_{uv}) reflected a pronounced increase in Reynolds stresses in the high-frequency end of the spectrum near the wall. On the other hand, the data also showed that the large-scale structures were *active* in the outer layer, but became *inactive* near the wall.

The velocity-pressure cross spectra provided additional evidence that p′ generation was dominated by the vortical structures in the outer part of the boundary layer, exhibiting a peak in the frequency range corresponding to the passage of the vortical structures for all heights within the boundary layer. On the other hand, the velocity-pressure spectral information also depicted growth in the sub-boundary layer contribution to p' with increase in ξ. However, this contribution remained negligible relative to that of the vortical structures over the streamwise extent covered in the present study.

Using u′-p′ and v′-p′ cross-correlation, the size of the flow structures in the outer part of the boundary layer (λ_o) was estimated to be approximately 0.9-1.0 X_r, which agreed reasonably with the dominant wavelength found from the wavenumber-frequency spectrum of the wall-pressure data and was about 30-40% higher than that reported in the literature of separating/reattaching flows. It is believed that the reason for this deviation is the increase in size of the vortices as they travel from the separation/reattachment zone to the developing boundary layer region where the current data are obtained. Such size increase may be associated with diffusion and vortex-merging effects. Near the wall, a

second, smaller length scale of about $\frac{1}{2}\lambda_o$ was also identified from the velocity-pressure correlation data. Later analysis of the wall-pressure flow sources revealed that this scale was associated with pressure-generation due to the modulation of the strong near-wall shear by the passage of the vortices. Moreover, when the cross-correlation results were coupled with the conditionally averaged wall-pressure and velocity-field, they revealed that positive and negative wall-pressure peaks coincide with "inrush" of high-speed fluid towards the wall and the passage of spanwise-vortex centers, respectively. The high-speed inrush was found in between two successive vortices and was associated with the formation of a saddle-point positive-pressure source, when viewed in a frame of reference traveling with the $0.81U_\infty$. The succession of vortex centers and saddle points resulted in the quasi-periodic character of p' reflected in all statistical measures of the wall-pressure obtained here.

Finally, multi-point Linear Stochastic Estimation of the flow field based on instantaneous wall-pressure information, while confirming the dominance of wall-pressure generation by the passage of the shear layer vortical structures and their mutual interaction, provided more insight into the quasi-instantaneous variability of the characteristics of these structures; e.g., their wall-normal location, scales, streamwise spacing, etc. More importantly, when the stochastic estimation results were coupled with analysis of the leading-order term of the wall-pressure sources from Poisson's equation, two important wall-pressure-generating mechanisms were revealed. The first was associated with strong dv'/dx disturbances that are produced by the passage of the high-vorticity vortex cores in the outer part of the flow. This produced a uniformly distributed wall-pressure source in the region $y/\delta > 0.2$. Closer to the wall, a stronger, more

localized source was found to result from coupling of weak dv'/dx disturbances resulting from the vortex passage with the strong mean-flow shear due to du/dy. Although this source was stronger in magnitude than the outer-shear layer source, because of its proximity to the wall and the strength of du/dy, it occupied a much smaller fraction of the boundary layer, and hence integration of all sources across the boundary layer is expected to result in practically equal importance of the outer and near-wall mechanisms for generating the wall pressure. It is important to realize that while it is likely that the former mechanism could be modeled by the wall-pressure field associated with quasi-periodic passing of vortices embedded in uniform inviscid flow, the latter mechanism requires proper account of viscous effects near the wall and associated mean shear.

5.2. Future Work

The following is a list of items suggested as a possible extension/refinement of the present study:

1. As demonstrated herein, the stochastically-estimated velocity based on the instantaneous wall-pressure information has a spectrum that is similar in shape but attenuated in magnitude in comparison to the actual velocity spectrum. A possible idea to remedy the attenuation in the estimate is to use time-delayed, as opposed to instantaneous, wall-pressure information to estimate the velocity. The time delay would be different for each sensor in the microphone array and taken equal to that corresponding to the maximum correlation between the pressure measured by the sensor and the velocity at the location of the estimate. To a certain extent, this approach is similar to that employed in phased, or beam-forming, microphone arrays which are used in aeroacoustic applications to

identify flow sources of noise. By phase-shifting and adding signals from the different microphones, the "net" array output can be made to respond to noise generated from a particular location in the flow, while canceling out contribution from other locations. It is recommended that such a "beam-forming" Stochastic Estimation be attempted on the current data set, and the results compared to the instantaneous velocity.

2. Conducting two-dimensional multi-point velocity measurements simultaneously with wall-pressure measurements to obtain the spatial characteristics of the flow field in the investigated zone. The velocity measurements could be conducted using Particle Image Velocimetry, or by traversing an X-hotwire over a two-dimensional spatial grid in x and y, instead of y only as done here.
3. Examine the space-time characteristics of the stochastically-estimated velocity field based on the results from the simultaneous measurements described in item 2 above.
4. Conduct an experiment using different X-wire configurations to measure u', v' and w' over a three-dimensional grid above the microphone array. This will enable calculations of the pressure-velocity correlation for all three components of the velocity and in three dimensions, yielding a stochastic estimation of the full three-dimensional flow structures. Subsequent analysis of the velocity field will not only allow understanding of the full three-dimensional nature of the pressure sources, but also assessing the importance of the non-linear sources of pressure, which is an issue that was raised but not addressed in the current work.

A. Derivation of Equation (2.6)

From the X-wire probe geometry shown in Figure 2.22, the effective velocities of HW #1 and HW #2 (U_{e1} and U_{e2}) may be given as follow:

$$U_{e1} = u\,F_1^2(90-\alpha_1) - v\,F_1^2(\alpha_1) \tag{A.1}$$

$$U_{e2} = u\,F_2^2(90-\alpha_2) + v\,F_2^2(\alpha_2) \tag{A.2}$$

Equation (A.1) can be solved for v to give:

$$v = \frac{u\,F_1^2(90-\alpha_1) - U_{e1}}{F_1^2(\alpha_1)} \tag{A.3}$$

plugging the above equation into equation (A.2):

$$U_{e2} = u\,F_2^2(90-\alpha_2) + \left(\frac{u\,F_1^2(90-\alpha_1) - U_{e1}}{F_1^2(\alpha_1)}\right)F_2^2(\alpha_2) \tag{A.4}$$

$$F_1^2(\alpha_1)\,U_{e2} + F_2^2(\alpha_2)\,U_{e1} = u\left(F_2^2(90-\alpha_2)\,F_1^2(\alpha_1) + F_1^2(90-\alpha_1)\,F_2^2(\alpha_2)\right) \tag{A.5}$$

and,

$$u = \frac{U_{e2}\,F_1^2(\alpha_1) + U_{e1}\,F_2^2(\alpha_2)}{F_1^2(90-\alpha_1)\,F_2^2(\alpha_2) + F_1^2(\alpha_1)\,F_2^2(90-\alpha_2)} \tag{A.6}$$

Finally, v can be obtained by solving equations (A.3) and (A.6) together:

$$v = \left(\frac{U_{e1}\,F_2^2(\alpha_2)\,F_1^2(90-\alpha_1) + U_{e2}\,F_1^2(\alpha_1)\,F_1^2(90-\alpha_1)}{F_1^2(90-\alpha_1)\,F_2^2(\alpha_2) + F_1^2(\alpha_1)\,F_2^2(90-\alpha_2)} - U_{e1}\right)\frac{1}{F_1^2(\alpha_1)} \tag{A.7}$$

$$v = \left(\frac{\begin{array}{c} U_{e1}\,F_2^2(\alpha_2)\,F_1^2(90-\alpha_1) + U_{e2}\,F_1^2(\alpha_1)\,F_1^2(90-\alpha_1) \\ -U_{e1}\,F_2^2(\alpha_2)\,F_1^2(90-\alpha_1) - U_{e1}\,F_1^2(\alpha_1)\,F_2^2(90-\alpha_2) \end{array}}{F_1^2(90-\alpha_1)\,F_2^2(\alpha_2)\,F_1^2(\alpha_1) + F_1^2(\alpha_1)\,F_2^2(90-\alpha_2)\,F_1^2(\alpha_1)}\right) \tag{A.8}$$

$$v = \left(\frac{U_{e2}\,F_1^2(90-\alpha_1) - U_{e1}\,F_2^2(90-\alpha_2)}{F_1^2(90-\alpha_1)\,F_2^2(\alpha_2) + F_1^2(\alpha_1)\,F_2^2(90-\alpha_2)}\right) \tag{A.9}$$

B. Data Acquisition Settings

Table B.1 shows a list of the signal connections to the A/D converter, and corresponding input range and gain used with each data acquisition channel. The first channel (channel #0) was connected to the pressure transducer that measured the static pressure upstream of the model to determine U_∞, while the fourth channel was connected to the output of the temperature sensor used to measure the flow temperature for calculation of the air density and temperature-correction of the hotwire output. Because it was important to acquire the mean voltage of the hotwire (HW) output, which ranged from 1 to 2 Volt, as well as resolve the substantially-smaller fluctuating voltage, the output of the each of the wires was acquired using two channels. The first channel, which was set with large input range (to accommodate the large mean voltage value) and low gain, was used to calculate the mean of the HW output, while the second channel, which was set with small input range and high gain, was employed to acquire the mean-removed HW output voltage, which was obtained using a high-pass filter, of a cut-off frequency of 0.2 Hz, that was built in a Larson & Davis (L&D) preamplifier (model 2200C). Subsequently, the time series of HW #1 and HW #2 were obtained by adding the mean voltage of channel #1 and channel #2 to the voltage time series of channel #4 and channel #5, respectively. Finally, the last ten A/D channels were connected to the last ten microphones (from microphone # 7 to #16).

Data were acquired with a total sampling frequency of 200,000 sample/s, which corresponded to 12,500 sample/s per channel. 2^{21} (2,097,152) samples per channel were acquired at each of the twenty six hotwire locations: from y = 4 to 54 mm in increments

of 2 mm. A LabView program was used to operate the data acquisition system, automatically traversing the HW probe, and acquiring/saving data from the 16 channels.

Table B.1. Data acquisition settings

A/D Channel #	Input Signal	Input range [V]	Gain
Channel # 0	Pressure Tansducer	± 5.0	1.0
Channel # 1	HW#1 signal	± 5.0	1.0
Channel # 2	HW#2 signal	± 5.0	1.0
Channel # 3	Temperature Sensor	± 0.5	10.0
Channel # 4	HPF HW#1 signal	± 0.5	10.0
Channel # 5	HPF HW#2 signal	± 0.5	10.0
Channel # 6	Most usptream microphone (Mic #7)	± 0.5	10.0
:	:		
Channel # 15	Most downstream microphone (Mic #16)		

References

Adrian, R. J., "On the Role of Conditional Averages in Turbulent Theory," Proceeding of the Fourth Biennial Symposium of Turbulence in Liquids, September 1975, Princeton, NJ, 1977, pp. 323.

Adrian, R. J., "Conditional Eddies in Isotropic Turbulence," Physics of Fluids, Vol. 22, pp. 2065, 1979.

Adrian, R. J. and Moin, P., "Stochastic Estimation of Organized Turbulent Structure: Homogeneous Shear Flow," Journal of Fluid Mechanics, Vol. 190, pp. 531, 1988.

Adrian, R. J., Moin, P., and Moser, R. D., "Stochastic Estimation of Conditional Eddies in Channel Flow," Report CTR-S87, Center of Turbulence Research, NASA Ames/Stanford, 1987.

Arie, M. and Rouse, H., "Experiments on Two-Dimensional Flow Over a Normal Wall," Journal of Fluid Mechanics, Vol. 1, pp. 129-141, 1956.

Blake, W. K., "Mechanics of Flow-Induced Sound and Vibration", Applied Mathematics and Mechanics, Academics, Orlando, FL, 1986.

Bonnet, J. P., Cole, D., Delville, J., Glauser, M. N. and Ukeiley, L., "Stochastic Estimation and Proper Orthogonal Decomposition: Complementary Techniques for Identifying Structures," Experiments in Fluids, Vol. 17, pp. 307-314, 1994.

Bonnet, J. P., Delville, J. and Glauser, M. N., "Coherent Structures in Turbulent Shear Flows: The Confluence of Experimental and Numerical Approaches," Proceedings of ASME FEDSM'02, Montreal, Quebec, Canada, July 14-18, 2002.

Bradshaw, P., "Inactive Motion and Pressure Fluctuations in Turbulent Boundary Layers," Journal of Fluid Mechanics, Vol. 30, pp. 241-258, 1967.

Bradshaw, P. and Wong, F. Y. F., "The Reattachment and Relaxation of a Turbulent Shear Layer," Journal of Fluid Mechanics, Vol. 52, pp. 113-135, 1972.

Brereton, G. J., "Stochastic Estimation as a Statistical Tool for Approximating Turbulent Conditional Averages", Physics of Fluids A, Vol. 4, No. 9, pp. 2046-2054, 1992.

Castro, I. P. and Epik, E., " Boundary Layer Development after a Separated Region," Journal of Fluid Mechanics, Vol. 374, pp. 91-116, 1998.

Castro, I. P. and Haque, A., "The Structure of a Turbulent Shear Layer Bounding a Separation Region," Journal of Fluid Mechanics, Vol. 179, pp. 439-468, 1987.

Chandrsuda, C. and Bradshaw, P., "Turbulence Structure a Reattaching Mixing Layer," Journal of Fluid Mechanics, Vol. 110, pp. 171-194, 1981.

Change, P.A., Piomelli, U. and Blake, W. K., "Relationship Between Wall Pressure and Velocity-Field Sources," Physics of Fluids, Vol. 11, pp. 3434-3448, 1999.

Cherry, N. J., Hillier, R., and Latour, M. E. M. P., "Unsteady Measurements in a Separated and Reattaching Flow," Journal of Fluid Mechanics, Vol. 144, pp. 13, 1984.

Choi, W. C. and Guezennec, Y. G., "On the Asymmetry of Structures in Turbulent Boundary Layers," Physics of Fluids A, Vol. 2, No. 4, pp. 628-630, 1990.

Coles, D., "The Law of the Wake in the Turbulent Boundary Layer", Journal of Fluid Mechanics, Vol. 1, pp. 191-226, 1956.

Driver, D. M., Seegmiller, H. L. and Marvin, J. G., "Time-Dependent Behavior of Reattaching Shear Layer," AIAA Journal, Vol. 25, No. 7, pp. 914-919, 1987.

Eaton, J. K. and Johnston, J. P., "Low Frequency Unsteadiness of a Reattaching Turbulent Shear Layer," In: Proceedings of the Third International Symposium on Turbulent Shear Flow, Springer, Berlin Heidelberg, pp. 162-170, 1982.

Farabee, T. M., "An Experimental Investigation of Wall Pressure Fluctuations Beneath Non-Equilibrium Turbulent Flows", Ph.D. Thesis, The Catholic University of America, May 1986.

Farabee, T. M. and Casarella, M. J., "Measurements of Fluctuating Wall Pressure for Separated/Reattached Boundary Layer Flows," Journal of Vibration, Acoustics, Stress, and Reliability in Design, Vol. 108, pp. 301-307, 1986.

Farabee, T. M. and Casarella, M. J., "Spectral Features of Wall Pressure Fluctuations Beneath Turbulent Boundary Layer," Physics of Fluids A 3, pp. 2410, 1991.

Fiedler, H. E., "Coherent Structures in Turbulent Flows", Prog. Aerospace Sci, Vol. 25, pp. 231-269, 1988.

Gence, J. N. and Mathieu, J., "The Return to Isotropy of an Homogeneous Turbulence Having Been Submitted to two Successive Plane Strains", Journal of Fluid Mechanics, Vol. 101, Part 3, pp. 555-566, 1980.

George, W. K., Beuther, P. D. and Arndt, R. G., "Pressure Spectra in Turbulent Free Shear Flows," Journal of Fluid Mechanics, Vol. 148, pp. 155-191, 1984.

Glauser, M., Eaton, E., Taylor, J., Cole, D., Ukeiley, L., Citriniti, J. H., George, W. K. and Stokes, S., "Low-Dimensional Descriptions of Turbulent Flows: Experiments

and Modeling", The 30th AIAA Fluid Dynamics Conference, June 28th – July 1st, Norfolk, VA, 1999.

Gravante, S., Naguib, A., Wark, C. and Nagib, H., "Reynolds Number Effects on Time-Resolved Measurement of the Wall Pressure Beneath a Turbulent Boundary Layer," Fluid Dynamics Research Center, Mechanical, Material, and Aerospace Engineering Department, Illinois Institute of Technology, Chicago, IL, December, 1995.

Gravante, S., Naguib, A., Wark, C. and Nagib, H., "Characterization of the Pressure Fluctuations Under a Canonical Turbulent Boundary Layer," AIAA Journal, Vol. 36, No. 10, pp. 1808-1816, 1998.

Guezennec, Y. G., "Stochastic Estimation of Coherent Structures in Turbulent Boundary Layers," Physics of Fluids A, Vol. 1, No. 6, pp. 1054-1060, June, 1989.

Guezennec, Y. G., Piomelli, U. and Kim, J., "Conditionally-Averaged Structures in Wall-Bounded Turbulent Flows," Proceedings of the 1987 Summer Program of Center for Turbulence Research, pp. 263, 1987.

Heenan, A. F. and Morrison, J. F., "Passive Control of Pressure Fluctuations Generated by separated Flow", AIAA Journal, Vol. 36, No. 6, June, 1998.

Ho, C. and Huerre, P., "Perturbed Free Shear Layers", Annual Review of Fluid Mechanics, 16, pp. 365-424, 1984.

Ho, C. and Huang, L., "Subharmonics and Vortex Merging in Mixing Layers", Journal of Fluid Mechaincs, Vol. 119, pp. 443-473, 1982.

Hudy, L. M., "Simultaneous Wall-Pressure Array and PIV Measurements in a Separating/Reattaching Flow region", M. Sc. Thesis, Dept. of Mechanical Engineering, Michigan State University, East Lansing, MI, 2001.

Hudy, L. M., Naguib, A. M. and Humphreys, W. M., "Wall-Pressure-Array Measurements Beneath a Separating/Reattaching Flow Region", Physics of Fluids, Vol. 15, No. 3, pp. 706-717, 2003.

Hussain, A. K. M. F. and Zedan, M. F., "Effects of the Initial Condition of the Axisymmetric Free Shear Layer: Effects of the Initial Momentum Thickness", Physics of Fluids, Vol. 21, No. 7, July, 1978.

Johansson, A. V., Her, J. Y., Haritonidis, J. H., "On the Generation of High-Amplitude Wall-Pressure Peaks in Turbulent Boundary Layers and Spots," Journal of Fluid Mechanics, Vol. 175, pp. 119, 1987.

Kim, J., "On the Structure of Pressure Fluctuations in Simulated Turbulent Channel Flow," Journal of Fluid Mechanics, Vol. 205, pp. 421, 1989.

Kinsler, L. E, Frey, A, R., Coppens, A. B. and Sanders, J. V., "Fundamentals of Acoustics", 3rd edition, John Wiley and Sons, New York, 1982.

Kiya, M. and Sasaki, K., "Structure of Large-Scale Vortices and Unsteady Reverse Flow in the Reattaching Zone of a Turbulent Separation Bubble," Journal of Fluid Mechanics, Vol. 154, pp. 463, 1985.

Kiya, M., Sasaki, K. and Arie, M., "Discrete-Vortex Simulation of a Turbulent Separation Bubble", Journal of Fluid Mechanics, Vol. 120, pp. 219-244, 1982.

Klebanoff, P. S., "Characteristics of Turbulence in a Boundary Layer with Zero Pressure Gradient", TN 3178, NACA, 1954.

Lee, I. and H. J. Sung, "Characteristics of Wall Pressure Fluctuations in Separated and Reattaching Flows Over a Backward-Facing Step: Part I. Time-Mean Statistics and Cross-Spectral Analyses," Experiments in Fluids, Vol. 30, pp. 262-272, 2001.

Lee, I. and H. J. Sung, "Multiple-Arrayed Pressure Measurement for Investigation of the Unsteady Flow Structure of a reattaching Shear Layer", Journal of Fluid Mechanics, Vol. 463, pp. 337-402, 2002.

Lueptow, R. M., "Spatio-temporal Development of Wall Pressure Events in Turbulent Wall-Bounded Flow," Eur. J. Mech. B/Fluids 16, pp. 191, 1997.

Lumely, J. L., "Interpretation of Time Spectra Measure in High-Intensity Shear Flows," Physics of Fluids, Vol. 8, pp. 1056-1062, 1965.

Monin. A. S. and Yaglom, A. M., "Statistical Fluid Mechanics: Mechanics of Turbulence", Vol. II, The MIT Press, Cambridge, MS, 1975.

Morris, S. C. and Foss, J. F., "Turbulent boundary layer to single-stream shear layer: the transition region," Journal of Fluid Mechanics, Vol. 494, pp. 187-221, 2003.

Murray, N.E. and Ukeiley, L. S., "Estimation of the Flowfield from Surface Pressure Measurements in an Open Cavity", AIAA Journal, Vol. 41, No. 5, pp. 969-972, 2003.

Murray, N.E. and Ukeiley, L. S., "Low-dimensional estimation of cavity flow dynamics", AIAA 2004-0681 42nd AIAA Aerospace Sciences Meeting and Exhibit, Reno, NV, January 5 – 8, 2004.

Naguib, A. M. and Koochesfahani, M. M., "On Wall-Pressure Sources Associated with the Unsteady Separation in a vortex-Ring/Wall Interaction", the 33rd AIAA Fluid Dynamics Conference and Exhibit, Orlando, Florida, June 23-26, 2003.

Naguib, A. M., Gravante, S. P. and Wark, C. E., "Extraction of Turbulent Wall-Pressure Time-Series Using an Optimal Filtering Scheme," Experiments in Fluids, Vol. 22, pp. 14-22, 1996.

Naguib, A. M., Hudy, L. M. and Humphreys, W. M., "Stochastic Estimation and Non-linear Wall-Pressure Sources in a Separating/Reattaching Flow", Proceeding of the 2002 Fluids Engineering Division Summer Meeting, Montreal, Quebec, Canada, July 14-18, 2002.

Naguib, A. M., Wark, K. and Juckenhoefel, O., "Stochastic Estimation and Flow Sources Associated with Surface Pressure Events in a Turbulent Boundary Layer," Physics of Fluids, Vol. 13, No. 9, pp. 2611-2625, 2001.

Panton, R. L. and Linbarger, J. H., "Wall Pressure Spectra Calculations for Equilibrium Boundary Layers", Journal of Fluid Mechanics, Vol. 65, Part 2, pp. 261-287, 1974.

Perry, A. E., Henbest, S. and Chong, M. S., "A Theoretical and Experimental Study of Wall Turbulence", Journal of Fluid Mechanics, Vol. 165, pp. 163-199, 1986.

Ruderich, R. and Fernholz, H. H., "An Experimental Investigation of a Turbulent Shear Flow with Separation, Reverse Flow, and Reattachment," Journal of Fluid Mechanics, Vol. 163, pp. 283-332, 1986.

Schmit, R. F. and Glauser, M. N. "Improvements in Low Dimensional Tools for Flow-Structure Interaction Problems: Using Global POD", AIAA 2004-0889, 42nd AIAA Aerospace Sciences Meeting and Exhibit, Reno, NV, January 5 – 8, 2004.

Smits, A. J., "Scaling Parameters for a Time-Averaged Separation Bubble," AIAA Journal, Vol. 104, pp. 178, 1982.

Song, S. and Eaton, J. K., "Reynolds Number Effects on a Turbulent Boundary Layer with Separation, Reattachment, and Recovery", Report No. TSD-146, Mechanical Engineering Department, Stanford University, Stanford, California, April, 2002.

Spazzini, P. G., Iuso, G., Onorato, M., Zurlo, N. and Di Cicca, G. M., "Unsteady Behavior of Back-Facing Step Flow," Experiments in Fluids, Vol. 30, pp. 551, 2001.

Taylor, G. I., "The Spectrum of Turbulence," Proc. R. Soc. London Ser. A 164, 476-490, 1938.

Taylor, J. and Glauser, M. N., "Towards Practical Flow Sensing and Control Via POD and LSE Based Low-Dimensional Tools", Proceedings of ASME FEDSM'02, Montreal Quebec, Canada, July 14 – 18, 2002.

Thomas, A. S. W. and Bull, M. K., "On the Role of Wall-Pressure Fluctuations in Deterministic Motions in Turbulent Boundary layer", Journal of Fluid Mechanics, Vol. 128, pp. 283, 1983.

Townsend, A. A., "Equilibrium Layers and Wall Turbulence," Journal of Fluid Mechanics, Vol. 11, pp. 97 –120, 1961.

Tung, T. C. and Adrian, R. J., "Higher-Order Estimates of Conditional Eddies in Isotropic Turbulence", Physics of Fluids, Vol. 23, No. 7, July, 1980.

Wark, C. and Naguib, A. M., "On the Relation Between the Wall Pressure and Velocity Field in a Turbulent Boundary Layer", the 29th AIAA Fluid Dynamics Conference, Albuquerque, NM, June 15-18, 1998.

Wei, T. and Willmarth, W. W., "Reynolds-Number Effects on the Structure of a Turbulent Channel Flow", Journal of Fluid Mechanics, Vol. 204, pp. 57-95, 1989.

Willmarth, W. W., "Pressure Fluctuations Beneath Turbulent Boundary Layers", Annual Review Fluid Mechanics, Vol. 7, pp. 13-38, 1975.

Wills, J. A. B., "On Convection Velocities in Turbulent Shear Flows", Journal of Fluid Mechanics, Vol. 20, Part 3, pp. 417-432, 1964.